ISSN:2538-516X

Journal of
Civil Engineering Researchers

Volume: 7; Number: 4; December 2025

J-Researchers

J-Researchers

JOURNAL OF
CIVIL
ENGINEERING
RESEARCHERS

Volume 7, Number 4, December 2025

Contents

J-Researchers

Journal of Civil Engineering Researchers

Journal homepage: www.journals-researchers.com

Optimizing Date Seed Utilization in Green Concrete: A Methodological Evaluation

Shadzi Rezaei,[a] Rasoul Shadnia,[a,*] Mojtaba Lezgi Nazarghah [a]

[a] *Department of Civil Engineering, Hakim Sabzevari University, Sabzevar, Iran*

ABSTRACT

Concrete is one of the most widely used construction materials globally; however, its production contributes significantly to carbon dioxide emissions. In the Middle East, annual date production is substantial, and date seeds, as a byproduct, are typically discarded. This study investigates three methods for incorporating date seeds into concrete: (1) Cement replacement: Using powdered date seeds (PDS) as a partial substitute for cement at 5%, 10%, 15%, and 20% levels; (2) Aggregate replacement: Replacing coarse aggregates with crushed date seeds (CDS) at 10%, 20%, and 30% ratios and (3) Hybrid approach: Combining PDS (0%, 5%, 10%, and 20%) with fly ash (fixed at 20%). Mechanical tests revealed that replacing cement with up to 10% PDS had no significant impact on compressive strength, whereas higher replacement levels reduced strength. Similarly, increasing the aggregate replacement percentage led to a decline in concrete strength. In contrast, the hybrid approach—combining PDS with 20% fly ash—enhanced compressive strength. Based on these findings, the third method emerged as the most effective for improving both the strength and sustainability of concrete. The optimized hybrid mixture was selected for further comprehensive evaluation, including tests for tensile strength, flexural strength, water absorption (porosity), sulfate resistance, and freeze-thaw durability. These assessments aimed to verify not only the mechanical properties but also the long-term durability of the modified concrete under diverse environmental conditions.

ARTICLE INFO

Received: June 09, 2025
Accepted: September 07, 2025

Keywords:
Date Seed Concrete
Cement, Aggregate
Fly Ash
Mechanical Properties
Durability
Carbon Footprint Reduction

DOI: 10.66224/JCER.7.4.12
DOR: 20.1001.1.2538516.2025.7.4.2.4

1. Introduction

Concrete is one of the most widely used construction materials globally, playing a vital role in modern infrastructure. However, cement production—a key component of concrete—poses significant environmental challenges, including substantial greenhouse gas emissions and the depletion of natural resources [1–4]. Consequently, the development of sustainable concrete and eco-friendly alternatives has emerged as a critical research priority. To address this, researchers have focused on reducing cement consumption by incorporating sustainable substitute materials. Among these, organic pozzolans have garnered increasing attention due to their demonstrated effectiveness in enhancing concrete properties [5–9].

[*] Corresponding author. Tel.: +980000000000; e-mail: r.shadnia@hsu.ac.ir (Associate Professor).

The impact of pozzolanic waste materials on the durability, physical, and mechanical properties of cementitious materials has been extensively studied [10–13]. The utilization of waste materials as substitutes for cement in concrete, particularly to mitigate the negative environmental impacts of cement production and enhance the mechanical properties and durability of concrete, has garnered significant attention in recent years. Recycling such waste materials offers a dual benefit: reducing ecological footprints while generating economic savings [14–17]. For instance, studies have explored food industry by-products (e.g., sugar factory residues) and agricultural wastes (e.g., date seeds, walnut shells, eggshells, and peanut shells) as viable cement replacements. These materials act as pozzolanic additives, improving concrete properties while lowering cement consumption and its associated environmental burden. Notably, combining them with supplementary pozzolans (e.g., fly ash) has shown further improvements in durability under harsh conditions.

Among sugar industry wastes, carbonated sludge has also been investigated [18]. Sugar production generates substantial by-products like bagasse, molasses, and calcium carbonate sludge, which can be repurposed for value-added applications. While molasses has been tested in cementitious systems [19–22], bagasse has found reuse across industries [23-30], particularly in food industry [31–33].

A promising strategy to reduce concrete's environmental impact involves partial replacement of conventional materials with agricultural wastes. Walnut shell is one of the agricultural wastes that has been recognized as a pozzolanic material in the concrete industry. Researchers have shown that walnut shell can improve the mechanical properties of concrete while reducing cement consumption [34-38]. These researchers have reported that the addition of walnut shell to concrete can enhance the compressive and flexural strengths while reducing porosity and improve the concrete performance under various environmental conditions, including freeze-thaw cycles. Eggshell has also been studied as another pozzolanic material in concrete research [39-44]. Studies indicate that this material, particularly when combined with other substances such as fly ash, can enhance the mechanical properties and durability of concrete [45-49]. These studies have shown that powdered eggshell, due to its high calcium content and mineral composition, can improve concrete performance under heavy loads and environmental cycles such as freeze-thaw conditions. Another agricultural waste that has been explored as a cement substitute in concrete is the peanut shell. This material, due to its pozzolanic properties, can strengthen the mechanical characteristics of concrete. Some studies have demonstrated that incorporating peanut shell into concrete mixtures enhances its microscopic and mechanical properties, resulting in a stronger and more durable material capable of withstanding various environmental conditions [50-53].

Of these, date seeds stand out due to their untapped potential [54–58]. With millions of tons produced annually, date seeds—largely discarded—contain pozzolanic compounds suitable for cement substitution [57, 58]. However, existing studies lack a systematic comparison of application methods (e.g., powder replacement vs. hybrid use with fly ash).

This study introduces a novel approach by not only investigating the use of date seeds as a substitute in concrete but also systematically evaluating and comparing different methods of its application. Unlike previous studies, which have not comprehensively assessed various techniques—such as grinding the date seeds into powder, using date seeds as a direct replacement, or combining date seeds with supplementary cementitious materials (e.g., fly ash), this study addresses this gap by: (1) Evaluating three different methods of date seeds incorporation including: cement replacement with powdered date seeds (PDS) (5–20%), aggregate replacement with crushed date seeds (CDS) (10–30%) and hybrid use of PDS (0–20%) + fly ash (20%); and (2) Comprehensively assessing mechanical properties (compressive/tensile/flexural strengths) and durability (water absorption, sulfate resistance, freeze-thaw cycles). By identifying the optimal approach, this work advances sustainable construction practices while offering a practical solution to repurpose agricultural waste, ultimately reducing the construction sector's environmental footprint.

2. Materials and Methods

2.1. Collection and Preparation of Materials

In all experiments, Type II Portland cement was used (see Table 1). The water-to-cement ratio (w/c) was maintained between 0.4 and 0.45 based on the test type: 0.42 for aggregate replacement with CDS and 0.45 for the other two cases, in accordance with ASTM C192 standards. We used drinking water from Sabzevar city, which met pH requirements (see Table 2 for complete characteristics).

All aggregates complied with ASTM C33 requirements. The sand used in this study had a maximum particle size of 4.75 mm, 5% moisture content, and a fineness modulus of 3.45. To enhance concrete's mechanical properties, coarse aggregates—including pea gravel (4.75-9.5 mm) and crushed stone (9.5-19 mm)—were used, both with 0% moisture content. All aggregates were sourced from Sarakhs Tangshur-Sardar Road, Iran.

Table 1.
Chemical Composition of Type II Portland Cement

Oxides		(%) MIN	(%) MAX	Key Factors		(%) MIN	(%) MAX
Silicon Dioxide	SiO_2	20.50	22.0	Lime Saturation Factor	LSF	92.0	97.0
Aluminium Oxide	Al_2O_3	4.60	5.30	Silica Module	SiM	2.40	2.60
Ferric Oxide	Fe_2O_3	3.50	4.00	Alumina Module	AlM	1.20	1.40
Calcium Oxide	CaO	63.00	65.00	Tricalcium Silicate	C_3S	50.00	60.00
Magnesium Oxide	MgO	1.50	2.50	Dicalcium Silicate	C_2S	15.00	25.00
Sulphur Trioxide	SO_3	1.50	2.50	Tricalcium Aluminate	C_3A	5.00	8.00
Potassium Oxide	K_2O	0.50	0.70	Tetracalcium Aluminate	C_4AF	10.0	12.00
Sodium Oxide	Na_2O	0.30	0.50				
Loss on Ignition	L.O.I	1.00	2.50				
Insoluble Residue	I.R.	0.10	0.70				
Free Lime	Free CaO	0.70	1.40				

Table 2.
Chemical and physical characteristics of drinking water used in experiments compared with relevant standards

Property	**Unit**	**Desired Maximum**	**Permissible**	**Used Water**
Odor	TON	Max 2 units at 12°C and Max 3 units at 25°C	-	3 at 25°C
Color	TCU	-	15	12
pH	-	6.5 - 8.5	6.5 - 9	7.2
Hardness	ppm	200	500	450
TDS	ppm	1000	1500	1400
Turbidity	NTU	≤ 1	5	4

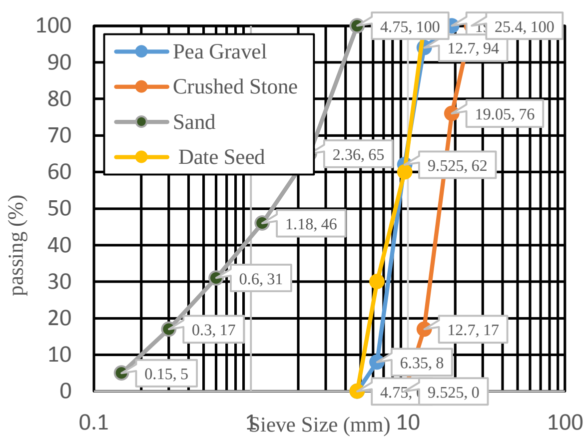

Figure 1. Aggregate Gradation Based on ASTM C33

All aggregates complied with ASTM C33 requirements. The sand used in this study had a maximum particle size of 4.75 mm, 5% moisture content, and a fineness modulus of 3.45. To enhance concrete's mechanical properties, coarse aggregates—including pea gravel (4.75-9.5 mm) and crushed stone (9.5-19 mm)—were used, both with 0% moisture content. All aggregates were sourced from Sarakhs Tangshur-Sardar Road, Iran.

Date seeds were primarily obtained from a date syrup production factory in Dashtestan, Bushehr Province, Iran - one of the country's main date processing centers that generates substantial date seed waste. After collection, the date seeds were transferred to the laboratory for processing. To evaluate date seed effects through three different approaches, processing occurred in three stages:

1. PDS as Partial Cement Replacement

Date seeds were dried in an oven at 110°C for 24 hours to reduce moisture content. After drying, they were ground using either a ball mill or hammer mill to achieve a particle size below 75 µm (comparable to cement). The powder was substituted for cement at replacement levels of 5%, 10%, 15%, and 20%.

1. CDS as Coarse Aggregate Replacement

Date seeds were first crushed with a jaw crusher, then sieved to match the size distribution of coarse aggregates. CDS replaced coarse aggregates at levels of 10%, 20%, and 30%.

3. Combined Use of PDS and Fly Ash

This method incorporated PDS (processed as in Method 1) with fly ash. A fixed 20% fly ash replacement was selected due to its well-documented benefits including: (1) Pozzolanic reaction with calcium hydroxide enhances strength and durability and (2) Reduces cement consumption and carbon emissions without compromising structural integrity. PDS were tested at 0%, 5%, 10%, and 20% alongside 20% fly ash baseline. The control sample contained 20% fly ash and 0% PDS.

To figure out the best method, compressive strength was measured for all three methods mentioned above. The optimal method underwent additional tests: splitting tensile and flexural strengths, water absorption, sulfate attack and freeze-thaw resistances.

3.1. Test Method

To evaluate the quality of the produced concrete, the following tests were conducted:

Compressive Strength: The compressive strength test was conducted in accordance with ASTM C39. The concrete cube specimens of 150 × 150 × 150 mm were prepared and cured for 7, 28, and 90 days. Before testing, their surfaces were inspected to ensure they were flat and free of irregularities. Then the specimens were centered in the compression testing machine, ensuring that the top surface was in direct contact with the loading plate. A continuous and uniform load was then applied at a specified rate (0.25 ± 0.10 MPa/s) until the specimen failed. Finally, the maximum load sustained before failure was recorded. The compressive strength was calculated by dividing the maximum load by the cross-sectional area of the specimen.

Splitting Tensile Strength: The splitting tensile strength test was conducted on cylindrical specimens with dimensions of 15x30 cm, following ASTM C496. This test evaluates the tensile strength of concrete by applying a diametral compressive load until failure. The applied load generates tensile stresses perpendicular to the loading direction, causing the specimen to split along its vertical axis. This test is essential for assessing the indirect tensile strength of concrete (as given by Eq. 1), which influences its cracking resistance and structural performance.

$$\sigma_t = \frac{2 \times P}{\pi \times d \times t} \tag{1}$$

Where σ_t, P, d and t are respectively the splitting tensile strength (MPa), applied compressive load at failure (N), diameter of the specimen (mm) and thickness (or length) of the specimen (mm).

Flexural Strength: The flexural strength test was conducted on beam specimens (10×10×50 cm) in accordance with ASTM C78. This test evaluates concrete's resistance to bending forces through a third-point or center-point loading until failure. It provides critical insights into the tensile behavior of concrete under flexural stress, which is essential for designing beams, pavements, and other structural elements subjected to bending loads. Flexural strength was calculated using Equation 2:

$$\sigma_{fb} = \frac{3 \times P \times l}{2 \times b \times d^2} \tag{2}$$

Where σ_{fb}, P, l, b and d are respectively flexural strength (MPa), maximum applied load at failure (N), span length (distance between supports, mm), width of the specimen (mm) and depth (or height) of the specimen (mm.)

Water Absorption (w): The water absorption test was conducted in accordance with ASTM C642 to evaluate concrete porosity. This test quantifies the water absorption capacity of concrete specimens, serving as a direct indicator of porosity. Specimens were first oven-dried at 105 ± 5°C until reaching constant mass (W_d). The dried specimens were then fully submerged in water at room temperature for 48 hours to achieve saturation. After removal from water, surface moisture was carefully removed with a damp cloth to determine the saturated surface-dry mass (W□). Finally, the specimen's submerged mass (W□$_{ub}$) was measured. Water absorption and total porosity were calculated using Equations 3 and 4, respectively.

$$Water\ Absorption(\%) = \frac{(Ws - Wd)}{Wd} \times 100 \tag{3}$$

$$Total\ Porosity\ (\%) = \frac{(Ws - Wd)}{(Ws - Wsub)} \times 100 \tag{4}$$

Sulfate Attack Resistance (Weight Loss Method): To assess the chemical durability of concrete against sulfate attack, 50 mm cube specimens were immersed in a 5% sodium sulfate ($Na_2\ SO_4$) solution for 90 days following standard durability testing protocols. Prior to immersion, all specimens were fully cured and surface-dried to ensure uniform exposure conditions. Sulfate attack resistance was quantified by measuring mass loss percentage, which indicates cement matrix degradation caused by sulfate-induced expansion and cracking. After exposure, specimens were removed, surface-dried, and weighed. The mass difference before and after immersion was used to calculate the percentage mass loss, with greater values corresponding to reduced chemical resistance. The sulfate attack resistance (expressed as percentage mass loss) was calculated using Equation 5.

$$R_s = \frac{Winitial - Wsulfate}{W\ initial} \times 100 \tag{5}$$

Where R_s, $Winitial$ and $Wsulfate$ are respectively sulfate attack resistance (expressed as percentage weight loss), initial weight of the specimen (before sulfate exposure) and weight of the specimen after sulfate exposure.

Resistance to Freeze-Thaw Cycles: The freeze-thaw resistance of concrete was evaluated in accordance with ASTM C666 (Method A) to assess durability under cyclic freezing and thawing conditions. After 14 days of initial curing, specimens were saturated in limewater prior to testing. Each freeze-thaw cycle consisted of: (1) Cooling to -18°C (freezing); (2) Heating to +4°C (thawing) and (3) Maintaining specimens fully submerged in water throughout. Specimens were periodically removed (every 30 cycles) for evaluation by: (1) Measuring mass loss of surface-dried specimens; (2) Recording length changes and (3) Conducting visual inspections for surface deterioration (cracking, spalling). Freeze-thaw resistance was quantified using Equation 6.

$$\text{Weight Loss (\%)} = \frac{Winitial - Wfinal}{W\ initial} \times 100 \tag{6}$$

Where $Winitial$ and $Wfinal$ are respectively the initial weight of the specimen before cycles and weight after a specified number of cycles (e.g., after 30 cycles).

4. Test Results

4.1. Compressive strength results

4.1.1. Effect of PDS as a Partial Cement Replacement

This study demonstrates the viability of PDS as a sustainable partial cement replacement in concrete. Compressive strength was evaluated at replacement levels of 5%, 10%, 15%, and 20% across 7-, 28-, and 90-day curing periods (see Figure 2). The results show a gradual decline in compressive strength as the replacement ratio increases. The control sample (with no substitution) achieved compressive strengths of 28 MPa, 38 MPa, and 45 MPa respectively at these intervals, providing a strong baseline for comparison. While the early-age strengths (7-day compressive strength) showed slight variations, the results were generally encouraging. At 5% and 10% replacement levels, the compressive strength decreased by approximately 3% to 7% across different ages. Specifically, at 7 days, the strength dropped from 28 MPa (control sample) to 27.16 MPa (5% PDS) and 26.32 MPa (10% PDS). This demonstrates that even at early curing stages, the integrity of the concrete remains intact with PDS.

A similar trend was observed at 28 and 90 days, with reductions of about 4% to 6% compared to the control sample, showcasing a performance that is well within the acceptable range for structural applications. These results highlight how small adjustments in cement composition can yield comparable mechanical properties while reducing cement consumption. The results also confirmed the suitability of PDS as a sustainable alternative. The strength reductions have been attributed to the limited pozzolanic reactivity of PDS and the dilution of cementitious compounds. However, the reduction remained within an acceptable range, indicating that up to 10% replacement could be feasible for sustainable concrete production. The long-term performance of the concrete was particularly impressive. At 90 days, strengths of 42.75 MPa and 40.3 MPa for 5% and 10% substitution levels indicate the ongoing pozzolanic activity of PDS. This underscores its ability to contribute to strength development over time, making it a promising supplementary cementitious material.

Even at higher substitution levels (15% and 20%), the results remained within a feasible range for applications where sustainability is prioritized over peak mechanical performance. At a 15% replacement ratio, a more noticeable strength decline occurred, with a 10% to 12% reduction in strength at different ages. The compressive strength at 28 days dropped from 38 MPa (control sample) to 33.44 MPa, highlighting the negative impact of excessive cement replacement. When the replacement level reached 20%, the strength loss became significant, with reductions of approximately 15% to 18%. The 90-day compressive strength decreased from 45 MPa (control sample) to 36.90 MPa, confirming that an excessive amount of PDS negatively affects the hydration process.

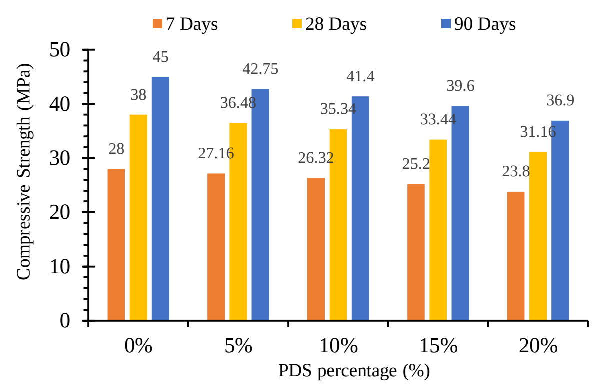

Figure 2. Compressive strength of concrete samples with different PDS replacement as cement at various ages

4.1.2. Effect of CDS as Coarse Aggregate Replacement

Figure 3 presents the compressive strength development of concrete mixtures containing CDS as partial coarse aggregate replacement at 0% (control), 10%, 20%, and 30% replacement levels. Strength measurements were conducted at 7, 28, and 90 days of curing. The results show a gradual reduction in compressive strength as the percentage of CDS replacing coarse aggregate increases. At 10% replacement, the compressive strength slightly decreases across all ages, with a reduction of about 4% to 5% compared to the control sample. However, the reduction at this level remains within an acceptable range, suggesting that small amounts of CDS replacement may still produce structurally viable concrete.

At 20% replacement, a more significant decline in compressive strength is observed, with reductions of approximately 10% to 14% at different curing ages. The decrease in the proportion of strong natural aggregates results in a less dense and cohesive microstructure, and thus further contributing to strength loss.

When 30% of the coarse aggregate is replaced, the compressive strength shows a substantial decline of 18% to 22% compared to the control sample. This considerable reduction suggests that at higher replacement levels, the weaker nature of date seed aggregates dominates the concrete matrix, leading to lower mechanical performance. Therefore, while partial replacement at lower percentages may be feasible, exceeding 20% to 30% replacement significantly compromises the mechanical integrity of the concrete and is not recommended for structural applications requiring high strength.

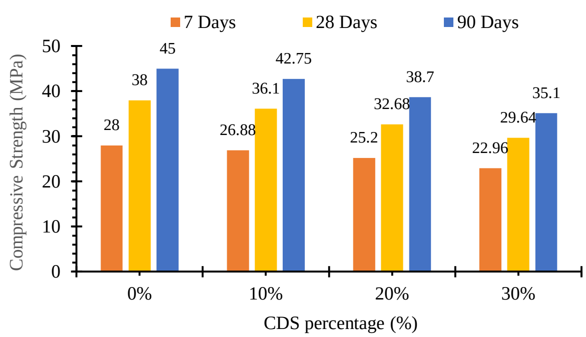

Figure 3. Compressive strength of concrete samples with different CDS replacement as coarse aggregate at various ages

4.1.3. Effect of Combining PDS with Fly Ash

This phase evaluated concrete mixtures containing PDS as a cement replacement alongside 20% fly ash. PDS replacement levels ranged from 0% to 20% (5% increments). The sample containing 20% fly ash and 0% PDS was considered the control mix for comparative evaluation. Compressive strength development was assessed at 7, 28, and 90 days (see Figure 4).

The results indicate a gradual decline in compressive strength with increasing percentages of PDS. At 7 days, the control mix showed the highest compressive strength of 29.5 MPa, which decreased slightly to 27.4 MPa for the mixture with 20% PDS. A similar trend is observed at 28 and 90 days, where the control sample reached 40.5 MPa and 48 MPa respectively, while the 20% replacement sample achieved 37.4 MPa and 44 MPa.

Although the reduction in compressive strength is evident with higher percentages of PDS, the results demonstrate that even with 20% substitution, the concrete maintained a reasonably high compressive strength. This suggests that PDS, when used in combination with fly ash, can be a feasible supplementary cementitious material, particularly in applications where environmental sustainability and resource efficiency are prioritized over maximum strength.

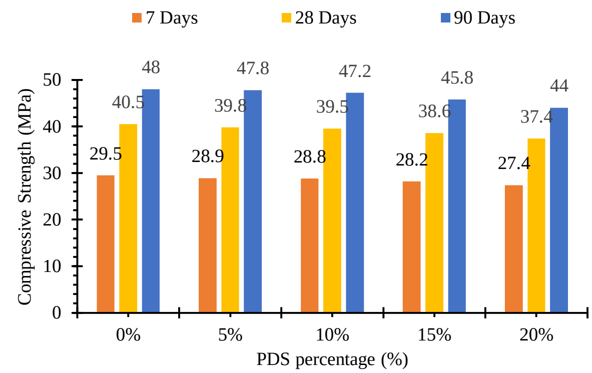

Figure 4. Compressive strength of concrete samples with different percentages of PDS replacement alongside 20% fly ash at different ages

Moreover, the rate of strength development between 28 and 90 days indicates continued pozzolanic activity, especially in the mixtures with lower percentages of PDS. This long-term gain highlights the potential for the use of agricultural waste such as date seeds in sustainable concrete production, supporting both waste valorization and carbon footprint reduction in the construction industry.

By getting precisely into the results, one can observe that at 5% replacement, the compressive strength decreased by 2.0% at 7 days, 1.7% at 28 days, and 0.4% at 90 days, compared to the control sample. The minimal strength loss at 90 days suggests that the pozzolanic activity of fly ash and fine organic particles from the PDS may compensate for the reduced cement content over time. At 10% replacement, the compressive strength showed a reduction of 2.4% at 7 days, 2.5% at 28 days, and 1.7% at 90 days relative to the control sample. This indicates that up to 10% PDS can still maintain acceptable strength levels, possibly due to improved particle packing and delayed pozzolanic contribution. At 15% replacement, strength losses became more pronounced, with 4.4% at 7 days, 4.7% at 28 days, and 4.6% at 90 days. The decrease is still within acceptable ranges for certain non-structural applications, though the trend shows that higher dosages begin to adversely affect mechanical performance. At the highest replacement level of 20% replacement, compressive strength declined by 7.1% at 7 days, 7.7% at 28 days, and 8.3% at 90 days. Although strength remains relatively high, this level of replacement may be more suitable for low-strength applications or where sustainability is prioritized over mechanical performance. In summary, incorporating PDS up to 10% as a partial cement replacement in the presence of fly ash results in minimal strength reduction, especially at later curing ages. This highlights the potential of agricultural waste utilization in green concrete technology, aligning with environmental goals without significantly compromising material performance.

4.1.4. Which Method Prevails? A Comparative Assessment

The compressive strength tests were performed for all three proposed methods of incorporating date seed into concrete including replacing cement with PDS, replacing coarse aggregate with CDS, and combining PDS with fly ash. The results indicated varying degrees of strength reduction depending on the replacement level and the method used. While partial cement and aggregate replacement with date seed showed acceptable performance at lower percentages, the third method—combining PDS with 20% fly ash—demonstrated superior compressive strength values, especially at 28 and 90 days of curing.

Based on these results, the third method was identified as the most effective and promising approach for enhancing both strength and sustainability in concrete. Therefore, this combination was selected for further investigation. Additional tests, including tensile strength, flexural strength, water absorption (porosity), sulfate attack and freeze-thaw resistances, were conducted to comprehensively evaluate the mechanical and durability performance of concrete containing this optimized mix.

4.2. Splitting Tensile Strength Results

The splitting tensile strength of concrete mixtures containing 20% fly ash and varying percentages of PDS was evaluated to assess the indirect tensile behavior of the modified concrete. As shown in Figure 5, a gradual decrease in tensile strength was observed with increasing replacement levels of PDS. The control mixture (0% PDS with 20% fly ash) achieved a tensile strength of 3.8 MPa. When 5% and 10% of cement were replaced with PDS, the tensile strength slightly declined to 3.6 MPa and 3.4 MPa, respectively. Despite the reduction, these values remain within acceptable limits for structural applications, especially where moderate tensile performance is sufficient.

The tensile strength exhibited a dose-dependent decrease at higher PDS substitution levels (15-20%), measuring 3.1 MPa (15%) and 2.8 MPa (20%). This trend can be attributed to the lower pozzolanic reactivity of organic materials compared to cement, as well as the dilution of the binder matrix. Nevertheless, the decline is consistent and indicates a predictable behavior, which is valuable for mix design optimization in sustainable construction.

Overall, the results suggest that the incorporation of up to 10% PDS alongside 20% fly ash can maintain adequate tensile strength, while higher levels may limit structural use but still offer potential in non-load-bearing or low-stress elements where environmental benefits are prioritized.

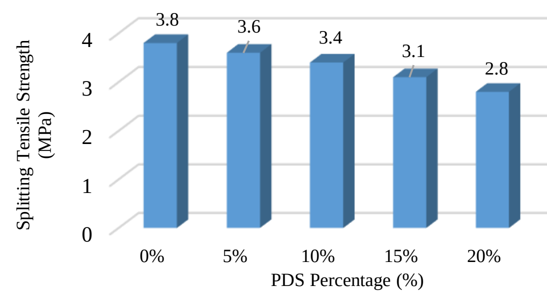

Figure 5. Splitting Tensile Strength of Concrete with Different Percentages of PDS and 20% Fly Ash

4.3. Flexural Strength Results

The flexural strength of concrete containing 20% fly ash with PDS replacements (0-20%) was evaluated through three-point bending tests. As shown in Figure 6, the results demonstrate a consistent decrease in flexural strength as the replacement percentage of PDS increased. The control mixture (0% PDS) exhibited the highest flexural strength of 5.5 MPa. Upon replacing 5% of the cement with PDS, the strength declined to 5.2 MPa, and further dropped to 4.9 MPa at the 10% replacement level. This trend of reduction continued as the replacement percentage increased: at 15%, the flexural strength decreased to 4.5 MPa, and at 20% replacement, it reached its lowest value of 4.2 MPa.

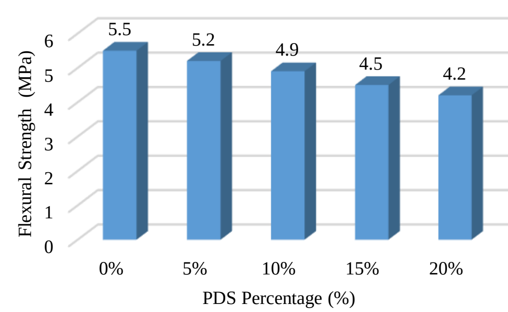

Figure 6. Flexural Strength of Concrete with Different Percentages of PDS and 20% Fly Ash

This progressive reduction in flexural strength is attributed to the decreasing cementitious content and the relatively lower binding capacity of organic materials like PDS. Despite the reductions, the values up to 10% replacement remain within the acceptable range for structural concrete, especially in applications where moderate flexural strength is sufficient. For higher replacement levels, although the strength decreases, the trend is predictable, which is valuable for sustainable concrete mix design.

4.4. Water Absorption and Porosity

Water absorption and porosity - critical indicators of concrete permeability and durability - were evaluated for mixtures containing 20% fly ash with PDS replacements (0-20%). As presented in Figure 7, both water absorption and porosity increased with the rising content of PDS. At 0% replacement, the control mix showed a water absorption of 5.2% and a porosity of 12.5%, indicating a relatively dense and impermeable matrix. With 5% and 10% replacement, water absorption rose to 5.5% and 5.9%, respectively, while porosity reached 13.1% and 13.8%. This slight increase is likely due to the less dense structure introduced by the organic date seed particles.

As the replacement level increased to 15% and 20%, the water absorption values rose to 6.3% and 6.8%, and porosity reached 14.4% and 15.0%, respectively. This behavior can be attributed to the reduced amount of cementitious material and the increased presence of porous, low-reactivity particles. The organic nature and irregular surface texture of PDS may also contribute to higher void content and moisture retention capacity in the hardened matrix. In conclusion, while the use of PDS enhances sustainability, it also leads to an increase in permeability-related properties. For durability-critical structures, the replacement level should ideally be limited to 10% to balance mechanical performance with long-term resilience.

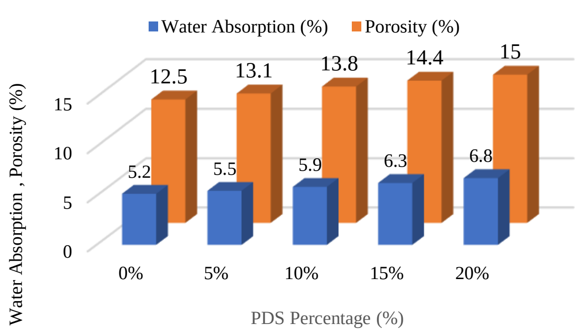

Figure 7. Water Absorption and Porosity of Concrete with Different Percentages of PDS and 20% Fly Ash

4.5. Sulfate Resistance – Weight Loss Analysis

Sulfate resistance for mixtures containing 20% fly ash and PDS (0-20%) was evaluated through 90-day immersion in 5% Na_2SO_4 solution, with results shown in Figure 8. The control sample (0% PDS) exhibited a weight loss of 2.1%, indicating good sulfate resistance due to the presence of fly ash, which helps reduce permeability and improves the matrix density. As the percentage of PDS increased, a gradual rise in weight loss was observed. At 5% and 10% replacement levels, the weight loss increased to 2.3% and 2.6%, respectively—still within acceptable durability thresholds. However, at 15% and 20% replacement, the weight loss reached 3.0% and 3.5%, respectively, suggesting a weakening resistance against sulfate attack. This can be attributed to the reduced content of reactive cementitious materials and the introduction of organic components, which may increase porosity and reduce the matrix's resistance to chemical degradation.

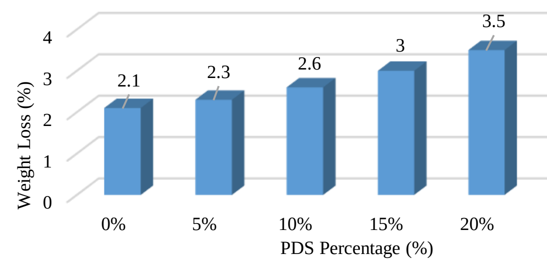

Figure 8. Weight Loss of Concrete Specimens after 90 Days of Sulfate Exposure with Different Percentages of PDS and 20% Fly Ash

These results highlight that while partial incorporation of PDS contributes to sustainability, higher substitution levels negatively affect chemical durability. To ensure long-term performance in sulfate-rich environments, it is recommended to limit the replacement level to 10% or lower when using this combination.

4.6. Freeze-Thaw Resistance

Freeze-thaw durability was assessed through three cycles of testing for concrete containing 20% fly ash and varying PDS contents (0-20%). The mass loss progression is detailed in Table 3 and Figure 9. The control sample (0% PDS) showed excellent resistance, with only 0.45% total weight loss after three cycles. Concrete with 5% and 10% PDS showed slightly higher but still acceptable weight losses of 0.65% and 0.83%, respectively, suggesting adequate durability under moderate freeze-thaw conditions. However, higher replacement levels (15% and 20%) resulted in more significant degradation. At 20% replacement, the total weight loss reached 1.50%, along with visible surface scaling and minor cracking. This decline in resistance is likely due to the increased porosity and reduced matrix density caused by the organic content of PDS. Overall, the results suggest that replacing cement with up to 10% PDS in combination with fly ash does not significantly compromise freeze-thaw resistance, but

Table 3.
Results of Freeze-Thaw Tests on Concrete Specimens including 20% Fly Ash and Different Percentages of PDS.

PDS (%)	Initial Weight (gr)	Weight after Cycle 1 (gr)	Weight Loss (%)	Weight after Cycle 2 (gr)	Weight Loss (%)	Weight after Cycle 3 (g)	Weight Loss (%)
0%	8000	7990	0.13%	7976	0.30%	7964	0.45%
5%	8010	7986	0.30%	7969	0.51%	7958	0.65%
10%	7995	7967	0.35%	7945	0.63%	7929	0.83%
15%	8030	7988	0.52%	7960	0.87%	7937	1.16%
20%	7985	7934	0.64%	7900	1.06%	7865	1.50%

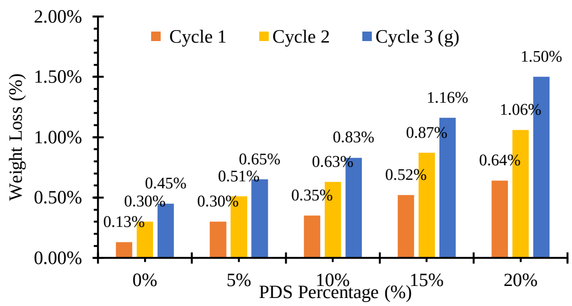

Figure 9. Weight loss (calculated from freeze-thaw tests) of concrete specimens including 20% fly ash and different percentages of PDS

higher replacement levels may lead to premature deterioration in harsh environments.

5. Conclusion

Based on the experimental findings, this study demonstrates that date seeds, an abundant agricultural byproduct in the Middle East, can be effectively incorporated into concrete to enhance sustainability while maintaining structural performance, reducing cement consumption and utilizing agricultural byproducts. Among the three methods investigated, the key findings are as follows:

1. PDS as Cement Replacement: Replacing cement with up to 10% PDS showed no significant reduction in compressive strength, whereas higher replacement levels (15–20%) led to decreased strength.
2. CDS as Coarse Aggregate Replacement: Partial replacement of coarse aggregates with CDS (10–30%) led to a consistent decrease in concrete strength, making this method less favorable for structural applications.
3. Combination of PDS and Fly Ash: The hybrid approach of blending PDS (up to 20%) with 20% fly ash improved compressive strength, suggesting a synergistic effect that enhances performance.
4. Based on these results, the optimal method for utilizing date seeds in concrete is their combination with fly ash, as it not only improves mechanical properties but also contributes to eco-friendly construction by reducing cement consumption, repurposing agricultural waste and promoting sustainability.
5. The optimal mix—5–10% PDS with 20% fly ash—maintained acceptable compressive, tensile, and flexural strengths while improving sustainability. Although higher replacement levels increased porosity and slightly reduced durability, mixes within the recommended range exhibited sufficient sulfate and freeze-thaw resistance for non-aggressive environments.
6. These findings support the use of date seed-fly ash blends in eco-friendly concrete production, offering a practical solution to reduce cement consumption and repurpose agricultural waste without compromising structural performance.
7. The study paves the way for further research into optimizing mix designs to maximize both environmental and performance benefits. Future research should explore long-term durability, thermal properties, economic feasibility for broader industrial adoption and other potential applications of date seed-modified concrete

References

[1] Belaïd, F. “How does concrete and cement industry transformation contribute to mitigating climate change challenges?” Resources, Conservation & Recycling Advances 15 (2022): 200084.

[2] Kajaste, R., and M. Hurme. “Cement industry greenhouse gas emissions–management options and abatement cost.” Journal of cleaner production 112 (2016): 4041-4052.

[3] Ali, N., A. Jaffar, M. Anwer, S. Khan, M. Anjum, A. Hussain, and X. Ming. “The greenhouse gas emissions produced by cement production and its impact on environment: a review of global cement processing.” International Journal of Research (IJR) 2.2 (2015).

[4] Miller, S. A., G. Habert, R. J. Myers, and J. T. Harvey. “Achieving net zero greenhouse gas emissions in the cement industry via value chain mitigation strategies.” One Earth 4.10 (2021): 1398-1411.

[5] Becerra-Duitama, J. A., and D. Rojas-Avellaneda. “Pozzolans: A review.” Engineering and Applied Science Research 49.4 (2022): 495-504.

[6] Sisman, C. B., and E. Gezer. "Performance characteristics of concrete containing natural and artificial pozzolans." J Food Agr Env 9.2 (2011): 132-136.
[7] Hossain, M. M., M. R. Karim, M. Hasan, M. K. Hossain, and M. F. M. Zain. "Durability of mortar and concrete made up of pozzolans as a partial replacement of cement: A review." Construction and building materials 116 (2016): 128-140.
[8] Paiva, H., A. Velosa, P. Cachim, and V. M. Ferreira. "Effect of pozzolans with different physical and chemical characteristics on concrete properties." Materiales de Construcción 66.322 (2016): e083.
[9] Bumanis, G., L. Vitola, L. Stipniece, J. Locs, A. Korjakins, and D. Bajare. "Evaluation of Industrial by-products as pozzolans: A road map for use in concrete production." Case studies in construction materials 13 (2020): e00424.
[10] Pachideh, G., M. Gholhaki, and H. Ketabdari. "Effect of pozzolanic wastes on mechanical properties, durability and microstructure of the cementitious mortars." Journal of Building Engineering 29 (2020): 101178.
[11] Gholhaki, M., M. Sharbatdar, and G. Pachideh. "An experimental investigation into the mechanical performance and microstructure of cementitious mortars containing recycled waste materials subjected to various environments." Journal of Building Engineering 61 (2022): 105275.
[12] Tayeh, B. A., H. M. Hamada, I. Almeshal, and B. A. Bakar. "Durability and mechanical properties of cement concrete comprising pozzolanic materials with alkali-activated binder: A comprehensive review." Case Studies in Construction Materials 17 (2022): e01429.
[13] Zdeb, T., T. Tracz, and M. Adamczyk. "Physical, mechanical properties and durability of cement mortars containing fly ash from the sewage sludge incineration process." Journal of Cleaner Production 345 (2022): 131055.
[14] Manjarrez, L., A. Nikvar-Hassani, R. Shadnia, and L. Zhang. "Experimental study of geopolymer binder synthesized with copper mine tailings and low-calcium copper slag." Journal of Materials in Civil Engineering 31.8 (2019): 04019156.
[15] Tavakoli, D., M. Hashempour, and A. Heidari. "Use of waste materials in concrete: A review." Pertanika J. Sci. Technol 26.2 (2018): 499-522.
[16] Shadnia, R., and L. Zhang. "Experimental study of geopolymer synthesized with class F fly ash and low-calcium slag." Journal of materials in civil engineering 29.10 (2017): 04017195.
[17] Mohajerani, A., D. Suter, T. Jeffrey-Bailey, T. Song, A. Arulrajah, S. Horpibulsuk, and D. Law. "Recycling waste materials in geopolymer concrete." Clean Technologies and Environmental Policy 21 (2019): 493-515.
[18] Heydari Z, R. Shadnia, D. Mostofinejad, and Sh. Rezaei. "The effect of the method of using waste carbonate cake on the compressive and tensile strength of green concrete." Journal of Ferdowsi Civil Engineering 37.3 (2025): 61-76.
[19] Gao, X., Y. Yang, and H. Deng. "Utilization of beet molasses as a grinding aid in blended cements." Construction and Building Materials 25.9 (2011): 3782-3789.
[20] Jumadurdiyev, A., M. H. Ozkul, A. R. Saglam, and N. Parlak. "The utilization of beet molasses as a retarding and water-reducing admixture for concrete." Cement and concrete research 35.5 (2005): 874-882.
[21] Ali, B., and L. A. Qureshi. "Durability of recycled aggregate concrete modified with sugarcane molasses." Construction and Building Materials 229 (2019): 116913.
[22] Huang, G., D. Pudasainee, R. Gupta, and W. V. Liu. "Utilization and performance evaluation of molasses as a retarder and plasticizer for calcium sulfoaluminate cement-based mortar." Construction and Building Materials 243 (2020): 118201.
[23] Puligundla, P., and C. Mok. "Valorization of sugar beet pulp through biotechnological approaches: recent developments." Biotechnology Letters 43.7 (2021): 1253-1263.
[24] Ziemiński, K., and M. Kowalska-Wentel. "Effect of different sugar beet pulp pretreatments on biogas production efficiency." Applied Biochemistry and Biotechnology 181 (2017): 1211-1227.
[25] Joanna, B., Michal B., Piotr D., Agnieszka W., Dorota K., and Izabela W. "Sugar beet pulp as a source of valuable biotechnological products." In Advances in biotechnology for food industry (2018): 359-392.
[26] Borysiuk, P., I. Jenczyk-Tolloczko, R. Auriga, and M. Kordzikowski. "Sugar beet pulp as raw material for particleboard production." Industrial Crops and Products 141 (2019): 111829.
[27] Alves de Oliveira, R., R. Schneider, B. Hoss Lunelli, C. E. Vaz Rossell, R. Maciel Filho, and J. Venus. "A simple biorefinery concept to produce 2G-lactic acid from sugar beet pulp (SBP): A high-value target approach to valorize a waste stream." Molecules 25.9 (2020): 2113.
[28] Rana, A. K., V. K. Gupta, J. Newbold, D. Roberts, R. M. Rees, S. Krishnamurthy, and V. K. Thakur. "Sugar beet pulp: Resurgence and trailblazing journey towards a circular bioeconomy." Fuel 312 (2022): 122953.
[29] Suffo, M., M. De La Mata, and S. I. Molina. "A sugar-beet waste based thermoplastic agro-composite as substitute for raw materials." Journal of cleaner production 257 (2020): 120382.
[30] Aljabri, M., S. Alharbi, R. N. Al-Qthanin, F. M. Ismaeil, J. Chen, and S. F. Abou-Elwafa. "Recycling of beet sugar byproducts and wastes enhances sugar beet productivity and salt redistribution in saline soils." Environmental Science and Pollution Research 28 (2021): 45745-45755.
[31] Schiavon, S., F. Tagliapietra, L. Bailoni, and A. Bortolozzo. "Effects of sugar beet pulp on growth and health status of weaned piglets." Italian Journal of Animal Science 3.4 (2004): 337-351.
[32] Wang, L. F., E. Beltranena, and R. T. Zijlstra. "Diet nutrient digestibility and growth performance of weaned pigs fed sugar beet pulp." Animal Feed Science and Technology 211 (2016): 145-152.
[33] Bodas, R., F. J. Giráldez, S. López, A. B. Rodríguez, and A. R. Mantecón. "Inclusion of sugar beet pulp in cereal-based diets for fattening lambs." Small Ruminant Research 71.1-3 (2007): 250-254.
[34] Beskopylny, A. N., S. A. Stel'makh, E. M. Shcherban', L. R. Mailyan, B. Meskhi, A. A. Shilov, and D. El'shaeva. "Effect of walnut-shell additive on the structure and characteristics of concrete." Materials 16.4 (2023): 1752.
[35] Chen, H., and J. Yang. "A new supplementary cementitious material: Walnut shell ash." Construction and Building Materials 408 (2023): 133852.
[36] Abdulwahid, M. Y., A. A. Akinwande, M. Kamarou, V. Romanovski, and I. A. Al-Qasem. "The production of environmentally friendly building materials out of recycling walnut shell waste: A brief review." Biomass Conversion and Biorefinery 14.20 (2024): 24963-24972.
[37] Shebli, A., J. Khatib, and A. Elkordi. "The effect of walnut shell ash on the properties of cement paste and mortar: a study on partial replacement of cement." BAU Journal-Science and Technology 5.1 (2023): 10.
[38] Ahmed, M. A., A. K. Ibrahim, N. Hilal, A. S. Aadi, and N. H. Sor. "Effects of coal ash and walnut shell on the impact resistance and mechanical properties of eco-efficient self-compacting concrete." Annales de Chimie. Science des Materiaux 47.4 (2023): 201.
[39] Tan, Y. Y., S. I. Doh, and S. C. Chin. "Eggshell as a partial cement replacement in concrete development." Magazine of Concrete Research 70.13 (2018): 662-670.

[40] Adamu, M., H. Alanazi, Y. E. Ibrahim, and M. Abdellatief. "Mechanical, microstructural characteristics and sustainability analysis of concrete incorporating date palm ash and eggshell powder as ternary blends cementitious materials." Construction and Building Materials 411 (2024): 134753.
[41] Sathiparan, N. "Utilization prospects of eggshell powder in sustainable construction material–A review." Construction and Building Materials 293 (2021): 123465.
[42] Nandhini, K., and J. Karthikeyan. "Sustainable and greener concrete production by utilizing waste eggshell powder as cementitious material–A review." Construction and Building Materials 335 (2022): 127482.
[43] Yang, D., J. Zhao, W. Ahmad, M. N. Amin, F. Aslam, K. Khan, and A. Ahmad. "Potential use of waste eggshells in cement-based materials: A bibliographic analysis and review of the material properties." Construction and Building Materials 344 (2022): 128143.
[44] Hamada, H. M., B. A. Tayeh, A. Al-Attar, F. M. Yahaya, K. Muthusamy, and A. M. Humada. "The present state of the use of eggshell powder in concrete: A review." Journal of Building Engineering 32 (2020): 101583.
[45] Ashraf Teara, and Doh Shu Ing. "Mechanical properties of high strength concrete that replace cement partly by using fly ash and eggshell powder." Physics and Chemistry of the Earth 120 (2020): 102942.
[46] Jhatial, A. A., N. Mohamad, K. H. Mo, and S. Sohu. "Incorporation of palm oil fuel ash and egg shell powder as supplementary cementitious materials in sustainable foamed concrete." Tehnički vjesnik 27.5 (2020): 1394-1402.
[47] Jhatial, A. A., W. I. Goh, K. H. Mo, S. Sohu, and I. A. Bhatti. "Green and sustainable concrete–the potential utilization of rice husk ash and egg shells." Civil Engineering Journal 5.1 (2019): 74-81.
[48] Sahibulla, S. M., and S. J. Jaisingh. "Pozzolanic biosilica, biochar, and egg shell in setting time, WVTR, and compression strength of biocement mortar: A Taguchi GRA validation." Biomass Conversion and Biorefinery 13.12 (2023): 10475-10482.
[49] Jhatial, A. A., W. I. Goh, N. Mohamad, S. Sohu, and M. T. Lakhiar. "Utilization of palm oil fuel ash and eggshell powder as partial cement replacement-a review." Civil Engineering Journal 4.8 (2018): 1977-1984.
[50] Amin, M., A. M. Zeyad, I. S. Agwa, and A. M. Heniegal. "Effect of peanut and sunflower shell ash on properties of sustainable high-strength concrete." Journal of Building Engineering 89 (2024): 109208.
[51] Horma, O., S. Channouf, A. El Hammouti, S. El Hassani, H. Miri, M. A. Moussaoui, and A. Mezrhab. "Enhancing concrete sustainability using crushed peanut shells: An analysis of thermophysical properties, durability, and application potential in construction." Journal of Building Engineering 90 (2024): 109434.
[52] Gupta, S., and A. Kashani. "Utilization of biochar from unwashed peanut shell in cementitious building materials–Effect on early age properties and environmental benefits." Fuel Processing Technology 218 (2021): 106841.
[53] Cotella, N. G., D. D. Gallo, K. Sapag, C. A. Barbero, D. F. Acevedo, and M. M. Bruno. "Peanut Shell Biochar as a Conductive Additive for Cement Composites." Waste and Biomass Valorization (2024).
[54] Hamraoui, S., D. Boukhelkhal, M. Guendouz, B. Abdennebi, and A. Fortas. "Development of a novel plant-based flowable sand concrete containing pretreated date seed as renewable aggregates." Studies in Engineering and Exact Sciences 6.1 (2025): e13458.
[55] Shah, S. J., S. Nath, A. Naeem, and E. Kakar. "Study on concrete mix with partial and full replacement of course aggregates with date seeds." Journal of Applied and Emerging Sciences 12.2 (2022): 219-224.
[56] Palh, A. R., S. A. Mangi, M. A. Odho, and A. A. Kalhoro. "Experimental study on concrete incorporating date seed as partial replacement of coarse aggregates." Neutron 20.2 (2021): 113-122.
[57] Amanah, B. H., and W. I. Khalil. "Effects of eggshells powder and date seeds on properties of sustainable concrete." In AIP Conference Proceedings 2864.1 (2024).
[58] Elazizi, C., H. Hammi, W. Marzouk, H. Majdoub, and A. M'nif. "Effect of a partial replacement of Portland cement by date seeds on the mechanical and chemical behavior of the mortar." Journal of the Tunisian Chemical Society 19 (2017): 326-334.

Journal of Civil Engineering Researchers

Journal homepage: www.journals-researchers.com

Numerical Investigation of a Steel Frame Braced with a Central-Cylinder Cable System Using Shape Memory Alloy

MohammadReza Oliaei,[a,*] MohammadHadi Moallemi [a]

[a] *Department of Civil Engineering, Ramsar Branch, Islamic Azad University, Ramsar, Iran*

ABSTRACT

Conventional steel braces increase the risk of structural damage during earthquakes due to compressive buckling. In this study, the performance of a steel frame equipped with a memory alloy cable brace with a central cylinder is investigated through numerical modeling in ABAQUS. This system is expected to exhibit superior seismic performance compared to traditional braces due to characteristics such as superelasticity, self-centering, and energy dissipation, and to return to its initial state after an earthquake. It can significantly enhance the seismic performance of steel frames with minimal construction interference and reduced construction time. After model validation, this study evaluates the effects of cable type, memory alloy properties, and cable diameter on the lateral performance of the steel frame with central cylinder cable braces. The results indicate that even using steel cables in this system significantly increases strength, stiffness, and energy absorption compared to a frame without braces, although ductility decreases by 25%. Replacing the steel cable with a memory alloy cable simultaneously improves strength, stiffness, energy absorption, and ductility (by 10%) compared to the steel-cable specimen, compensating for the ductility reduction. Furthermore, enhancing the superelastic properties of the memory alloy increases the load-bearing capacity and absorbed energy, while increasing the memory alloy cable diameter (from 6 to 16 mm) improves all performance indicators, especially stiffness and strength, without significant loss of ductility. Overall, the results demonstrate that using memory alloy cables, along with optimizing their properties and diameter, is an effective approach for simultaneously improving strength, stiffness, ductility, energy dissipation, and seismic behavior of structures.

ARTICLE INFO

Received: November 09, 2025
Accepted: November 25, 2025

Keywords:
Numerical Development
Braced Steel Frame
Cable Brace System
Memory Alloy
ABAQUS

DOI: 10.66224/JCER.7.4.12
DOR: 20.1001.1.2538516.2025.7.4.2.4

1. Introduction

In lateral-resistant structures, permanent deformations caused by earthquakes reduce ductility and increase repair costs [1]; conventional strengthening methods also face drift and high acceleration limitations [2]. Experiments show that ordinary steel braces buckle during earthquakes, increasing the risk of collapse [3]; the Kobe earthquake investigation indicated that parts of structures collapsed or were severely damaged, highlighting the need to develop damage-reducing and self-centering systems [4]. Despite

* Corresponding author. Tel.: +989113924331; e-mail: m.r.oliaei@gmail.com.

higher construction costs, self-centering systems reduce life-cycle costs and improve seismic stability [5].

To enhance the lateral performance of braces, the use of high-strength steel cables has been proposed. These cables are lightweight, strong, and elastic, returning to their initial state after an earthquake, but they function only as tensile members [6]. Cable bracing systems absorb energy more effectively than traditional braces and improve stability [7]. Only-tension bracing systems and modern cable–cylinder systems have been introduced to overcome limitations, although low ductility remains a challenge [8][9]. The use of prestressed and post-tensioned cables combined with a central spring cylinder helps control lateral displacement, improve ductility, reduce seismic damage, and minimize the need for additional structural reinforcement [10]. This system is an improved version of the moment-resisting frame bracing, in which steel cables and pre-compressed springs reach ultimate strength under large displacements while remaining within the elastic range. This design reduces initial lateral stiffness and strength but increases stiffness during structural recovery, achieving more effective performance compared to ordinary braces [6].

Shape memory alloys (SMAs), with superelastic and self-recovering properties, are suitable for self-centering systems. SMA cables can recover large strains (up to 6–8%) without external stimuli and, with high energy dissipation, reduce drift and seismic response. By absorbing seismic energy and returning to their original shape, they decrease structural damage and repair requirements in braced frames [11][12].

This study investigates a steel frame with only-tension cross-cable bracing and a central spring cylinder, including a sample of SMA cable, under lateral loading using three-dimensional modeling in ABAQUS [13]. Validation is performed using the experimental results of Mehrabi et al. [14]. The effects of cable material type (steel and SMA) and cable diameter on the lateral behavior of the structure—including strength, stiffness, ductility, lateral energy dissipation, and deformations—are evaluated through numerical analysis and parametric studies. Results are presented and compared using load–displacement curves and analytical tables to propose a novel approach for improving the seismic performance of frames.

2. Validation of the Model Simulation Process

The modeling and seismic analysis of structures, particularly using the finite element method (FEM), have advanced significantly in recent decades. This approach, utilizing software such as ANSYS and ABAQUS, enables detailed and complex analyses of structural systems. Today, ABAQUS is recognized as a critical tool for nonlinear structural analysis and engineering design.

The present study investigates the damage in steel frames braced with tension cables through nonlinear quasi-static analysis using ABAQUS, and compares the results with various experimental tests. This highlights the importance of calibrating analytical software to ensure the accuracy of both modeling and results in nonlinear analyses.

To evaluate the accuracy of finite element modeling in this study, three steel frames braced with tension cables, previously tested by Mehrabi et al. [14], were selected. The experiments (as shown in Figure 1) included three laboratory specimens (each with a column length of 1595 mm and a beam length of 1275 mm): an unbraced steel frame (BF), a cable-cross-braced steel frame without cable

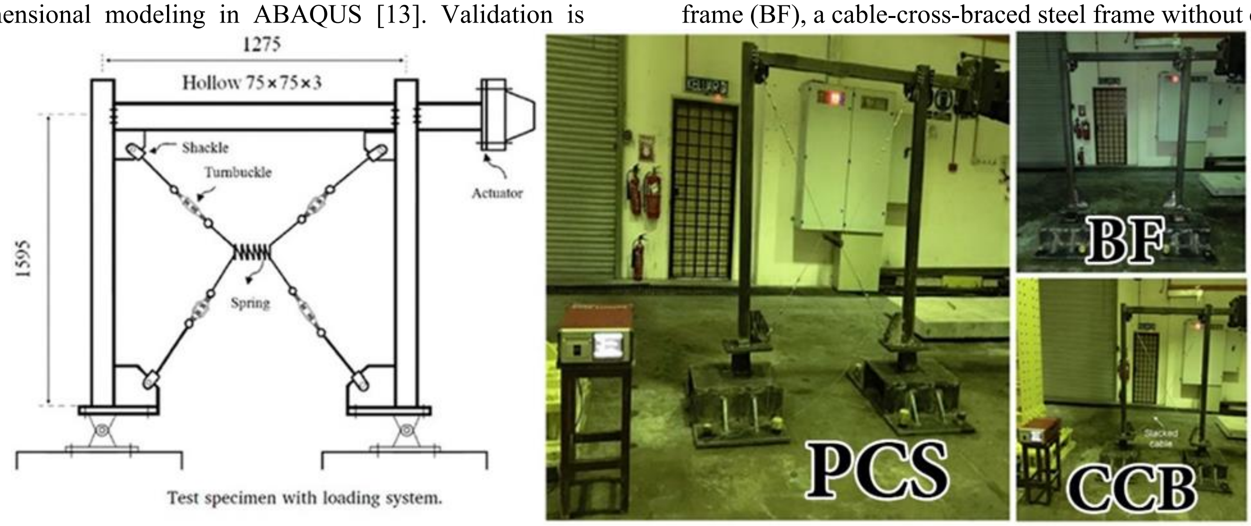

Figure 1 – Image of the three laboratory specimens and dimensional details of the cable- and spring-braced moment frame studied by Mehrabi et al. [14] under lateral cyclic loading.

connections at the frame center (CCB), and a cable-cross-braced steel frame with a spring connection at the frame center (PCS). The cable bracing system used steel cables with a nominal diameter of 6 mm and a full prestress corresponding to approximately 2% lateral column displacement. The steel frames had pinned supports, with beam and column sections measuring 75 × 75 mm, flange thickness 3 mm, and web thickness 2 mm.

The specimens were subjected to lateral cyclic loading, and their experimental results—based on material properties (including steel, cable, and spring) listed in Table 1—were obtained in the lateral load–displacement hysteresis curves (Figure 2). Subsequently, numerical modeling was performed using ABAQUS (Figure 2), and the results were compared with experimental data.

For load application and boundary conditions at the lower support, a reference point with a coupling constraint was created at the top of the specimen using ABAQUS Interaction module. Additionally, as shown in Figure 2, for the CCB and PCS specimens, the interaction between the steel plate and the cable required four Tie constraints with full fixation. In the PCS specimen, due to the presence of the spring system, surface contact was defined with a friction coefficient of 0.30 between the steel, cable, and spring.

In the numerical simulation, increasing mesh density improves accuracy but also increases computation time, so a balance must be maintained. To reduce computational costs, quasi-static analysis was conducted using C3D8R elements for springs and S4R elements for the steel frame.

Comparison of the load–displacement curves of the specimens (Figure 2) with experimental and numerical results showed that the numerical model adequately simulated the behavior of the specimens, confirming model validation. Moreover, finite element analysis results indicate that the maximum shear forces for the experimental specimens and the finite element models are nearly identical, with only a 5.7% difference in peak values.

Table 1
Material properties (steel, cable, and spring) used in the three laboratory specimens [14].

Mechanical Properties of Steel in Frame

Type	Steel Grade	Yield Strength (MPa)	Ultimate Strength (MPa)	Elastic Modulus (GPa)	Density (kg/m³)
Column	A36	360	420	205	7800
Beam	A36	360	420	205	7800

Mechanical Properties of Wire Rope Unit

Type	Dia. (mm)	Yield Strength (MPa)	Yield Strain	Tensile Strength (MPa)	Elastic Modulus (GPa)	L (mm)	W (mm)
Wire Rope	6	1016	0.01	1765	123.5	–	–
Hook and Eye Turnbuckle	8	305	0.004	515	205	–	–
DEE Shackles	10	305	0.004	515	205	25	13

Material Properties of Spring

Material	Spring Length (mm)	Spring Diameter (mm)	Elastic Modulus (GPa)	Modulus of Rigidity (GPa)	Density (kg/m³)
Stainless Steel	100	40	193	69	7920

3. Analysis of Findings

In this study, after validating the laboratory results (with good agreement), the effects of various parameters such as cable type, properties of the shape memory alloy (SMA) material, and cable diameter on lateral performance are evaluated. In this section, to extend the numerical work of Kherabi et al. [14], cyclic load–displacement hysteresis diagrams will be used to illustrate lateral performance, and metrics such as strength, stiffness, ductility, and lateral energy dissipation will be calculated and compared to assess the structural lateral behavior. Therefore, this section includes the following:

- Evaluation and comparison of the lateral performance of steel frames
- Effect of using SMA cables on the lateral performance of the cable-braced frame system with a central cylinder instead of steel cables
- Effect of changing the superelastic properties of SMA cables on the lateral performance of the cable-braced frame system with a central cylinder
- Effect of changing the diameter of SMA cables on the lateral performance of the cable-braced frame system with a central spring cylinder

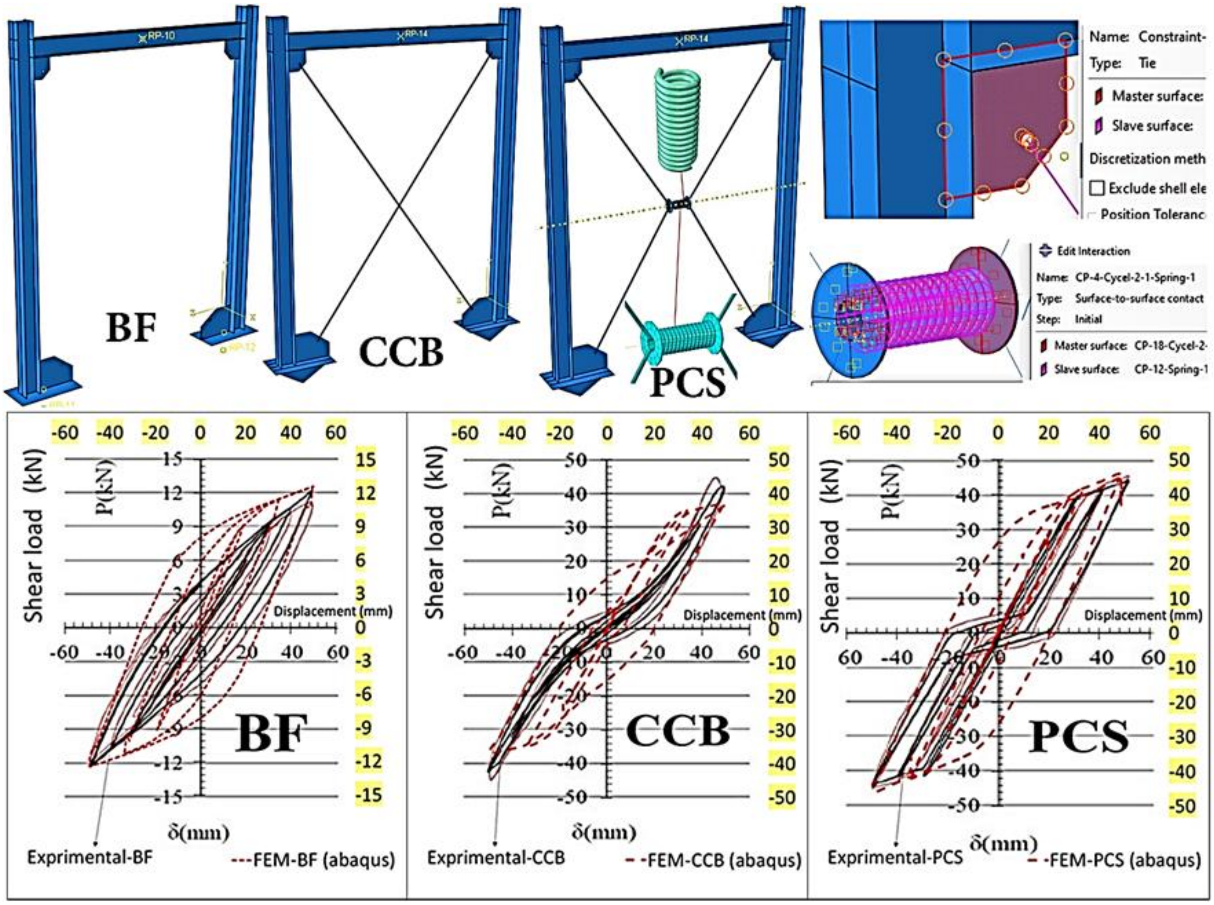

Figure 2 – Numerical modeling and validation for the three laboratory specimens [14] of the cable-braced moment frame.

3.1. Lateral Performance of Steel Frames under Study

In this part of the research, since a reference specimen is required to compare the other parametric samples against, the lateral performance of the reference specimens is examined. Two frames were selected as reference specimens: a bare frame (denoted as "BF") and a cable-braced frame with a central cylinder (denoted as "RF"). Figure 3 shows the comparison of their hysteresis diagrams.

As shown in Figure 3, the load–displacement hysteresis diagrams of BF and RF indicate how these specimens respond to lateral cyclic loading. Additionally, Figure 3 presents the envelope of the hysteresis and its bilinear approximation, where the envelope is obtained from the maximum resistances corresponding to each cyclic displacement. The bilinear diagram uses the equivalent energy method to convert the multi-linear envelope into a simpler form so that the areas under both diagrams are equal, ensuring that the absorbed energy remains the same. In this diagram, the failure point is recognized as the yield point; for the positive and negative directions, the effective ultimate displacement is denoted by Δu, the displacement at the failure point by Δy, and the resistance at the failure point by Vy.

In the analysis of these specimens or similar systems, the lateral load–displacement diagram serves as the basis for evaluating lateral performance, where:

- Maximum lateral resistance (P) represents the frame strength
- Initial stiffness (K), obtained by dividing the yield resistance by the yield displacement (Vy/Δy)
- Ductility (μ), calculated as the ratio of effective ultimate displacement to yield displacement (Δu/Δy)
- Energy dissipation, computed from the area inside the hysteresis loops

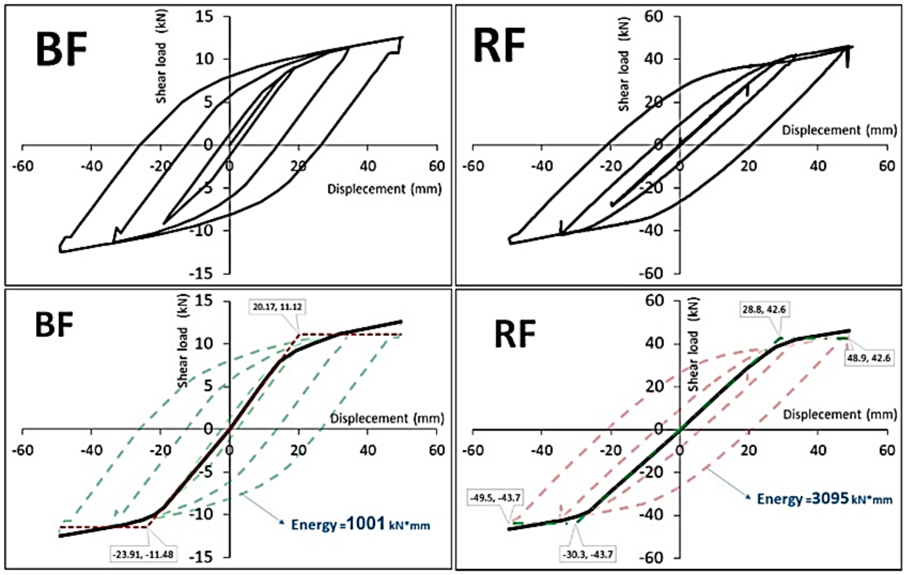

Figure 3. Comparison of load–displacement hysteresis diagrams of the two reference specimens: bare frame "BF" and cable-braced frame with a central cylinder "RF".

Table 2
Comparison of lateral performance: bare frame "BF" and cable-braced frame with a central cylinder "RF".

Spectrum	Energy (kN·mm)	P+ (Pos) kN	P- (Neg) kN	System Hardness K+ (Pos) kN/m	K- (Neg) kN/m	μ+ (Pos) kN/m	μ- (Neg) kN/m
RF	3095	46.2	46.4	1481	1444.5	1.7	1.64
BF	1001	12.6	12.5	551.4	480.19	2.45	2.05
	209%	267%	272%	169%	201%	-31%	-20%

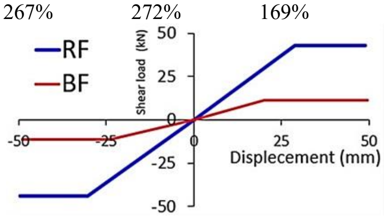

This energy-based approach, aided by finite element software, allows precise determination of performance parameters and provides a suitable basis for pushover analysis and retrofit design.

To determine the energy dissipation of the bare frame and the steel frame braced with a cable system, the area inside the load–displacement hysteresis loops must be calculated, which can be done using Excel by analyzing numerical data. According to Table 2, the results show that using a steel cable-braced frame system with a central cylinder, compared to a bare frame, significantly improves lateral performance, with an average increase of 209% in energy dissipation, 270% in strength, and 185% in stiffness, while ductility decreases by 25%.

Based on Table 2, the improved performance of the RF specimen can be attributed to the increase in displacement and yield resistance. By providing lateral bracing with crossed steel cables along with a central cylinder, the frame exhibits higher displacement and resistance at yielding, which increases the resistance, stiffness, and energy dissipation of the RF specimen.

3.2. Effect of Using SMA Cables on Lateral Performance

This section of the study investigates how the lateral performance of a steel frame equipped with a cable bracing system changes if memory alloy (SMA) cables are used instead of steel cables. Additionally, it examines the difference in lateral performance compared to a steel frame with a central-cylinder steel cable bracing system. To this end, it is first necessary to have a good understanding of the SMA material intended for the cables. Accordingly, the superelastic and reversible behavior of the SMA materials used in this study is explained below:

In recent years, SMAs have attracted significant attention in civil engineering due to their excellent

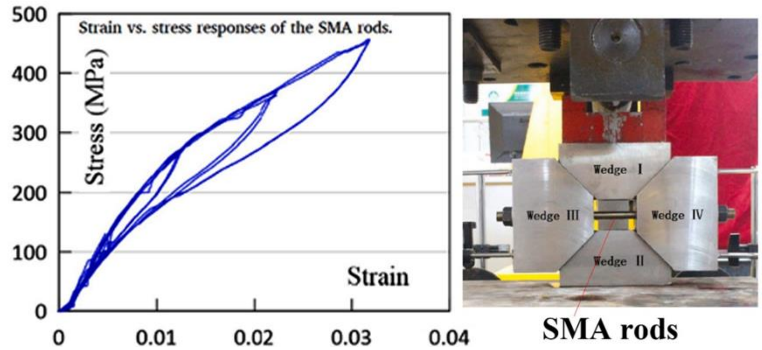

Figure 4 – Sample and stress-strain diagram of the superelastic SMA rod studied by Zhang et al. [11].

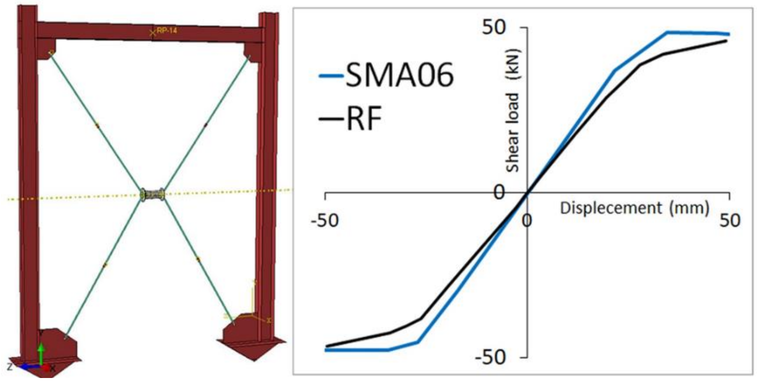

Figure 5 – Numerical model of the steel frame with SMA cable bracing system and comparison with the steel cable frame

superelastic capabilities and moderate energy dissipation. Derivatives of these materials have been considered for self-centering systems because of the inherent nonlinear elastic behavior of SMAs [15]. SMAs are metallic alloys that can recover their original shape after deformation due to a solid-to-solid phase transformation. Superelastic SMAs can recover large deformations after unloading without any external stimulus [15].

The stress-strain diagram of these materials (as shown in Figure 4) exhibits a "flag-shaped" form in tension and compression, with two stages or phases. The initial linear behavior, like other materials, has a defined elastic modulus and Poisson's ratio [16]. In Abaqus software (version 2019 onward), superelastic material properties are included. According to this, the martensite Young's modulus (EM) and martensite Poisson's ratio (νM) in the second tensile phase must be defined. Key input parameters for defining superelastic materials include: strain range between the Young's modulus and martensite modulus (εL), initial and final stress of loading and unloading in tension, initial stress of loading in compression, reference temperature, and loading parameters. The final plastic strain of the SMA material can also be defined in its settings.

The stress-strain curve of the superelastic SMA rod tested in the lab was taken from a centrally damped specimen with SMA rods under lateral loading, studied by Zhang et al. [16], as shown in Figure 4. The material properties of the SMA were recorded in the numerical model based on this data.

Numerical loading (as shown in Figure 5) was applied to the steel frame equipped with the SMA cable bracing system, designated as "SMA06." This designation refers to the sample being modeled and analyzed with 6 mm diameter SMA cables. Figure 5 shows the hysteresis load-displacement curve of the "SMA06" specimen compared with the corresponding curve of the reference steel cable bracing frame, "RF," indicating that the "SMA06" specimen exhibits higher performance.

According to the hysteresis loading results on the "SMA06" specimen, the hysteresis loop area, representing the system's energy dissipation, is calculated as 3553 kN·mm. By evaluating lateral performance indices such as strength, stiffness, ductility, and energy dissipation, the lateral performance of the SMA-braced steel frame can be quantified. Table 3 presents these performance metrics alongside the reference steel cable frame (RF).

From Table 3, it can be inferred that implementing an SMA central-cylinder cable bracing system improves the lateral performance of the steel frame compared to the steel cable bracing system. This improvement includes increases in system strength, stiffness, ductility, and energy dissipation, with lateral energy dissipation increasing by 15%, mean lateral strength by 4.5%, mean lateral stiffness by 18.5%, and mean lateral ductility by 10%. These

Table 3
Lateral performance of steel frames with SMA cable bracing and central-cylinder steel cable bracing systems.

		Reaction Force		System Hardness		Ductility	
Spectrum	Energy (kN*mm)	P+ (Pos) (kN)	P- (Neg) (kN)	K+ (Pos) (kN/m)	K- (Neg) (kN/m)	μ+ (Pos) (kN/m)	μ- (Neg) (kN/m)
RF	3095	46.2	46.4	1481	1444.5	1.7	1.64
SMA06	3553	48.8	47.9	1726	1727.3	1.83	1.83
	15%	6%	3%	17%	20%	8%	12%

Table 4
SMA samples considered for application in steel frames with central-cylinder cable bracing systems

Mechanical Property	E_A (GPa)	E_M (GPa)	σ_{StL} (MPa)	σ_{EtL} (MPa)	σ_{StU} (MPa)	σ_{EtU} (MPa)
SMA06	27	31	170	455	250	50
SMA06-01	54	62	340	910	500	100
SMA06-02	13.5	15.5	85	227.5	125	25

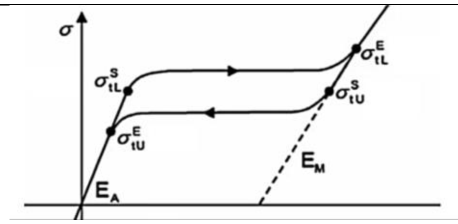

Table 5
Lateral performance of steel frames with central-cylinder SMA cable bracing and effect of modified SMA properties.

		Reaction Force		System Hardness		Ductility	
Spectrum	Energy (kN*mm)	P+ (Pos) (kN)	P- (Neg) (kN)	K+ (Pos) (kN/m)	K- (Neg) (kN/m)	μ+ (Pos) (kN/m)	μ- (Neg) (kN/m)
RF	3095	46.2	46.4	1481	1444.5	1.7	1.64
SMA06	3553	48.8	47.9	1726	1727.3	1.83	1.83
SMA06-01	3878	52.6	56.6	1793	1825.1	1.75	1.6
SMA06-02	3432	45.4	44.5	1587	1618.5	1.77	1.81

changes highlight the advantages of using SMAs to enhance the performance of braced structures.

3.3. Effect of Changing SMA Cable Superelastic Properties on Lateral Performance

This section examines how changes in the SMA material properties assigned to the steel cable bracing system affect the lateral performance of the steel frame. Additionally, it evaluates the differences in lateral performance compared to the central-cylinder steel cable bracing frame. Several factors are considered for modifying SMA properties, as shown in Table 4.

As seen in Table 4, SMA samples are introduced for use in steel frames with central-cylinder cable bracing. The first sample, "SMA06," is the default SMA whose lateral performance was detailed in the previous section. The "SMA06-01" and "SMA06-02" samples differ from the default SMA06. By examining the table, it can be observed that the properties of SMA06-01 are twice those of the default SMA06, while SMA06-02 properties are half.

These properties include two elastic moduli (EA and EM) for the two linear behaviors of the superelastic material. σStL and σEtL correspond to the start and end stresses of linear deformation during loading, while σStU and σEtU correspond to the start and end stresses during unloading. The modified SMA materials must be assigned in a separate file to replace the default SMA cables.

To determine the energy dissipated by the steel frame with the modified SMA cables, the area inside all new hysteresis load-displacement curves must be calculated. The energy dissipation of the double-property SMA sample is 3887 kN·mm, and that of the half-property SMA sample is 3432 kN·mm. By evaluating lateral performance indices such as strength, stiffness, ductility, and energy dissipation, the lateral performance of the steel frame with modified SMA cables can be quantified. Table 5 presents these values alongside the reference frame.

From Table 5, it can be concluded that doubling the elastic properties of the SMA cable increases energy dissipation, lateral strength, and stiffness by 9.1%, 7.9%, and 3.9%, respectively, but reduces ductility by 4.7%.

Conversely, halving the SMA elastic properties decreases energy dissipation, strength, and stiffness by 3.4%, 13.7%, and 11.5%, respectively, while ductility increases by 1.5%.

3.4. Effect of SMA Cable Diameter on Lateral Performance

This section of the study addresses the question of how the lateral performance of a steel frame equipped with a central-cylinder cable bracing system changes if the diameter of the cable modeled with a shape memory alloy (SMA) is altered. In this context, three cable diameter scenarios were considered. The existing cable diameter is 6 mm, and the two new diameters to be evaluated are 10 mm and 16 mm. The new specimens for these two diameters are labeled "SMA10" and "SMA16," respectively.

Numerical loading (as shown in Figure 5) was applied to the steel frame specimens "SMA10" and "SMA16," and their hysteresis loading results were obtained. To determine the energy absorbed by the steel frame equipped with the central-cylinder cable bracing system with the new SMA, the area of the loops within the hysteresis load–displacement diagram was calculated. This represents the energy absorption for cable diameters of 10 and 16 mm, which were found to be 3585 and 3612 kN·mm, respectively. By evaluating the lateral performance criteria—strength, stiffness, ductility, and energy absorption—of the SMA cable-braced steel frame specimens, the lateral performance levels can be quantified. Table 6 presents these performance measures alongside the reference steel frame (steel frame braced with a central-cylinder steel cable system).

From the results in Table 6, it can be inferred that implementing a central-cylinder cable bracing system with SMA cables of 10 and 16 mm diameter improves the lateral performance of the steel frame compared to the lateral performance of the reference steel frame with a central-cylinder steel cable bracing system. The results indicate that increasing the SMA cable diameter from 6 mm to 10 mm and finally to 16 mm increases the lateral energy absorption by 14.8%, 15.8%, and 16.7%, respectively, compared to the reference steel cable frame. Similarly, the lateral ductility increases by 10%, 5%, and 5.2%, respectively. The lateral strength increases by 4.3%, 9.8%, and 19.3%, and the lateral stiffness increases by 18.1%, 23.9%, and 34.6% with the same diameter increments.

4. Overall Comparison of Results

In this part of the study, the lateral performance data obtained for the central-cylinder steel cable-braced frame and the various scenarios are compiled to evaluate their overall behavior under lateral loading. Table 7 summarizes all the specimens considered in this study.

Table 6
Lateral performance of SMA cable specimens with diameters of 10 and 16 mm for use in steel frames braced with a central-cylinder cable system

		Reaction Force		System Hardness		Ductility	
Spectrum	Energy (kN*mm)	P+ (Pos) (kN)	P- (Neg) (kN)	K+ (Pos) (kN/m)	K- (Neg) (kN/m)	μ+ (Pos) (kN/m)	μ- (Neg) (kN/m)
RF	3095	46.2	46.4	1481	1444.5	1.7	1.64
SMA06	3553	48.8	47.9	1726	1727.3	1.83	1.83
SMA10	3330	51.3	50.5	1783	1841	1.8	1.7
SMA16	3587	55.8	54.8	1956	1980.4	1.83	1.68

Table 7
Comprehensive table of all studied specimens, central-cylinder cable-braced steel frames under lateral loading.

		Reaction Force		System Hardness		Ductility	
Spectrum	Energy (kN*mm)	P+ (Pos) (kN)	P- (Neg) (kN)	K+ (Pos) (kN/m)	K- (Neg) (kN/m)	μ+ (Pos) (kN/m)	μ- (Neg) (kN/m)
RF	3095	46.2	46.4	1481	1444.5	1.7	1.64
SMA06	3553	48.8	47.9	1726	1727.3	1.83	1.83
SMA06-01	3878	52.6	56.6	1793	1825.1	1.75	1.6
SMA06-02	3432	45.4	44.5	1587	1618.5	1.77	1.81
SMA10	3330	51.3	50.5	1783	1841	1.8	1.7
SMA16	3587	55.8	54.8	1956	1980.4	1.83	1.68

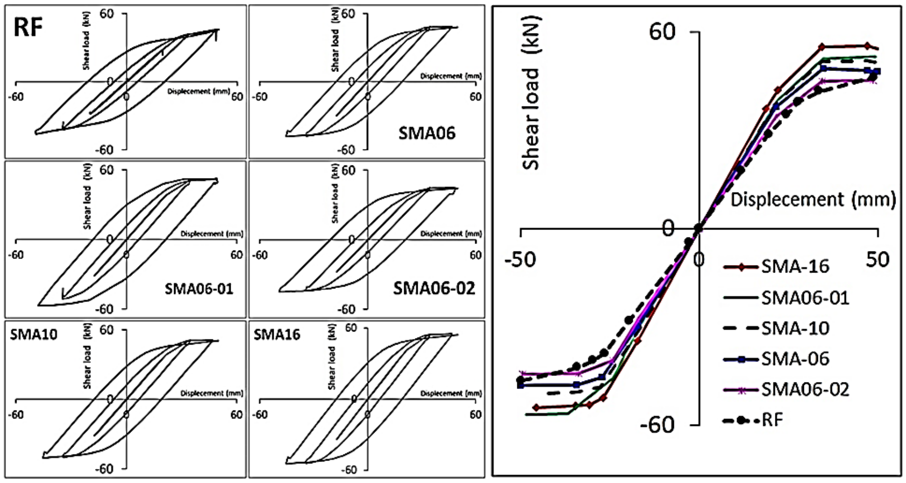

Figure 5. Hysteresis load–displacement and lateral envelope curves for all numerical specimens under study.

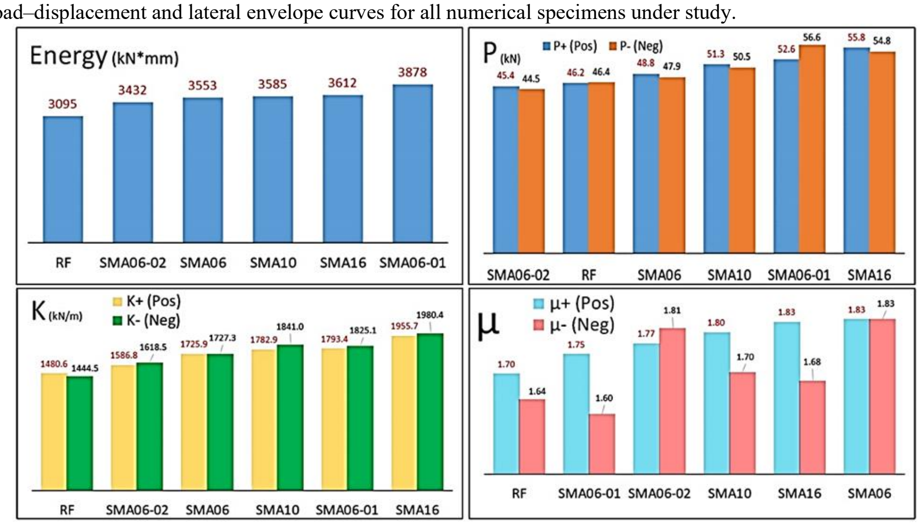

Figure 6 – Lateral energy absorption, strength, stiffness, and ductility of all numerical specimens under study.

According to Table 7, the four seismic performance criteria—energy absorption, strength, stiffness, and lateral ductility—can be compared across the six central-cylinder steel cable-braced frame configurations. Figures 5 and 6 illustrate the hysteresis and envelope curves, as well as the lateral energy absorption, strength, stiffness, and ductility for all numerical specimens considered.

Based on Figures 5 and 6, the following observations can be made regarding the hysteresis and envelope curves, as well as energy absorption, strength, stiffness, and ductility of all specimens:

- The comparison of lateral performance in cyclic loading shows that the main criteria—energy absorption, strength, stiffness, and ductility—were evaluated for six different cases, and the related plots illustrate the differences and advantages of each system.
- The results indicate that the SMA cable-braced steel frame specimen with double elastic properties ("SMA06-01") exhibited the highest lateral energy absorption, followed by the specimens with cable diameters of 16 mm, 10 mm, and 6 mm ("SMA16," "SMA10," and "SMA06," respectively). Even the specimen with half the initial elastic properties ("SMA06-02") performed better in energy absorption than the reference steel cable frame.
- In terms of lateral strength, the SMA cable-braced specimen with 16 mm diameter ("SMA16") had the highest value, followed by "SMA06-01," "SMA10," and "SMA06," while "SMA06-02" showed lower strength than the reference steel cable-braced frame.
- The SMA 16 mm specimen ("SMA16") also exhibited the highest lateral stiffness, followed by "SMA06-01," "SMA10," and "SMA06," with "SMA06-02" still outperforming the reference steel cable frame in stiffness.
- Regarding ductility, the 6 mm SMA cable frame ("SMA06") had the highest lateral ductility,

followed by 16 mm and 10 mm SMA specimens ("SMA16" and "SMA10"), while the reference steel cable frame had the lowest.

5. Conclusion

Considering the importance of improving the seismic performance of steel structures, this study evaluated the effects of cable type, SMA properties, and cable diameter on steel frames equipped with central-cylinder cable bracing systems. The goal was to investigate changes in strength, stiffness, ductility, and lateral energy absorption under different scenarios and to propose effective strategies for enhancing seismic behavior. The research methodology was based on numerical simulations and comparison with baseline data, with performance metrics extracted from hysteresis load–displacement and bilinear envelope curves. The main findings are as follows:

- Using the system, even with steel cables, increased strength, stiffness, and energy absorption by 270%, 185%, and 209%, respectively, compared to the unbraced frame, although ductility decreased by 25%. Replacing steel cables with SMA simultaneously increased strength (4.5%), stiffness (18.5%), energy absorption (15%), and ductility (10%), compensating for the ductility reduction.
- Doubling the superelastic properties of SMA increased load capacity and energy absorption but slightly decreased ductility; halving these properties had the opposite effect. Increasing the SMA cable diameter from 6 to 10 and 16 mm improved all indices, especially stiffness (up to 34.6%) and strength (up to 19.3%), without noticeable ductility loss.
- Load–displacement curves showed that the SMA cable with double properties and 6 mm diameter ("SMA06-01") had the highest energy absorption, while the 16 mm cable specimen ("SMA16") exhibited the greatest strength and stiffness. Even the half-property specimen ("SMA06-02") outperformed the conventional steel system in stiffness and energy absorption. In ductility, the 6 mm SMA cable performed best, and the conventional steel system performed worst.
- The central-cylinder cable bracing system, even with steel cables, significantly increases strength, stiffness, and energy absorption, but reduces ductility. Using SMA cables instead of steel simultaneously enhances strength, stiffness, energy absorption, and ductility, offsetting ductility loss.
- Enhancing SMA elastic properties improves strength and energy absorption but slightly reduces ductility; decreasing these properties has the opposite effect. Increasing SMA cable diameter is an effective way to improve all lateral performance indicators, especially stiffness and strength.

In summary, the results demonstrate that using SMA cables in central-cylinder cable bracing systems, along with optimization of properties and cable diameter, is an efficient approach to increase strength, stiffness, ductility, and energy absorption and to improve seismic performance.

References

[1] Hu, X., J.-W. Bai, K. Khandelwal, and M. Bruneau. “Mitigation of residual deformations in eccentrically braced frames through a low-cost re-centering mechanism.” Earthquake Engineering & Structural Dynamics 50.14 (2021): 3660–3678. https://doi.org/10.1002/eqe.4113

[2] Lavan, O. “Seismic design and retrofit procedure for total accelerations and inter-story drifts reduction of buildings with protective systems.” In Proceedings of the 9th U.S. National and 10th Canadian Conference on Earthquake Engineering (Paper No. 359). Toronto, Canada (2010).

[3] Issa, A., S. Stephen, and A. Mwafy. “Unveiling the seismic performance of concentrically braced steel frames: A comprehensive review.” Sustainability 16.1 (2024): 427. https://doi.org/10.3390/su16010427

[4] Sakellariadis, L., I. Anastasopoulos, and G. Gazetas. “Fukae bridge collapse (Kobe 1995) revisited: New insights.” Soils and Foundations 60.6 (2020): 1450–1467. https://doi.org/10.1016/j.sandf.2020.09.005

[5] Hu, S., W. Wang, M. S. Alam, and K. Ke. “Life-cycle benefits estimation of self-centering building structures.” Engineering Structures 284 (2023): 115982. https://doi.org/10.1016/j.engstruct.2023.115982

[6] Xu, G., T. Guo, and A. Li. “Development and investigation of a self-centering cable brace with variable slip stiffness for braced frame structure.” Journal of Building Engineering 76 (2023): 107383. https://doi.org/10.1016/j.jobe.2023.107383

[7] Ghasemi, M., C. Zhang, H. Khorshidi, and L. Sun. “Seismic performance assessment of steel frames with slack cable bracing systems.” Engineering Structures 250 (2022): 113437. https://doi.org/10.1016/j.engstruct.2021.113437

[8] Xu, G., T. Guo, A. Li, Y. Wu, H. Zhang, and G. Zhi. “Innovative self-centering tension-only braces for enhanced seismic resilience in frame structures: An experimental and numerical analysis.” Engineering Structures 319 (2024): 118816. https://doi.org/10.1016/j.engstruct.2024.118816

[9] Fanaie, N., and E. Afsar Dizaj. “Cable-cylinder bracing system: Theoretical background, structural behavior, and seismic design coefficients.” In Seismic Evaluation, Damage, and Mitigation in Structures, edited by I. Mansouri and P. O. Awoyera, 51–94. Woodhead Publishing (Elsevier) (2022). https://www.sciencedirect.com/book/9780323885317

[10] Chou, C.-C., and L.-Y. Huang. “Mechanics and validation tests of a post-tensioned self-centering brace with adjusted stiffness and

deformation capacities using disc springs." Thin-Walled Structures 195 (2024): 111430. https://doi.org/10.1016/j.tws.2024.111430

[11] Casagrande, L., C. Menna, D. Asprone, M. Ferraioli, and F. Auricchio. "Buildings." In Shape Memory Alloy Engineering (2nd ed.), 689–729. Elsevier (2021). https://doi.org/10.1016/B978-0-12-819264-1.00021-2

[12] Askariani, S. S., S. Garivani, I. Hajirasouliha, and N. Soleimanian. "Innovative self-centering systems using shape memory alloy bolts and energy dissipating devices." Journal of Constructional Steel Research 190 (2022): 107127. https://doi.org/10.1016/j.jcsr.2021.107127

[13] ABAQUS-V6.19-1. "Finite Element Analysis Software." Johnston, RI, USA. ABAQUS/Standard theory. Manual, Dassault Systèmes Simulia Corp. (2019).

[14] Mehrabi, M. H., Z. Ibrahim, S. S. Ghodsi, and M. Suhatril. "Seismic characteristics of X-cable braced frames bundled with a precompressed spring." Soil Dynamics and Earthquake Engineering 116 (2019): 732–746. https://doi.org/10.1016/j.soildyn.2018.10.014

[15] Lagoudas, D. C., and J. G. Boyd. "Shape memory alloys in civil engineering: Applications and challenges." Materials Science and Engineering: R: Reports 140 (2019): 1-22. https://doi.org/10.1016/j.mser.2019.01.001

[16] Zhang, S., et al. "Tests of a novel re-centering damper with SMA rods and friction wedges." Engineering Structures 236 (2021): 112125. https://doi.org/10.1016/j.engstruct.2021.112125

J-Researchers

Journal of Civil Engineering Researchers

Journal homepage: www.journals-researchers.com

A Comparative Analysis of Ensemble NWP Models for Flood Forecasting

Saleh Aminyavari [a,*]

[a] *Department of Civil Engineering, Cha.C., Islamic Azad University, Chalous, Iran*

ABSTRACT

This study presents the first application of gamma quantile mapping to bias-correct ensemble precipitation forecasts from seven global NWP models (ECMWF, NCEP, UKMO, CMA, JMA, ECCC, NCMRWF) in the data-scarce Saliyan Basin, Iran. The integration of these models with advanced bias correction techniques significantly improves flood forecasting accuracy. To address systematic biases in the raw forecasts, gamma quantile mapping was applied, significantly enhancing the reliability of the precipitation inputs. These bias-corrected forecasts were then used as inputs for the GR4J hydrological model to simulate river flow and predict flood events. The study period included a major flood event in March 2019, which was used to evaluate the performance of the ensemble forecasting system. Results demonstrated that bias correction using gamma quantile mapping substantially improved the accuracy of flood forecasts, with the ECMWF and UKMO models showing the highest skill scores. The ensemble approach effectively captured the uncertainty in flood predictions, providing valuable insights for risk assessment and decision-making. This research highlights the importance of bias correction in ensemble forecasting and offers a robust framework for flood prediction in data-scarce regions. The findings have significant implications for improving flood early warning systems and mitigating flood-related damages in similar basins worldwide.

ARTICLE INFO

Received: October 13, 2025
Accepted: Novembre 01, 2025

Keywords:
Flood Forecasting
Ensemble Numerical Weather Prediction (NWP)
Gamma Quantile Mapping
Uncertainty Analysis
Iran

DOI: 10.66224/JCER.7.4.23
DOR: 20.1001.1.2538516.2025.7.4.3.5

1. Introduction

Weather forecasts play a crucial role in hydrological applications. Predicting the likelihood of floods provides an opportunity for disaster managers to plan for damage reduction, manage water distribution, and mitigate potential damages. Therefore, managers need an index of forecast uncertainty to assess the risks associated with management decisions. Today, significant advancements have been made in improving weather forecasts, one of which is numerical weather predictions (NWP). NWP values are generated by solving the governing equations of the atmosphere using three-dimensional numerical methods for various temporal and spatial scales. Improving numerical precipitation forecasts is a primary goal of forecasting centers and a major challenge for the hydrometeorological research community. The weaknesses of NWP models in accurately describing atmospheric processes, along with unavoidable random errors in solving numerical equations, result in significant

[*] Corresponding author. Tel.: +989112912393; e-mail: saleh1161a@gmail.com.

uncertainty in NWP forecasts. Since the data from NWP models are used as inputs for hydrological models to predict flow, the accuracy of these data affects the simulated flow results. Thus, NWP model results impose considerable uncertainty on hydrological models. Given the limitations of deterministic forecasts in atmospheric states and changes in initial conditions, ensemble forecasting methods have been developed to improve the capability of numerical and probabilistic forecasts. Ensemble forecasts involve multiple individual forecasts generated with different physical parameterizations or initial conditions [1]. One of the key issues in using ensemble precipitation forecasts in hydrological models is addressing input uncertainty. Extensive research has been conducted on the application of ensemble forecasts in hydrological applications, some of which are discussed below.

Thirel et al. (2008) evaluated the capabilities of two ensemble forecasting systems, ECMWF and PEARP, for river flow forecasting across France. The results showed that ensemble flow forecasts based on PEARP data were better for floods and small basins, while ECMWF data performed better for large basins and low flows [2]. He et al. (2010) used TIGGE meteorological data to create a flood warning system for the upper Huai River basin in China. A grand ensemble was created from five centers with equal weight coefficients. Precipitation was classified into low, medium, and high categories, and the results showed that evaluation scores decreased from low to heavy precipitation, indicating that the equal weight coefficients needed further investigation [3]. Alfieri et al. (2014) evaluated the European Flood Awareness System (EFAS), which uses outputs from ECMWF and DWD models. The results indicated that model performance significantly decreased for basins smaller than 300 km² due to underestimation of runoff in mountainous areas [4]. Bennett et al. (2014) developed a continuous ensemble hydrological forecasting system (SCHEF) for nine Australian basins using NWP forecasts. NWP forecasts were post-processed using the BJP method, and the GR4H rainfall-runoff model was used for hydrological modeling. The results showed that SCHEF effectively predicted river flow, especially for a 1- to 6-day forecast horizon [5]. Zomerdijk (2015) examined the development of a flood ensemble forecasting system in Quzhou, eastern China, for a 1- to 10-day forecast horizon and evaluated flood forecasts using precipitation forecasts from four meteorological centers: ECMWF, NCEP, UKMO, and CMA. The integrated GR4J hydrological model was used for flood forecasting. Ensemble precipitation forecasts were corrected using quantile mapping, and the results showed that all models had good flood forecasting capabilities, with ECMWF performing the best and CMA the worst [6]. Thiemig et al. (2015) assessed the capabilities of the African Flood Forecasting System (AFFS) based on ECMWF forecasts. The results showed that AFFS correctly predicted 70% of floods [7]. Matsueda and Nakazawa (2015) created a rapid warning system using ensemble forecasts from UKMO, NCEP, ECMWF, and JMA models in the TIGGE database. They assessed the probability of extreme weather events and found that these models successfully predicted severe events like the 2010 Russian heatwave, the 2010 Pakistan floods, and Hurricane Sandy in 2012 [8]. Cai et al. (2019) studied uncertainty in precipitation forecasts from four TIGGE centers in China's Huai River basin during flood season. They introduced a new model using fuzzy probabilities and Bayesian theory (GPDF), finding it highly accurate, reliable, and sharp. Uncertainty rose with forecast horizon, and the model provided acceptable accuracy for flood risk analysis up to three days [9].

Zhang et al. (2020) demonstrated that advanced bias correction methods, such as gamma quantile mapping, can significantly enhance the accuracy of precipitation forecasts [10]. Similarly, Li et al. (2021) investigated the impact of high-resolution ensemble NWP models on flood forecasting in small basins and found that these models can effectively reduce uncertainty [11]. In another study, Wang et al. (2022) combined ensemble NWP models with machine learning techniques for flood prediction and observed a notable improvement in forecast accuracy [12]. Additionally, Kumar et al. (2023) examined the influence of input data quality on flood forecasting accuracy and highlighted the critical role of bias correction in improving results [13]. Martinez et al. (2021) conducted an uncertainty analysis in flood forecasting using ensemble NWP models and advanced statistical methods, showing that these approaches can effectively manage uncertainty [14]. Finally, Lee et al. (2023) explored the impact of regional characteristics on the performance of flood forecasting methods and emphasized the importance of selecting appropriate techniques for each region [15].

In evaluating TIGGE ensemble precipitation forecasts for Iran, Aminyavari et al. (2018) examined forecasts from three centers (ECMWF, UKMO, and NCEP) in eight different precipitation groups across Iran. The results showed that ECMWF performed better in most regions, UKMO in mountainous areas, and NCEP along the Persian Gulf coast [16]. Aminyavari et al. (2018) post-processed TIGGE forecast data in the Beshar basin using a combination of quantile mapping and Bayesian averaging. They concluded that the forecasting skill of the models for the Beshar basin improved, and the VR histogram obtained from each model showed a uniform distribution. The combined BMA forecast had higher skill than individual models [17]. Aminyavari et al. (2019) evaluated NWP models (ECMWF, UKMO, NCEP) and GPM satellite for 2019 floods in Iran. Satellite estimates were more accurate

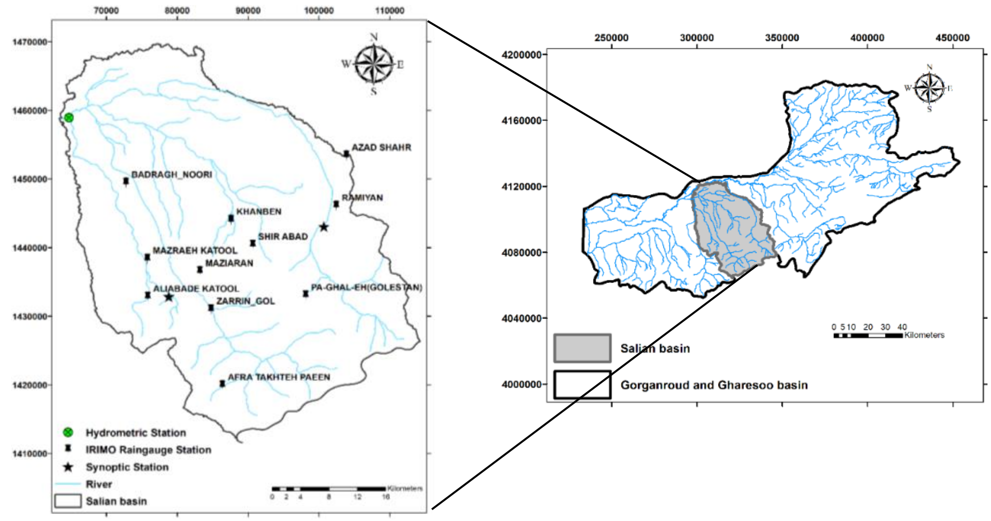

Figure 1. Layout of rain gauge of Research Basin

Table1.

Specifications of seven NWP models in TIGGE database

Center	No. of Ensemble Members	Horizontal Archived	Resolution	Forecast Length (day)	Initial Perturbation Method
ECMWF	50	N320(~0.28°) N160(~0.56°)		0-10 10-15	EDA-SVINI
NCEP	20	1.0°×1.0°		0-16	BV-ETR
UKMO	17	0.83°×0.56°		0-15	ETKF
CMA	14	0.56°×0.56°		0-10	BV
JMA	26	1.25°×1.25°		0-11	SV
ECCC	20	1°×1°		0-16	EKF
NCMRWF	11	0.25°×0.25°		0-10	ETKF

for precipitation amount, UKMO excelled in spatial distribution, NCEP's performance decreased with higher thresholds, and ECMWF had better POD and lower false alarms at specific thresholds [18]. Hoghoughinia et al. 2024 evaluated three post-processing methods—Quantile Mapping (QM), Support Vector Machine (SVM), and Random Forest (RF)—applied to ECMWF precipitation forecasts over Iran. The RF method significantly improved forecast accuracy, particularly in regions with higher precipitation rates, demonstrating the importance of post-processing for enhancing flood forecasting and management [19].

Despite advances in ensemble forecasting, the combined use of seven NWP models with gamma quantile mapping remains unexplored, particularly in regions prone to flash floods due to complex topography and sparse data.

In this study, ensemble precipitation forecasts from seven centers (UKMO, ECMWF, NCEP, ECCC, JMA, NCMRWF, and CMA) were extracted from the TIGGE database for the Saliyan basin and bias-corrected using gamma quantile mapping. The bias-corrected ensemble precipitation forecasts were then used as inputs for the G4RJ rainfall-runoff model. In terms of innovation, no research has been conducted on bias-correcting ensemble precipitation forecasts from seven NWP models using gamma quantile mapping and analyzing uncertainty in ensemble flood forecasts for the Saliyan basin in 2019.

2. Materials and Methods

2.1. Study Basin Characteristics and Forecast Data

The main river of the Saliyan basin is the Saliyan Tappeh or Habib Eshan River. This river is formed by the confluence of the Qarasu Ramian, Siah Jub, Zarringol, and Kabul Val rivers and flows into the Gorgan River near the village of Habib Eshan after the Gorgan Dam. The basin area up to the Baghe Saliyan hydrometric station is approximately 1800 km². Eleven rain gauge stations from the Meteorological Organization, whose characteristics and locations in the basin are shown in Figure 1 based on UTM coordinates, were selected for precipitation.

The Baghe Saliyan hydrometric station was chosen for observed discharge, and the Aliabad Katul synoptic station was selected for temperature. The precipitation data from the 11 rain gauge stations and the Saliyan hydrometric station were tested for trends using the Mann-Kendall test. The results showed that p-values for all stations were above 0.05, indicating no trend in the observed data, and the Sen's slope was approximately zero for all stations. The Pettitt non-parametric test was also applied to test the homogeneity of the 11 rain gauge stations, and no significant changes were observed in the precipitation time series.

Ensemble precipitation forecast data from seven centers (UKMO, ECMWF, NCEP, ECCC, JMA, NCMRWF, and CMA) were extracted from the TIGGE database (https://apps.ecmwf.int/datasets/data/tigge/levtype=sfc/type=pf/) for the Saliyan basin with a resolution of 50 km. Their specifications are listed in Table 1.

Since forecast values are located at the center of the forecast grid points, which are 50 km apart and differ from the spatial coordinates of the rain gauge stations, these data need to be interpolated to the locations of the ground observation stations for accurate evaluation. Various interpolation methods exist but based on successful experiences in similar studies [20, 21, 22], the inverse distance weighting (IDW) method was used. IDW is a non-linear interpolation method that uses a weighted average of forecast values near the target station. In this study, four grid points around each station were selected, weighted based on their diagonal distance to the target station, and used in the IDW formula to calculate the forecast precipitation at the selected station. This step was performed for all seven models over the study years for each day with all ensemble members.

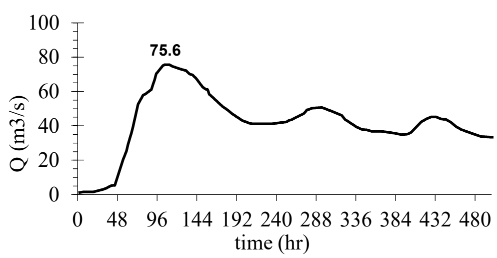

Figure 2. Flood hydrograph of Research Basin

On March 17, 2019, heavy rainfall in the northern provinces of Iran, including Golestan, Mazandaran, and North Khorasan, caused flooding. Many factors contributed to the flooding, but the most significant were soil erosion due to excessive forest exploitation, continuous rainfall, and the release of water from dams, leading to flooding in the two northern provinces of Iran March 2019. In this study, most sub-basins of the Gorgan River were examined, and the Saliyan sub-basin was selected for evaluating the performance of numerical models in flood forecasting due to the availability of statistical data and calibration results. Figure 2 shows the flood hydrograph for this basin. The hydrograph starts on March 17, 2019, with a peak flow of 75.6 m^3/s occurring on April 1, 2019, lasting for six hours (8 AM to 2 PM). The total flood volume was 75.32 million cubic meters. According to the Golstan Regional Water Authority, the total precipitation in the basin was approximately 250 mm, which, based on statistical analysis, was unprecedented in the past 50 years. The training period (October 2018–March 2019) was chosen to encompass seasonal variability in precipitation, ensuring robust calibration of the gamma function.

2.2. Study Basin Characteristics and Forecast Data

Most ensemble precipitation forecasts have bias errors that need correction. Bias can be unconditional (systematic) or conditional. Systematic bias refers to the difference between the mean forecasts and observations over the study period, which is not influenced by the user, while conditional bias is based on thresholds set by the user. The goal of bias correction is to correct systematic bias errors. Gamma quantile mapping was selected for its ability to handle zero-inflated, skewed precipitation distributions (Piani et al., 2010), unlike methods assuming normality (e.g., linear scaling). This is critical for the Saliyan Basin, where 80% of annual rainfall occurs in sporadic, high-intensity events [23]. The gamma distribution is the best fit for this type of data [24]. To perform bias correction, the cumulative distribution function (CDF) of observations and forecasts is first extracted based on the gamma distribution. Then, using the following formula, quantiles (Qn) from the forecast CDF are extracted, and new precipitation values are calculated from the observed CDF based on the obtained quantiles.

$$BC_{fcst}=CDF_{obs}^{-1}(CDF_{fcst}(Fcst))=CDF_{obs}^{-1}\left(Q_n\right) \quad (1)$$

The gamma quantile mapping method was implemented using the hyfo package [25] in R. The training period for bias correction was from October 1, 2018, to March 15, 2019, and forecasts from March 15, 2019, to April 15, 2019, were bias-corrected based on the fitted function from the training period. This process was performed separately for each ensemble member of each numerical model. In other words, bias correction was performed 158 times (50+20+17+14+26+20+11) for each day based on the third column of Table 1 (number of ensemble members).

2.3. Flow forecasting

The GR4J integrated continuous conceptual rainfall-runoff model was used to predict the flow of the Baghe Saliyan River during the study years. The model was implemented using the airGR package in R [26]. This model was selected based on reputable research [6, 7, 17] in flood forecasting. The main inputs for the model are precipitation, temperature, and potential evapotranspiration, which must be averaged over the basin. The Thiessen polygon method was used to calculate the average values of the required inputs for the Saliyan basin. First, observed precipitation and forecasts from all seven models were interpolated to the 11 selected stations in the basin using the Thiessen polygon method. This was done separately for each ensemble member for the 11 stations. After preparing the precipitation, discharge, and potential evapotranspiration data for the Saliyan basin, these values were merged based on common days, resulting in 5170 days from December 31, 2001, to August 22, 2017, available for calculating optimal parameters. A one-year warm-up period was set before the calibration period for model initialization. Thus, the period from December 31, 2001, to December 15, 2002 (some days lacked data), was used as the warm-up period, from December 16, 2002, to May 4, 2014, as the calibration period, and from May 5, 2014, to August 22, 2017, as the validation period. The optimal parameters obtained from the model were then used to predict floods using numerical precipitation forecasts from the seven centers from March 17, 2019, to April 15, 2019. The GR4J model has four parameters for flow forecasting, which must be optimized during calibration and tested during validation. Parameter (X1) represents the maximum soil moisture capacity of the basin. Soil moisture acts like a reservoir that is filled with precipitation and empties with potential evapotranspiration. Parameter (X2) indicates the influence of groundwater on the routing reservoir. A positive value indicates groundwater inflow into the routing reservoir, while a negative value indicates a decrease in the routing reservoir height and inflow into groundwater. A negative value suggests that some precipitation in the basin enters groundwater. Parameter (X3) represents the capacity of the routing reservoir, and parameter (X4) is the base time of the unit hydrograph for routing. In this study, four optimization methods were used to calculate the optimal parameters during calibration: the Michel optimization algorithm (available in GR4J) [27], the differential evolution algorithm (DE), the improved particle swarm optimization algorithm (PSO), and the memetic algorithm with local search (MA-LS).

For calibration and validation of the GR4J rainfall-runoff model and calculation of optimal parameters, daily observed data from the Saliyan basin, including discharge, precipitation, and temperature from 2002 to 2017, were used. Optimal parameters were calculated using four optimization methods. The RMSE index was used as the optimization criterion. The optimal parameters for all four methods are shown in Table 2. As evident from the table, the parameters were nearly identical across all methods.

The simulated discharges with optimal parameters were evaluated based on RMSE, bias in mean and standard deviation of simulated and observed discharges, the Nash-Sutcliffe efficiency (NSE), and the correlation coefficient (R2) for both calibration and validation periods, as shown in Table 3. The results were relatively good for the validation period.

Table 2.
Optimal parameters obtained in 4 optimization methods

Model	X1 (mm)	X2 (mm/d)	X3 (mm)	X4 (d)
airGR	391.937	-19.52	122.983	2.48
DE	387.927	-19.802	123.833	2.484
PSO	388.205	-19.763	123.727	2.482
MA-LS	387.258	-19.769	123.594	2.509

Table 3.
Streamflow simulation results with observational data on calibration and validation periods

	RMSE (mm/day)	$BIAS_{sd}$	$BIAS_{mean}$	NSC	R^2
Calibration	0.17	0.93	0.8	0.76	0.83
Validation	0.20	0.51	0.5	0.53	0.55

3. Results

In this section, all numerical precipitation forecasts from the seven models with all ensemble members were bias-corrected using gamma quantile mapping. Seventy percent of the data were used for training, and the remaining 30% were bias-corrected based on the fitted function from the training period. Based on the optimal parameters obtained in the previous section, flow forecasts were performed using raw and bias-corrected numerical precipitation model inputs. Figure 3 shows the flow forecast results for the CMA, ECMWF, JMA, NCEP, UKMO, ECCC, and NCMRWF models in both raw and bias-corrected states. As evident from the figures, the CMA model performed poorly in the raw state but improved after bias correction, although it still slightly underestimated the flood volume. The ECMWF model performed better in the raw state compared to other models and excelled after bias correction The JMA model performed poorly in the raw state and overestimated the flood volume after bias correction, likely due to inherent regional biases in its convective parameterization, which struggles to resolve orographic precipitation in the Saliyan Basin's steep topography (see Figure 1). The UKMO model performed relatively well in the raw state and excelled after bias correction. The ECCC model had moderate performance in the raw state and slightly underestimated the flood volume after bias correction, but all ensemble members improved. The NCMRWF model performed poorly in the raw state but improved after bias correction, although it still slightly underestimated the flow.

For a better comparison of the numerical models' performance in ensemble flow forecasting after bias

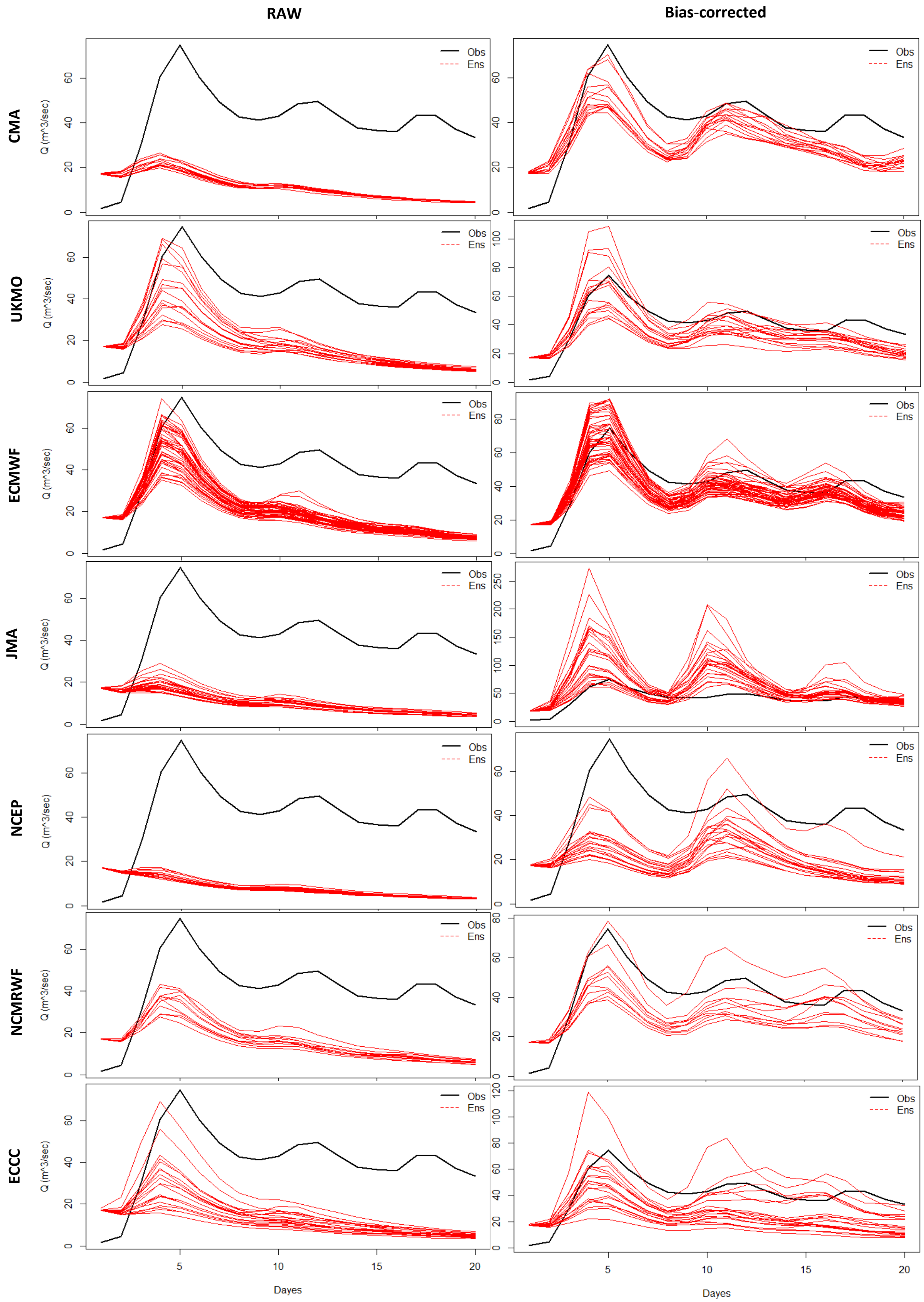

Figure 3. Ensemble flow forecast in two raw and bias-corrected modes of models

correction versus the raw state, box plots of the NSE values for the ensemble members of each numerical model are shown in Figure 4. As evident, the NSE values in the bias-corrected state were mostly above 0.5, indicating good model performance after bias correction. The ECMWF and UKMO models performed exceptionally well after bias correction, with nearly 50% of ensemble members achieving NSE values above 0.7. This superior performance likely stems from their higher spatial resolution (N320/0.28° for ECMWF and 0.83°×0.56° for UKMO; see Table 1) and advanced perturbation methods (EDA-SVINI for ECMWF and ETKF for UKMO), which enable better capture of localized rainfall dynamics in the Saliyan Basin. For the JMA model, although some ensemble members had very poor NSE values (as low as -2.5), most members had NSE values between 0.2 and 0.6.

Figure 5 shows the results of probabilistic flow forecasting evaluation for the seven numerical models using the continuous ranked probability score (CRPS) in both raw and bias-corrected states. As evident, all models performed poorly in the raw state and were weaker than the reference forecasts. After bias correction, the CRPS scores of all models improved significantly, with the UKMO and ECMWF models achieving positive scores. The cumulative distribution function (CDF) of the flow forecasts after bias correction became closer to the observed CDF.

Figure 6 shows the results of probabilistic flow forecasting evaluation for the seven models using the Brier skill score (BSS) in both raw and bias-corrected states. As evident, all models performed poorly in the raw state and were weaker than the reference forecasts. After bias correction, the BSS scores of all models, especially JMA, increased, indicating that the numerical models better predicted the probability of floods after bias correction. Additionally, the increase in BSS scores indicates that after bias correction, the uncertainty of all seven numerical models decreased, and their resolution increased.

Rank histograms were used to evaluate the performance of probabilistic flow forecasts from the seven numerical ensemble precipitation models. Figure 7 shows the rank histograms for the seven models in both raw and bias-corrected states.

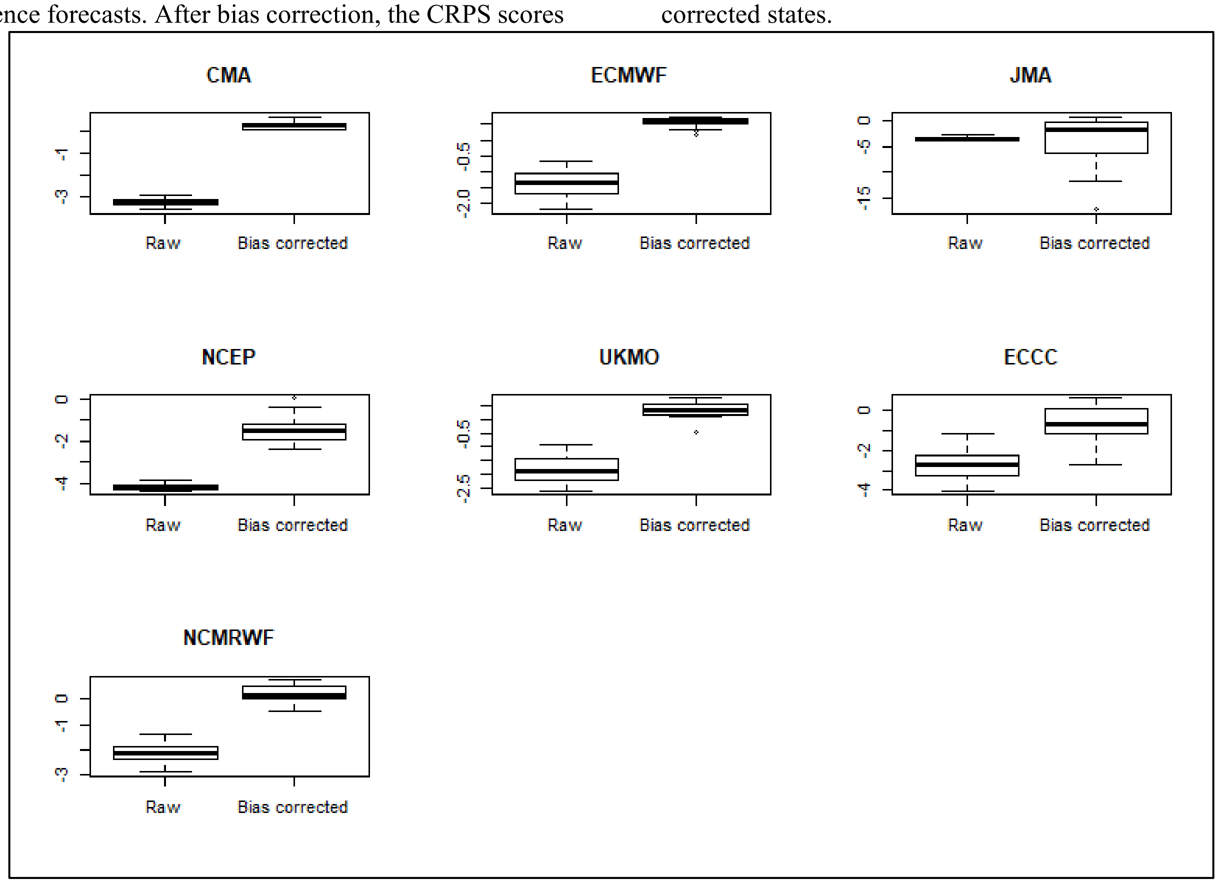

Figure 4. Boxplot for ensemble flow forecast in two raw and bias-corrected states for the Nash-Sutcliffe criterion

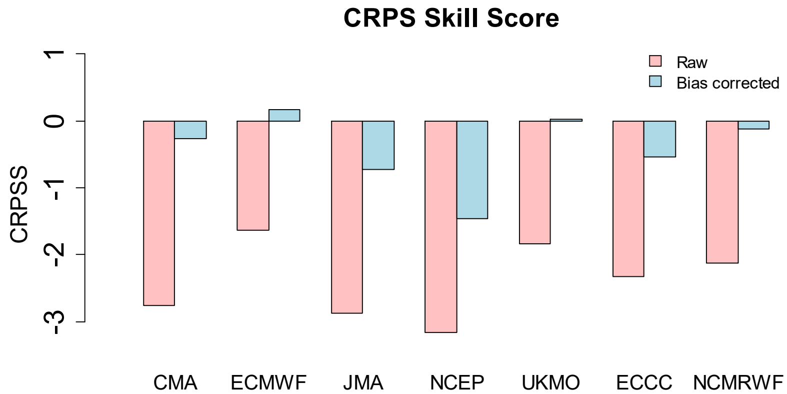

Figure 5. Results of ensemble flow forecasting evaluation of models with CRPS skill score

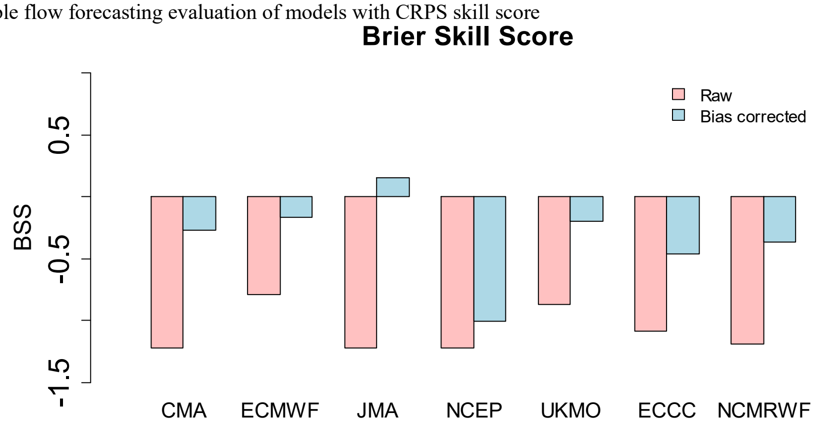

Figure 6. Results of ensemble flow forecasting evaluation of models with Brier skill score

The NCMRWF model has 11 ensemble members. After sorting the ensemble members in ascending order for each day, most observed discharges were higher than the ensemble forecasts, indicating that the model underestimated in the raw state. After bias correction, some observed discharges fell within the higher ensemble members, indicating improved flow forecasting. The CMA model has 14 ensemble members. Similar to the previous model, no observed discharges fell within the ensemble members in the raw state, but after bias correction, a few observed discharges fell within the higher ensemble members, although the model still underestimated flood discharges. The UKMO model has 17 ensemble members. In the raw state, a few observed discharges fell within the ensemble members. In the bias-corrected state, most of the 20 observed discharges fell within the ensemble members, indicating that the model effectively identified uncertainties. The ECCC model has 20 ensemble members. In the raw state, 4 observed discharges fell within the ensemble members, and in the bias-corrected state, 15 observed discharges fell within the ensemble members, indicating good flood forecasting performance. The NCEP model also has 20 ensemble members but captured the fewest observed discharges in both raw and bias-corrected states compared to other models. The JMA model has 26 ensemble members and performed poorly in the raw state, with almost all observed discharges falling into higher ranks. In contrast, in the bias-corrected state, most observed discharges fell within the lower ranks, indicating overestimation. Finally, the ECMWF model has 50 ensemble members. In the raw state, 4 observed discharges fell within the ensemble members, and in the bias-corrected state, 15 observed discharges fell within the ensemble members. The ECMWF model was the only one with observed discharges uniformly distributed among the ensemble members, indicating better performance compared to other models.

4. Discussion

The results demonstrate that high-resolution models like ECMWF/UKMO are particularly effective in topographically complex regions like northern Iran, where localized rainfall dynamics dominate flood risks. This aligns with Lee et al. (2023), who emphasized region-specific model selection for flood forecasting. The application of gamma quantile mapping effectively reduced systematic biases in the raw ensemble precipitation forecasts, leading to more reliable inputs for

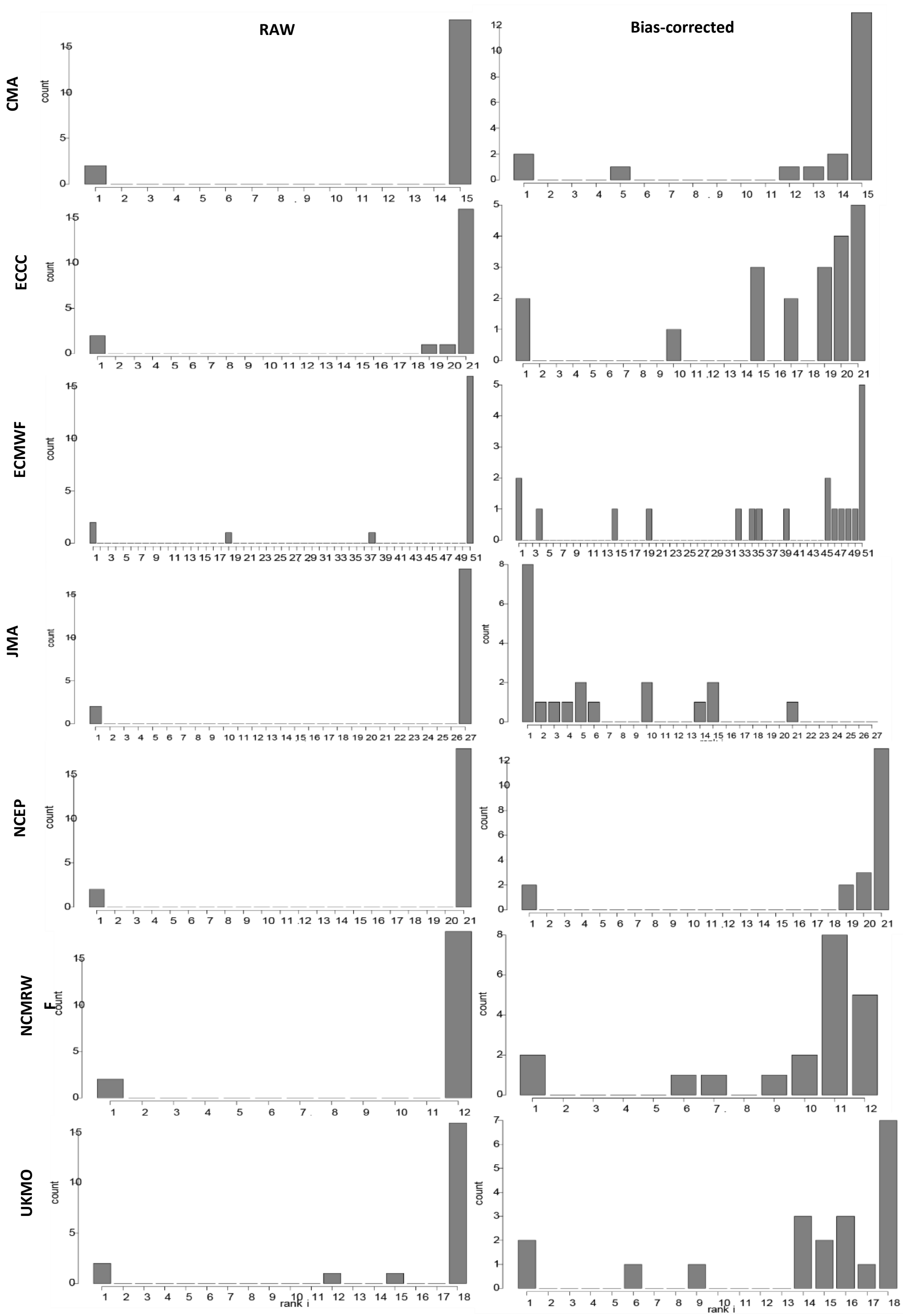

Figure 7. Rank histogram of probabilistic streamflow forecasts with raw numerical forecasts and bias-corrected precipitation for 7 models

the GR4J hydrological model. This improvement was particularly evident in the performance of the ECMWF and UKMO models, which consistently showed higher skill scores in predicting flood events. The ensemble approach also provided valuable insights into the uncertainty associated with flood forecasts, enabling better risk assessment and decision-making for flood management. The findings align with recent studies that have highlighted the importance of bias correction in ensemble forecasting. For instance, Zhang et al. (2020) [10] and Li et al. (2021) [11] emphasized the role of advanced bias correction methods in enhancing the accuracy of precipitation forecasts, especially in data-scarce regions. Similarly, the improved performance of the ECMWF and UKMO models observed in this study is consistent with the results of Wang et al. (2022) [12], who demonstrated the effectiveness of high-resolution ensemble NWP models in flood prediction. However, the relatively poor performance of the NCEP and JMA models, even after bias correction, suggests that the quality of initial conditions and model physics may play a critical role in the accuracy of ensemble forecasts. This observation is supported by Kumar et al. (2023) [13], who found that input data quality significantly influences flood forecasting outcomes. One of the key contributions of this study is the application of gamma quantile mapping to multiple ensemble NWP models, which has not been extensively explored in previous research. The results indicate that this method can effectively address systematic biases and improve the reliability of flood forecasts, particularly in regions with complex hydrological and meteorological conditions, such as the Saliyan Basin. However, the study also highlights the need for further research to optimize bias correction techniques and explore their applicability in different climatic and hydrological contexts.

5. Conclusion

This study investigated the potential of ensemble NWP models combined with gamma quantile mapping for improving flood forecasting in the Saliyan Basin, Iran. The results demonstrated that bias correction using gamma quantile mapping significantly enhanced the accuracy of precipitation forecasts, leading to more reliable flood predictions. The ECMWF and UKMO models emerged as the top-performing models, while the NCEP and JMA models showed relatively weaker performance, even after bias correction. The ensemble approach effectively captured the uncertainty in flood forecasts, providing valuable insights for flood risk management and decision-making. The findings of this study have important implications for improving flood early warning systems, particularly in data-scarce regions. By integrating ensemble NWP models with advanced bias correction techniques, it is possible to reduce the uncertainty associated with flood forecasts and enhance the reliability of hydrological predictions. Future research should focus on optimizing bias correction methods, exploring the use of machine learning techniques for post-processing ensemble forecasts, and evaluating the performance of these methods in different hydrological and climatic settings. Overall, this study contributes to the growing body of knowledge on flood forecasting and provides a robust framework for improving flood risk management in similar basins worldwide.

Acknowledgements

The author would like to thank the Islamic Azad University, Chalous Branch, for providing the necessary infrastructure and support to conduct this research. Appreciation is also extended to the Iranian Meteorological Organization and the Golestan Regional Water Authority for providing access to essential hydrological and meteorological data.

References

[1] Swinbank, R., M. Kyouda, P. Buchanan, L. Froude, T.M. Hamill, T.D. Hewson, et al. "The TIGGE project and its achievements." Bulletin of the American Meteorological Society 97.1 (2016): 49–67. https://doi.org/10.1175/BAMS-D-13-00191.1

[2] Thirel, G., F. Rousset-Regimbeau, E. Martin, and F. Habets. "On the impact of short-range meteorological forecasts for ensemble streamflow predictions." Journal of Hydrometeorology 9.6 (2008): 1301–1317. https://doi.org/10.1175/2008JHM951.1

[3] He, Y., F. Wetterhall, H. Bao, H. Cloke, Z. Li, F. Pappenberger, et al. "Ensemble forecasting using TIGGE for the July–September 2008 floods in the Upper Huai catchment: a case study." Atmospheric Science Letters 11.2 (2010): 132–138. https://doi.org/10.1002/asl.267

[4] Alfieri, L., F. Pappenberger, F. Wetterhall, T. Haiden, D. Richardson, and P. Salamon. "Evaluation of ensemble streamflow predictions in Europe." Journal of Hydrology 517 (2014): 913–922. https://doi.org/10.1016/j.jhydrol.2014.06.035

[5] Bennett, J.C., D.E. Robertson, D.L. Shrestha, Q.J. Wang, D. Enever, P. Hapuarachchi, and N.K. Tuteja. "A System for Continuous Hydrological Ensemble Forecasting (SCHEF) to lead times of 9 days." Journal of Hydrology 519 (2014): 2832–2846. https://doi.org/10.1016/j.jhydrol.2014.07.034

[6] Zomerdijk, L. "Performance of multi-model ensemble combinations for flood forecasting." Master Thesis; University of Twente: Netherlands (2015).

[7] Thiemig, V., B. Bisselink, F. Pappenberger, and J. Thielen. "A Pan-African medium-range ensemble flood forecast system." Hydrology and Earth System Sciences 19.8 (2015): 3365–3385. https://doi.org/10.5194/hess-19-3365-2015

[8] Matsueda, M. and T. Nakazawa. "Early warning products for severe weather events derived from operational medium-range ensemble

forecasts." Meteorological Applications 22.2 (2015): 213–222. https://doi.org/10.1002/met.1456

[9] Cai, C., J. Wang, and Z. Li. "Assessment and modelling of uncertainty in precipitation forecasts from TIGGE using fuzzy probability and Bayesian theory." Journal of Hydrology 577 (2019): 123995. https://doi.org/10.1016/j.jhydrol.2019.123995

[10] Zhang, Y., X. Wang, and J. Li. "Improving precipitation forecast accuracy using gamma quantile mapping." Journal of Hydrology 585 (2020): 124789. https://doi.org/10.1016/j.jhydrol.2020.124789

[11] Li, H., Y. Chen, and Q. Zhang. "The impact of high-resolution ensemble NWP models on flood forecasting in small basins." Water Resources Research 57.5 (2021): e2020WR028945. https://doi.org/10.1029/2020WR028945

[12] Wang, L., X. Liu, and T. Zhang. "Combining ensemble NWP models with machine learning for flood prediction." Hydrology and Earth System Sciences 26.3 (2022): 1234-1245. https://doi.org/10.5194/hess-26-1234-2022

[13] Kumar, R., P. Singh, and A. Sharma. "The influence of input data quality on flood forecasting accuracy." Journal of Hydrometeorology 24.2 (2023): 567-580. https://doi.org/10.1175/JHM-D-22-0123.1

[14] Martinez, G., M. Rodriguez, and J. Lopez. "Uncertainty analysis in flood forecasting using ensemble NWP models." Natural Hazards and Earth System Sciences 21.7 (2021): 2345-2358. https://doi.org/10.5194/nhess-21-2345-2021

[15] Lee, S., H. Kim, and J. Park. "The impact of regional characteristics on flood forecasting performance." Water Resources Management 37.4 (2023): 1456-1470. https://doi.org/10.1007/s11269-023-03456-8

[16] Aminyavari, S., B. Saghafian, and M. Delavar. "Evaluation of TIGGE ensemble forecasts of precipitation in distinct climate regions in Iran." Advances in Atmospheric Sciences 35.4 (2018): 457–468. https://doi.org/10.1007/s00376-017-7063-9

[17] Aminyavari, S., B. Saghafian, and E. Sharifi. "Assessment of Precipitation Estimation from the NWP Models and Satellite Products for the Spring 2019 Severe Floods in Iran." Remote Sensing 11.23 (2019): 2741. https://doi.org/10.3390/rs11232741

[18] Aminyavari, S., B. Saghafian, and E. Sharifi. "Assessment of Precipitation Estimation from the NWP Models and Satellite Products for the Spring 2019 Severe Floods in Iran." Remote Sensing 11.23 (2019): 2741. https://doi.org/10.3390/rs11232741

[19] Hoghoughinia, K., B. Saghafian, and S. Aminyavari. "Evaluation of precipitation temporal distribution pattern of post-processed sub-daily ECMWF forecasts." Theoretical and Applied Climatology 155.8 (2024): 8401–8414. https://doi.org/10.1007/s00704-024-04923-9

[20] Abdolmanafi, A., B. Saghafian, and S. Aminyavari. "Evaluation of global ensemble prediction models for forecasting medium to heavy precipitations." Meteorology and Atmospheric Physics 133.1 (2021): 15–26. https://doi.org/10.1007/s00703-020-00772-1

[21] Saedi, A., B. Saghafian, S. Moazami, and S. Aminyavari. "Performance evaluation of sub-daily ensemble precipitation forecasts." Meteorological Applications 27.1 (2020): e1872. https://doi.org/10.1002/met.1872

[22] Hoghoughinia, K., B. Saghafian, and S. Aminyavari. "Analysis of precipitation temporal pattern of sub-daily ECMWF forecasts." Meteorology and Atmospheric Physics 134.5 (2022): 87. https://doi.org/10.1007/s00703-022-00920-7

[23] Piani, C., J.O. Haerter, and E. Coppola. "Statistical bias correction for daily precipitation in regional climate models over Europe." Theoretical and Applied Climatology 99.1–2 (2010): 187–192. https://doi.org/10.1007/s00704-009-0134-9

[24] Liu, J. and Z. Xie. "BMA probabilistic quantitative precipitation forecasting over the Huaihe Basin Using TIGGE multimodel ensemble forecasts." Monthly Weather Review 142.4 (2014): 1542–1555. https://doi.org/10.1175/MWR-D-13-00171.1

[25] Xu, Y. "Hyfo: hydrology and climate forecasting R package for data analysis and visualization." R Package Version 1.0 (2015).

[26] Coron, L., G. Thirel, O. Delaigue, C. Perrin, and V. Andréassian. "The suite of lumped GR hydrological models in an R package." Environmental Modelling & Software 94 (2017): 166–171. https://doi.org/10.1016/j.envsoft.2017.03.010

[27] Michel, C. "Hydrologie Appliquee Aux Petits Bassins Ruraux (Applied Hydrology for Small Catchments)." Internal Report; Cemagref Antony: France (1991).

J-Researchers

Journal of Civil Engineering Researchers

Journal homepage: www.journals-researchers.com

Damage Identification in Beams and Plates Using Wavelet Theory and Firefly Optimization Algorithm

Saeed Fallahian,[a,*] Seyed Mohammad Seyedpoor,[a] Himan Khodaei[a]

[a] Department of Civil Engineering, Shomal University, Amol, Iran

ABSTRACT

The ability to identify structural damage in its earliest stages cannot be overstated in terms of importance. This study uses a two-step procedure based on wavelet theory and an optimization method to identify the location and severity of damage in beams and plates. The damage simulates through the introduction of cracks at targeted locations. Acceleration responses obtained from a dynamic analysis using finite element method undergo wavelet transformation, enabling detailed analysis of the dynamic response signals. Through filtering processes, the structural response signal details are extracted. Disturbances appearing in the signal detail plots indicate the presence of damage, leading to the development of a quantitative index for determining probable damage locations. The second phase is used to properly determine the location and magnitude of the damage using firefly optimization algorithm. To assess the effectiveness of the proposed method, three numerical examples including two beams with 16 and 27 elements, and a plate with different support conditions, one with two-edge fixed supports and another with four-edge fixed supports are considered. Different damage scenarios with noise interferences are considered for the structures. The findings indicate that the proposed methodology shows outstanding results in terms of identifying the location and severity of damage using acceleration responses with considering noise.

ARTICLE INFO

Received: July 19, 2025
Accepted: September 07, 2025

Keywords:
Damage Detection
Wavelet Theory
Optimization
Firefly Algorithm
Beams and Plates

DOI: 10.66224/JCER.7.4.34
DOR: 20.1001.1.2538516.2025.7.4.4.6

1. Introduction

The occurrence of damage during the service life of structures is inevitable and it can be considered one of the main causes of failure in structural systems. Structural damage typically manifests locally in specific members or connections, progressively spreading over time. Failing to detect local damage promptly can lead to a sudden catastrophic failure. Therefore, proper identification of damaged members in structures, along with timely repair and replacement, increases operational life of structures and prevents any probable global damage. Damage causes changes in dynamic and static responses, materials, geometry, and other characteristics of structures. Structural Health Monitoring (SHM) is basically the observation and discovering of such changes in structures during their lifetime, aiming to identify damage. As a result, the health monitoring of structures, either permanently or by periodic testing, can enhance safety, integrity, and proper behavior of structures. Wavelet transforms represent one of the

* Corresponding author. Tel.: + 98 11 2203726; e-mail s.fallahian1@gmail.com.

damage detection methods in structures based on vibration data and signal processing, holding significant importance in damage identification. In recent years, the application of wavelet transforms using vibration responses has garnered much attention for damage detection in structures.

In 2001, Cook et al. successfully identified crack occurrence in beams using Haar and Gabor wavelet functions. Their investigation examined the influence of various crack characteristics including length, orientation, and width, as well as different boundary conditions such as simply supported and fixed supports. The findings demonstrated superior effectiveness of Haar wavelets for identifying discrete cracks [1]. In 2004, Okafor and Swarez conducted health monitoring evaluations on single-story, single-bay beams and frames under static and dynamic loading using discrete and continuous transforms. The damage manifested through disruption and disturbance in structural responses. These disturbances, which remain undetectable through direct structural response analysis, become apparent when evaluated using continuous wavelet transform coefficients or detailed signals from discrete transforms. The results demonstrated highly accurate identification and detection of spatial damage locations [2]. Loutridis et al. (2005) used two-dimensional wavelet transforms in the detection of cracks in plate structures. The crack position and size were well reflected in the transformed response, where the vibration behavior of a cracked plate was transformed into the wavelet domain. Quantitative crack depth estimation was performed using maximum values and energy content of wavelet coefficients. They examined plates with cracks of varying depths and positions. The effects of increased noise on method accuracy were investigated using stress noise testing. The proposed method gained significant attention due to its computational simplicity and high result accuracy [3]. In 2006, Roca and Wilde focused on vibration-based structural damage identification using continuous wavelet transforms. They experimentally tested a plexiglass cantilever beam and a four-edge fixed steel plate. Laboratory-obtained modal shapes from the structures (beams and plates) were analyzed using continuous Gaussian and orthogonal inverse wavelet transforms. The proposed wavelet analysis effectively identified damage locations without prior knowledge of structural characteristics or mathematical models [4]. In 2012, Jiang and Liang evaluated multiple damage in thin plate structures using a two-stage approach. They initially applied two-dimensional wavelet transforms for damage location determination, then assessed damage severity at identified locations using particle swarm optimization algorithms. Subsequently, they examined the relationship between damage severities and natural frequencies through finite element analyses. It has been shown that the suggested approach is properly effective in identifying various damages, despite the fact that natural frequencies could not be accurately determined. In general, the findings showed that there was a good assessment of the damage severities by using natural frequencies [5]. In 2013, Jahangir and Esfahani evaluated damage in reinforced concrete beams using wavelet transforms of biorthogonal vibration modes—normal and inverse—under incremental loading effects. Results provided a suitable index for identifying spatial damage locations in beams through detailed signals from inverse biorthogonal wavelet transforms applied to the first strain mode [6]. In 2014, Ezzaldin et al. presented spatial location identification and crack magnitude determination in beams using discrete wavelet transforms in ANSYS software. The disturbances present in the plots demonstrated increased effects of crack depth relative to crack width [7]. In 2016, Hajizadeh et al. evaluated damage detection methods in plates based on two-dimensional wavelets, utilizing both dynamic responses (modal deformations) and static responses (including rotation, stress, and displacement). The results indicated successful evaluation and detection of cracks in plate structures using both static and dynamic responses [8]. In 2019, Ahmadi et al. conducted the identification and simulation of simply supported steel beams in ABAQUS software through comparative evaluation of analytical results from continuous wavelet transforms under primary and secondary conditions of vibration modal shapes. The interpolated modal shape vectors of beams in healthy and defective states were applied as input for Coiflet5 continuous wavelet transforms in MATLAB software. The results indicated the presence of disturbances and irregularities in wavelet coefficients generated at spatial locations of damage occurrence in secondary wavelet analyses compared to primary analyses [9]. In 2020, Guo et al. introduced a novel method for identifying structural microcracks based on wavelet transforms and an Improved Particle Swarm Optimization (IPSO) algorithm. Initially, the specific characteristics of wavelet coefficients were used to determine damage location in the structure, and subsequently, the IPSO algorithm was employed to determine the severity of structural damage. To evaluate the performance of the proposed method in the research, structural microcrack intensity was considered up to a maximum of 10%, and the structure was examined through numerical simulation and experimental testing under various damage scenarios. The IPSO algorithm was compared to the standard Particle Swarm Optimization, Genetic Algorithm (GA), and Bat Algorithm (BA). Wavelet transforms were very effective in the process of identifying the location of damage, and the IPSO algorithm was more effective in identifying the severity of the structural damage than other main algorithms [10]. In 2023, Luo et al. addressed structural damage identification based on one-dimensional convolutional neural network groups, considering sensor errors on a simply supported steel bridge. Based on the sensor configuration, several convolutional neural network sub-models were created to extract features from raw vibration data for sensor fault detection and structural damage identification. Subsequently, two convolutional neural network groups—the sensor fault detection group and the damage identification group—were designed based on the performance of each model. The sensor fault detection group determines whether sensor data is abnormal and cuts off abnormal signals. The remaining normal signals enter the damage identification group, and final damage identification results are calculated based on a statistical decision-making module. Results showed that the detection accuracy for sensor faults and damage identification of each model varies at different noise levels, while the accuracy of final damage identification results reaches one hundred percent [11]. In 2024, Abdushkour et al. focused on structural damage identification using wavelet transforms based on signal derivatives. Derivative-Based Wavelet Transform (DBWT) represents one of the innovative approaches in signal analysis that reveals damage-sensitive regions and is utilized to enhance accuracy in damage detection and structural changes. The study addressed the impact of digital signal types on wavelet transform accuracy in engineering applications and presented an efficient wavelet function based on signal derivatives for improving damage detection in beam structures. Consequently, signals obtained from steel beam modal shapes were utilized to evaluate the effectiveness of derivative-based wavelet transforms. They pointed out the relevance of the choice of signal type in improving the accuracy of wavelet transforms in erroneous and damaged signal detection. The outcomes revealed that the use of signal derivatives in wavelet transforms can identify the location of damage with high precision in all the circumstances of damage [12]. In 2025, Zhao et al. presented edge damage detection in structural members using wavelet transforms and Immune-Genetic Algorithm (I-GA). Due to the capability of Wavelet Transform (WT) in identifying damage details in strain modes, the method has attracted considerable attention. Typically, when applying wavelet transforms, damage at structural edges remains ambiguous and undetectable, primarily due to edge effects. To fix this, the analysis is performed carefully at the location of the damage with the help of wavelet transforms by introducing a suitable suffix to the original vibration signal that essentially minimises the edge effects. Besides, an I-GA that integrates a genetic and immune algorithm is utilized to avoid the shortcomings of conventional intelligent algorithms in determining the severity of the damage. The efficiency of this approach for detecting the location of edge damage was validated, and influential parameters, such as the location of damage, noise effects, and damage severity, were measured [13].

In this research a two-stage method based on wavelet theory and optimization method to identify the location and severity of damage to beam and plate structures has been proposed. To identify the location and approximate magnitude of damage in a structure, acceleration responses obtained from a finite element analysis are subjected to wavelet transforms. Subsequently, dynamic response signals are analyzed, and response signal details are extracted using filters. Disturbances in the response signal detail plots indicate the presence of damage. This principle can lead to the introduction of a quantitative index for determining probable damage locations. Then, in the second stage, precisely identifying damage location and magnitude are performed using Firefly Optimization Algorithm. To ensure the effectiveness of the proposed method, two beam structures with different characteristics as well as a plate structure with various support conditions are examined under different damage scenarios. During assessing the method under investigation, the impact of different parameters affecting the efficiency of the method such as, noise effects, number of damaged elements and so on are also studied

2. Finite Element Simulation of structures

2.1. Beams

For beam simulation, the finite element method is employed through coding in the MATLAB software environment. The Newmark method is used to determine acceleration responses. Damage (crack) is simulated as stiffness reduction at specific locations in the beams. Figure 1 shows the triangular variation of stiffness in beam elements [14,15].

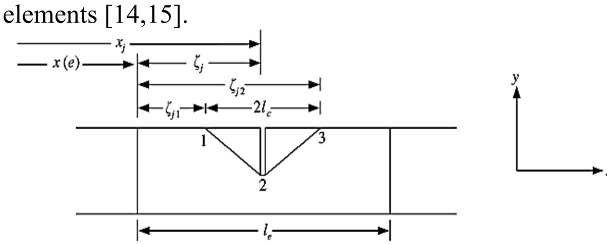

Figure 1. Triangular stiffness variation for crack simulation in different beam elements [14,15]

In this study, crack simulation in beams is performed using stiffness variation with assumptions including: uniform crack depth across the entire beam width and no change in beam mass due to the presence of cracks. Equation (1) represents the flexural stiffness magnitude in the crack region of the beam.

$$EI_e(\xi) = \begin{cases} EI_0 - E(I_0 - I_{cj})\dfrac{(\xi - \xi_{j1})}{(\xi_j - \xi_{j1})} & \text{if } \xi_{j1} \le \xi \le \xi_j \\ EI_0 - E(I_0 - I_{cj})\dfrac{(\xi_{j2} - \xi)}{(\xi_{j2} - \xi_j)} & \text{if } \xi_j \le \xi \le \xi_{j2} \end{cases} \tag{1}$$

$$\xi_{j1} = \xi_j - l_c \quad , \quad \xi_{j2} = \xi_j + l_c$$

$$I_0 = \frac{wd^3}{12} \quad , \quad I_{cj} = \frac{w(d-d_{cj})^3}{12}$$

where the symbols ξ_j, ξ_{j1}, and ξ_{j2}, represent the location of the j-th crack in the e-th element, along with the starting and ending positions of the crack, respectively. The parameters d_{cj}, I_0 and I_{cj} represent the crack depth, the moment of inertia of the intact beam cross-section and the cracked cross-section, respectively. Also, *w* and *d* represent the width and depth of the beam, befor any damage.

Based on definition above, equation (2) can now be used to compute the stiffness matrix of cracked beam element.

$$K_{e.crack} = K_e - K_{cj} \tag{2}$$

where the matrices K_e and K_{cj} represent the stiffness matrix of the intact element and its reduction due to the j-th crack, respectively [14].

2.2. Plates

For simulating plate structures, the finite element method has been employed within the MATLAB software environment. The Newmark method was used to determine acceleration responses. Damage in plates is simulated here as a thickness reduction within an element, as shown in Figure 2. For thin plates, the flexural rigidity is calculated according to equation (3) [5,16].

$$D_0 = \frac{E\,t^3}{12(1-\mu^2)} \tag{3}$$

where E, t, and μ represent elastic modulus, thickness, and Poisson's ratio of the plate, respectively.

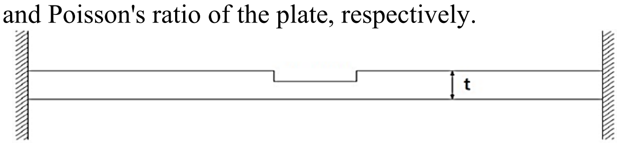

Figure 2. Stiffness variations (thickness reduction) in plates to create damage in different elements [16].

3. Damage Localization Using Wavelet Theory

In recent decades, wavelet transforms have gained widespread application in structural health monitoring and damage detection. These transforms are based on time-frequency analyses and convert signals into small wavelets. Generally, mathematical transformations are applied to signals to extract hidden data within them. Wavelet transforms perform localized regional analyses through large-scale signals, thus possessing the capability to execute local analyses. Wavelet transforms have the ability to perform localized analyses on signals. Through wavelet transforms, signals appear as peaks at discontinuity locations. Furthermore, using wavelet transforms in structures, damage locations are detected as peak locations and disturbances on the graph of base or mother wavelet coefficients. In fact, wavelet analyses have the ability to detect and identify spatial locations of very small damage and discontinuities. In wavelet analyses, the factors used are obtained directly from the time history response of systems using simple tools, and these factors, unlike modal domain-based methods, do not require modal analysis and extraction of natural frequencies of the system and operate independently of them. This means that wavelet analysis is a powerful method that can extract important information from structural response without requiring modal analysis to be performed first. This feature can be a major advantage in some cases, as modal analysis may be time-consuming and complex. In this study, Symlet wavelet functions have been used to identify damage in the structures under investigation, and the structural response used is acceleration. A wavelet is an oscillatory function with a real, periodic, or complex nature with an average value of zero and finite length. Generally, changes in size, location, and final shape of the mother (generator) wavelet function occur through translation and scaling in the signal application range according to equation (4) [17,18].

$$\psi_{u,s}(x) = \frac{1}{\sqrt{s}}\psi\left(\frac{x-u}{s}\right) \tag{4}$$

$$\psi(x) \in L^2(R)$$

where $\psi_{u,s}(x)$, $\psi(x)$, and $L^2(R)$ represent continuous wavelet functions, mother function, and Hilbert space with the capability of measuring square-integrable functions, respectively. Also, the parameters s and u in equation (4), which are real numbers, represent the scaling factor (scale characteristic) and translation (temporal, spatial positions, or center of influence) of wavelets, respectively. For the signal of interest, continuous wavelet transforms are shown in equation (5).

$$w\,f(u,s) = [f,\ \psi_{u,s}] = \frac{1}{\sqrt{s}}\int_{-\infty}^{+\infty} f(x)\,\psi\left(\frac{x-u}{s}\right)dx \tag{5}$$

$$f(x) \in L^2(R)$$

where $w\,f(u,s)$ is the wavelet coefficients of the function $\psi_{u,s}(x)$, and x is the spatial coordinate. Computing and measuring these wavelet coefficients will allow us to capture the variations of the signal in the neighborhood of parameter u, which is proportional to the scaling factor s.

In this research, the structures under investigation are modeled using the finite element method in MATLAB software. Mass and stiffness matrices are formed, and dynamic responses are computed. The applied load takes the form of a trapezoidal impact, and acceleration responses are determined using the Newmark method. Subsequently, the acceleration responses obtained from a dynamic analysis via finite element method undergo wavelet transformation for dynamic response signal analysis. Through filtering, detailed characteristics of the structural response signal are extracted. In such signals, it can be seen that the occurrence of the irregularities and the peak areas can be used to estimate which areas might be damaged, and the appropriate damage indices can be set. Disturbances in the detailed response signal plots indicate structural damage, leading to the introduction of a wavelet index for identifying probable damage locations.

4. Damage Localization and Quantification Using an Optimization Method

The optimization problem formulation for damage identification in structures can be given in equation (6) [15]:

$$\begin{aligned} &\text{Find: } X^T = \{X_1, X_2, \dots, X_n\} \\ &\text{Minimize: } W(X) \\ &X^T \leq X_i \leq X^u \end{aligned} \tag{6}$$

where X, X^T, and X^u represent the damage variable vector containing unknown damage location and severity, and the upper and lower bounds of the damage vector, respectively. The variable W represents the objective function, which constitutes one of the most critical components of an optimization problem and serves as a criterion for calculating convergence values and determining algorithm termination. The objective function in this paper is according to equation (7) and it is needed to be minimized [15].

$$W(X) = -\frac{1}{2}\left[\frac{|\Delta R^T.\delta R(X)|^2}{(\Delta R^T.\Delta R)(\delta R(X)^T.\delta R(X))} + \frac{1}{n_p}\sum_{i=1}^{n_p}\frac{\min(R_{x,i}, R_{di})}{\max(R_{x,i}, R_{di})}\right] \tag{7}$$

where R_{di} and R_{xi} represent the i-th components of the response vector in the damaged state R_d and the numerical model response vector R_x, respectively, the vectors ΔR and $\delta R(X)$ represent the structural response changes relative to the healthy state under damage occurrence and those derived from the numerical model, respectively. Also, n_p is the number of elements in the structural response vector [15]. The response considered in this research is the nodal acceleration, and the firefly algorithm is used to perform the optimization task [19]. Because the main part of the damage identification procedure is the first part, therefore any optimization algorithm can be emplyed here without having an important effect on the performance of the whole method.

5. Numerical Examples

In order to assess the performance of the proposed method, two beams with different properties and elements of 16 and 27 and a plate with two different support conditions of two-sided and four-sided fixed are considered. Damage in beams is defined as a crack on the desired elements according to Sinha et al. [14] and Yazdanpanah and Seydpoor [15], while for plates, damage is simulated using stiffness reduction based on Jiang and Liang [5]. The process entails the modeling of the target structures using finite element method in MATLAB, the construction of mass and stiffness matrices and followed by extracting the dynamic responses, such as natural frequencies, modal deformations and acceleration responses. The loads applied have a short-term non-periodic type of impact, which is in the shape of a trapezoidal force, as shown in Figure 3. The acceleration responses obtained from dynamic analysis undergo wavelet transformations, followed by dynamic response signal analysis. Through filtering, detailed characteristics of the structural response signal are extracted. Disturbances in the detailed structural signal plots indicate the damage presence within the structure. High values of the wavelet index within a specific time window indicate sudden and significant changes in the acceleration response signal during that time interval, which may result from damage occurrence. After damage localization, the firefly algorithm is employed to accurately determine damage locations within structures as well as damage severity. The best values for optimization parameters have been chosen according to Ref. [19] and the optimization will stop if there is no significant improvement in the objective function for a few successive iterations.

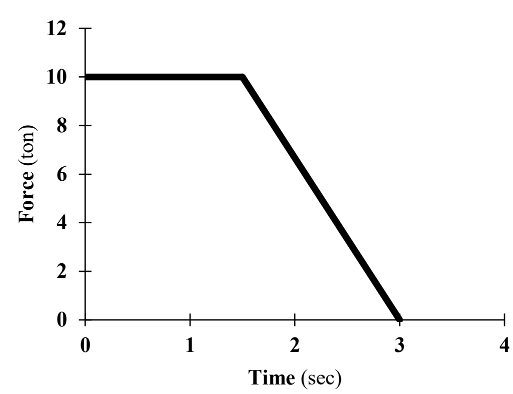

Figure 3 - Applied Force Diagram for Structural Loading

5.1. Sixteen-Element Cantilever Beam

A sixteen-element aluminum cantilever beam with seventeen nodes with two degrees of freedom per node serves as the first example. The boundary conditions of the beam include the translational as well as the rotational springs as shown in Figure 4. The dimensions of the beam are 996 mm, 50 mm and 25 mm in length, width, and depth, respectively and the material properties are Youngs modulus 69.79 GN/m^3, density 2600 kg/m^3, Poisons ratio 0.33, translational spring stiffness (Kt) 26.50 MN/m and rotational spring stiffness (Ktheta) 150 kNm/rad. The beam is initially modeled in MATLAB software, then subjected to a short-term, non-periodic trapezoidal impact load as shown in Figure 3. Dynamic acceleration responses are obtained, and damage identification results are presented through graphical representations. Figure 4 illustrates the finite element model of the beam with a single crack located at the center of element 5 positioned 275 mm from the beam's left end. Table 1 lists three scenarios of damage undertaken in the beam.

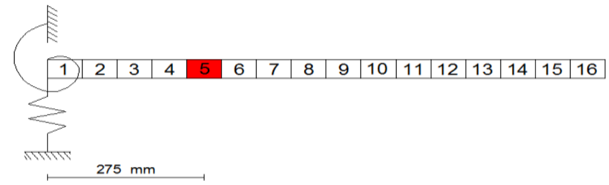

Figure 4. Finite Element Model of Sixteen-Element Cantilever Beam (Red-colored element indicates crack location)

Table 1:
Damage Conditions at 275 mm Position from Beam Left end (Element 5)

Damage Case	Crack depth (mm)	Crack Depth to Beam Depth
First	4	0.16
Second	8	0.32
Third	12	0.48

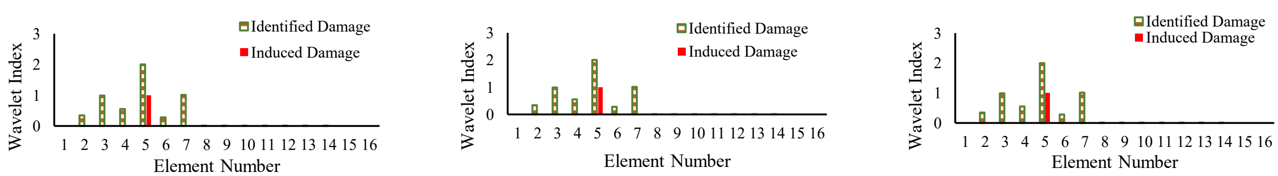

First Damage State Second Damage State Third Damage State

Figure 5. Damage Location for Different Damage States Using Wavelet Index Under Noise-Free Condition

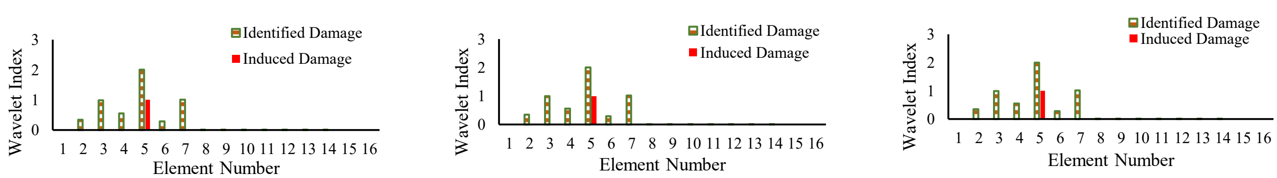

First Damage State Second Damage State Third Damage State

Figure 6. Damage Location for Different Damage States Using Wavelet Index Under 3% Noise Condition

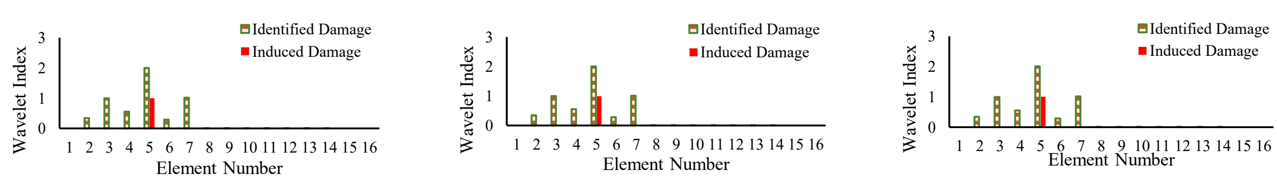

First Damage State Second Damage State Third Damage State

Figure 7. Damage Location for Different Damage States Using Wavelet Index Under 5% Noise Condition

The beam undergoes under the specified damage conditions with and without considering 3% and 5% noise levels. Figures 5, 6, and 7, respectively, demonstrate damage location assessment for different damage states using the wavelet index applied to acceleration responses under noise-free condition and with 3% and 5% noise considerations. Figures 8, 9, and 10, respectively, show the damage location and severity identification in the second step for various damage cases of the beam under noise-free condition and with 3% and 5% noise considerations.

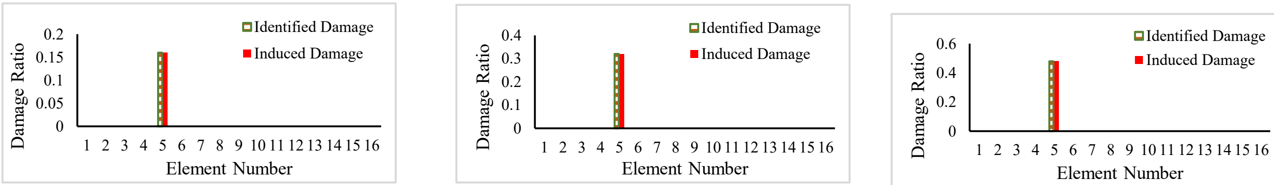

First Damage State Second Damage State Third Damage State

Figure 8. Location and Damage Severity for Different Damage States Under Noise-Free Condition

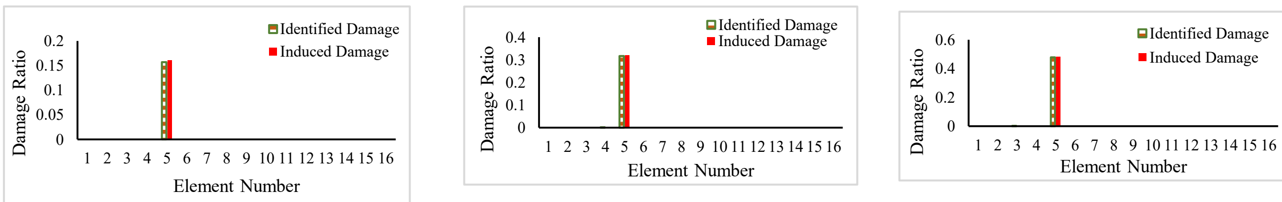

First Damage State Second Damage State Third Damage State

Figure 9. Location and Damage Severity for Different Damage States Under 3% Noise Condition

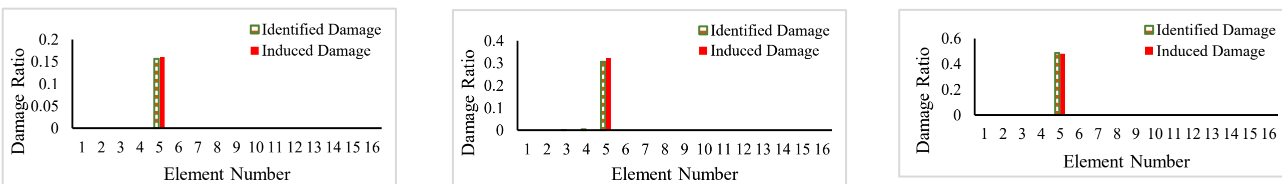

First Damage State Second Damage State Third Damage State

Figure 10. Location and Damage Severity for Different Damage States Under 5% Noise Condition

Considering the damage identification charts for the sixteen-element cantilever beam, the probable damage location (element 5) is effectively detected by the wavelet index regardless of whether noise is present in the data. This method demonstrates excellent capability in identifying both damage location and severity with high precision. The detection results of damage severity compared to precise values under 3% and 5% noise are listed in Table 2.

5.2. Twenty-Seven Element Simply Supported Beam

A twenty-seven-element aluminum simply supported beam with twenty-eight nodes, having two degrees of freedom per node, considered as the second example. The beam dimensions include length, width, and depth of 1832mm, 50mm, and 25mm, respectively, with Young's modulus of 69.79 GN/m², density of 2600 kg/m³, and Poisson's ratio of 0.33. The beam finite element model with a single crack at element 9 (position is 595mm off the origin) and two cracks at elements 9 and 12 (position is 595mm and 800mm off the beam origin) are shown in Figure 11a and b, respectively. Damage conditions including single and double damage cases are shown in Table 3.

The beam was evaluated under the specified damage conditions, both with noise free, 3% and 5% noise considerations. Figures 12 to 17, respectively, show damage location assessment for various single and double damage conditions using the wavelet index on acceleration responses under noise-free and noisy conditions (3% and 5% noise).

Table 2

Error Rate of identifying Damage severity for Different Cases Under 3% and 5% Noise

Noise (%)	**Damage Case**	**Actual Damage Severity (%)**	**Error Rate (%)**
	First	16	1.75
3%	Second	32	1.16
	Third	48	0.30
	First	16	2.03
5%	Second	32	4.15
	Third	48	1.19

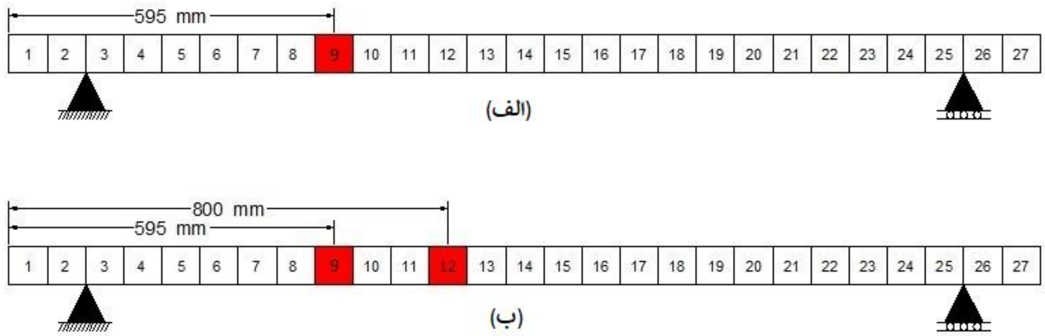

Figure 11. Finite Element Model of a Twenty-Seven Element Simply Supported Beam (a) Single damaged element and (b) Two damaged elements (Red elements indicate crack locations)

Table 3
Different Damage Conditions of twenty-seven-element simply supported beam

Damage Condition	Damage Case	Damaged Element	Crack depth (mm)	Crack depth to Beam Depth
Single Damage	First	9	4	0.16
	Second	9	8	0.32
	Third	9	12	0.48
Double Damage	First	9	12	0.48
		12	4	0.16
	Second	9	12	0.48
		12	8	0.32
	Third	9	12	0.48
		12	12	0.48

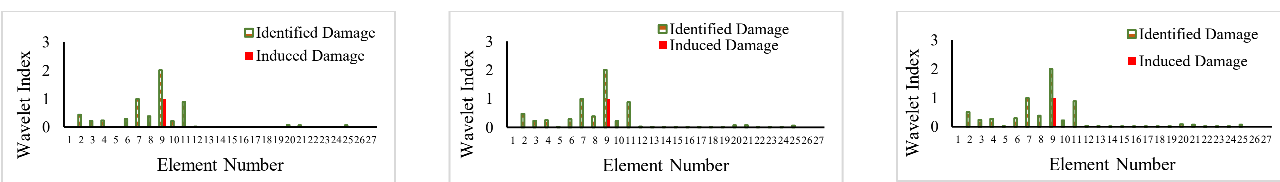

Figure 12. Location for single damage condition under various damage cases using wavelet index without noise

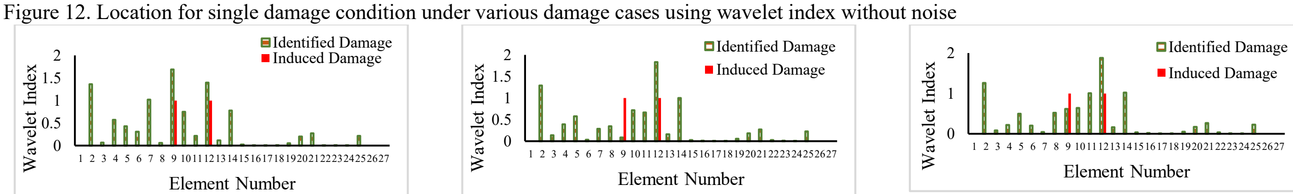

First failure state Second failure state Third failure state

Figure 13. Location for double damage condition under various damage cases using wavelet index without noise

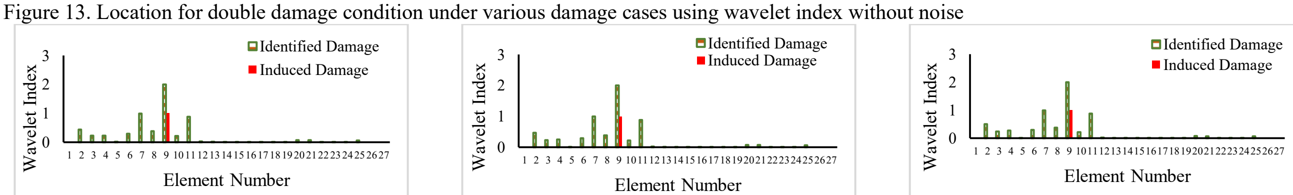

First failure state Second failure state Third failure state

Figure 14. Location for single damage condition under various damage cases using wavelet index with 3% noise

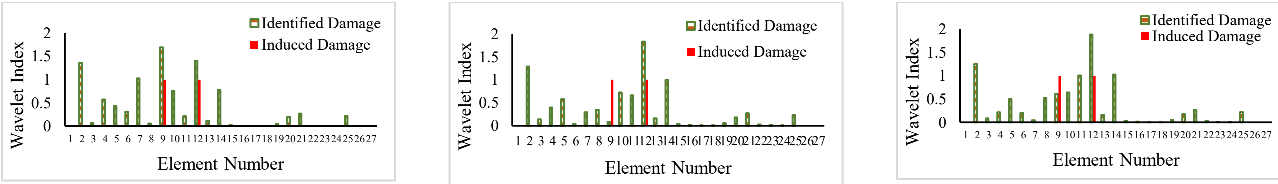

First failure state Second failure state Third failure state

Figure 15. Location for double damage condition under various damage cases using wavelet index with 3% noise

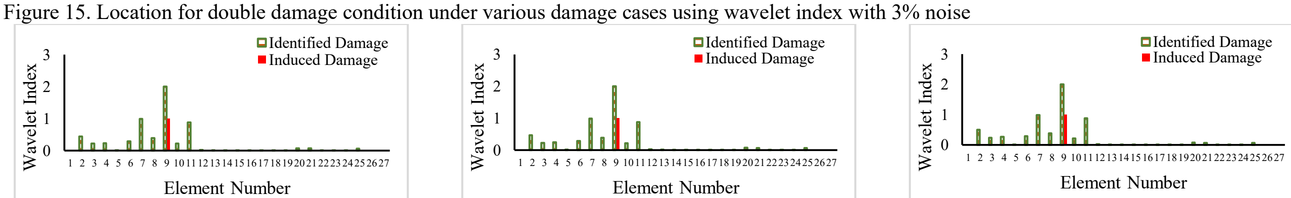

First failure state Second failure state Third failure state

Figure 16. Location for single damage condition under various damage cases using wavelet index with 5% noise

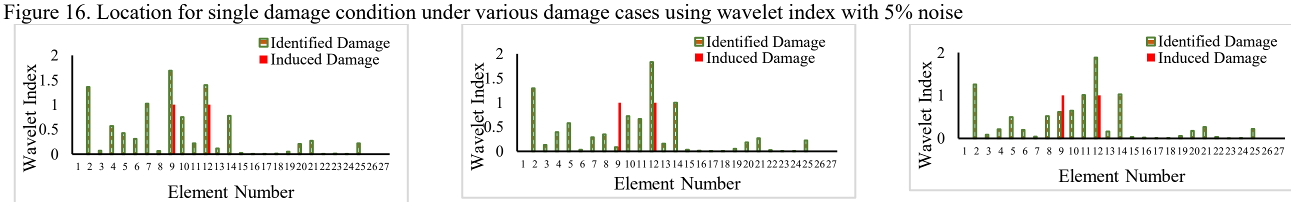

First failure state Second failure state Third failure state

Figure 17. Location for double damage condition under various damage cases using wavelet index with 5% noise

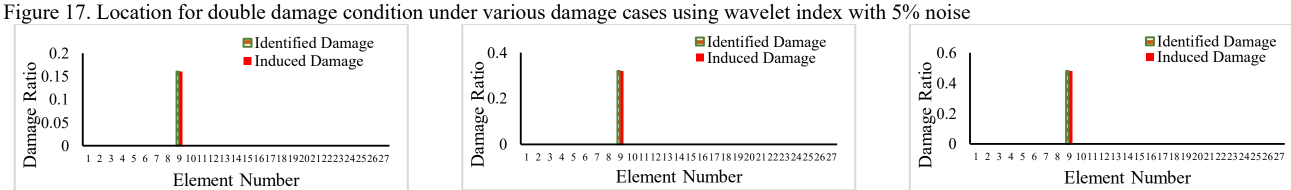

First failure state Second failure state Third failure state

Figure 18. Damage location and severity for single damage condition under various cases without noise

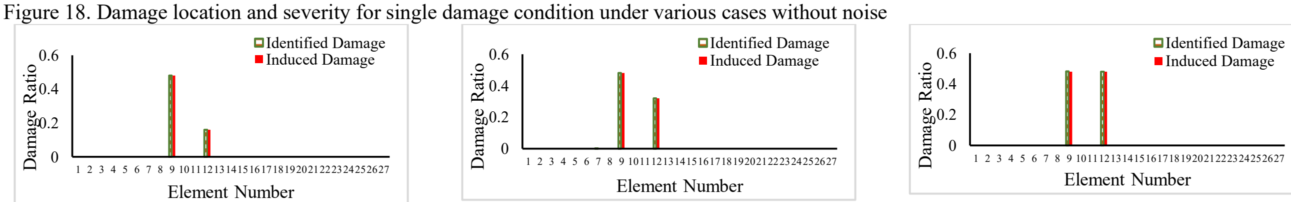

First failure state Second failure state Third failure state

Figure 19. Damage Location and severity for double damage condition under various cases without noise

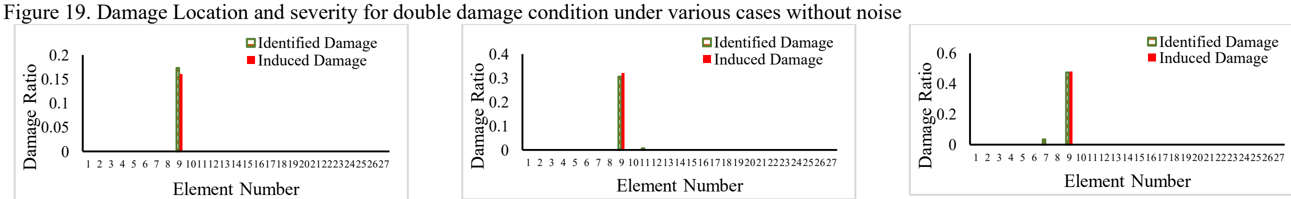

First failure state Second failure state Third failure state

Figure 20. Damage Location and severity for single damage condition under various cases with 3% noise

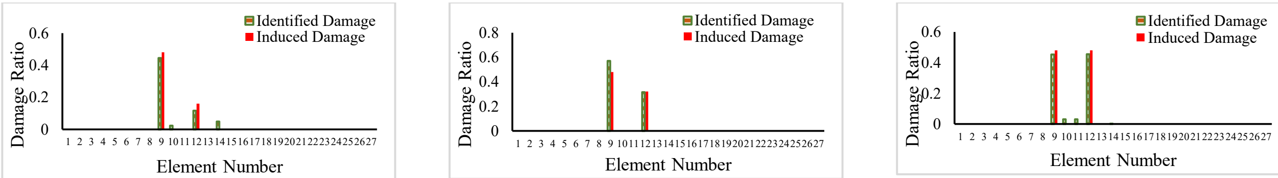

First failure state Second failure state Third failure state

Figure 21. Damage Location and severity for double damage condition under various cases with 3% noise

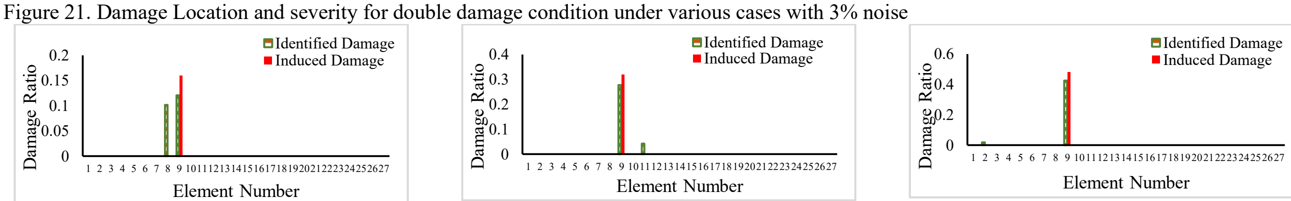

First failure state Second failure state Third failure state

Figure 22. Damage Location and severity for single damage condition under various cases with 5% noise

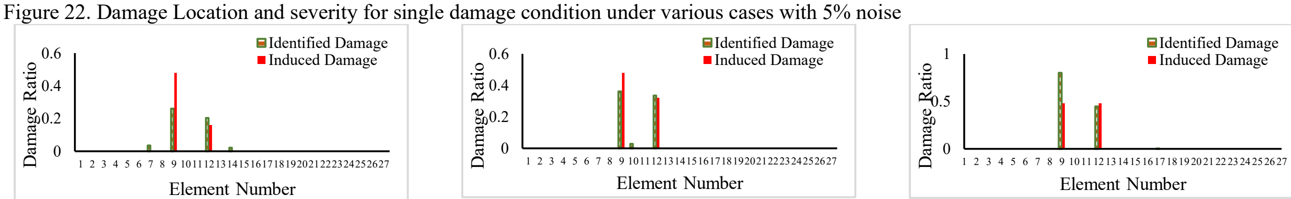

First failure state Second failure state Third failure state

Figure 23. Damage Location and severity for double damage condition under various cases with 5% noise

Table 4

Error Rate of identifying Damage severity for Different Cases Under 3% and 5% Noise

Damage Condition	**Damage Case**	**Actual Damage Severity (%)**	**Error Rate (%)**	
			(Noise 3%)	**(Noise 5%)**
Single Damage	First	16	8.14	24.46
	Second	32	4.55	13.34
	Third	48	1.28	11.49
Double Damage	First	48	7.17	45.66
		16	27.07	26.91
	Second	48	19.06	24.63
		32	1.09	4.91
	Third	48	5.69	66.66
		48	5.11	6.8

Figures 18 through 23 demonstrate damage location and severity identification in the second step for various damage.

According to the damage identification charts for the twenty-seven-element simply supported beam under both single and double damage conditions, the probable damage locations are successfully detected by the wavelet index. For both single and double damage cases, the method demonstrates excellent capability in identifying both damage location and severity with high accuracy, regardless of noise presence in the data. The detection results of damage severity compared to their exact values are given in Table 4.

5.3. Plate with Different Support Conditions

A square plate with dimensions of 560×560 mm and different support conditions including two-edge and four-edge clamped are considered as third example. Each plate edge is divided into 28 elements, resulting in a mesh configuration of 28×28 elements. The plates are 2 mm thick, comprise 841 nodes, and possess 784 elements whose dimensions are 20 mm. The plates have the Young modulus of 200 GPa, a density of 7850 kg/m³ and the Poisson ratio of 0.3. The plates subjected to the trapezoidal impact loading are modeled using MATLAB. Acceleration responses are obtained, and damage identification results are presented graphically. Damage in the plates includes four different scenarios, with each damage scenario comprising sixteen elements (4×4 configuration). Each damage scenario includes four different thickness reduction values according to Table 5. The length and width of each damage area (sum of four elements in each direction) are 80 mm.

Table 5
Damage Cases in Four Scenarios for Two-Edge and Four-Edge Clamped Plates

Damage Case	Thickness Reduction (mm)	Thickness Reduction (%)	Remaining thickness (mm)
1	0.5	25	1.5
2	1.0	50	1.0
2	1.5	75	0.5
4	1.75	87.5	0.25

Damage locations for scenarios 1 to 4 in the two-edge and four-edge clamped plates are shown in Figures 24 and 25, respectively.

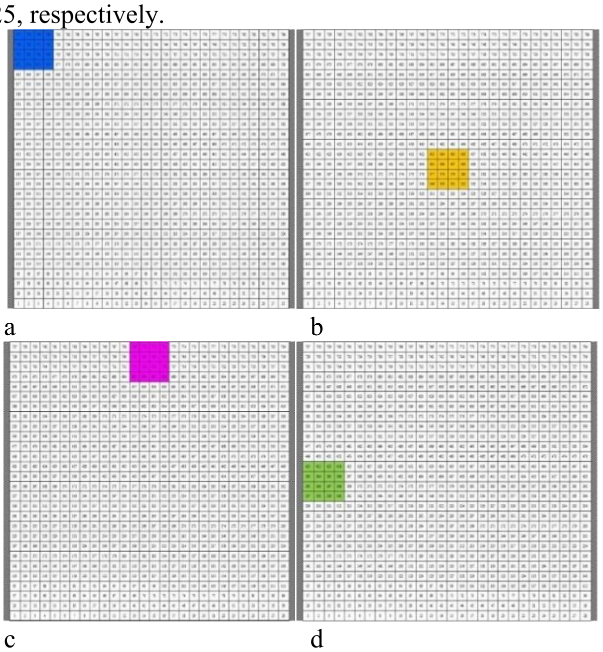

Figure 24. Damage Locations in Scenarios: (a) First, (b) Second, (c) Third, and (d) Fourth for a two-edge clamped plate

Figures 26 to 33 show damage location detection for scenarios 1 to 4 with damage severities of 25%, 50%, 75%, and 87.5% using wavelet analysis without noise consideration for both two-edge and four-edge clamped plates, respectively. Figures 34 to 41, respectively, show damage location assessment for scenarios 1 to 4 with damage severities of 25%, 50%, 75%, and 87.5% for both two-edge and four-edge clamped plates using wavelet analysis with 3% noise applied.

Figures 42 through 49 demonstrate location and severity identification in the second step for scenarios one through four with damage severities of 25%, 50%, 75%, and 87.5% for both two-edge and four-edge clamped plates without noise consideration. Figures 50 through 57 demonstrate location and severity identification in the second step for scenarios one through four with damage severities of 25%, 50%, 75%, and 87.5% for both two-edge and four-edge clamped plates with 3% noise applied.

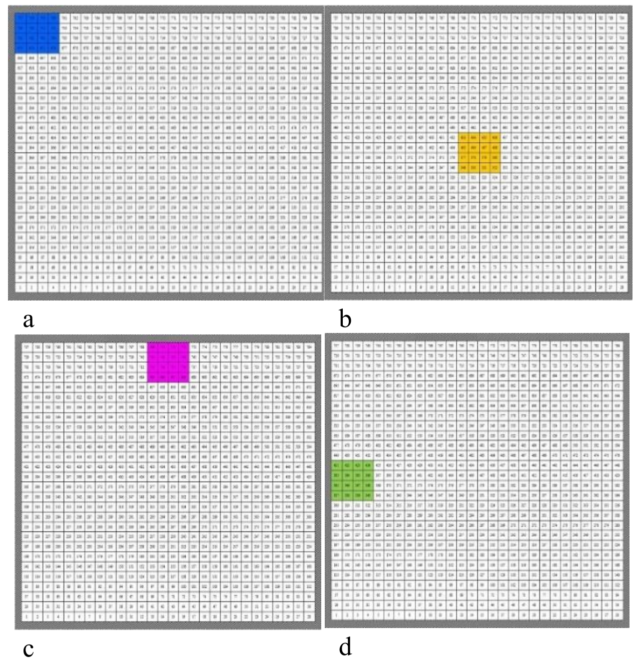

Figure 25. Damage Locations in Scenarios: (a) First, (b) Second, (c) Third, and (d) Fourth for a four-edge clamped plate

As evident from the diagrams, damage location identification in cases with and without noise consideration for both two and four edge clamped plates demonstrates acceptable accuracy. In the 25% damage condition, without considering noise and in scenarios 1 to 4, damage intensity in two edge clamped plates is obtained with differences of 0%, 2.9%, 6.8%, and 8%, respectively, while in four edge clamped plates, the differences were 3.7%, 2.8%, 3.8%, and 12.72%, respectively. In the 50% damage condition, without noise application and in scenarios 1 to 4, damage intensity for two edge clamped plates is evaluated with differences of 4%, 0%, 8.1%, and 15.8%, respectively, while in plates with other boundry conditions, the differences are 19.4%, 5.8%, 14%, and 23.75%, respectively. In the 75% damage condition, without noise application and in scenarios 1 to 4, damage intensity in two edge clamped is evaluated with differences of 0%, 1.3%, 2.7%, and 6.4%, respectively, while in plates clamped on four sides, the differences were 0%, 2.53%, 1.33%, and 0%, respectively. In the 87.5% damage condition, without noise application and in scenarios 1 to 4, damage intensity in simply supported plates on two sides is evaluated with differences of 0%, 1.7%, 1.7%, and 2.3%, respectively, while in plates clamped on four sides, the differences were 0.57%, 3.7%, 1.71%, and 0.57%, respectively.

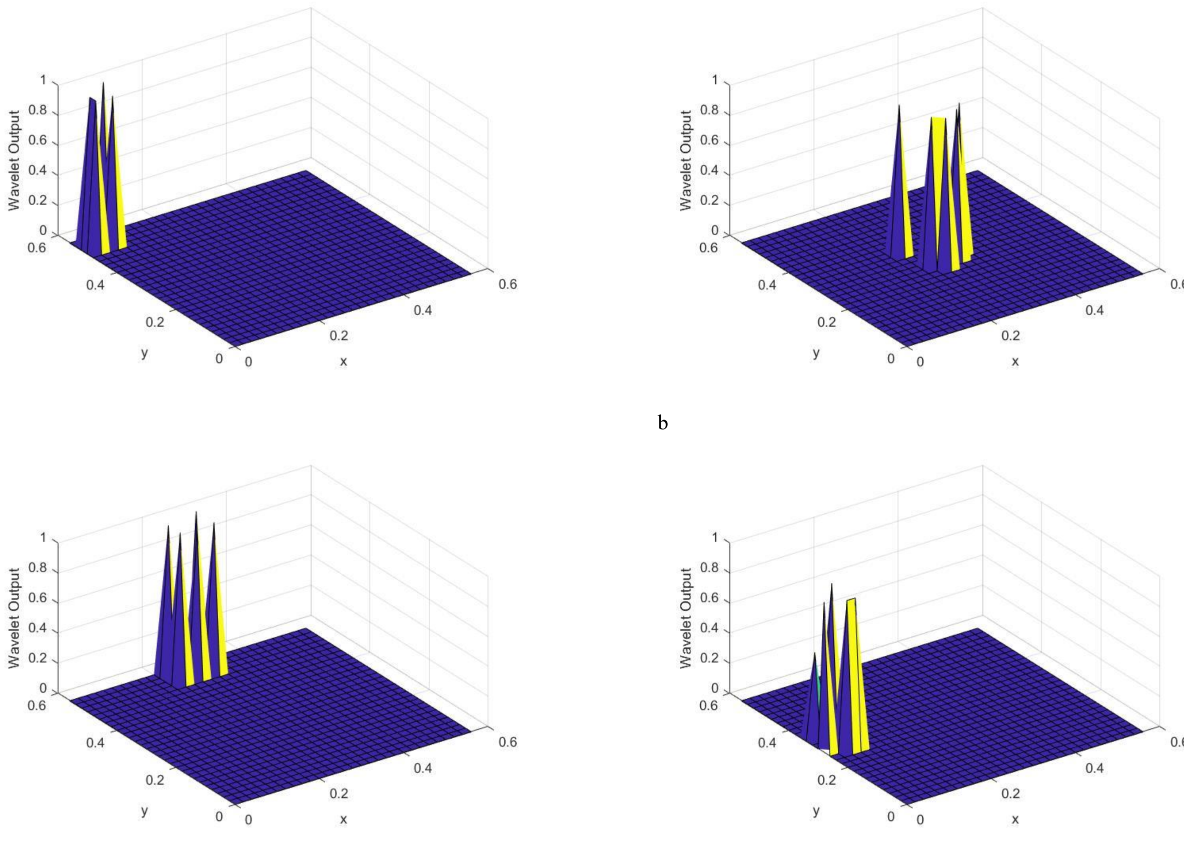

a b

c d

Figure 26. Damage localization in scenarios (a) first, (b) second, (c) third, and (d) fourth with 25% damage severity in two-edge clamped plate using wavelet analysis without considering noise

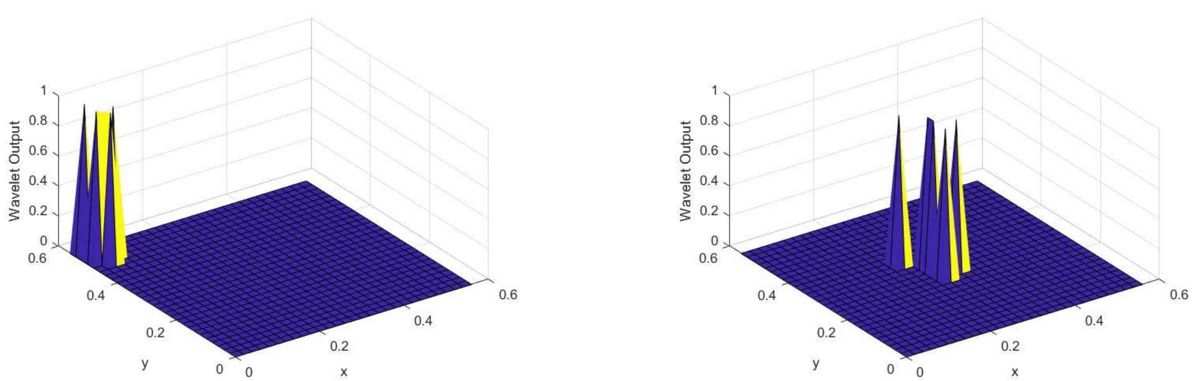

a b

Figure 27. Continued on next page

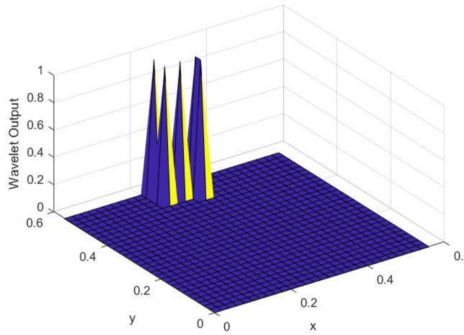

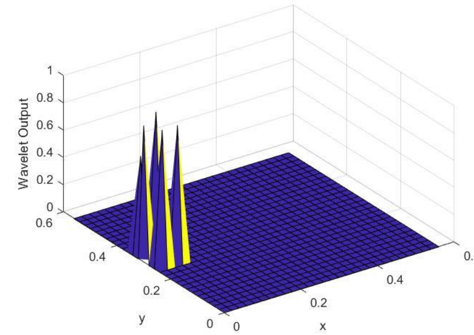

c d

Figure 27. Damage localization in scenarios (a) first, (b) second, (c) third, and (d) fourth with 50% damage severity in two-edge clamped plate using wavelet analysis without considering noise

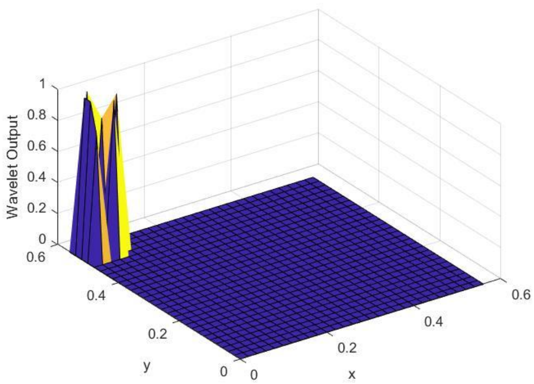

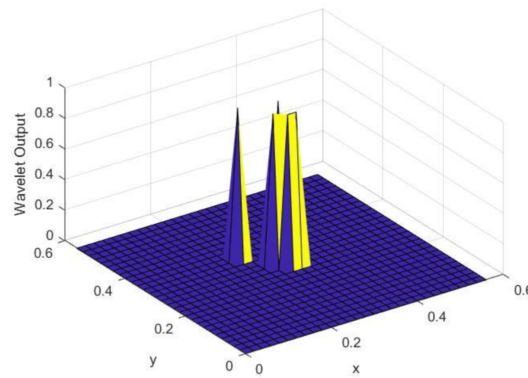

a b

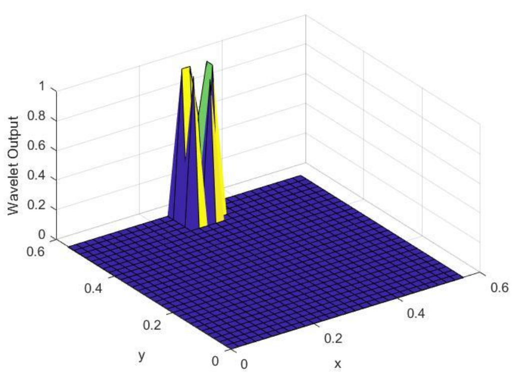

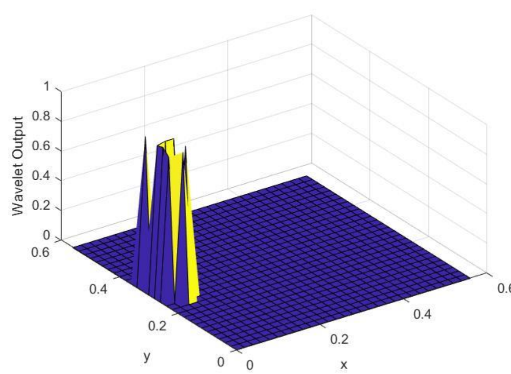

c d

Figure 28. Damage localization in scenarios (a) first, (b) second, (c) third, and (d) fourth with 75% damage severity in two-edge clamped plate using wavelet analysis without considering noise

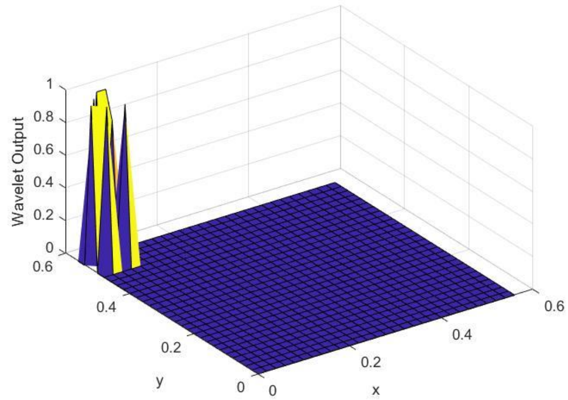

a

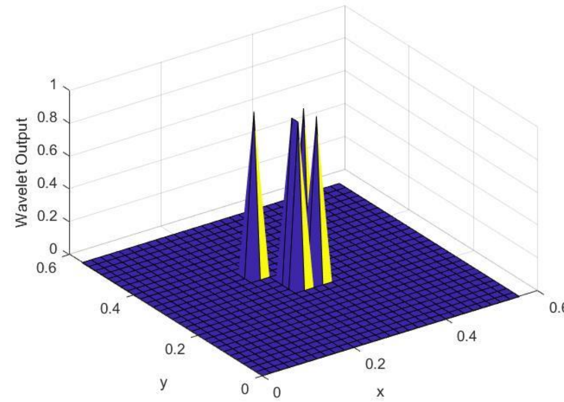

b

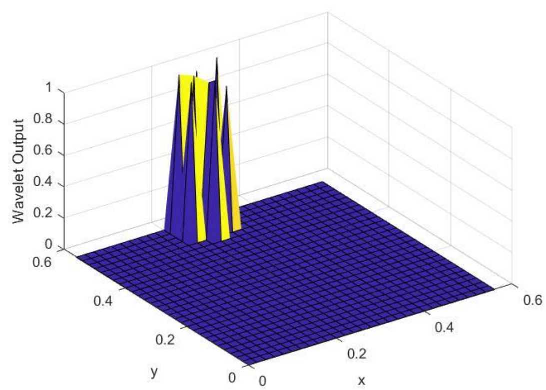

c

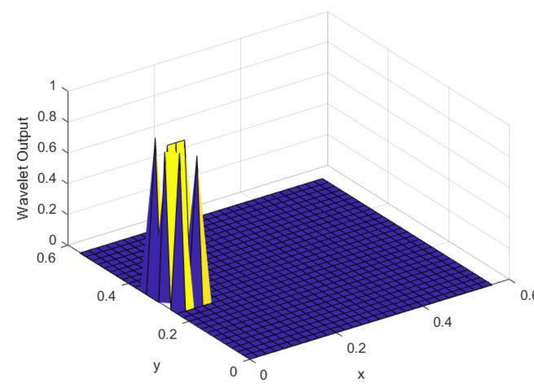

d

Figure 29. Damage localization results for scenarios a) first, b) second, c) third, and d) fourth, with 87.5% damage severity in two-edge clamped plates using wavelet analysis without considering noise

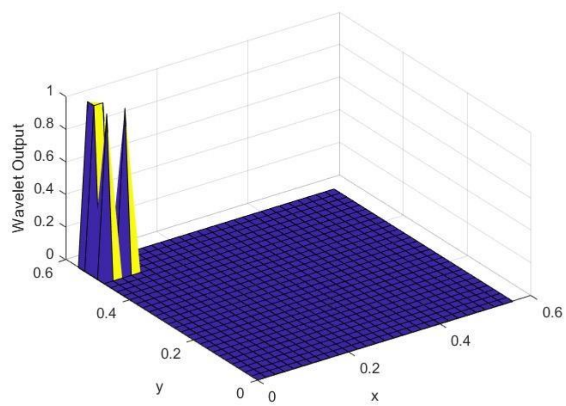

a

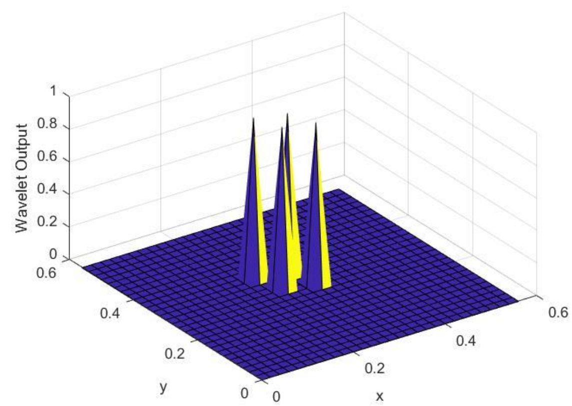

b

Figure 30. Continued on next page

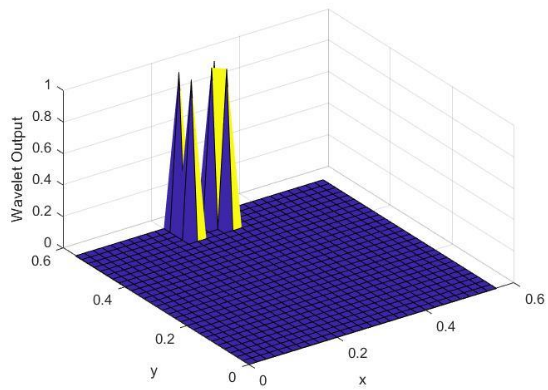

c

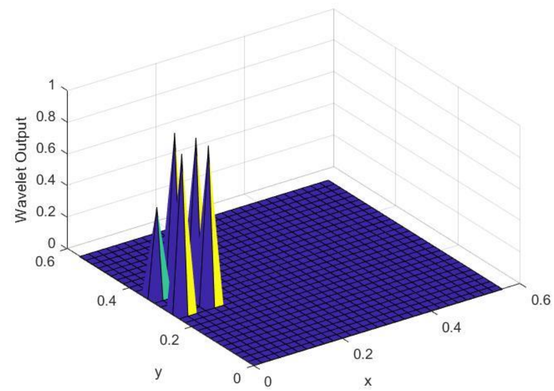

d

Figure 30. Damage localization results for scenarios a) first, b) second, c) third, and d) fourth with 25% damage severity in four-edge clamped plates using wavelet analysis without considering noise

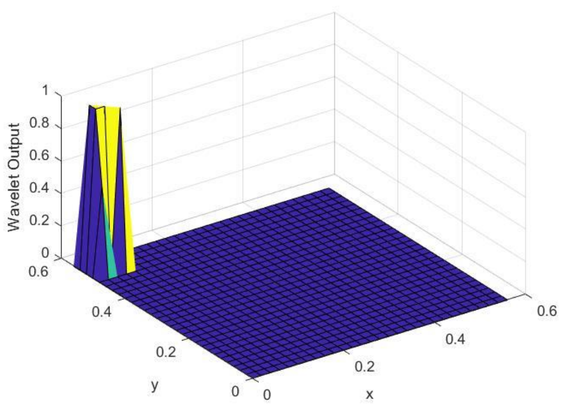

a

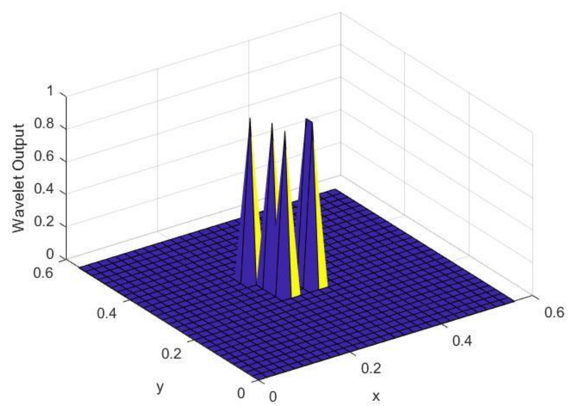

b

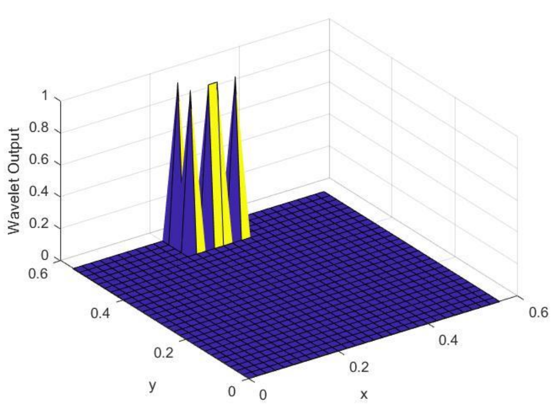

c

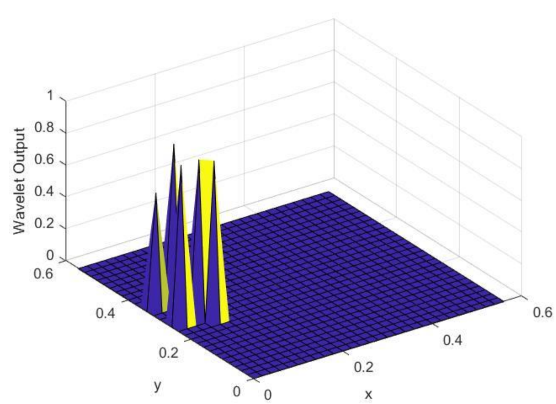

d

Figure 31. Damage localization results for scenarios a) first, b) second, c) third, and d) fourth with 50% damage severity in four-edge clamped plates using wavelet analysis without considering noise

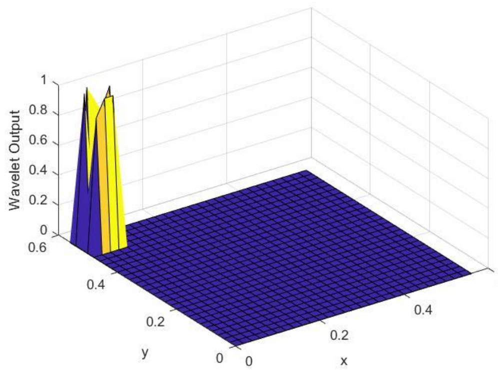

a

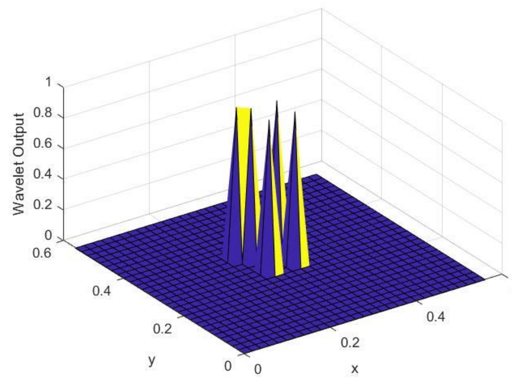

b

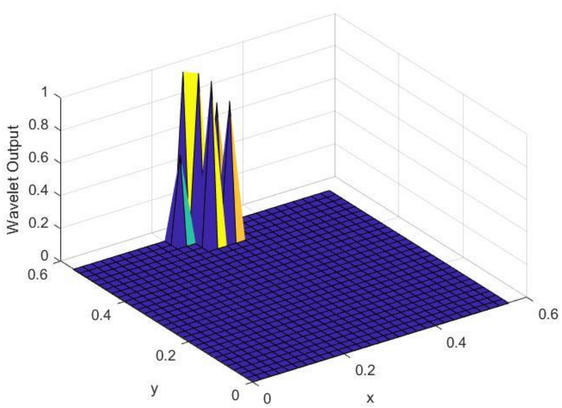

c

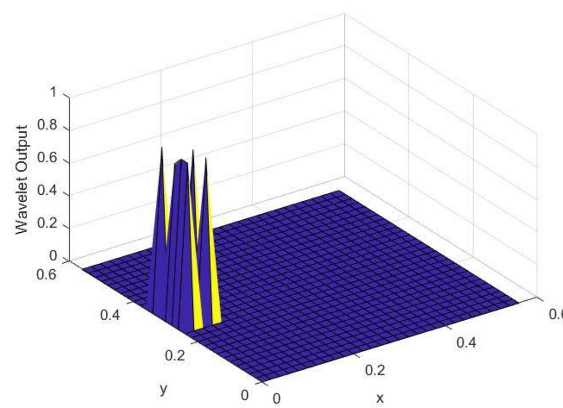

d

Figure 32. Damage localization results for scenarios a) first, b) second, c) third, and d) fourth with 75% damage severity in four-edge clamped plates using wavelet analysis without considering noise

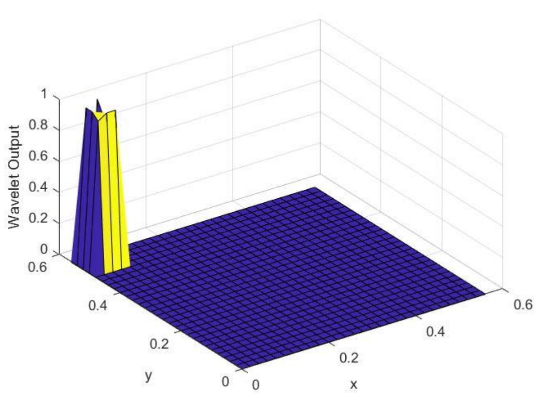

a

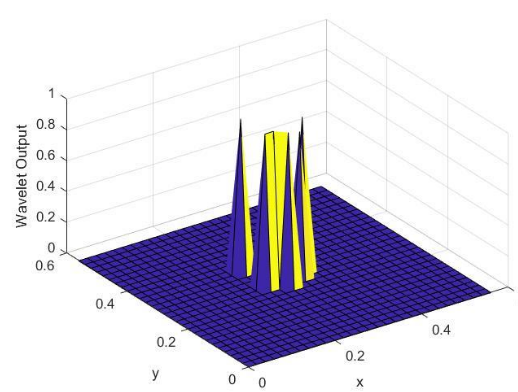

b

Figure 33. Continued on next page

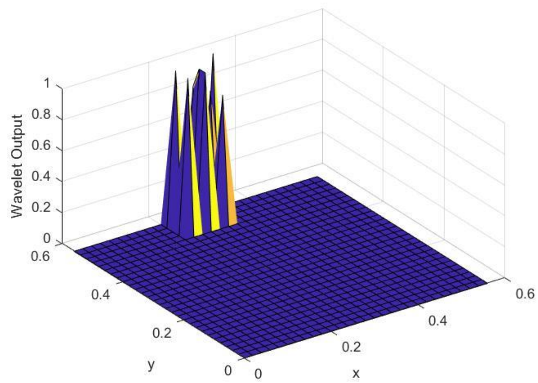

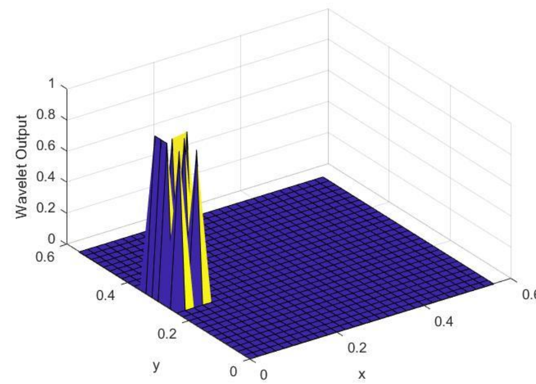

c d

Figure 33. Damage localization results for scenarios a) first, b) second, c) third, and d) fourth, with 87.5% damage severity in four-edge clamped plates using wavelet analysis without considering noise

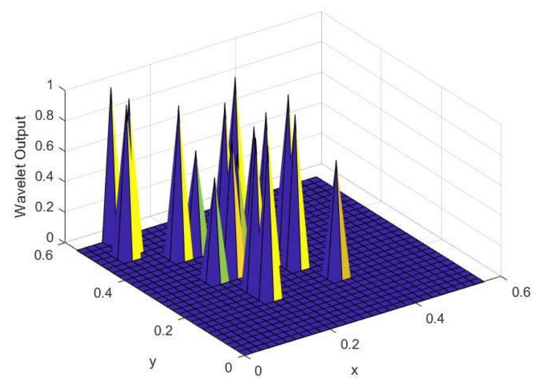

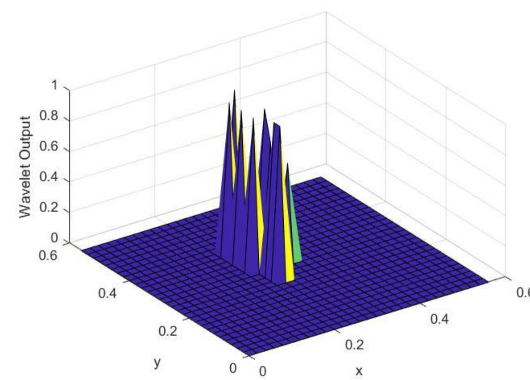

a b

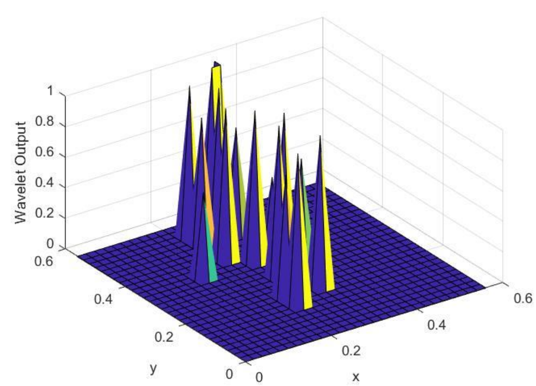

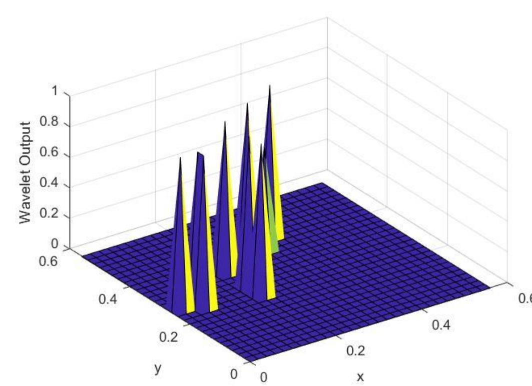

c d

Figure 34. Damage localization results for scenarios a) first, b) second, c) third, and d) fourth with 25% damage severity in two-edge clamped plates using wavelet analysis with considering 3% noise

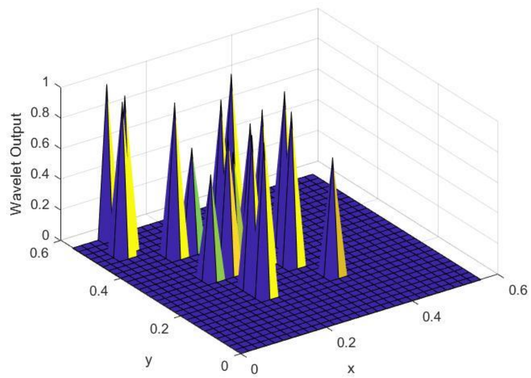

a

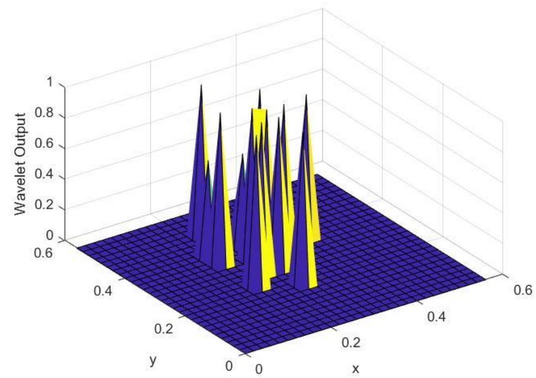

b

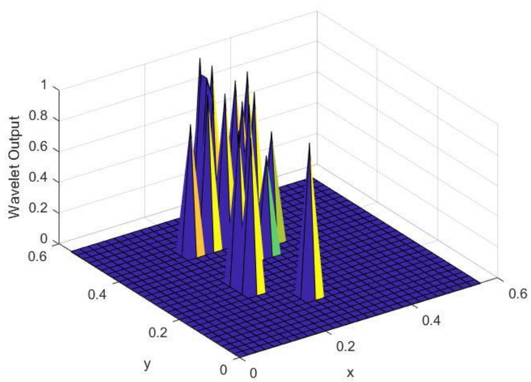

c

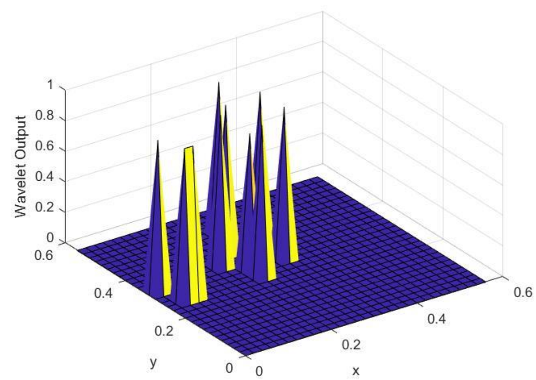

d

Figure 35. Damage localization results for scenarios a) first, b) second, c) third, and d) fourth with 50% damage severity in two-edge clamped plates using wavelet analysis with considering 3% noise

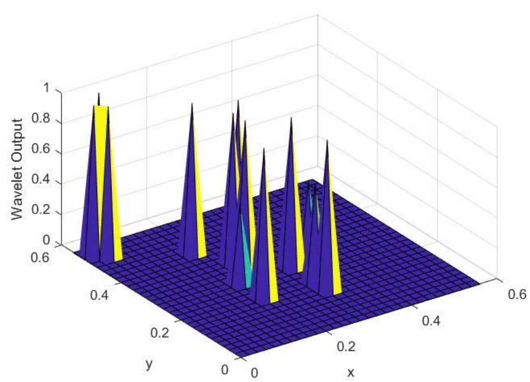

a

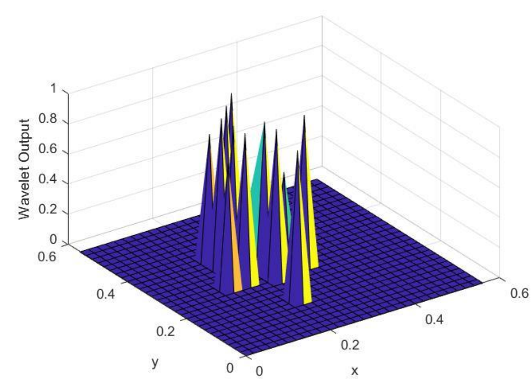

b

Figure 36. Continued on next page

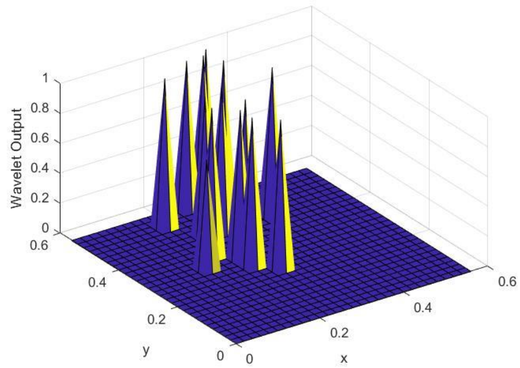

c

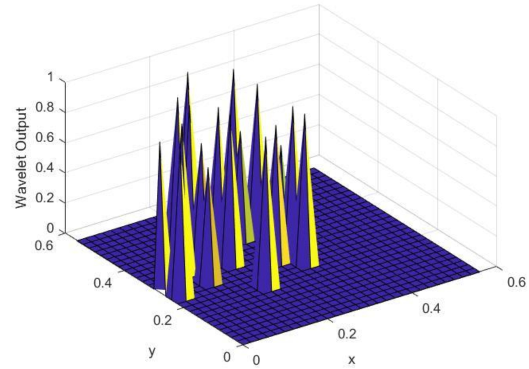

d

Figure 36. Damage localization results for scenarios a) first, b) second, c) third, and d) fourth with 75% damage severity in two-edge clamped plates using wavelet analysis with considering 3% noise

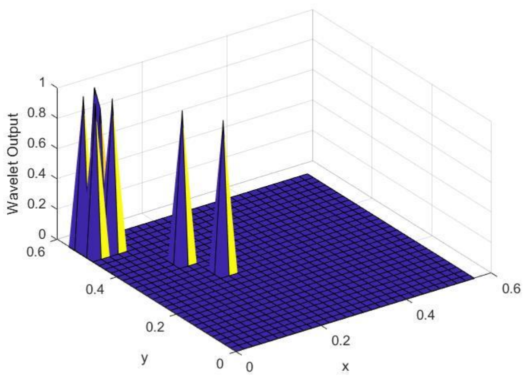

a

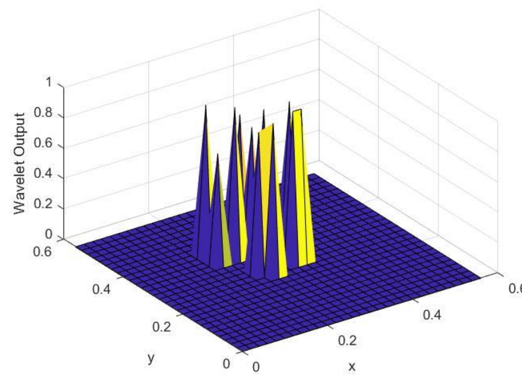

b

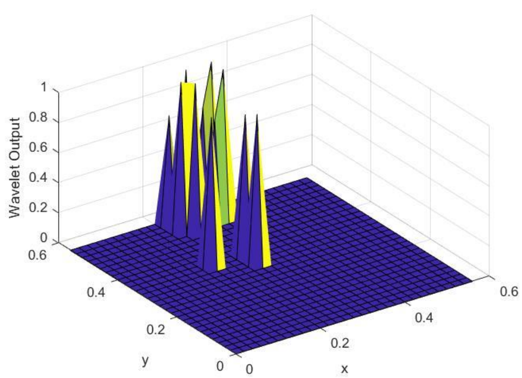

c

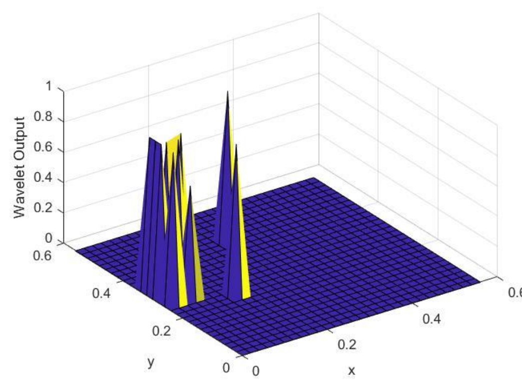

d

Figure 37. Damage localization results for scenarios a) first, b) second, c) third, and d) fourth, with 87.5% damage severity in two-edge clamped plates using wavelet analysis with considering 3% noise

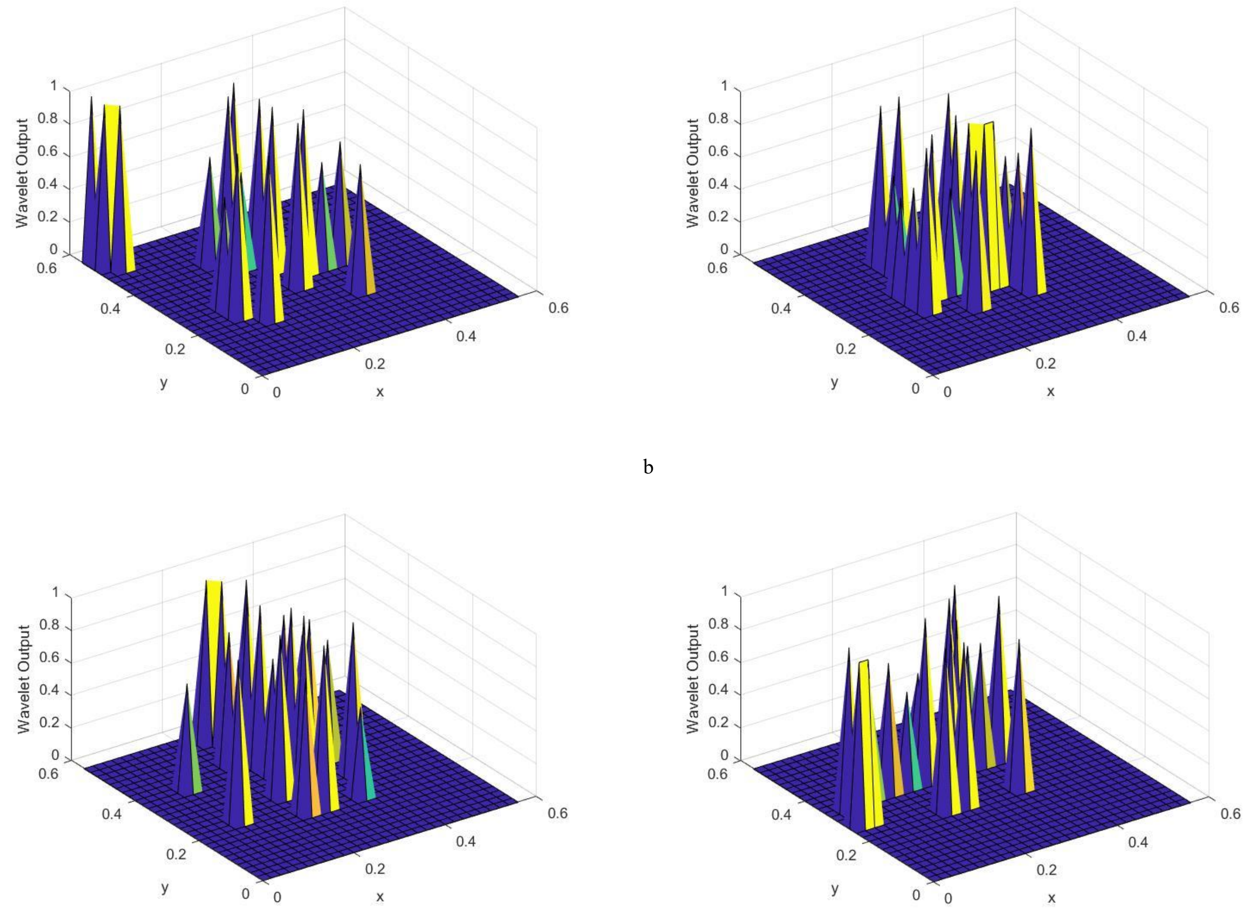

a b

c d

Figure 38. Damage localization results for scenarios a) first, b) second, c) third, and d) fourth with 25% damage severity in four-edge clamped plates using wavelet analysis with considering 3% noise

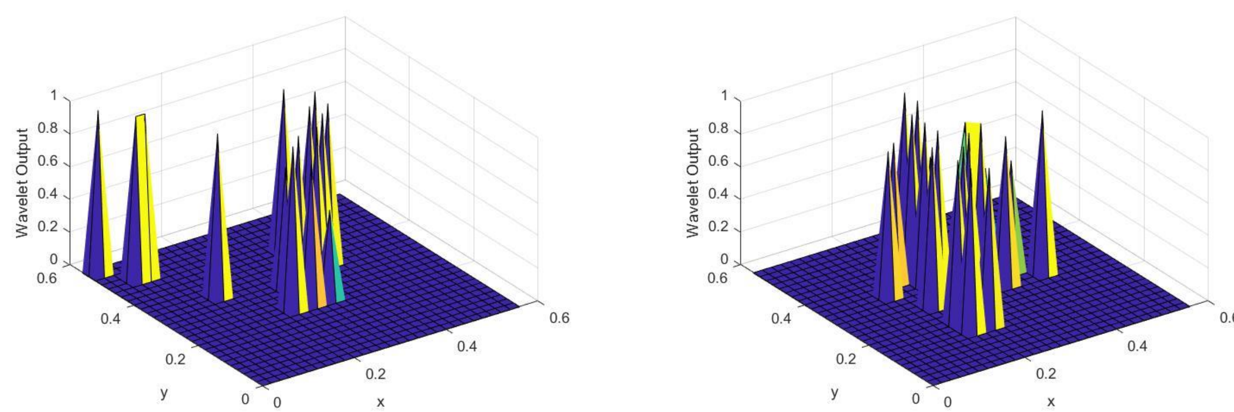

a b

Figure 39. Continued on next page

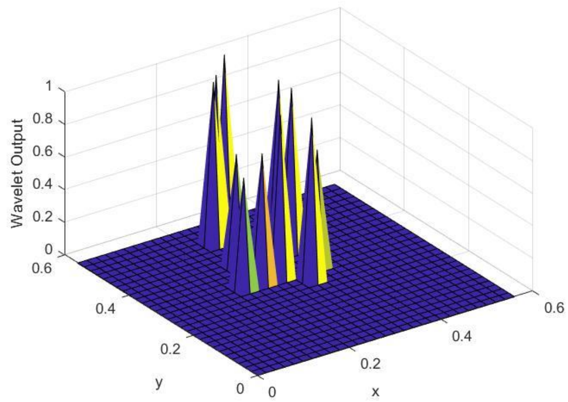

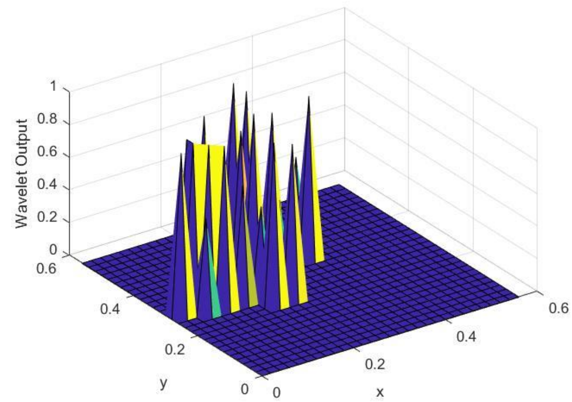

c d

Figure 39. Damage localization results for scenarios a) first, b) second, c) third, and d) fourth with 50% damage severity in four-edge clamped plates using wavelet analysis with considering 3% noise

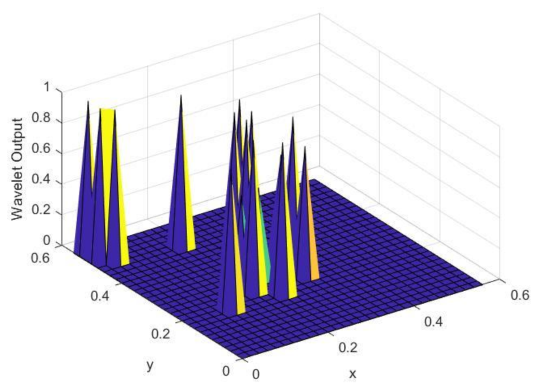

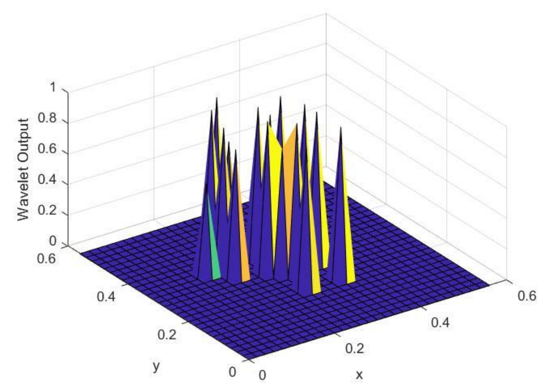

a b

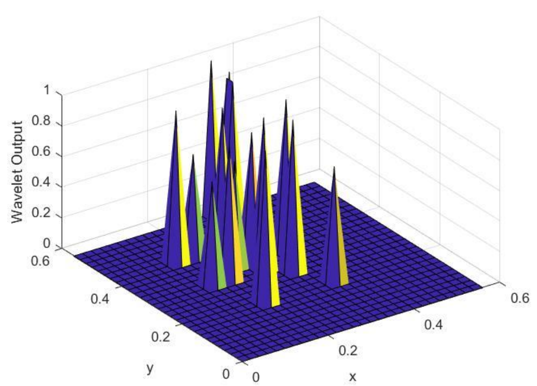

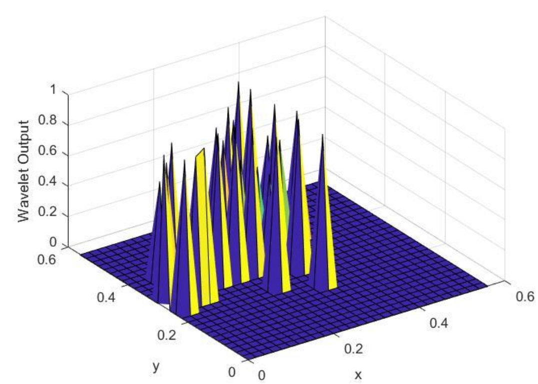

c d

Figure 40. Damage localization results for scenarios a) first, b) second, c) third, and d) fourth with 75% damage severity in four-edge clamped plates using wavelet analysis with considering 3% noise

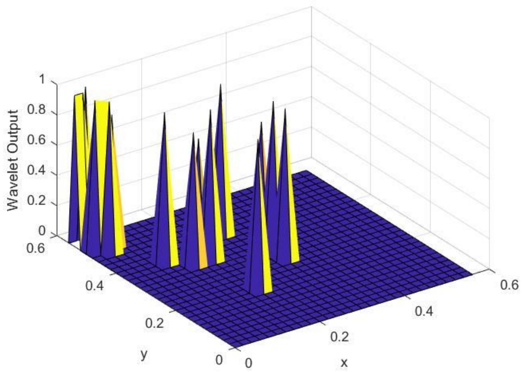

a

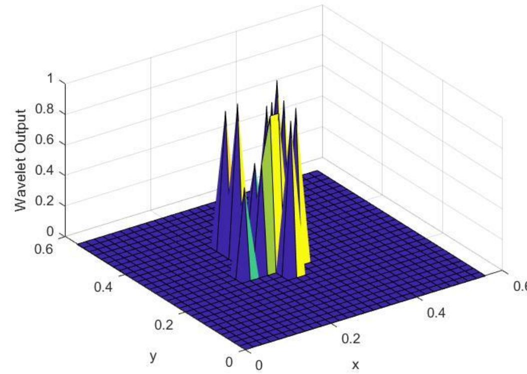

b

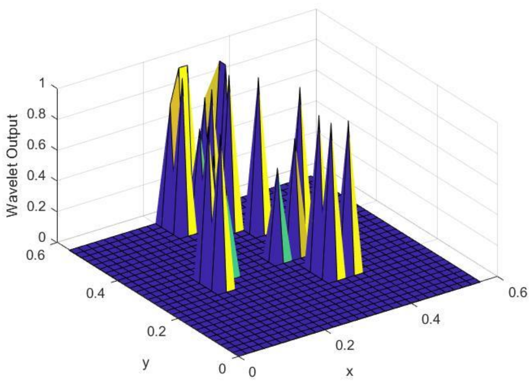

c

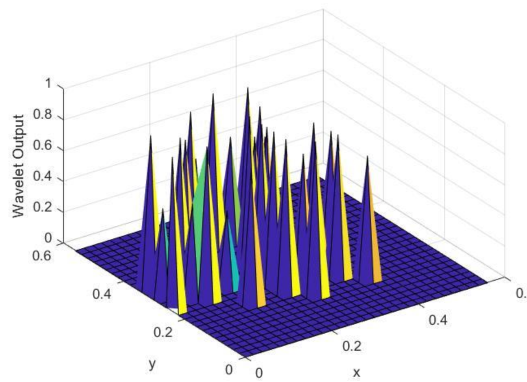

d

Figure 41. Damage localization results for scenarios a) first, b) second, c) third, and d) fourth, with 87.5% damage severity in four-edge clamped plates using wavelet analysis with considering 3% noise

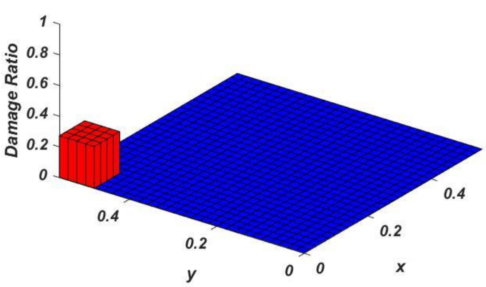

a

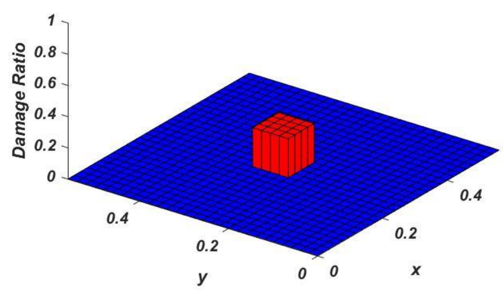

b

Figure 42. Continued on next page

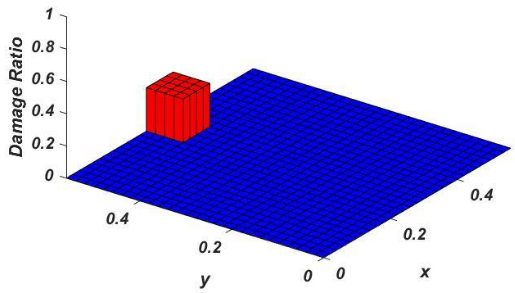

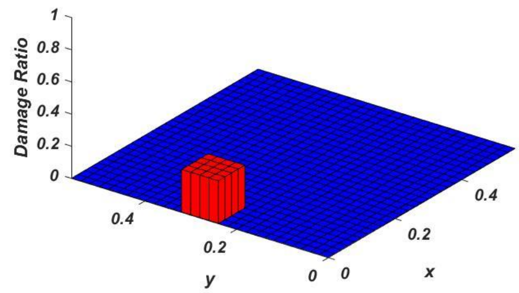

c d

Figure 42. Damage location and severity assessment for scenarios a) first, b) second, c) third, and d) fourth with 25% damage intensity in two-edge clamped plates without considering noise

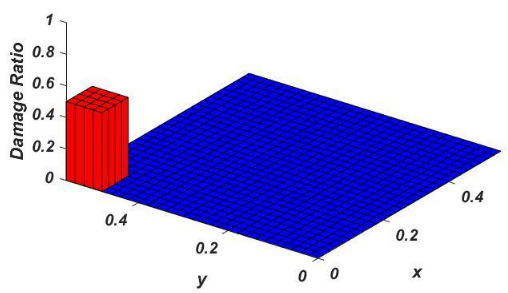

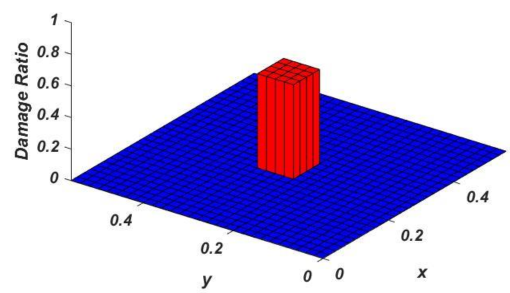

a b

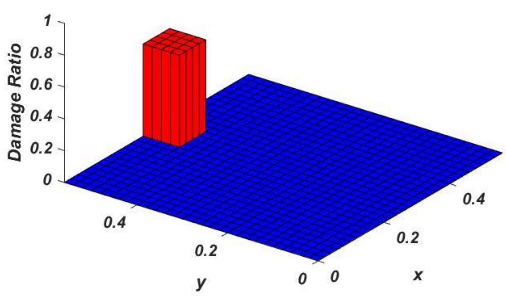

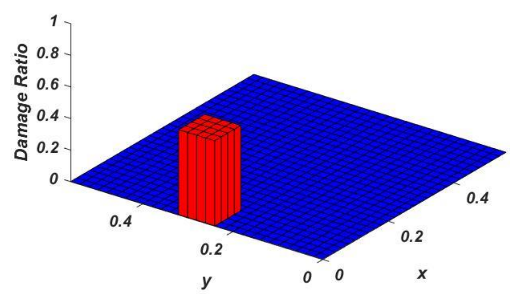

c d

Figure 43. Damage location and severity assessment for scenarios a) first, b) second, c) third, and d) fourth with 50% damage intensity in two-edge clamped plates without considering noise

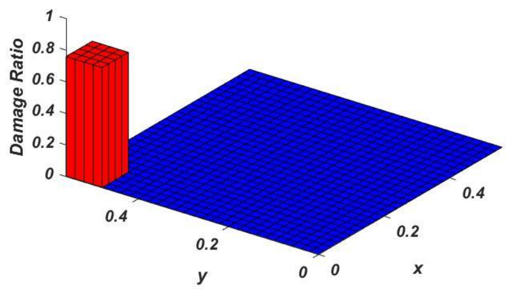

a

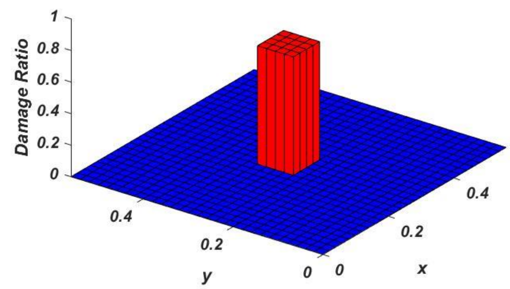

b

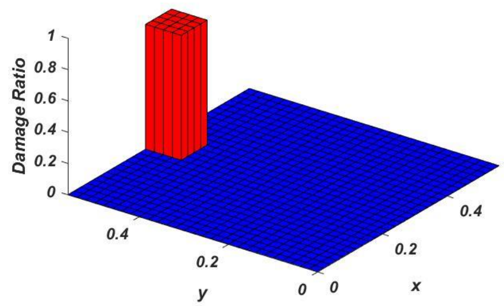

c

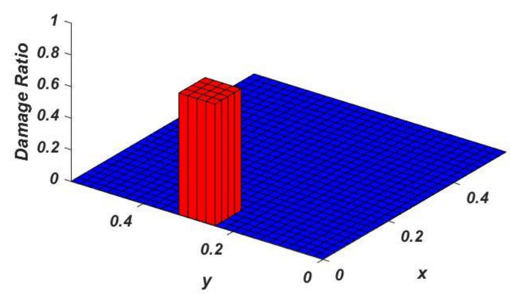

d

Figure 44. Damage location and severity assessment for scenarios a) first, b) second, c) third, and d) fourth with 75% damage intensity in two-edge clamped plates without considering noise

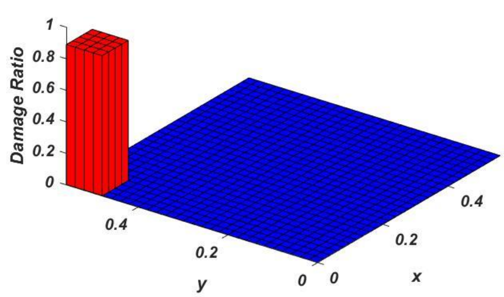

a

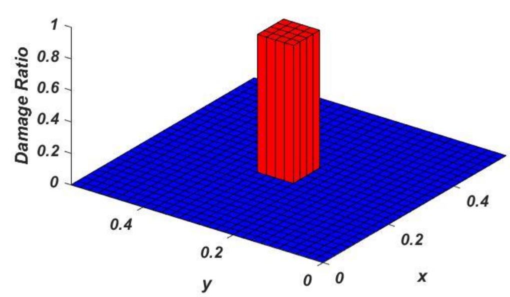

b

Figure 45. Continued on next page

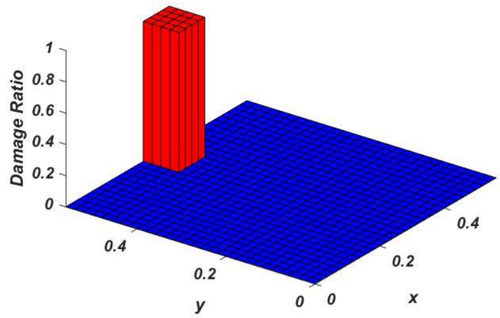

c

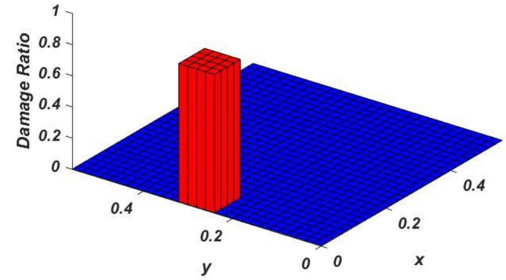

d

Figure 45. Damage location and severity assessment for scenarios a) first, b) second, c) third, and d) fourth, with 87.5% damage intensity in two-edge clamped plates without considering noise

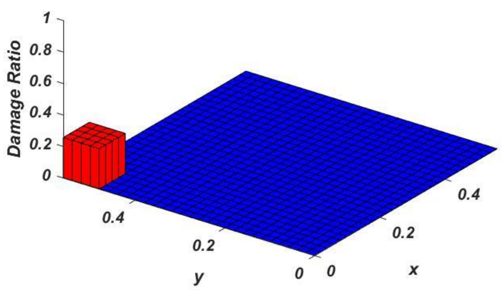

a

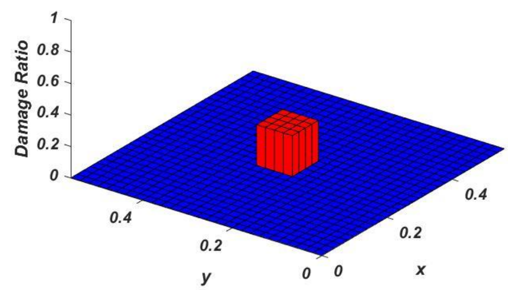

b

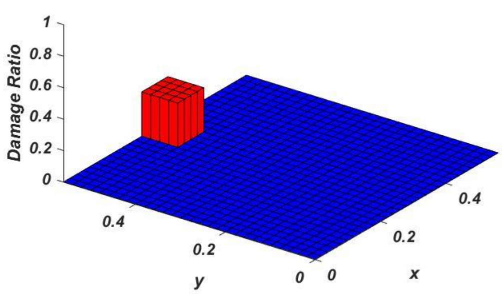

c

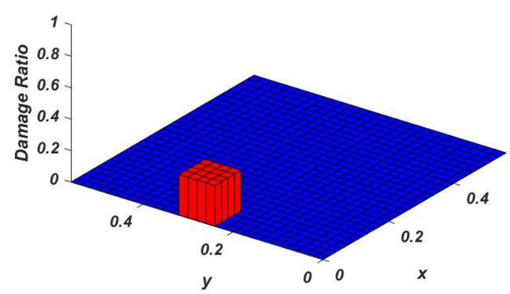

d

Figure 46. Damage location and severity assessment for scenarios a) first, b) second, c) third, and d) fourth with 25% damage intensity in four-edge clamped plates without considering noise

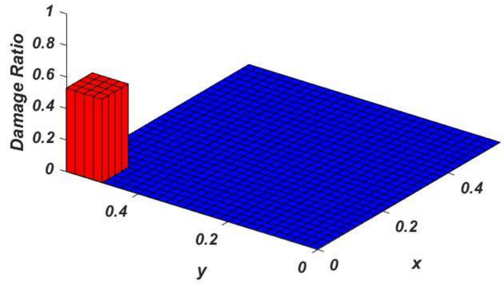

a

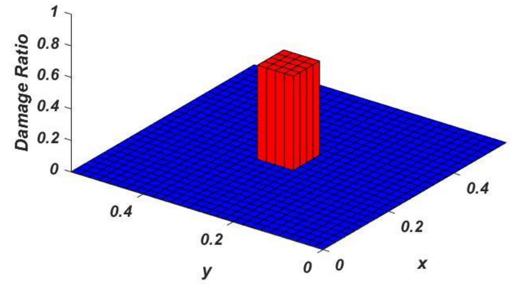

b

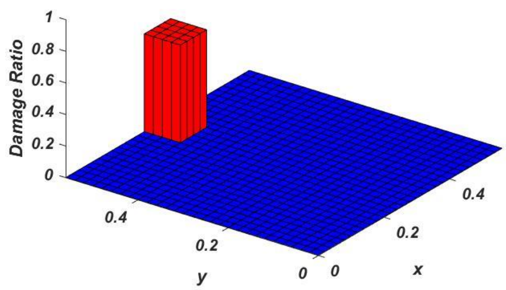

c

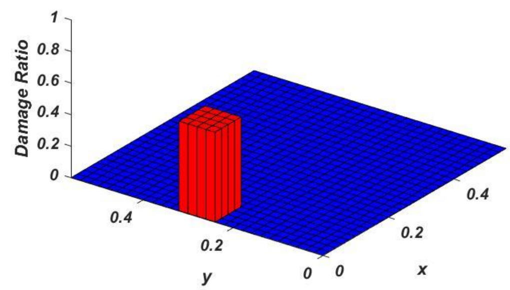

d

Figure 47. Damage location and severity assessment for scenarios a) first, b) second, c) third, and d) fourth with 50% damage intensity in four-edge clamped plates without considering noise

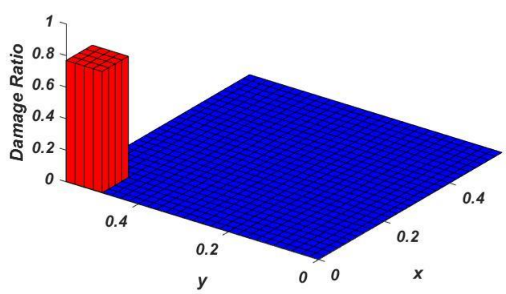

a

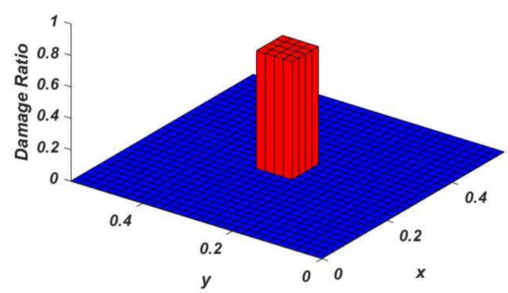

b

Figure 48. Continued on next page

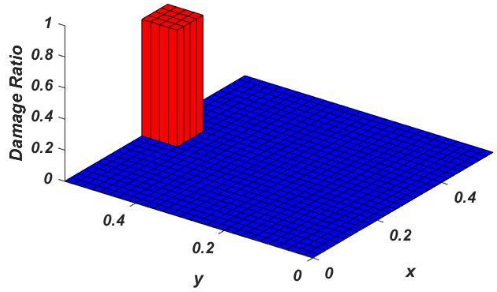

c

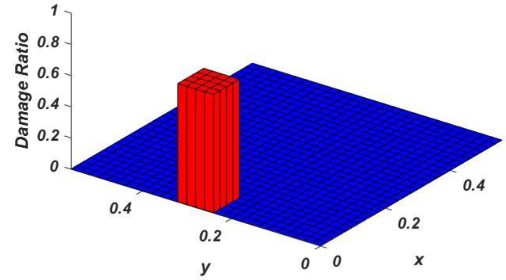

d

Figure 48. Damage location and severity assessment for scenarios a) first, b) second, c) third, and d) fourth with 75% damage intensity in four-edge clamped plates without considering noise

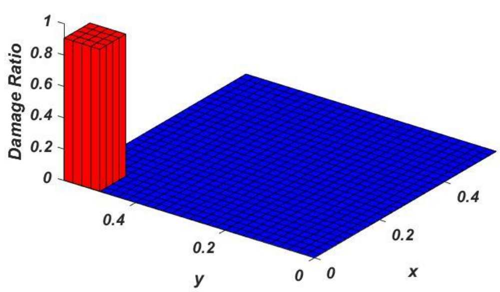

a

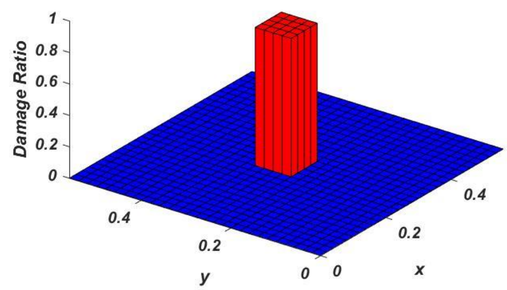

b

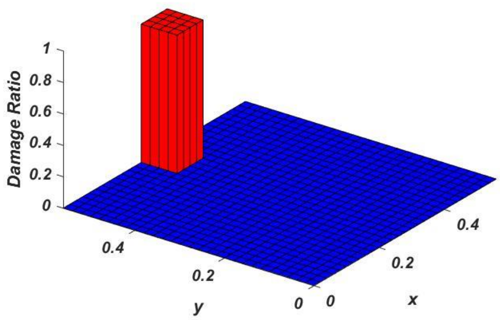

c

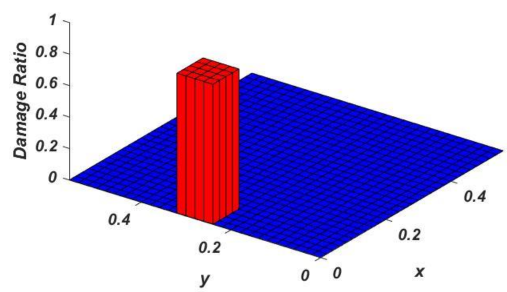

d

Figure 49. Damage location and severity assessment for scenarios a) first, b) second, c) third, and d) fourth, with 87.5% damage intensity in four-edge clamped plates without considering noise

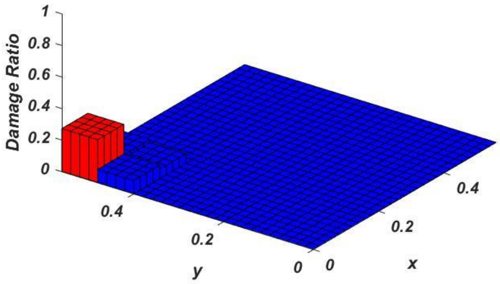

a

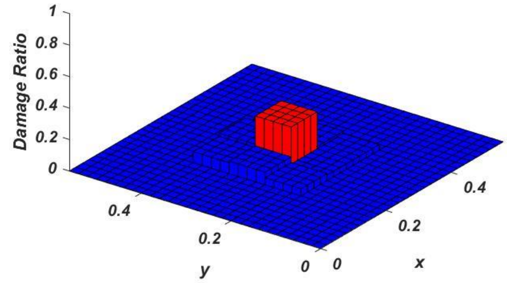

b

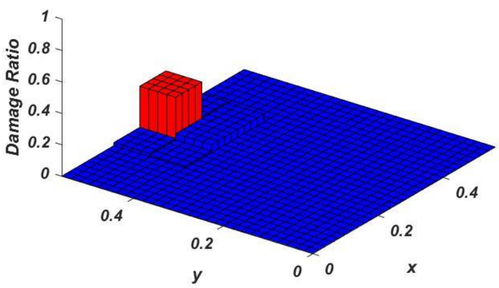

c

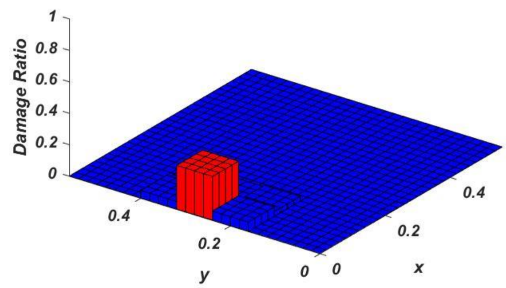

d

Figure 50. Damage location and severity assessment for scenarios a) first, b) second, c) third, and d) fourth with 25% damage intensity in two-edge clamped plates with considering 3% noise

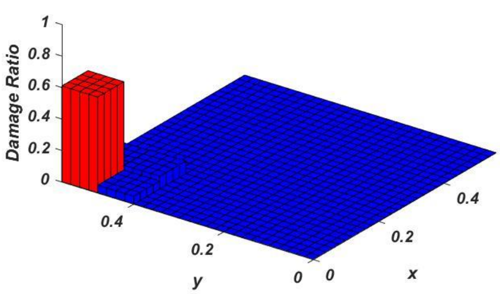

a

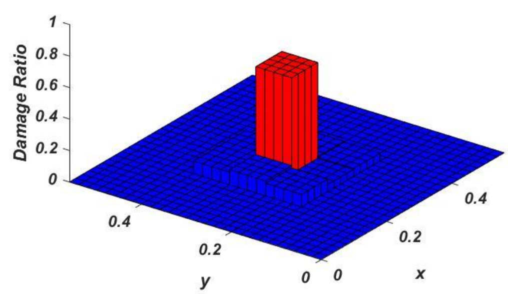

b

Figure 51. Continued on next page

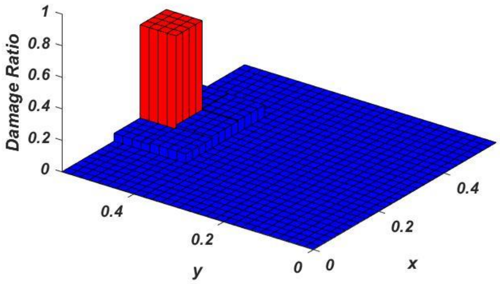

c

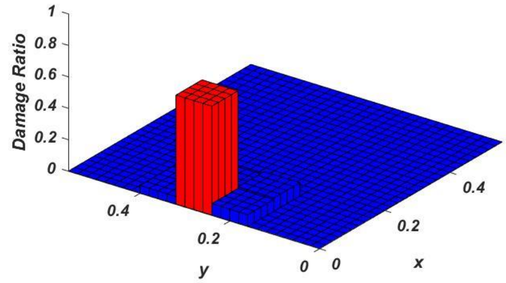

d

Figure 51. Damage location and severity assessment for scenarios a) first, b) second, c) third, and d) fourth with 50% damage intensity in two-edge clamped plates with considering 3% noise

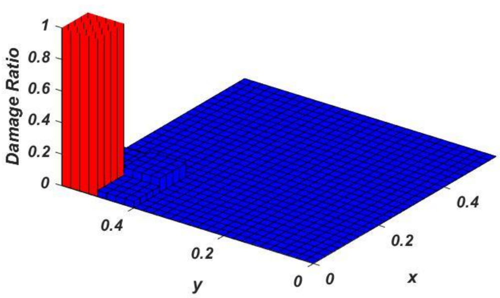

a

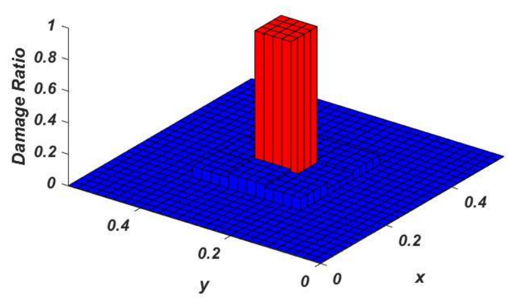

b

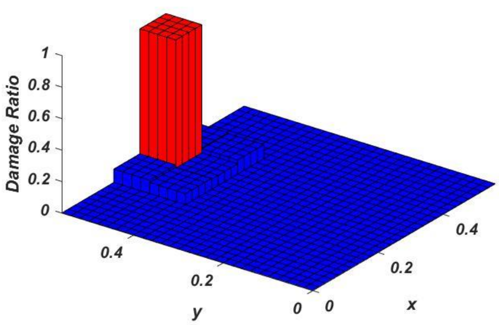

c

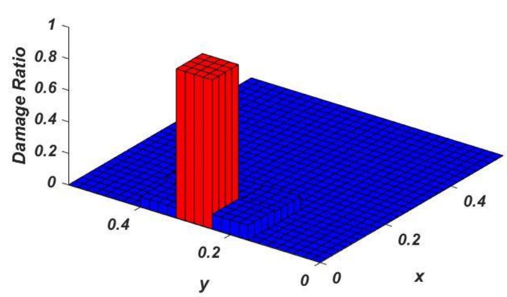

d

Figure 52. Damage location and severity assessment for scenarios a) first, b) second, c) third, and d) fourth with 75% damage intensity in two-edge clamped plates with considering 3% noise

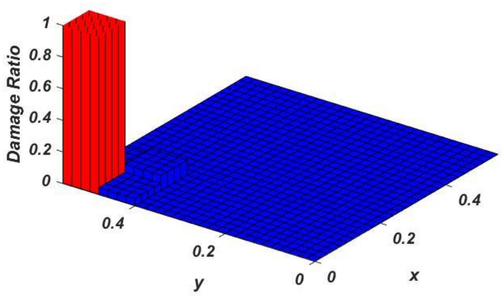

a

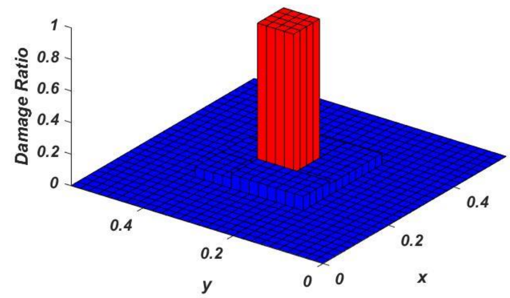

b

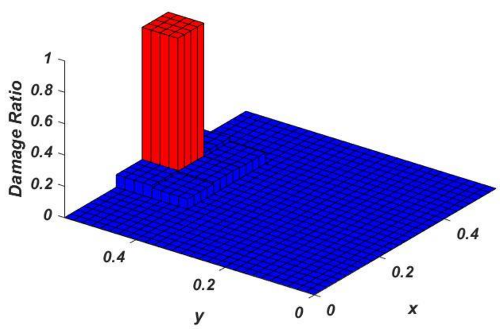

c

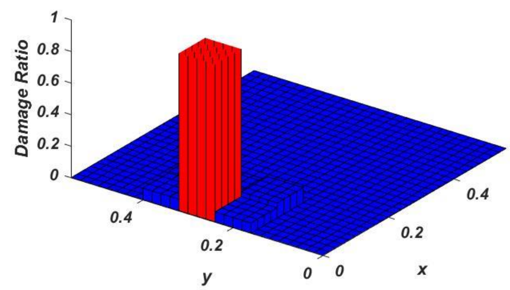

d

Figure 53. Damage location and severity assessment for scenarios a) first, b) second, c) third, and d) fourth, with 87.5% damage intensity in two-edge clamped plates with considering 3% noise

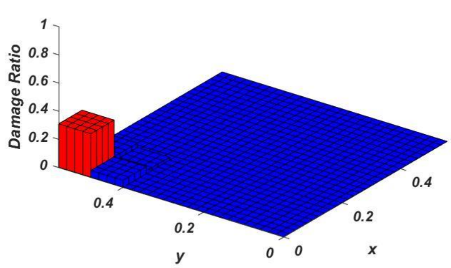

a

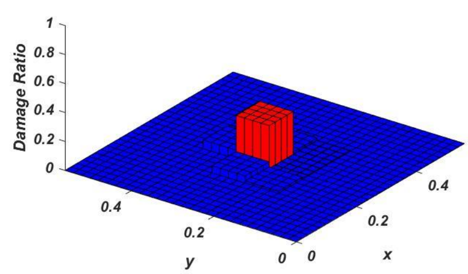

b

Figure 54. Continued on next page

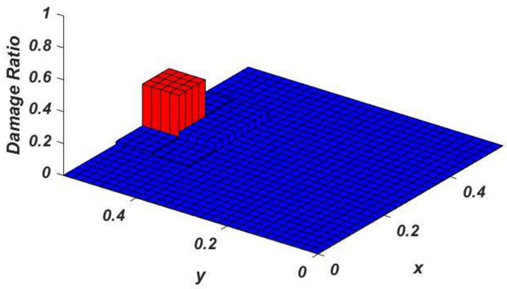

c

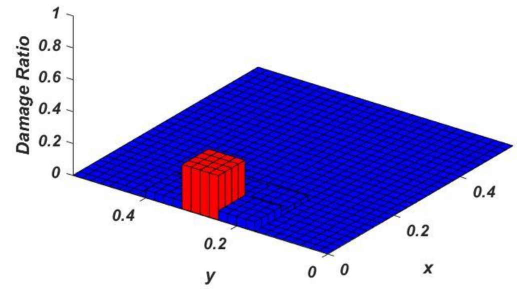

d

Figure 54. Damage location and severity assessment for scenarios a) first, b) second, c) third, and d) fourth with 25% damage intensity in four-edge clamped plates with considering 3% noise

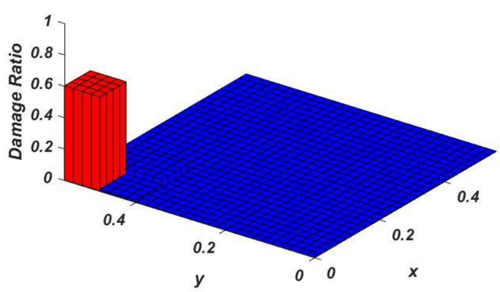

a

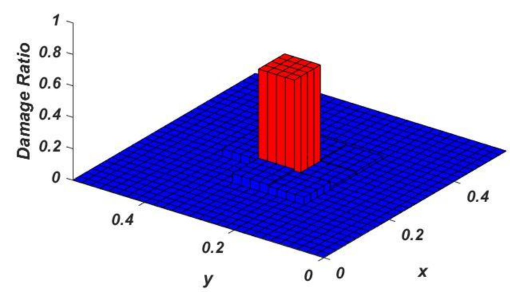

b

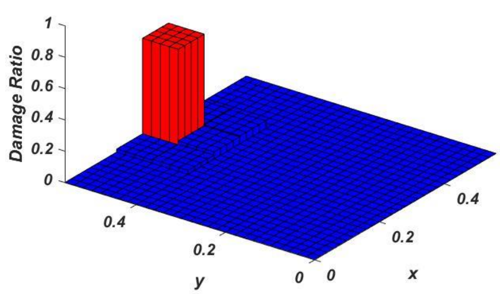

c

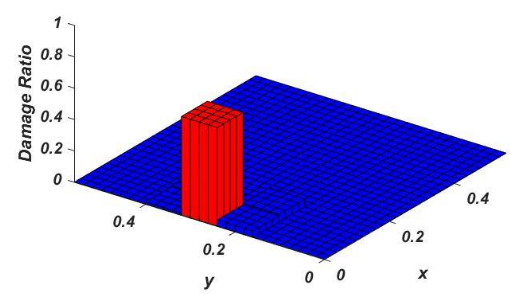

d

Figure 55. Damage location and severity assessment for scenarios a) first, b) second, c) third, and d) fourth with 50% damage intensity in four-edge clamped plates with considering 3% noise

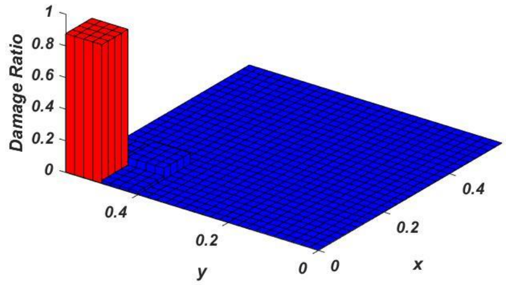

a

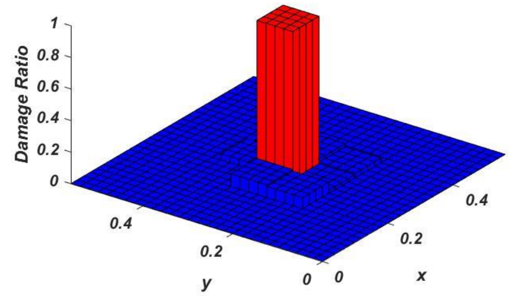

b

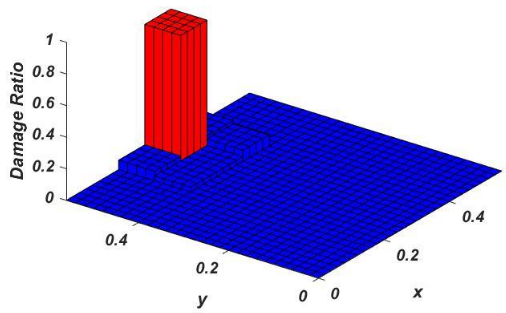

c

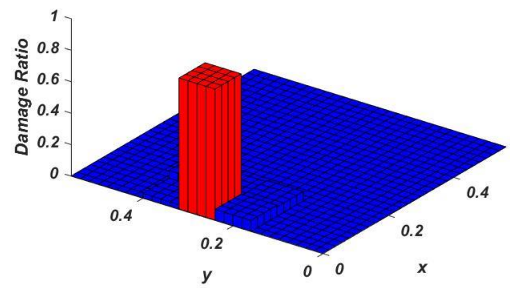

d

Figure 56. Damage location and severity assessment for scenarios a) first, b) second, c) third, and d) fourth with 75% damage intensity in four-edge clamped plates with considering 3% noise

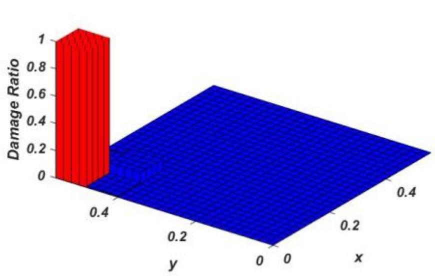

a

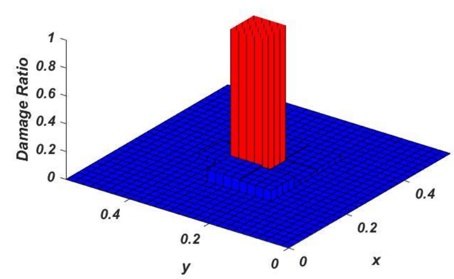

b

Figure 57. Continued on next page

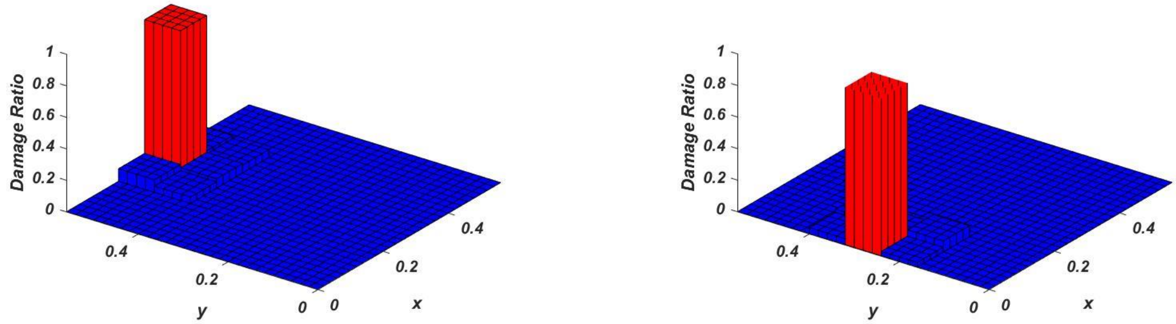

c d

Figure 57. Damage location and severity assessment for scenarios a) first, b) second, c) third, and d) fourth, with 87.5% damage intensity in four-edge clamped plates with considering 3% noise

In the 25% damage condition, with 3% noise application and in scenarios 1 to 4, damage intensity in simply supported plates on two sides is identified with differences of 8%, 9.29%, 136.94%, and 180.16%, respectively, while in plates fixed on four sides, the differences are 20%, 24.20%, 12%, and 12.72%, respectively. In the 50% damage condition, with 3% noise consideration and in scenarios 1 to 4, damage intensity in simply supported plates on two sides is identified with differences of 30.6%, 22.01%, 38.99%, and 28.20%, respectively, while in plates clamped on four sides, the differences are 25.37%, 20.49%, 26.06%, and 25.84%, respectively. In the 75% damage condition, with 3% noise consideration and in scenarios 1 to 4, damage intensity in simply supported plates on two sides was identified with differences of 20.45%, 77.48%, 26.34%, and 17.15%, respectively, while in plates clamped on four sides, the differences are 27.22%, 17.04%, 11.25%, and 9.71%, respectively. In the 87.5% damage condition, with 3% noise consideration and in scenarios 1 to 4, damage intensity in simply supported plates on two sides is identified with differences of 8.57%, 44.91%, 17.82%, and 5.53%, respectively, while in plates fixed on four sides, the differences are 26.07%, 19.15%, 51.61%, and 6.08%, respectively.

6. Conclusion

In this study, a damage identification method has been introduced using wavelet transforms and firefly optimization algorithm. In the first stage, the acceleration responses of structures obtained by utilizing a finite element analysis software have been subjected to wavelet transforms. Disturbances in response data indicate the presence of damage in the structure. Using filters, structural response signal details are extracted, and this principle leads to introducing a quantitative index for determining probable damage locations. In the second stage, the firefly optimization algorithm has been employed to accurately identify the damage location and severity. According to the results obtained from the beams with 16 and 27 elements, the wavelet index successfully identified damage location in both single and double damage cases. In the second step, slight differences have been observed, particularly in cases of double damage cases. In plate structures for both support conditions considered, during detection by the wavelet index, damaged locations have been identified within acceptable ranges, even with noise presence. In the case of plates clamped on four sides compared to two sides, more effective performance has been achieved in terms of damage intensity accuracy. Based on results, despite higher-level noise in the data, the suggested method has still provided the damage location and severity with rather high accuracy, which proves that the proposed method is very effective. Therefore, the results indicate that the method possesses good capability in identifying damage location and severity.

References

[1] Quek, S. T., Q. Wang, L. Zhang, and K.-K. Ang. "Sensitivity analysis of crack detection in beams by wavelet technique." International Journal of Mechanical Sciences 43.12 (2001): 2899-2910.

[2] Ovanesova, A. and L. E. Suarez. "Applications of wavelet transforms to damage detection in frame structures." Engineering Structures 26.1 (2004): 39-49.

[3] Loutridis, S., E. Douka, L. J. Hadjileontiadis, and A. Trochidis. "A two-dimensional wavelet transform for detection of cracks in plates." Engineering Structures 27.9 (2005): 1327-1338.

[4] Rucka, M. and K. Wilde. "Application of continuous wavelet transform in vibration based damage detection method for beams and plates." Journal of Sound and Vibration 297.3-5 (2006): 536-550. https://doi.org/10.1016/j.jsv.2006.04.020
[5] Xiang, J. and M. Liang. "A two-step approach to multi-damage detection for plate structures." Engineering Fracture Mechanics 91 (2012): 73-86. https://doi.org/10.1016/j.engfracmech.2012.04.027
[6] Hashem Jahangir and Mohammad Reza Esfahani. "Using wavelet transform of vibration modes for damage assessment of reinforced concrete beams." Fourth National Conference on Concrete of Iran, Tehran (2013).
[7] Ezzoldin, Amir, Hossein Naderpour, Ali Kheyroddin, and Gholamreza Ghodrati Amiri. "Crack location and magnitude detection in beams using wavelet transform." Modeling in Engineering 12.39 (2014): 89-99.
[8] Hajizadeh, A., E. Salajegheh, and J. Salajegheh. "2–d discrete wavelet–based crack detection using static and dynamic responses in plate structures." Asian Journal of Civil Engineering 17.6 (2016): 713-735.
[9] Ahmadi, Mohtasham Khan, Omid Rezaei Far, and Majid Gholhaki. "Fault detection in steel beams using comparison of continuous wavelet transform analytical results of primary and secondary mode shapes." Third International Conference on Applied Research in Structural Engineering and Construction Management, Tehran (2019).
[10] Guo, J., D. Guan, and J. Zhao. "Structural damage identification based on the wavelet transform and improved particle swarm optimization algorithm." Advances in Civil Engineering 2020 (2020): 8869810. https://doi.org/10.1155/2020/8869810
[11] Luo, Y., L. Wang, X. Guo, J. Zheng, F. Liao, and Z. Guo. "Structural Damage Identification Based on Convolutional Neural Network Group Considering the Sensor Fault." KSCE Journal of Civil Engineering 27.8 (2023): 3403-3417. https://doi.org/10.1007/s12205-023-2070-0
[12] Abdushkour, H. A., M. Saadatmorad, S. Khatir, B. Benaissa, F. Al Thobiani, and A. U. Khawaja. "Structural Damage Detection by Derivative-Based Wavelet Transforms." Arabian Journal for Science and Engineering 49.11 (2024): 15701-15709. https://doi.org/10.1007/s13369-024-09289-8
[13] Zhao, J., Z. Zhou, D. Guan, and L. Gong. "Structural edge damage detection based on wavelet transform and immune genetic algorithm." Scientific Reports 15.1 (2025): 4376. https://doi.org/10.1038/s41598-025-88974-4
[14] Sinha, J. K., M. Friswell, and S. Edwards. "Simplified models for the location of cracks in beam structures using measured vibration data." Journal of Sound and Vibration 251.1 (2002): 13-38. https://doi.org/10.1006/jsvi.2001.3988
[15] Yazdanpanah, O. and S. Seyedpoor. "A new damage detection indicator for beams based on mode shape data." Structural Engineering and Mechanics 53.4 (2015): 725-744. https://doi.org/10.12989/sem.2015.53.4.725
[16] Abdulkareem, M., N. Bakhary, M. Vafaei, N. M. Noor, and R. N. Mohamed. "Application of two-dimensional wavelet transform to detect damage in steel plate structures." Measurement 146 (2019): 912-923. https://doi.org/10.1016/j.measurement.2019.07.017
[17] Sadowsky, J. "Investigation of signal characteristics using the continuous wavelet transform." Johns Hopkins APL Technical Digest 17.3 (1996): 258-269.
[18] Jordan, D., R. Miksad, and E. Powers. "Implementation of the continuous wavelet transform for digital time series analysis." Review of Scientific Instruments 68.3 (1997): 1484-1494. https://doi.org/10.1063/1.1147636
[19] Yang, X. S. "Firefly algorithm, Levy flights and global optimization." In Research and Development in Intelligent Systems XXVI, Springer (2010): 209-218. https://doi.org/10.1007/978-1-84882-983-1_15

J-Researchers

Journal of Civil Engineering Researchers

Journal homepage: www.journals-researchers.com

Numerical Development of a Re-centering Damper with High Seismic Performance, Including Friction Wedges and SMA Rods

Jalal AkbarKamali,[a] Mahdi Mashhadiyan,[a,*] Esmaeil Mousapoor [a]

[a] *Department of Civil Engineering, Ramsar Branch, Islamic Azad University, Ramsar, Iran*

ABSTRACT

Re-centering dampers, developed using shape memory alloy (SMA)-based dampers and their superelasticity capability, absorb earthquake energy and provide a re-centering capability for the structure. In this study, the laboratory sample of Zhang's re-centering damper was first validated using ABAQUS software, followed by parametric analysis involving changes in the number and diameter of SMA rods, the friction coefficient of the wedges, and the placement configuration of two dampers, which were numerically investigated. The results indicated that increasing the diameter and number of rods, as well as the friction coefficient, enhances seismic resistance and stiffness but reduces ductility; excessive increase in friction only boosts the stiffness and ductility of the damper's compressive section while reducing seismic resistance. A friction coefficient of approximately 0.12 is recommended, whereas Zhang assumed 0.09. Additionally, the results showed: in parallel configuration, resistance and stiffness are higher but ductility is lower, whereas in series configuration, all three parameters decrease.

ARTICLE INFO

Received: November 18, 2025
Accepted: November 29, 2025

Keywords:
Numerical Development
Re-Centering Damper
SMA
Friction Wedge
Seismic Performance

DOI: 10.66224/JCER.7.4.68
DOR: 20.1001.1.2538516.2025.7.4.5.7

1. Introduction

Modern building codes can reduce base shear by employing a behavior factor (R), but conventional systems often result in permanent deformations and structural damage. To address this issue, dampers are utilized, as they absorb and dissipate input energy, reducing lateral displacements and applied forces, thereby enhancing safety, stability, and the service life of structures, particularly in seismic-prone areas where their necessity is greater [1]. A damper is a device used to absorb and dissipate energy from dynamic forces such as earthquakes or wind in structures, reducing vibrations and deformations, preventing damage to main members, and improving the seismic performance of the structure [2].

Re-centering dampers are an advanced type of damper used to reduce permanent deformations and restore the structure to its initial state after an earthquake. These dampers improve the seismic performance of the structure by absorbing energy and generating a restoring force, preventing damage to main members, and thus increasing building safety and stability [3]. Despite these advantages, challenges of re-centering dampers include complex design, nonlinear material behavior, high construction and

[*] Corresponding author. Tel.: +989111962921; e-mail: mahdi.mashhadiyan@gmail.com.

installation costs, sensitivity to temperature and environmental conditions, and a lack of laboratory data; nevertheless, they are highly effective in improving structural seismic performance [4]. Due to these limitations, their widespread application remains restricted. Researchers have addressed these issues by improving numerical modeling, conducting extensive experiments, and developing simpler, more economical designs with optimized materials and mechanisms to facilitate practical use in structures [5].

In recent years, shape memory alloys have garnered significant attention in civil engineering due to their superelasticity and ability to recover their original shape and dissipate energy, particularly in self-centering systems, with applications in bolts, steel elements, concrete rebars, braces, base isolators, and bridges [6]. The most prominent is nickel-titanium (Nitinol), used in civil engineering, aerospace, automotive, and medical fields due to its superelasticity and shape memory properties, though it has limitations such as fatigue, transformation temperature, and production costs [7]. However, SMA energy dissipation alone is insufficient for high-performance self-centering systems, leading to the design of hybrid dampers that combine SMA with friction wedges or metallic tools [8]. Studies show that SMA-based dampers can reduce permanent displacements and residual deformations in structures, absorb earthquake energy, and effectively control seismic vibrations in buildings and small bridges through self-re-centering without requiring repairs after severe earthquakes [9]. Recent research indicates that SMA superelastic rods and dampers exhibit stable hysteretic behavior and strong self-centering under cyclic loading [10]. Studies by Wang et al. with SMA rods and U-shaped dampers showed stable flag-shaped hysteretic loops, over 98% deformation recovery, and minor strain rate effects [11].

In this study, the numerical development of Zhang's re-centering dampers with high seismic performance, including friction wedges and SMA rods, will be investigated. First, nonlinear three-dimensional analysis using ABAQUS software [12] and cyclic seismic loading is performed, with model validation against experimental data. Subsequently, parametric studies examine the effects of the number and diameter of SMA rods, wedge friction coefficient, and the arrangement of two dampers (series or parallel) on the damper's resistance, stiffness, and ductility. The results demonstrate that these parameters play a crucial role in energy absorption capacity and damper performance, with numerical results and load-displacement diagrams illustrating the effects of parametric variables on the damper's seismic behavior.

2. Numerical Validation of the Curved Damper

In this study, to validate the finite element modeling and align numerical results with actual performance, experimental data from Zhang et al. [8] on a re-centering damper with friction wedges and SMA rods under quasi-static and cyclic compressive loading were used. Zhang et al. tested eight samples, and the selected sample for validation includes dimensional details of the wedges and SMA rods, presented schematically along with laboratory images in Figure 1. Cyclic compressive loading in the laboratory requires a specific pattern, so Figure 1 shows the compressive loading pattern for the studied re-centering damper with SMA rods. As per Figure 1, the compressive loading has 20 displacements, forming 10 back-and-forth compressive cycles in total, with the load applied via a hydraulic jack from the top to wedge No. 1, while wedge No. 2 has a support below it. According to the compressive loading pattern, the displacement ranges from 0.3 mm to 6.3 mm, only in compression. With damper displacement, the results are plotted as a compressive load-displacement hysteretic diagram, with load in kilonewtons and displacement in millimeters.

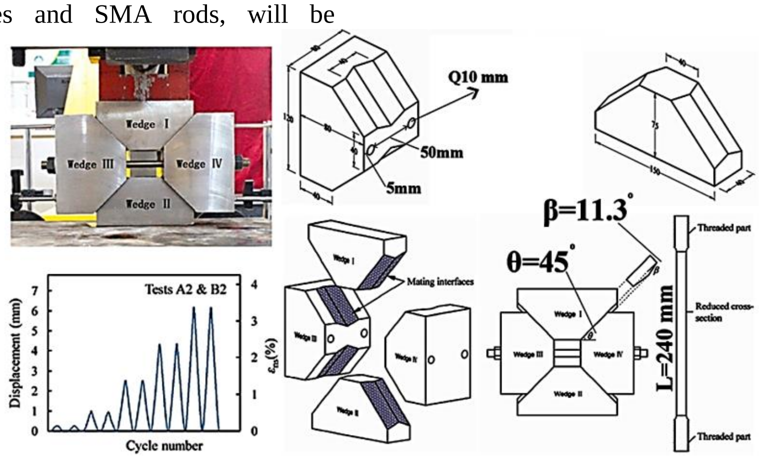

Figure 1- Dimensional characteristics of wedges and SMA rods used in compressive loading tests in Zhang et al. [8].

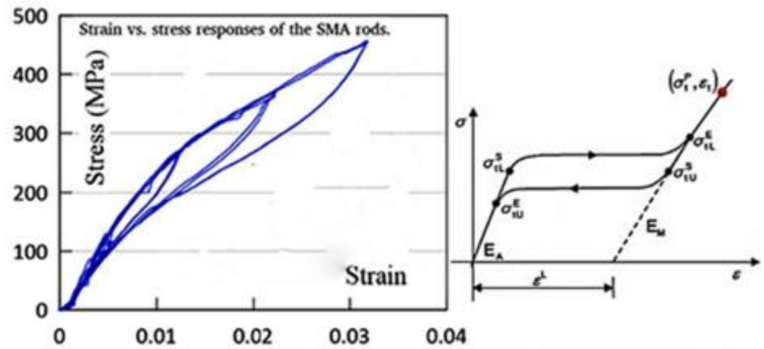

Martensite's Young's Modulus E_M	Martensite's Poisson's Ratio ϑ_M	Transformation Strain ε^L	Start of Transformation (Loading) σ_{StL}	End of Transformation (Loading) σ_{EtL}	Start of Transformation (Unloading) σ_{StU}	End of Transformation (Unloading) σ_{EtL}
3000000000 N/Pa	0.33	0.02	17000000 Pa	45000000 Pa	20000000 Pa	5000000 Pa

Figure 2- Sample display, diagram, and stress-strain values of the superelastic shape memory alloy rod from Zhang et al. [8].

As per Figure 1, the operation of the re-centering damper with SMA rods is as follows: This damper consists of 4 steel wedges (two vertical and two horizontal), two SMA rods, and 4 nuts. The vertical wedges (1 and 2) and horizontal wedges (3 and 4) interact on common contact surfaces (with frictional surfaces) and specific grooves. The damper operates generally as follows:

- In tension: When the damper is under tensile load, the backs of the vertical wedges (1 and 2) rest against the outer steel frame, and the tensile force is transferred through the frame. In this state, the SMA rods are not activated.
- In compression: When the damper is under compressive load, the vertical wedges (1 and 2) apply force to the horizontal wedges (3 and 4) at a 45-degree angle between the vertical and horizontal wedges, causing the SMA rods to stretch and engage, thus the damper performs and absorbs energy.

In summary, the wedges transfer axial forces to the SMA rods, and the damper primarily dissipates energy under compressive loads, while under tensile loads, the force is transferred through the outer steel frame.

In the continuation of this study, numerical analysis is performed to examine the performance of the shape memory alloy re-centering damper. The superelastic property and flag-shaped stress-strain diagram of the shape memory alloy material used in this study are shown in Figure 2. As per Figure 2, the stress-strain diagram of the superelastic SMA rod indicates that SMA materials exhibit no permanent deformation even with strains up to about 3% and return to their initial state after unloading. The elastic modulus of the superelastic SMA rod in the re-centering damper can be extracted from this diagram. Furthermore, Zhang explicitly stated that the steel used for all metallic components has a yield stress of 240 MPa, ultimate stress of 300 MPa, and elastic modulus of 200 GPa.

For validation, a numerical sample (matching the laboratory sample) was created in ABAQUS software to achieve similar results. The re-centering damper sample was modeled by creating four elements according to laboratory dimensions and assembling them. Steel and SMA rod properties were defined in the material properties module and assigned to the components. In ABAQUS (version 2019 and later), parameters such as Young's modulus, Poisson's ratio, start and end stresses of the material phases for the shape memory alloy in Zhang et al.'s [8] re-centering damper with SMA rods are defined, and material specifications are determined based on the stress-strain diagram (parameters from Figure 2) of the laboratory superelastic rod sample. As per Figure 3, for applying cyclic compressive load and defining boundary conditions, reference points at the top (for load application) and bottom (for support definition) are created with coupling constraints, and the two side surfaces of the sample are constrained in out-of-plane displacement and lateral movement. For interaction between the SMA rod and its nut, 4 fully tied constraints must be applied at 4 connections as per Figure 3. Additionally, in the numerical sample, for interaction between steel wedges and SMA rod and wedge sliding, surface contact must be defined with a friction coefficient of 0.088 between steel wedges and SMA rod.

To apply load and support conditions in ABAQUS's loading module, gravity loading is first defined for the sample, then the bottom surface is fixed as a clamped support in terms of displacement and rotation, while the upper coupling reference point is subjected to cyclic displacement-controlled compressive loading. With

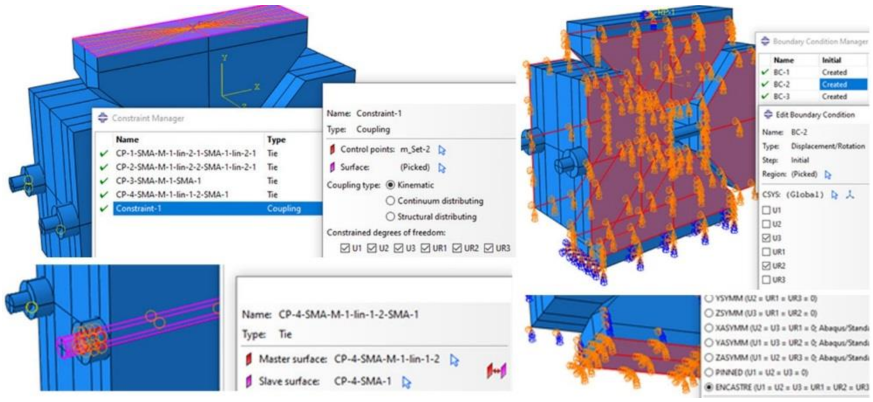

Figure 3- Sample display, diagram, and stress-strain values of the superelastic shape memory alloy rod from Zhang et al. [8].

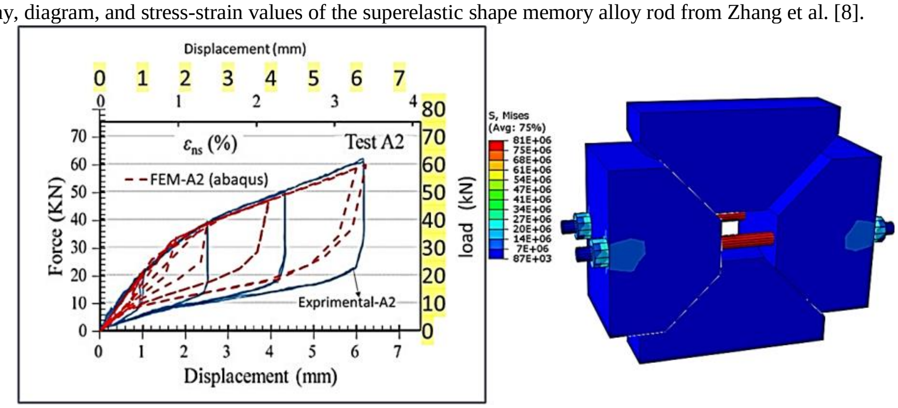

Figure 4- Stress results on the re-centering damper model – Alignment of numerical results with experimental results from Zhang et al. [8].

appropriate meshing (1 cm for wedges and 2 mm for rods), the numerical model is prepared, and the re-centering damper sample is analyzed using quasi-static analysis and applied loading. As per Figure 4, the von Mises stress results of the obtained sample after lateral loading and the load-displacement diagram indicate that the stress share in the SMA rod is higher than in other parts, and the hysteretic load-displacement diagram output confirms the re-centering behavior of the damper with a flag-shaped output. In the re-centering damper with SMA rods, compressive force is converted to tensile force in the rods, with maximum stress concentrated in the SMA rods, and the alignment of numerical and experimental results validates the model. Furthermore, as per Figure 5 in the compressive load-displacement hysteretic diagram output, the maximum numerical sample resistance and sample stiffness (initial slope of the load-displacement diagram) are almost aligned, so the numerical and experimental samples match relatively well, confirming that the numerical sample is validated against the experimental one.

3. Analysis of Findings

Due to the cost and limitations of structural experiments, the finite element method serves as an accurate and low-cost alternative for examining structural behavior. In this part of the study, micro-model analysis of the re-centering damper, including friction wedges and SMA rods is conducted to investigate the application of the re-centering damper in steel frames, the seismic performance of the re-centering damper, and the effects of the number and diameter of SMA rods, friction coefficient, and damper arrangement (series or parallel) on their seismic performance.

3.1. Application of the Re-centering Damper in Steel Frames

In this section, to apply the re-centering damper, including friction wedges and SMA rods in steel frames, necessary preparations were made to evaluate the actual performance of the damper at the frame scale. For this purpose, as per Figure 5, the holding chamber, steel connectors between the damper and connection plates, steel frame including beams, columns, and stiffeners, two diverging braces, and connection plates were designed and modeled, then transferred to ABAQUS for analysis. The steel frame with 2.34 m columns, 2.46 m beams, double IPE sections, and 120 mm channel sections for braces was assembled in ABAQUS's assembly module, then lateral loading coupling points and support conditions were defined to enable quasi-static analysis and cyclic loading.

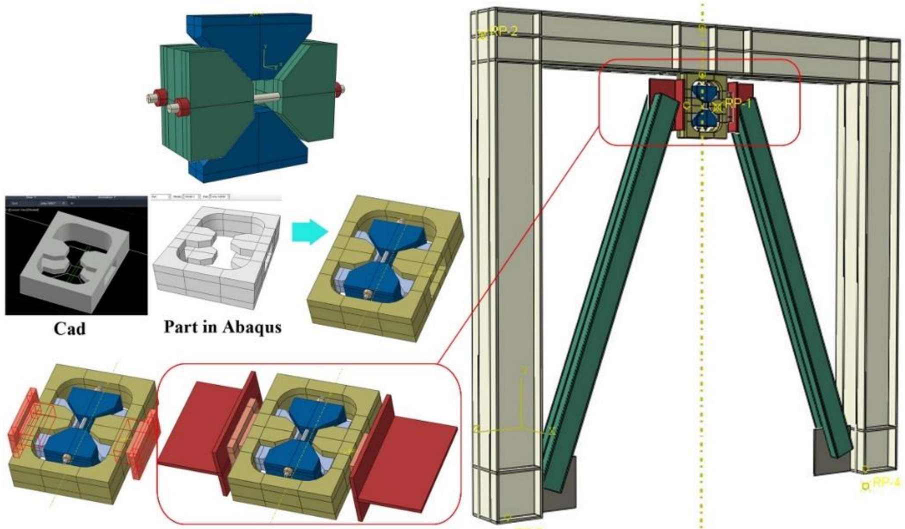

Figure 5- Design and modeling of steel frame components for applying the re-centering damper, including friction wedges and SMA rods.

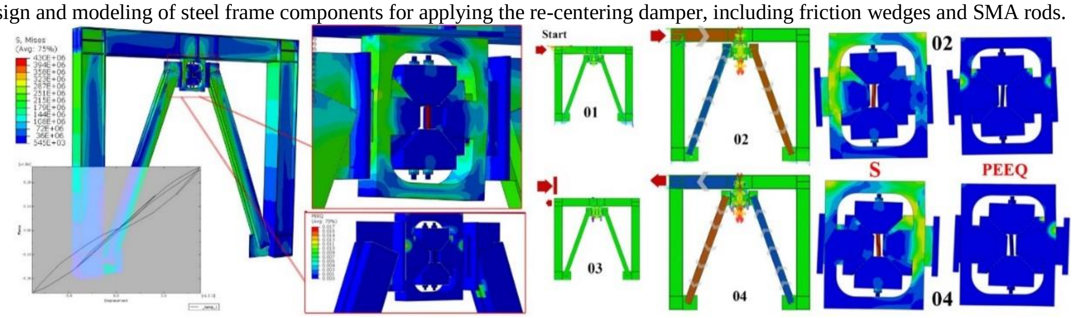

Figure 6- Stress and permanent deformations on the initial steel frame model with rigid connection to the re-centering damper assembly.

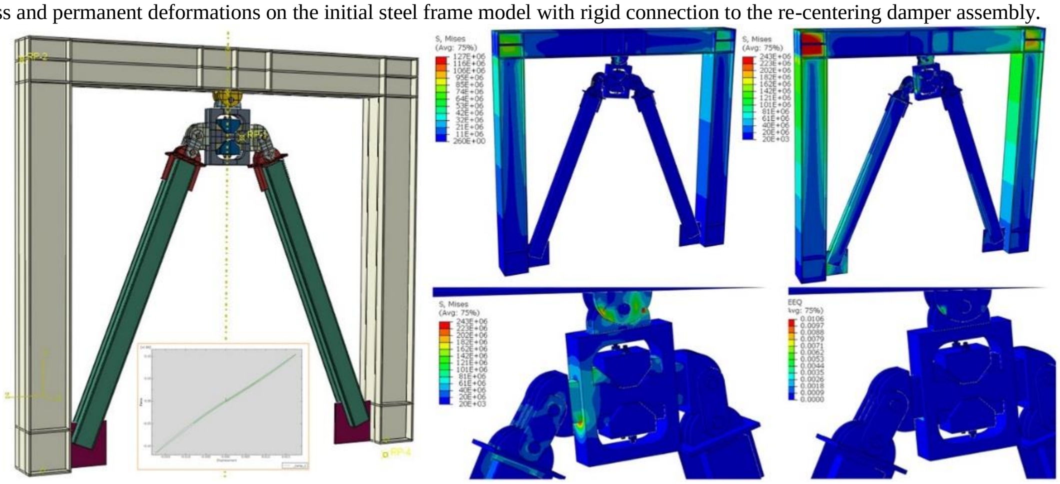

Figure 7- Stress on the secondary steel frame model with a hinged connection to the re-centering damper assembly

After modeling and assembly, in this stage, the re-centering damper with friction wedges and SMA rods is rigidly connected to the central beam in the steel frame, such that its proper performance is ensured when all deformations are concentrated in the SMA rods, absorbing and dissipating stresses while maintaining self-reversibility; otherwise, the placement and definition of the damper would be incorrect. Initial lateral loading results showed that although the load-displacement diagram, as per Figure 6, is flag-shaped and passes through the coordinate origin, some permanent deformation is observed at the brace ends and damper holding chamber due to rotation and additional moment. Stress vector analysis, as per Figure 6, also indicated that excessive rigidity of the chamber and connectors causes these permanent deformations.

To resolve this issue in the next stage, the connections of the damper holding chamber and steel connectors were designed as hinged as per Figure 7. The new analysis results indicate significant improvement in damper performance, with no permanent deformation observed in frame members and the damper holding chamber, and the load-displacement diagram obtained is linear and fully reversible.

3.2. Seismic Performance of the Re-centering Damper

In this section, since reference samples are needed for comparison with other parametric samples, the seismic performance of the baseline re-centering damper in the study is first examined. This sample is based on the experimental model of Zhang et al. [2] but validated; the main difference from Zhang's model, as per Figure 8, is increasing the width of the upper and lower wedges from 4 to 12 cm and adding two extra SMA rods for effective performance in both compression and tension directions. Quasi-static analysis, as per Figure 8, showed that stresses on the rods are absorbed in both compressive and tensile states, and the damper acts as self-centering. The resulting load-displacement diagram shows flag-shaped and reversible behavior, indicating no permanent deformation. Then, by bilinearizing the load-displacement diagram using the equivalent energy method, seismic parameters including initial stiffness (slope of the line) (K), maximum resistance (P), and ductility (ratio of ultimate displacement to yield displacement) (μ) were extracted, as per Figure 8, serving as the basis for evaluating the seismic performance of the re-centering damper in this study. Note that the reference sample in this study is labeled "N2Q10F09*", where N2 means two rods connected to each wedge, Q10 means each damper rod diameter is 10 mm, and F09 means the initial friction coefficient between the two grooved wedge surfaces is 0.09. The asterisk denotes the reference sample.

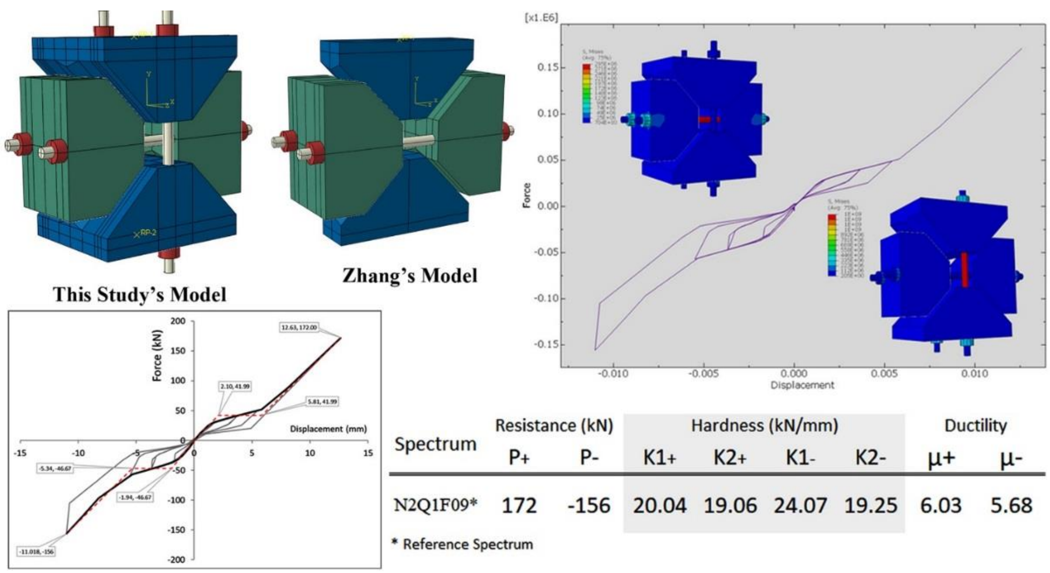

Figure 8- Results (stresses and performances) of hysteretic loading in both directions of the re-centering damper introduced in this study.

Table 1-
Results (stresses and performances) of hysteretic loading in both directions of the re-centering damper introduced in this study.

Spectrum	Number of SMA rods connected to each wedge	Diameter of each SMA rod (mm)	Coefficient of friction between two grooved wedge surfaces	Arrangement of two re-centering dampers relative to each other
N2Q10F09*	2	10	0.09	-
N3Q10F09	3	10	0.09	-
N4Q10F09	4	10	0.09	-
N2Q15F09	2	15	0.09	-
N2Q20F09	2	20	0.09	-
N2Q10F12	2	10	0.12	-
N2Q10F15	2	10	0.15	-
N2Q10F25	2	10	0.25	-
N2Q10F09-Se	2	10	0.09	Series
N2Q10F09-Pa	2	10	0.09	Parallel

* Reference Spectrum

3.3. Examination of Parametric Samples

In the continuation of the study, to examine parametric samples, the effects of the number and diameter of shape memory alloy rods, changes in friction coefficient between wedges, and the arrangement of two re-centering dampers relative to each other on the seismic performance of the re-centering damper, including friction wedges and SMA rods, are evaluated. Accordingly, Table 1 shows the naming of parametric samples with their specific features.

Table 1 displays variables regarding the number of shape memory alloy rods (2/3/4), diameter of each shape memory alloy rod (10/15/20 mm), friction coefficient between wedges (0.09/0.12/0.15/0.25), and arrangement of two re-centering dampers relative to each other (series/parallel), with modeling of these samples shown in Figure 9 and results of applied seismic hysteretic loading in Figure 10.

The results of back-and-forth hysteretic loading on parametric samples, as per Figure 10, show that increasing the number and diameter of SMA rods, as well as increasing the friction coefficient, increases the seismic resistance and stiffness of the re-centering damper but reduces its ductility. In a parallel configuration, resistance and stiffness are higher, but ductility is lower, whereas in a series configuration, all three parameters of resistance, stiffness, and ductility decrease. Consequently, increasing the resistance components improves load-bearing capacity but makes the damper behavior stiffer and less flexible. By

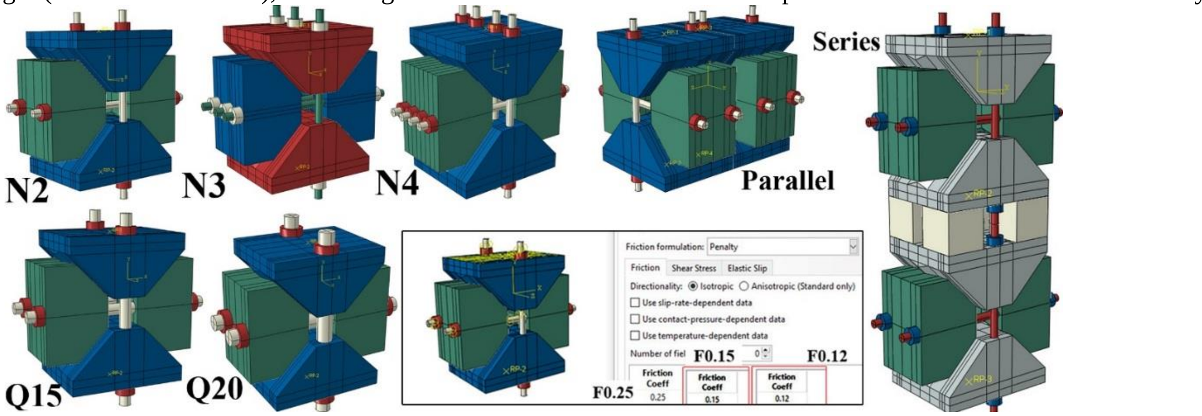

Figure 9- Display and introduction of parametric samples used in this study.

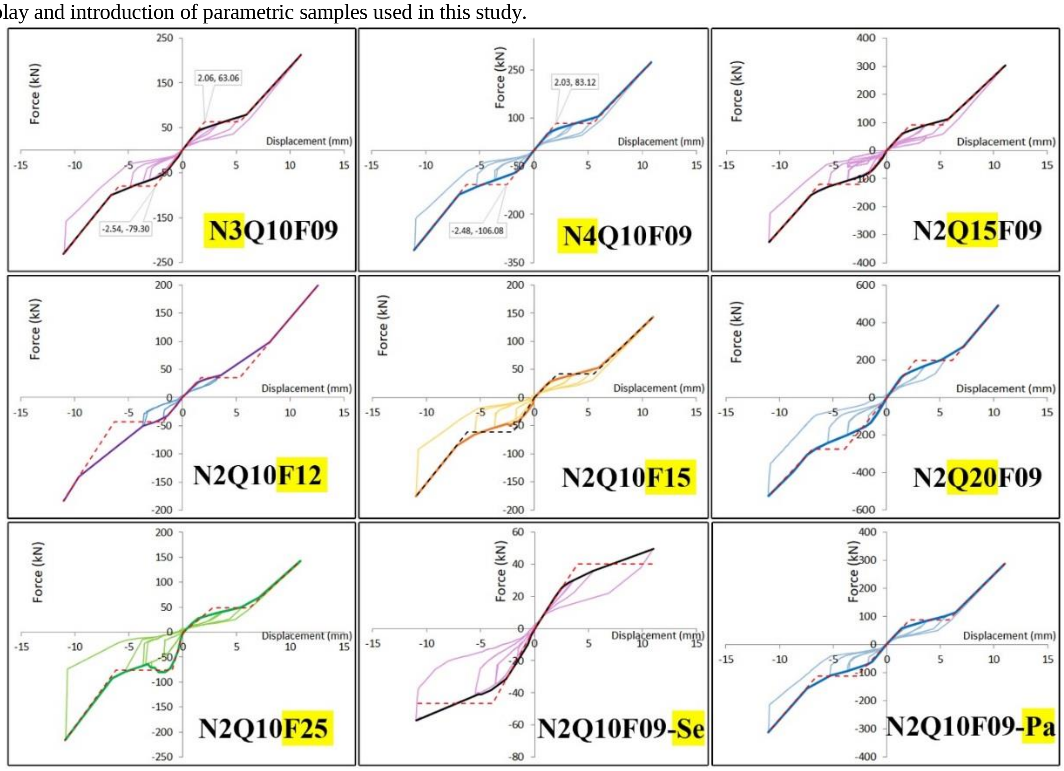

Figure 10- Results of applied seismic hysteretic loading on parametric samples.

Table 2
Details of seismic performance of parametric samples of the re-centering damper introduced in this study.

Spectrum	Resistance (kN)		Hardness (kN/mm)				Ductility	
	P+	P-	K1+	K2+	K1-	K2-	μ+	μ-
N2Q10F09*	172	-156	20.04	19.06	24.07	19.25	6.03	5.68
N3Q10F09	212	-230	30.59	26.00	31.18	29.43	5.35	4.34
N4Q10F09	275	-311	40.95	35.54	42.77	42.20	5.33	4.46
N2Q15F09	304	-326	42.10	36.14	49.57	43.85	5.06	4.53
N2Q20F09	491	-525	73.67	66.76	70.09	60.69	3.85	2.81
N2Q10F12	149	-183	22.85	22.54	25.44	29.64	7.21	5.98
N2Q10F15	143	-176	19.55	18.25	31.17	23.91	3.85	2.81
N2Q10F25	143	-216	17.54	19.73	77.54	29.56	3.90	11.21
N2Q10F09-Pa	287	-313	41.00	38.35	40.15	44.01	5.19	3.92
N2Q10F09-Se	49	-57	10.07	0	31.17	0	2.77	2.81

* Reference Spectrum

calculating the seismic performance of parametric samples, Table 2 details their performance.

Therefore, as per Table 2, the parametric examination results showed that increasing the number of SMA rods in the re-centering damper, including friction wedges and SMA rods, significantly improves seismic resistance and stiffness but reduces ductility. Specifically, increasing the number of rods from 2 to 3 and 4 increases seismic resistance in tension by 23% and 60%, and in compression by 4% and 100%, respectively. Initial seismic stiffness in tension increases by 52% and 100%, and in compression by 52% and 77%, while ductility in tension decreases by about 11% and in compression by 23% and 21%, respectively. As a result, increasing the number of rods leads to more resistant but brittle seismic performance in the re-centering damper, requiring a balance between resistance and ductility in design.

Additionally, the results of examining the effect of changing SMA rod diameter on the seismic performance of the re-centering damper showed that increasing rod diameter significantly increases damper seismic resistance and stiffness, such that increasing diameter from 1 cm to 1.5 and 2 cm increases seismic resistance in tension by 77% and 185%, and in compression by 109% and 237%, respectively. Initial seismic stiffness in tension increases by 110% and 268%, and in compression by 106% and 191%. However, seismic ductility decreases, in tension by 16% and 36%, and in compression by 20% and 51%. Therefore, increasing rod diameter improves damper resistance and stiffness but is accompanied by reduced ductility.

Furthermore, the results show that increasing the friction coefficient of friction wedges in the re-centering damper significantly increases seismic resistance and stiffness in the negative (compressive) section, while its effect on the positive (tensile) section is less noticeable, such that increasing the friction coefficient from 0.09 to 0.12, 0.15, and 0.25 increases seismic resistance in the positive section by 13%, 17%, and 17%, and in the negative section by 17%, 13%, and 39%, respectively. The initial seismic stiffness criterion in the positive section has minor changes, and in the negative section, especially at 0.25, increases up to 222%. Ductility in the positive section slightly increases or decreases with friction coefficient changes, and in the negative section shows more fluctuations (from 51% decrease to 97% increase). Overall, increasing the friction coefficient improves damper resistance and stiffness but reduces its ductility.

The examination of the effect of the placement status of two re-centering dampers, including friction wedges and SMA rods, showed that parallel placement leads to increased seismic resistance and stiffness and reduced ductility, while series placement causes a decrease in seismic resistance, stiffness, and ductility, and loss of secondary stiffness. Quantitatively, changing from series to parallel increases seismic resistance in the positive (tensile) section by up to 67% and in the negative (compressive) section by up to 101%, while ductility decreases in the positive section by up to 14% and in the negative by up to 31%. Therefore, according to the conclusion, parallel damper configuration is effective for enhancing structural resistance and stiffness, but at the cost of reduced ductility, and the series configuration for dampers is not recommended at all.

4. Overall Comparison of Results

In this section of the research, to comprehensively evaluate seismic performance, all samples of the re-centering damper, including friction wedges and SMA rods, were examined and compared. Accordingly, the seismic performance of the samples in terms of resistance, stiffness, and ductility in both positive (tensile) and negative (compressive) directions is analyzed, and by sorting data from highest to lowest values, bar charts related to resistance, stiffness in both positive and negative directions, and seismic ductility are shown in Figure 11.

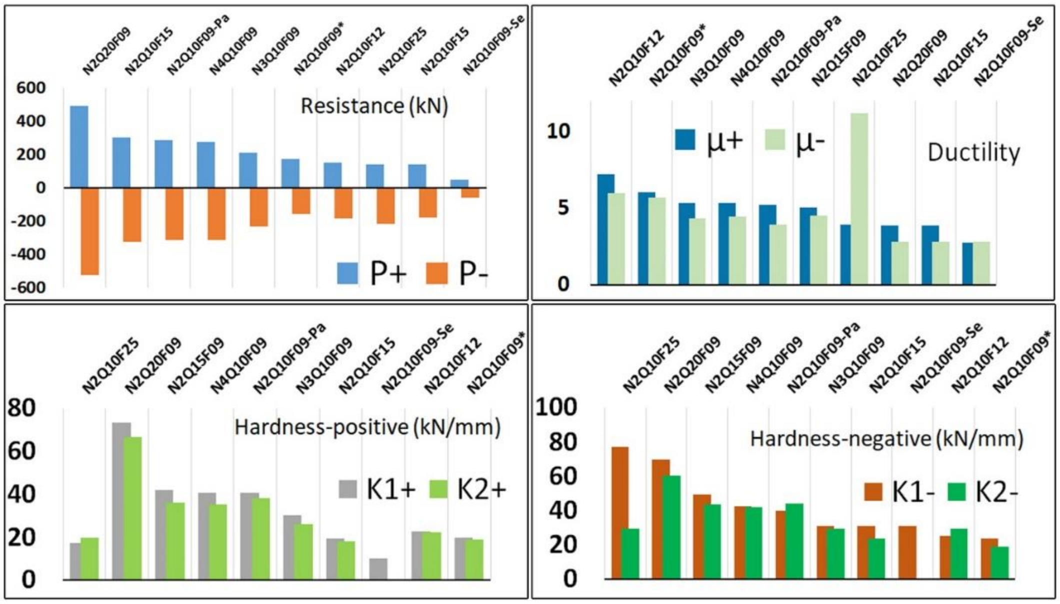

Figure 11- Bar chart results of comparative parametric samples in three criteria: resistance, stiffness, and seismic ductility.

The results of these charts provide a comprehensive view of the seismic behavior of different dampers and show that by simultaneously comparing the mentioned indices, the relative performance of each sample can be evaluated.

As per the bar chart results of comparative parametric samples in three criteria: resistance, stiffness, and seismic ductility in Figure 11, the following can be deduced:

- Based on the bar chart results, the highest seismic resistance was observed in samples N2Q20F09, N2Q15F09, and N2Q10F09-Pa, respectively, while the lowest resistance belonged to samples N2Q10F09-Se, N2Q10F15, and N2Q10F25, respectively.
- Also, in the tensile (positive) section of the bar chart, initial and secondary stiffness results (K1 and K2) showed that samples N2Q20F09, N2Q15F09, and N2Q10F09-Pa had the highest initial seismic stiffness, respectively, and samples N2Q10F09-Se, N2Q10F25, and N2Q10F15 had the lowest stiffness, respectively.
- In the compressive (negative) section of the bar chart, initial and secondary stiffness results (K1 and K2) showed that samples N2Q10F25, N2Q20F09, and N2Q15F09 had the highest stiffness, respectively, and samples N2Q10F09*, N2Q10F12, and N2Q10F09-Se had the lowest stiffness, respectively.
- In ductility evaluation, the highest performance belonged to samples N2Q10F12, N2Q10F09*, and N3Q10F09, and the lowest ductility was observed in samples N2Q10F09-Se, N2Q10F15, and N2Q20F09. Of course, the ductility criterion in the compressive (negative) section of the bar chart for sample N2Q10F25 differs greatly from other samples, and in this section, this sample has high ductility, which can be attributed to its feature, namely, a very high friction coefficient between the wedges.

5. Conclusion

In this research, aiming to improve the performance of re-centering dampers, the behavior of Zhang's damper was reviewed and numerically developed. By modifying the connection method and adding two SMA rods in the tension direction, full performance in compression and tension cycles was enabled. Then, the effects of parameters such as the number and diameter of SMA rods, wedge friction coefficient, and damper arrangement (series or parallel) on seismic resistance, stiffness, and ductility were examined, with the results of these analyses forming the basis for the final research conclusions as follows:

1. According to the examinations, it was determined that Zhang's re-centering damper assembly (designed only for the compressive section, stretching SMA rods with friction wedges) should not be rigidly connected to the lower part of the beam in chevron braces. For proper frame and damper performance, hinges must be provided between the damper chamber and brace, as well as at the lower part of the beam, to transfer lateral load without creating additional moment. Furthermore, in this study, by numerically developing Zhang's damper and adding two SMA rods directly in the tension direction through

increasing wedge width, the damper could create a full compression and tension cycle. The flag-shaped load-displacement diagram and its passage through the coordinate origin indicate the correct performance, reversibility, and re-centering of the new idea.

2. Parametric studies of the re-centering damper (in full compression and tension cycle) show that increasing the number and diameter of SMA rods increases seismic resistance and stiffness but decreases ductility. Also, increasing the friction coefficient of friction wedges, due to its direct effect on resistance and stiffness in the compressive section, increases seismic resistance and stiffness in the compressive section, while no noticeable change is seen in the tensile section, but overall, damper ductility decreases.
3. Parametric study results of the re-centering damper (in full compression and tension cycle) show that in parallel configuration, seismic resistance and stiffness increase, but ductility decreases. It was also observed that parallel configuration results are almost equal to the case with 4 rods, concluding no difference between parallel dampers and using four rods. In contrast, in a series configuration, resistance, stiffness, and ductility significantly decrease; therefore, using a series configuration for the re-centering damper is not recommended at all.
4. Post-analysis phase results of this research show that the effect of increasing damper diameter on seismic performance (resistance and stiffness) is much greater than increasing the number and friction coefficient, and excessive increase in friction between wedges only increases initial seismic stiffness in the compression section but simultaneously reduces seismic resistance.
5. Additionally, post-analysis phase results of this research show that if the friction coefficient approaches 0.12, it has higher seismic ductility than the baseline sample with a 0.09 friction coefficient, and overall, all reinforced samples have lower ductility compared to the baseline sample

References

[1] Almajhali, K. Y. M. "Review of passive energy dissipation devices and techniques of installation for high-rise building structures." Structures 51 (2023): 1019-1029. https://doi.org/10.1016/j.istruc.2023.03.025

[2] Zhang, H., A. Li, Y. Su, G. Xu, and B. Sha. "Viscoelastic dampers for civil engineering structures: A systematic review of constructions, materials, and applications." Journal of Building Engineering 96 (2024): 110597. https://doi.org/10.1016/j.jobe.2024.110597

[3] Avşar, Ö., S. Cao, and O. E. Ozbulut. "Development and characterization of self-centering friction dampers with confined shape memory alloy bars." Journal of Building Engineering 90 (2024): 109504. https://doi.org/10.1016/j.jobe.2024.109504

[4] Riaz, R. D., U. J. Malik, M. U. Shah, M. Usman, and F. A. Najam. "Enhancing Seismic Resilience of Existing Reinforced Concrete Building Using Non-Linear Viscous Dampers: A Comparative Study." Actuators 12.4 (2023): 175. https://doi.org/10.3390/act12040175

[5] Jiang, H., Z. Huang, and H. N. Li. "Deformation-amplified self-centering energy-dissipation device for seismic control: Design, testing and simulation." Engineering Structures 280 (2023): 115671. https://doi.org/10.1016/j.engstruct.2023.115671

[6] Mohammadgholipour, A., and A. H. M. M. Billah. "Mechanical properties and constitutive models of shape memory alloy for structural engineering: A review." Journal of Intelligent Material Systems and Structures 34.20 (2023): 2335-2359. https://doi.org/10.1177/1045389X231185458

[7] Fang, C., C. Qiu, and Y. Zheng. "Shape memory alloys for civil engineering." Materials 16.2 (2023): 787. https://doi.org/10.3390/ma16020787

[8] Zhang, S., H. Hou, B. Qu, Y. Zhu, K. Li, and X. Fu. "Tests of a novel re-centering damper with SMA rods and friction wedges." Engineering Structures 245 (2021): 112125. https://doi.org/10.1016/j.engstruct.2021.112125

[9] Asfaw, A. M., L. Cao, O. E. Ozbulut, and J. Ricles. "Development of a shape memory alloy-based friction damper and its experimental characterization considering rate and temperature effects." Engineering Structures 270 (2022): 115101. https://doi.org/10.1016/j.engstruct.2022.115101

[10] Mohammadi Nia, M., S. Moradi, and T. Yang. "Performance-based seismic design of self-centering steel moment frames with SMA-bolted connections." Journal of Constructional Steel Research 208 (2023): 107990. https://doi.org/10.1016/j.jcsr.2023.107990

[11] Wang, B., and S. Zhu. "Superelastic SMA U-shaped dampers with self-centering functions." Smart Materials and Structures 27.5 (2018): 055003. https://doi.org/10.1088/1361-665X/aab52d

[12] ABAQUS-V6.19-1. "Finite Element Analysis Software." Johnston, RI, USA. ABAQUS/Standard theory. Manual, Dassault Systèmes Simulia Corp., 2019.

Journal of Civil Engineering Researchers

Journal homepage: www.journals-researchers.com

Optimal Placement of Viscoelastic Layers in Sandwich Beams for Maximum Vibration Attenuation and Minimum Creep Deflections

A.R. Gorji, [a] M. Lezgy-Nazargah, [a,*] A. Ghafourian-Mojaver, [a] M. Tayebinia [a]

[a] *Department of Civil Engineering, Faculty of Engineering, Hakim Sabzevari University, Sabzevar 9617976487-397, Iran*

ABSTRACT

Until now, various mathematical models have been proposed to characterize the behavior of viscoelastic materials and facilitate their implementation in finite element software. However, it remains unclear which configuration of the viscoelastic layer along the thickness and length of the beam yields the lowest creep deflection and highest damping effect under applied forces. To fill this literature gap, efforts are undertaken in this study to identify the optimal placement of the viscoelastic layers in the sandwich beam. To reach this aim, the creep and dynamic behaviors of sandwich beams with different boundary conditions and various configurations of the viscoelastic layer along the thickness and length were investigated using a finite element model. The obtained results indicate that the damping capability and creep deformations of the sandwich beam are strongly affected by the position of the viscoelastic layers.

ARTICLE INFO

Received: June 30, 2025
Accepted: September 08, 2025

Keywords:
Sandwich beams
Viscoelastic layers
Vibration attenuation
Optimal position
Finite element

DOI: 10.66224/JCER.7.4.78
DOR: 20.1001.1.2538516.2025.7.4.6.8

1. Introduction

In recent years, the application of viscoelastic materials has increased significantly. The growing interest in these materials arises from their ability to dissipate significant amounts of energy through shear deformation. These materials are predominantly utilized as energy dampers. On the other hand, sandwich structures are widely utilized in industries such as construction, bridge building, and shipbuilding, owing to their high bending stiffness-to-weight ratio and the adaptability to modify fundamental structural parameters to meet specific design requirements. Sandwich beams with viscoelastic cores, known for their effective damping properties under dynamic loads, are among the most widely used components in industrial structures.

Banks et al. [1] provided a comprehensive overview of elastic and viscoelastic materials, aiming to enhance the understanding of their properties and applications. Lakes [2] conducted experimental studies to explore the properties of viscoelastic materials across a range of substances, including polymers, metals, piezoelectric materials, damping alloys, composites, and biological materials. Galuppi and Royer-Carfagni [3] analyzed the time-dependent behavior of a sandwich beam with viscoelastic core. The analyzed beam comprises two elastic layers at the top and bottom, with a viscoelastic core sandwiched between them. Galuppi and Roier-Carfagni

[*] Corresponding author. Tel.: +980000000000; e-mail: m.lezgy@hsu.ac.ir.

compared the results obtained from their analytical model with those obtained from three-dimensional finite element analysis. Kpeky et al. [4] investigated the vibration behavior of sandwich structures featuring soft and flexible cores. Given the substantial differences in the mechanical properties between the core and the top and bottom layers of sandwich structures, modeling these systems using higher-order elements or three-dimensional elements is more suitable. However, this approach increases the number of degrees of freedom and extends the analysis time. To mitigate this time-consuming process, Kpeky and colleagues proposed a hexahedral solid-shell linear element as an alternative.

Mohammadi and Nasirshoaibi [5] detailed the modeling process for viscoelastic materials using ABAQUS software. This reference emphasizes that the behavior of viscoelastic materials can be effectively simulated by precisely defining the storage and loss shear moduli. The simulation results were then compared with experimental data. Pelayo et al. [6] investigated the temperature- and time-dependent behavior of polyvinylbutyral (PVB) material, commonly used in the construction of sandwich beams. This reference examines the mechanical behavior of laminated glass elements in which PVB, a viscoelastic material, is used as an interlayer. In this research, PVB samples were subjected to dynamic tests using a dynamic mechanical thermal analysis (DMTA) device across a temperature range of -15°C to 50°C. Subsequently, master curves at different temperatures were constructed using the Williams-Landel-Ferry model, and the Young's modulus of PVB was determined in both time and frequency domains.

Froli and Lani [7] investigated the adhesion, creep, and stress relaxation behavior of laminated glass incorporating a viscoelastic PVB interlayer. In this reference, glass specimens were subjected to tensile loading at a 45-degree angle relative to their longitudinal axis. A modified shear-compression testing method was utilized to assess evaluate the ultimate shear strength of the PVB interlayers. Various specimens of this material were fabricated and experimentally tested. Following the experimental investigations, the viscoelastic properties of the material, specifically shear behavior, creep, and stress relaxation, were characterized and subsequently used in numerical modeling. Ehrich et al. [8] proposed a new methodology for examining the properties of encapsulated ethylene-vinyl acetate (EVA) and PVB. The newly developed method for characterizing encapsulated materials demonstrated high effectiveness, cost-efficiency, and practicality for laboratory-scale applications. Hána et al. [9] conducted both experimental and numerical studies to evaluate the mechanical properties of polymer interlayers used in laminated glass manufacturing. These researchers investigated the sensitivity of shear stiffness in two commonly used polymers in glass panel construction—PVB and EVA—to variations in time and temperature. Hána et al. [10] investigated the four-point bending behavior of glass panels with PVB interlayers using both numerical and experimental approaches. The analyzed glass panels were composed of glass sheets bonded by polymer interlayers, which enabled the transfer of shear stresses between the glass layers. Hána, Eliášová and colleagues determined the time- and temperature-dependent shear stiffness using a discrete Maxwell model, with Prony series coefficients derived from the thermo-dynamic analysis of the polymer interlayer.

Zemanová et al. [11] analyzed the modal characteristics of multilayered glass beams. Given that in laminated glass, rigid glass layers are bonded with soft interlayers whose mechanical behavior is frequency and temperature-dependent, the system exhibits viscoelastic characteristics. In this reference, Zimanová et al. employed four distinct approaches to address to solve the nonlinear eigenvalue problem: complex eigenvalue computation based on the Newton-Raphson method, the modal kinetic energy method, the dynamic effective thickness method, and the enhanced effective thickness method. Li et al. [12] presented a state-space method for analyzing the dynamic response of double-layer beams with a viscoelastic interlayer. The considered double-layer system consists of two parallel Euler-Bernoulli elastic beams connected by a generalized viscoelastic interlayer. In this reference, a novel state-space approach is developed by introducing mode shape constants to address the coupling effects induced by the viscoelastic interlayer. Schuster et al. [13] investigated the linear viscoelastic behavior of polymeric interlayers used in laminated glass. This study examined a three-layer system consisting of rigid outer layers and a soft acoustic PVB core, emphasizing the impact of temperature and loading on the materials mechanical properties. The experimental data analysis included DMTA and creep testing under bending conditions. In this reference, the results were compared with analytical models developed using the generalized Maxwell model and a simplified model that combined multiple rheological models.

Based on the studies conducted so far, it can be concluded that accurately predicting the dynamic behavior of sandwich beams with viscoelastic layers using the finite element method necessitates a precise determination of the structural properties and constitutive relationships of viscoelastic materials. Various methods are available to define the characteristics of viscoelastic materials, including the utilization of dynamic storage and loss moduli, creep or relaxation test data, or directly specifying of Prony series parameters. However, no comprehensive study has been conducted to date to determine the optimal placement of the viscoelastic layer. This research seeks to determine the optimal positioning of viscoelastic layers along the thickness and length of the beam to maximize damping performance.

2. Sandwich beam with viscoelastic layers

2.1. Geometry and mechanical properties

The considered sandwich beams of the present study are prismatic, featuring a rectangular uniform cross-section of width b, height h, and length L. These sandwich beams comprising three glass layers and two viscoelastic layers made of PVB material. The total thickness of glass layers is $3h_G$, while the total thickness of PVB layers is $2h_V$. Laminated glass beams are widely used in diverse structural applications. They form the primary support ribs or secondary purlins for large overhead glazed roofs, entrance canopies, and atria. They also serve as load-bearing elements for glass floors, bridges, and stair stringers/treads where transparency is desired for visual connection or light penetration. Since the failure of glass structures is rather brittle, PVB laminates are incorporated as safety-critical enhancements. The PVB layers provide essential post-breakage integrity. If a laminated glass beam is impacted (e.g., by hail, falling debris), the PVB holds shattered glass fragments in place, preventing collapse and protecting people below. Additionally, PVB laminates enhance vibration damping.

To identify the optimal position of the viscoelastic layers along the beam's thickness, four distinct lay-up schemes are assumed for the sandwich beams. These considered lay-up schemes are illustrated in Fig. 1. Notably, in all these lay-up schemes, the total cross-sectional area of the viscoelastic layers remains identical.

In this paper, the optimal placement of viscoelastic layers along the beam's longitudinal axis is also investigated. For this purpose, various configurations for positioning the PVB layer along the beam's length are considered. As illustrated in Fig. 2, the three considered axial configurations for the placement of the PVB layer along the beam length are:

- The first third of the beam,
- The middle third of the beam,

The last third of the beam.

2.2. Constitutive relations for viscoelastic materials

This section focuses on the constitutive equations of linear viscoelastic materials and their corresponding linear constitutive relations. Linear viscoelasticity is generally applicable only to small deformations or to materials that exhibit linear mechanical behavior.

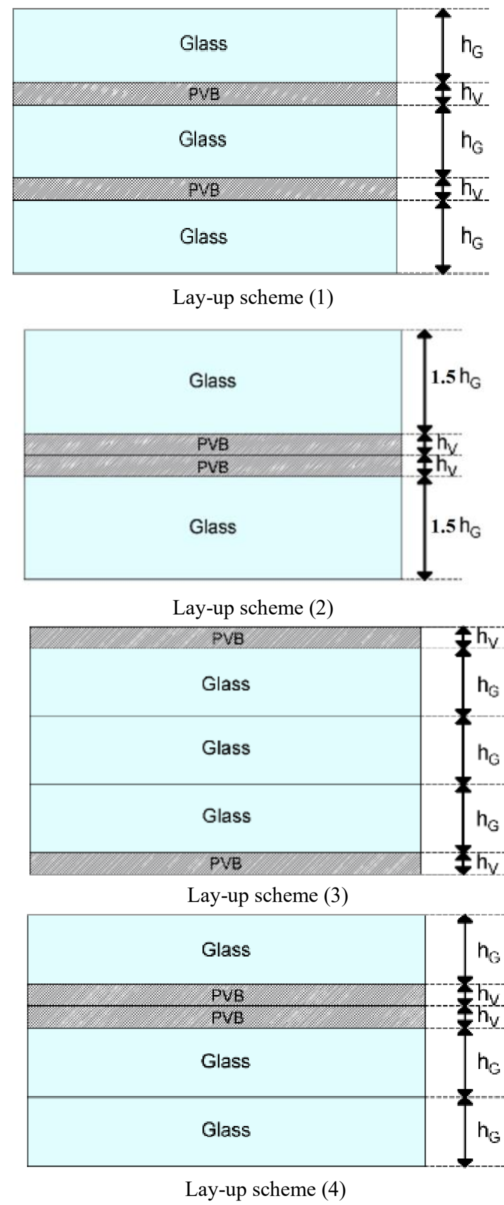

Fig. 1 Different lay-up schemes considered for the sandwich beams

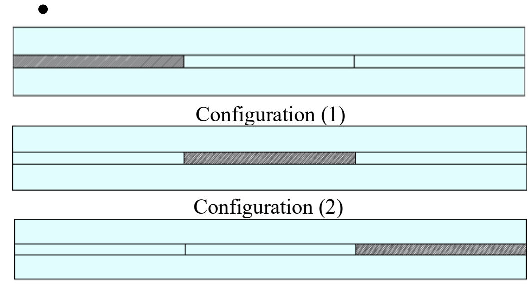

Configuration (3)

Fig. 2. Different configurations for the placement of the viscoelastic layers along the beam's longitudinal axis

Therefore, the theory of infinitesimal strains is typically employed in the analysis of such materials. One of the most widely used and general approaches for modeling linear viscoelastic materials is the Boltzmann superposition principle, originally introduced by Ludwig Boltzmann Lakes [2]. The Boltzmann Superposition Principle asserts that the total response of a system is equal to the sum of the individual responses caused by each component acting independently. To predict the stress history in viscoelastic materials, it is assumed that a specific strain is applied to the material. Relaxation and recovery experiments are commonly conducted to verify the linearity of this principle, ensuring that the material's response adheres to the principle under the applied conditions. The time-dependent relaxation stress is expressed as:

$$\sigma_0 = \varepsilon_0 E(t) \tag{1}$$

where ε_0 represents the initial strain, and $E(t)$ is the relaxation modulus. Based on the Boltzmann Superposition Principle, an arbitrary strain history can be represented as a combination of two sequential unit step strains:

$$\varepsilon(t) = \varepsilon_0[H(t) - H(t - t_1)] \tag{2}$$

where $H(t)$ denotes the Heaviside step function. Thus, as described in Fig. 3, the resulting stress is:

$$\sigma(t) = \varepsilon_0[E(t) - E(t - t_1)] \tag{3}$$

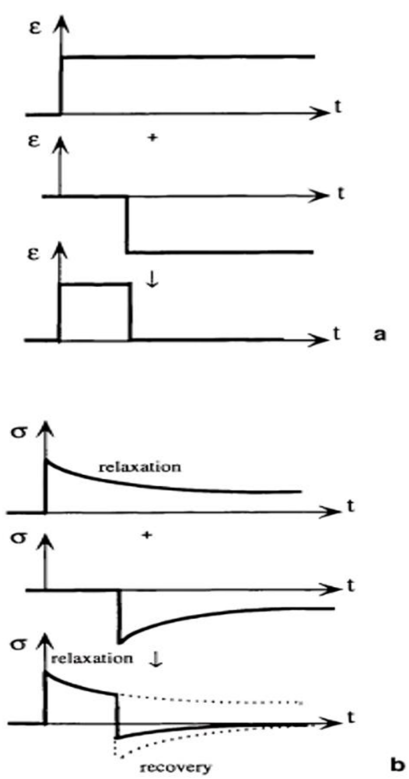

Fig. 3. (a) Application of the Boltzmann Superposition Principle to generate a strain pulse, (b) Calculation of relaxation stress in response to a strain pulse using the Boltzmann Superposition Principle

The stress resulting from the delayed strain $\varepsilon_0 H(t - t_1)$ is expressed as $\varepsilon_0 E(t - t_1)$, similar to the stress $\varepsilon_0 E(t)$, generated by the preceding strain step $\varepsilon_0 H(t)$. This relationship holds under the assumption that the material properties remain constant over time. Depending on the material's viscoelastic characteristics, the stress may diminish to zero or recover as time t progresses Lakes [2]. The strain history $\varepsilon(t)$ is defined as a function of time t, as depicted in Fig. 4. It is assumed that the strain remains zero before $t = 0$. A specific segment of this strain history, ranging from $t - \tau$ to $t - \tau + \Delta\tau$ (where τ is a time variable, analogous to the constant t_1 in the earlier equations), is illustrated in Fig. 4. This segment of the strain history can be mathematically represented as:

$$\varepsilon(t) = \varepsilon(\tau)[H(t - \tau) - H(t - \tau + \Delta\tau)] \tag{4}$$

The equation above effectively describes a strain pulse.

Using Eq. (3), the variation in stress within the viscoelastic material resulting from the strain pulse history can be formulated as:

$$d\sigma(t) = \varepsilon(\tau)[E(t - \tau) - E(t - \tau + \Delta\tau)] \tag{5}$$

On the other hand, we have:

$$\frac{dE(t - \tau)}{d\tau} = \lim_{\Delta t \to 0} \frac{E(t - \tau + \Delta\tau) - E(t - \tau)}{\Delta\tau} \tag{6}$$

Thus, the stress increment can be written as:

$$d\sigma(t) = -\varepsilon(t)\frac{dE(t - \tau)}{d\tau} \tag{7}$$

The entire strain history can be broken down into discrete strain pulses. The stress at any given time t is determined by summing the stress contributions from all preceding pulses. Importantly, only the effects of strain pulses that occur before the present time t are included in the computation. Contributions from potential future strain pulses are not accounted for, ensuring causality in the stress-strain relationship.

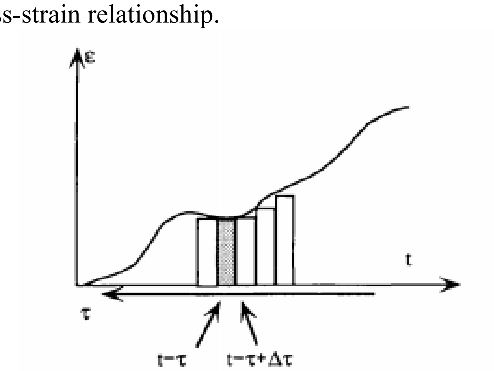

Fig. 4. Decomposition of the strain history into a series of strain pulses

If the width of the strain pulses, denoted as $\Delta\tau$ approaches an infinitesimally small value, the summation converges to an integral, yielding the following expression for stress:

$$\sigma(t) = -\int_0^t \varepsilon(\tau)\frac{dE(t - \tau)}{d\tau} d\tau + E(0)\varepsilon(t) \tag{8}$$

The second term in this equation arises due to the following rationale: After the strain pulse or a series of strain pulses, the strain often returns to zero. However, for an arbitrary strain history, the final strain, $\varepsilon(t)$, at time t is generally nonzero. The stress increment associated with the final strain is given by $E(0)\varepsilon(t)$, as there is insufficient time for stress relaxation to occur in this scenario Lakes [2]. To derive the final form of Boltzmann's superposition principle, integration by parts is applied. In this formulation, t represents time, and τ represents the time variable for integration:

$$\sigma(t) = \int_0^t E(t-\tau)\frac{d\varepsilon(\tau)}{d\tau}d\tau \tag{9}$$

If the roles of stress and strain in the preceding discussions are interchanged, the complementary relationship below is obtained:

$$\varepsilon(t) = \int_0^t J_E(t-\tau)\frac{d\sigma(\tau)}{d\tau}d\tau \tag{10}$$

Consequently, if the response of a viscoelastic material to a unit step stress or strain is experimentally measured, the material's behavior under any arbitrary load history can be computed.

The effect of temperature θ on the behavior of a viscoelastic material can be explained by using the concept of reduced time. In this case, the stress-strain relation is rewritten as:

$$\sigma(t) = E_0(\theta)\gamma - \int_0^t \dot{E}\big(\xi(s)\big)\varepsilon(t-s)ds \tag{11}$$

where $\dot{E}(\xi) = \frac{dE}{d\xi}$. In addition, $\xi(t)$ is the reduced time defined as:

$$\xi(t) = \int_0^t \frac{ds}{\alpha(\theta(s))} \tag{12}$$

In the above equation, $\alpha(\theta(s))$ is time transmission function defined as:

$$\log(\alpha) = -\frac{C_1(\theta-\theta_0)}{C_2+(\theta-\theta_0)} \tag{13}$$

where θ_0 is the reference temperature at which the viscoelastic material response is measured. C_1 and C_2 are the calibration constants measured at this temperature.

The previous paragraphs examined the constitutive relations in a one-dimensional state. For a viscoelastic material in three dimensions, the constitutive relationship can be expressed in the following form:

$$\sigma_{ij}(t) = \int_0^t C_{ijkl}(t-\tau)\frac{d\varepsilon_{kl}(\tau)}{d\tau}d\tau \tag{14}$$

where C_{ijkl} denotes elastic constants of a viscoelastic material. The above equation can be rewritten as the following matrix form:

$$\boldsymbol{\sigma}(t) = \boldsymbol{C}(t)\boldsymbol{\varepsilon}(t) \tag{15}$$

2.3. Finite element modeling

The finite element model employed to analyze the viscoelastic sandwich beam utilizes an 8-node continuum solid element. Each node has three degrees of freedom corresponding to translations along the global coordinate axes of x_1, x_2, and x_3. The vector of displacement components $\boldsymbol{u} = [u \quad v \quad w]^T$ may be written in terms of the nodal variables vectors $\boldsymbol{u}_u^e$ as follows:

$$u = N_{uu}u_u^e \tag{16}$$

where

$$\boldsymbol{u}_u^e = \{u_1 \quad u_2 \quad \cdots \quad u_8 \quad \vdots \quad v_1 \quad v_2 \quad \cdots \quad v_8 \quad \vdots \quad w_1 \quad w_2 \quad \cdots \quad w_8\}^T$$

In Eq. (16), $\boldsymbol{N}_{uu}$ denotes displacements Lagrange interpolation matrix. For brevity, the expression for $\boldsymbol{N}_{uu}$ is not included here.

The Strain components at any point within the viscoelastic beam can be expressed in the following matrix form:

$$\boldsymbol{\varepsilon} = \boldsymbol{L}_{uu}\boldsymbol{u} \tag{17}$$

where

$$\boldsymbol{L}_{uu} = \begin{bmatrix} \partial/\partial x & 0 & 0 \\ 0 & \partial/\partial y & 0 \\ 0 & 0 & \partial/\partial z \\ 0 & \partial/\partial z & \partial/\partial y \\ \partial/\partial z & 0 & \partial/\partial x \\ \partial/\partial y & \partial/\partial x & 0 \end{bmatrix}$$

$$\boldsymbol{\varepsilon} = [\varepsilon_{11} \quad \varepsilon_{22} \quad \varepsilon_{33} \quad 2\varepsilon_{23} \quad 2\varepsilon_{13} \quad 2\varepsilon_{12}]^T$$

Given that the displacement components of the sandwich beam with viscoelastic layers are small, the linear strain-displacement relationships are utilized in Eq. (6). For a 8-node continum finite element with three degrees of freedom per node, and by using Eq. (16), strain vector may be expressed as follows:

$$\boldsymbol{\varepsilon} = \boldsymbol{L}_{uu}\boldsymbol{u} = \boldsymbol{L}_{uu}\boldsymbol{N}_{uu}\boldsymbol{u}_u^e = \boldsymbol{B}\boldsymbol{u}_u^e \tag{18}$$

where $\boldsymbol{B}$ denotes strain interpolation matrix.

The Hamilton's principle is used to derive governing equations of the viscoelastic sandwich beam. According to this principle, for a viscoelastic medium with volume Ω and regular boundary surface Γ, The following relationship applies:

$$\delta\left[\int_0^t (U_0 - T_k)dt\right] = 0 \tag{19}$$

where

$$U_0 = \frac{1}{2}\int_\Omega \boldsymbol{\varepsilon^T\sigma}d\Omega - \int_\Gamma \boldsymbol{u}^T\boldsymbol{F}_S d\Gamma - \int_\Omega \boldsymbol{u}^T\boldsymbol{F}_V d\Omega \tag{20}$$

$$T_k = \frac{1}{2}\int_V \rho\frac{\partial\boldsymbol{u}^T}{\partial t}\frac{\partial\boldsymbol{u}}{\partial t}dV, \tag{21}$$

and ρ is the density. In addition, $\boldsymbol{F_S}$ and $\boldsymbol{F_V}$ are surface force vector, respectively. Substituting Eqs. (15), (16), and (18) into Eq. (19), and assembling the element equations result in the following general equation:

$$\boldsymbol{M}\ddot{\boldsymbol{q}}(t) + \boldsymbol{K}(t)\boldsymbol{q}(t) = \boldsymbol{F}(t) \tag{22}$$

The matrices and vectors in the above equation include the stiffness matrix $\boldsymbol{K}(t) = \int_\Omega \boldsymbol{B}^T\boldsymbol{C}\mathbf{B}d\Omega$, mass matrix $\boldsymbol{M} = \int_\Omega \rho\mathbf{N}_{uu}^T\boldsymbol{N}_{uu}d\Omega$, and loads vector $\boldsymbol{F}(t) = \int_\Omega {\boldsymbol{N}_{uu}}^T\boldsymbol{F_V}d\Omega + \int_\Gamma {\boldsymbol{N}_{uu}}^T\boldsymbol{F_S}d\Gamma$.

3. Numerical Results and Discussion

In this section, numerical examples are presented to investigate the influence of viscoelastic layers' position on the natural frequency, damping capability, and creep deformations of sandwich beams. Firstly, the finite element model is validated by comparing its results with experimental data. Then, the optimal placement of viscoelastic layers within sandwich beams is determined.

All sandwich beams examined in this section have a length of 1000 mm, a width of 100 mm, and their overall thickness is 12.76 mm. The thickness of each glass layer is 4 mm, while the thickness of each viscoelastic layer is 0.38 mm. The layers are assumed to be perfectly bonded, ensuring no slippage at the interfaces. The mechanical properties of the glass and the viscoelastic material (i.e., PVB) are summarized in Table 1. Thermal effects are neglected, and the analyses are performed at the constant temperature of 20°C.

All numerical simulations are carried out using ABAQUS software. The eight-node brick element (C3D8R) available in the library of this software was employed for modeling the glass and PVB layers. Static analysis was adopted for simulating the creep problems. Dynamic implicit analysis was used for predicting the transient creep responses. Free vibration tests were also carried out by employing the eigenvalue solver available in the ABAQUS software.

Table 1
Mechanical Properties of Glass and PVB [6]

Material	Elastic Modulus (MPa)	Poisson's Ratio	Density (kg/m³)	C_1	C_2
Glass	72000	0.22	2,500	12.6010	74.76
PVB	1240.3	0.49	1100	12.6010	74.76

3.1. Validating example

Free vibration analysis of a sandwich beam with viscoelastic layers is studied in this subsection. The sandwich beam under consideration has clamped boundary conditions at both ends.. Lamination configuration of the sandwich beam is lay-up 1 (see Fig. 1). The viscoelastic layers are located all over the length of the beam. This analysis aims to assess and compare the accuracy of the 3D finite element simulations. Experimental data from Pelayo et al. [6], who previously studied this beam, are employed to validate the numerical results.

Table 2 summarizes the first four natural frequencies of the viscoelastic sandwich beam, calculated using the finite element model. The numerical results are compared with the experimental data reported by Pelayo et al. [6].

Table 2
Natural Frequencies (Hz) of the clamped-clamped sandwich beam with lay-up scheme no. 1

Vibrating Mode	Experimental	Present
1	36.14	36.47
2	98.28	97.40
3	188.94	188.22
4	306.13	303.35

Table 2 demonstrates that the numerical results from the finite element model align exceptionally well with the experimental data, showing a maximum percentage discrepancy of just 0.9%.

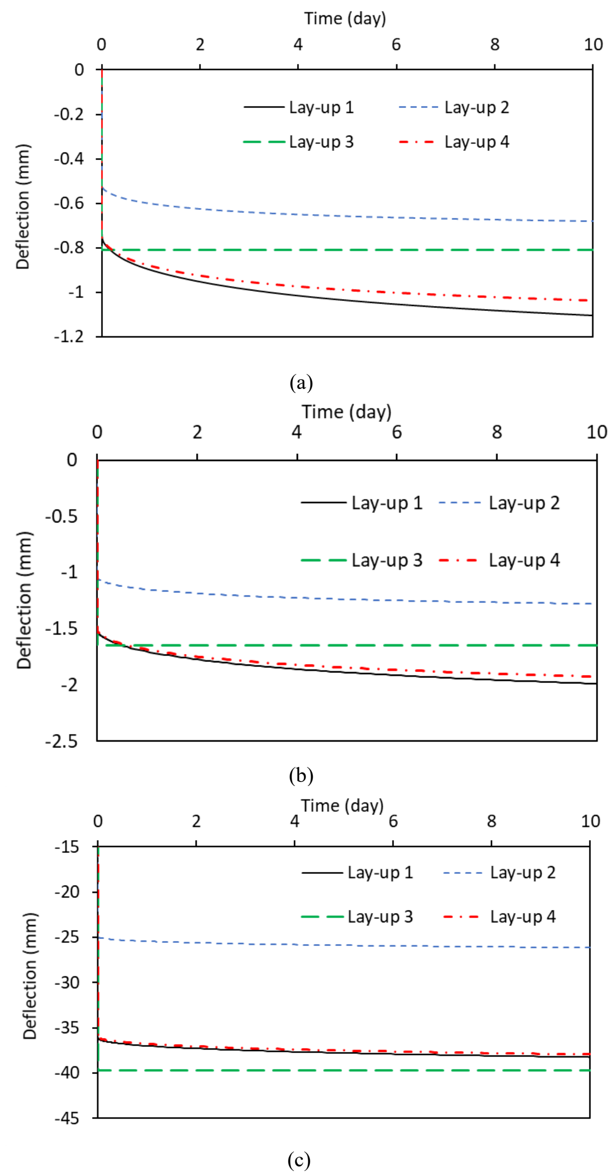

Fig. 5. Effect of lay-up scheme on the long-term deflection of sandwich beams: (a) clamped-clamped, (b) simply support, (c) clamped-free

Table 4
Effect of lamination configuration on the natural frequencies (Hz) of the sandwich beams

Boundary condition	Mode no.	Laminaion configuration			
		Lay-up 1	Lay-up 2	Lay-up 3	Lay-up 4
Fixed-Fixed	1	36.472	52.195	51.463	40.587
	2	97.402	142.44	141.72	110.13
	3	188.22	277.84	277.89	214.49
	4	303.35	312.00	372.07	351.18
Simply support	1	18.09	24.02	22.22	18.95
	2	64.43	92.09	88.99	70.99
	3	139.96	204.85	200.67	157.22
	4	245.21	257.67	257.67	257.67
Clamped-free	1	7.2641	9.1232	7.9996	7.4169
	2	37.688	52.293	50.076	40.871
	3	59.945	59.945	59.950	59.946
	4	99.072	143.06	140.19	110.49

3.2. *Effect of PVB stacking sequence on natural frequency, creep deformations, and damping capability*

This section investigates how the through-thickness positioning of viscoelastic layers affects the long-term creep deformations, natural frequencies, and damping capability of the sandwich beams. In the examined sandwich beams of this section, it is assumed that the viscoelastic layers are located all over the length of the structure (configuration 4).

3.2.1. Creep deformations.

The creep deformations of the beam under a uniform load of $2000\ N/m^2$ were calculated for four different lay-up schemes shown in Fig. 1 over a ten-day period. Variations of maximum deflection with respect to time are shown in Figs. 5a, 5b, and 5c. Moreover, the percentage increase in the beam's creep deformation during this time frame is summarized in Table 3.The analysis reveals that, irrespective of the boundary conditions, the third lay-up scheme leads to the minimum rate of time-dependent deflections. For instance, in a cantilever sandwich beam, the percentage increase in deformations for lay-up scheme 1, through 4 are 5.99%, 4.87%, 0.59%, and 5.41%, respectively. The corresponding increases in deformation for other boundary conditions are summarized in Table 3.

Table 3
Percentage increase (%) in the long-term deflection of the sandwich beam for different lay-up schemes

Boundary Conditions	Lay-up 1	Lay-up 2	Lay-up 3	Lay-up 4
Clamped-Free	5.99%	4.87%	0.59%	5.41%
Clamped-Clamped	33.48%	24.70%	0.59%	29.36%
Simply supported	24.92%	19.13%	0.59%	25.59%

3.2.2. *Natural frequencies.*

Table 4 shows the first four natural frequencies of sandwich beams for different lay-up schemes and various boundary conditions. It is seen that the natural frequencies are very sensitive with respect to the lay-up scheme chosen for the sandwich beam. Regardless of the type of boundary conditions, lay-up scheme 2 leads to the highest frequency, and lay-up scheme 1 leads to the lowest frequency among other lamination configurations.

As observed in Figs. 8-10, the second viscoelastic layer configuration provides superior damping performance under different boundary conditions, leading to faster dissipation of beam vibrations. For example, for a sandwich beam with a clamped-free boundary condition, vibrations are reduced by more than 99% within 3.96 seconds when using the second configuration. In contrast, the corresponding reduction times for the first, third, and fourth lamination configurations are 4.29, 4.32, and 4.68 seconds, respectively. The results for other boundary conditions are summarized in Table 5.

Table 5.
Effect of different lamination configurations on the vibration decay time

Boundary Conditions	Lay-up 1	Lay-up 2	Lay-up 3	Lay-up 4
Clamped-Free	4.29 s	3.96 s	4.32 s	4.68 s
Clamped-Clamped	2.67 s	2.12 s	2.78 s	2.74 s
Simply supported	2.15 s	1.70 s	2.56 s	2.39 s

3.2.3. Damping capability

The influence of the lay-up configuration on the reduction of dynamic vibrations and the damping behavior of sandwich beams is investigated in this subsection. For the four distinct lay-up schemes shown in Fig. 1, the time history of the beams' maximum deflection is estimated using the finite element simulation. It is worth noting that the analyzed sandwich beams were initially subjected to a predefined initial deformation and subsequently released. The analyzed sandwich beams are assumed to have three different boundary conditions: clamped-free, simply supported, and clamped-clamped. The deflection time-history of sandwich beams with different boundary conditions are shown in Figs. 6a, 6b, and 6c.

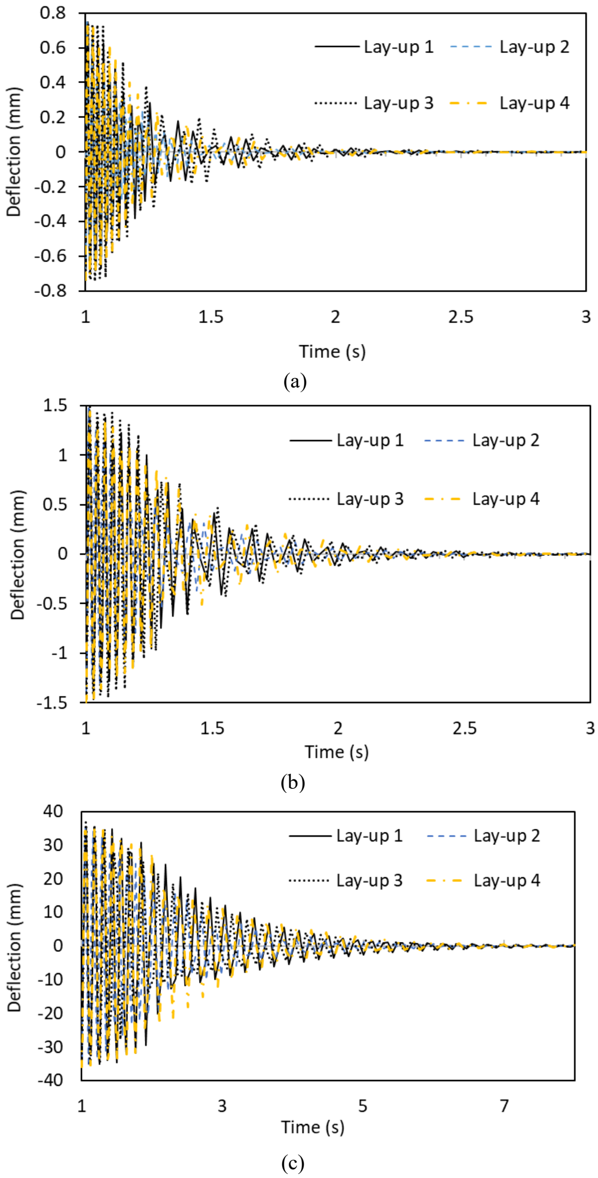

Fig. 6. Effect of lay-up configuration on the time-history response of sandwich beams: (a) clamped-clamped, (b) simply support, (c) clamped-free

3.3. Effect of axial location of PVB layers on creep deformations and damping capability

In the previous section, the optimal placement of the viscoelastic layers across the beam's thickness was investigated. The results indicated that, regardless of the boundary conditions, placing the viscoelastic layers at the central part of the beam's thickness (i.e., lay-up scheme 2) provides the highest damping efficiency. In this section, the effects of axial location of PVB layers on creep deformations and damping capabilities are investigated. Based on the results of Section 3.2, the lamination configuration of all examined sandwich beams of this section is lay-up no. 2 (see Fig. 1).

3.3.1. Creep deformations

For three different configurations of PVB layer placement, the creep deformation of the beam under a uniform distributed load of $2000\ N/m^2$ was evaluated after ten days. The results are illustrated in Figs. 7a, 7b, and 7c. Moreover, the percentage increase in the beam's creep deformation during this time frame is summarized in Table 6.

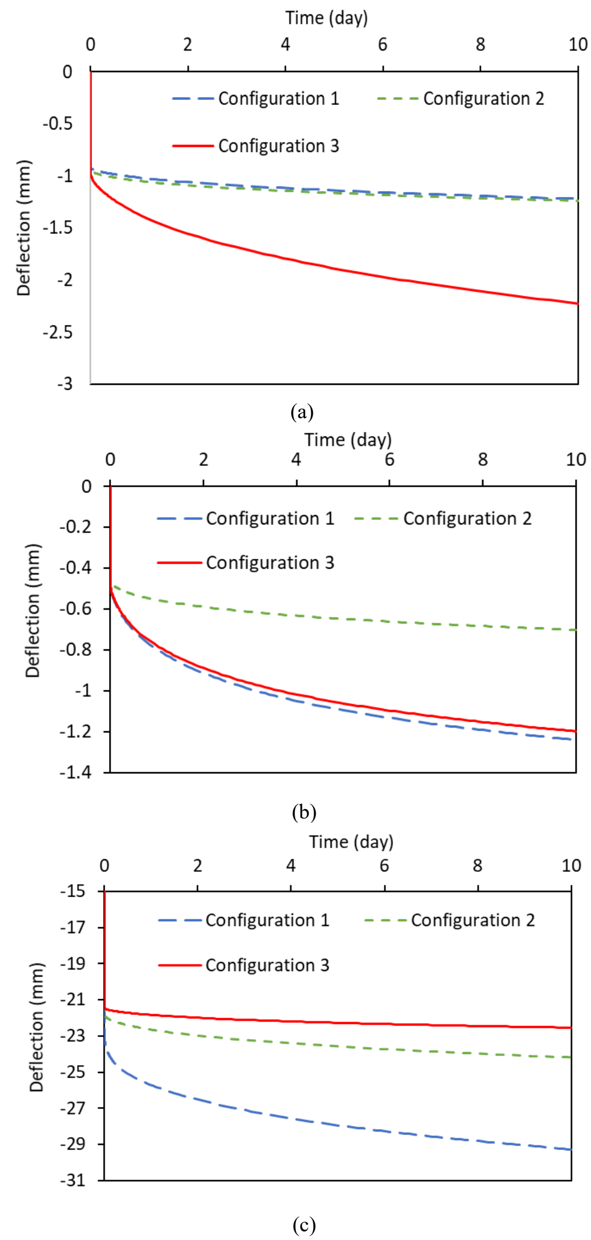

Fig. 7 Effect of the longitudinal position of the PVB layer on the maximum creep deformation of sandwich beam: (a) simply support, (b) clamped-clamped, (c) clamped-free

Table 6.
Percentage increase (%) in long-term deflection of the sandwich beam for different longitudinal positions of the PVB layers

Boundary Conditions	Configuration 1	Configuration 2	Configuration 3
Clamped-Free	25.04	14.60	4.94
Clamped-Clamped	63.86	36.52	63.86
Simply support	33.17	66.86	33.17

Table 6 shows that for simply supported and clamped-clamped sandwich beams, placing the PVB layer within the middle third of the beam's length minimizes the rate of time-dependent creep deflections. In contrast, for clamped-free sandwich beams, the minimum rate of creep deformations occurs when the PVB layer is located in the last third of the beam.

3.3.2. Damping capability

For three different axial locations of the PVB layers shown in Fig. 2, the time-history of the maximum deflection of the beams are estimated using the finite element simulation. The analyzed sandwich beams were subjected to an initial deformation, with various boundary conditions assumed, including clamped-free, simply supported, and clamped-clamped, are assumed for them.

Fig. 8a shows the deflection time history of sandwich beams with clamped-free end conditions. As shown in Figure 19, placing the PVB layer near the free end of the cantilever beam leads to a faster attenuation of transverse vibrations compared to other configurations. The beam vibration amplitude are reduced by more than 99% after 5.82, 5.74, and 5.71 seconds for configurations 1, 2, and 3, respectively. Although the differences in decay times are minor, the results highlight that the damping performance is sensitive to the longitudinal position of the viscoelastic interlayer, with improved performance observed when the layer is placed closer to the free end.

Fig. 8b illustrates the dynamic response of a clamped-clamped sandwich beam under different longitudinal configurations of the PVB layer. Compared to the cantilever beams, the clamped-clamped sandwich beams show significantly faster vibration decay due to increased global stiffness. The vibrations are nearly damped out within 0.4 seconds in all cases. Although differences between the three configurations are minimal, the highest damping is achieved when the PVB layer is positioned in the middle third of the beam.

Fig. 8c shows the deflection time history of a simply supported sandwich beam under different longitudinal configurations of the PVB layer. All configurations demonstrate rapid vibration decay, with displacements significantly reduced within approximately 2.5 seconds. Among the three configurations, configuration 3 (red curve) slightly outperforms the others in damping effectiveness, as it achieves smaller amplitudes sooner. Fig. 8c indicates that placing the PVB layer in the last third closest to the hinged support leads to the greatest damping. When the viscoelastic layer is located in the middle third of the beam, vibrations dissipate by more than 99% after 2.14 seconds. For positions in the first or last thirds of the beam (positions 1 and 3), this value is 2.15 and 2.09 seconds, respectively. This suggests that placing the PVB layer in the last third of the beam contributes to improved energy dissipation for simply supported beams.

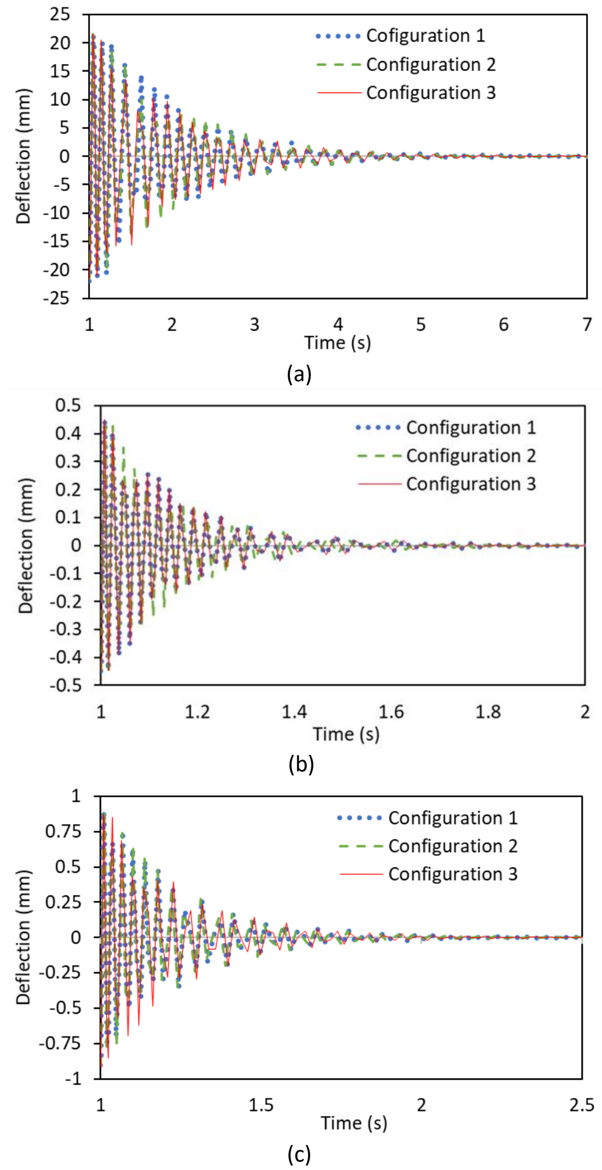

Fig. 8 Effect of axial location of the PVB layer on the time-history response of sandwich beams: (a) clamped-free, (b) clamped-clamped, (c) simply support

These results indicate that the viscoelastic layer's optimal longitudinal positioning strongly depends on the beam’s boundary conditions and correlates with the regions of maximum dynamic deformation. Proper placement of the PVB layer can significantly enhance the damping capacity and reduce the duration of vibrational responses.

4. Conclusion

This study examined the creep and dynamic behaviors of sandwich beams including viscoelastic layers using three-dimensional finite element modeling. Additionally, the study aimed to identify the optimal position of viscoelastic layers through the thickness and along the beam's length to maximize damping performance and minimize creep deformations. The accuracy of the finite element model was confirmed by comparing its results with experimental results available in the literature. The key findings of this research are summarized as follows:

- The developed three-dimensional finite element model demonstrated high accuracy in predicting both the creep behavior and the free vibration of sandwich beams incorporating viscoelastic layers.
- The inclusion of viscoelastic layers had a pronounced impact on the dynamic response of the sandwich beams, notably enhancing their damping capacity.
- Despite improving damping performance under dynamic loads, the viscoelastic layers contributed to creep behavior, resulting in increased long-term deformations under sustained service loads.
- Independent of the sandwich beam's boundary conditions, placing the viscoelastic layer near the neutral axis (i.e., at the mid-thickness) maximizes the damping effect.
- Positioning viscoelastic layers far from the neutral axis of the beam (i.e., at the top and bottom of the host beam) minimizes long-term creep deformations, irrespective of the boundary conditions.
- For clamped-free sandwich beams, placing the viscoelastic layer in the last third of the beam’s length (near the free end) provides the highest damping performance. For simply supported beams, placing the PVB layer in the last third closest to the hinged support leads to improved energy dissipation. In contrast, for the clamped-clamped boundary condition, the optimal damping is achieved when the viscoelastic layer is positioned in the central third of the beam.

References

[1] Harvey Thomas Banks, Shuhua Hu, Zackary R. Kenz, "A Brief Review of Elasticity and Viscoelasticity for Solids", Advances in Applied Mathematics and Mechanics 3(1) (2011): 1-51. https://doi.org/10.4208/aamm.10-m1030

[2] Roderic S Lakes, Viscoelastic solids (1998), CRC press2017.

[3] Laura Galuppi, Gianni Royer-Carfagni, "Laminated beams with viscoelastic interlayer", International Journal of Solids and Structures 49(18) (2012): 2637-2645. https://doi.org/10.1016/j.ijsolstr.2012.05.028

[4] Fessal Kpeky, et al., "Modeling of viscoelastic sandwich beams using solid–shell finite elements", Composite Structures 133 (2015): 105-116. https://doi.org/10.13140/RG.2.1.4092.6565

[5] Nader Mohammadi, Mehrdad Nasirshoaibi, "Simulation of viscoelastic materials by ABAQUS", Mathematical Models in Engineering 1(2) (2015): 67-71.

[6] F. Pelayo, et al., "Study of the time-temperature-dependent behaviour of PVB: Application to laminated glass elements", Thin-Walled Structures 119 (2017): 324-331. https://doi.org/10.1016/j.tws.2017.06.030

[7] Maurizio Froli, Leonardo Lani, "Adhesion, Creep and relaxation Properties of PVB in Laminated Safety Glass", Glass performance days (2011): 218-21.

[8] Christian Ehrich, et al., "Development of a Novel Technique for Mechanical Characterization of Polymer Encapsulates in Laminated Glass Beams", 26th European Photovoltaic Solar Energy Conference and Exhibition, Hamburg, Germany, 2011.

[9] Tomáš Hána, et al., "Experimental and Numerical Study of Viscoelastic Properties of Polymeric Interlayers Used for Laminated Glass: Determination of Material Parameters", Materials 12(14) (2019): 2241. https://doi.org/10.3390/ma12142241

[10] Tomáš Hána, et al., "Four-Point Bending Tests of Double Laminated Glass Panels with EVA Interlayer in Various Loading Rates", Engineering Mechanics (2019): 145-148. https://doi.org/10.21495/71-0-145

[11] Alena Zemanová, et al., "On modal analysis of laminated glass: Usability of simplified methods and Enhanced Effective Thickness", Composites Part B: Engineering 151 (2018): 92-105. https://doi.org/10.1016/j.compositesb.2018.05.032

[12] Y. X. Li, et al., "State-space method for dynamic responses of double beams with general viscoelastic interlayer", Composite Structures 268 (2021): 113979. https://doi.org/10.1016/j.compstruct.2021.113979

[13] Miriam Schuster, et al., "Quantification of the linear viscoelastic behavior of multilayer polymer interlayers for laminated glass", Glass Structures & Engineering 8(4) (2023): 457-469. https://doi.org/10.1007/s40940-023-00229-w

J-Researchers

Journal of Civil Engineering Researchers

Journal homepage: www.journals-researchers.com

Mechanical Performance and Freeze–Thaw Durability of Expansive Clay Stabilized with Graphene Oxide and Fly Ash: A Laboratory Study

Abdolah Ataeifar, [a] Ata Jafary Shalkoohy,[a,*] Payam Eshghi, [a] Hamidreza Ghaderi Niri [b]

[a] Department of Civil Engineering, BaA.C., Islamic Azad University, Bandar Anzali, Iran

[b] Department of Civil Engineering, Qa.C., Islamic Azad University, Qazvin, Iran

ABSTRACT

Expansive clay soils are characterized by their high-water affinity and significant volume changes, which frequently result in structural issues such as swelling, settlement, and cracking, particularly under freeze–thaw (F–T) conditions. This study investigates a dual-stabilization method using fly ash (FA: 5–15%) and graphene oxide (GO: 0.05–0.15%) to enhance the mechanical strength and durability of such soils. After 28 days of curing, samples underwent 3, 6, and 9 F–T cycles, followed by unconfined compressive strength (UCS) testing. Results show that the GO–FA combination significantly improved soil performance, with the optimal mix (10% FA + 0.1% GO) achieving a 76% increase in UCS at zero cycles and reducing strength loss after nine cycles by over 45% compared to untreated soil. These outcomes demonstrate the promise of GO–FA stabilization as a sustainable and effective solution for expansive soils in cold-region geotechnical engineering.

ARTICLE INFO

Received: July 17, 2025
Accepted: September 07, 2025

Keywords:
Expansive Clay
Freeze–thaw Cycles
Graphene Oxide
Fly Ash
Soil Stabilization

DOI: 10.66224/JCER.7.4.88
DOR: 20.1001.1.2538516.2025.7.4.7.9

1. Introduction

Freeze-thaw cycles are among the most important environmental phenomena in cold and temperate regions, directly and significantly affecting the geotechnical behavior of various types of soils, particularly fine-grained soils with high swelling potential. These cycles occur when the ambient temperature alternately passes the freezing point of water, leading to the freezing and then successive thawing of water within the soil mass. As a result of this process, significant changes are created in the microscopic structure, physical and mechanical properties, as well as the engineering performance of the soil.

Expansive soils, such as clay soils with a mineral structure of montmorillonite or illite, have a high capacity for water absorption and volume change due to their specific mineralogical nature and are prone to expansion and contraction behaviors. Under the influence of freeze-thaw cycles, the water in the pores of these soils freezes and increases in volume by about 9%, creating internal stresses in the soil. These stresses can lead to structural failure within the soil, the development of microcracks, and, in the long term, to a reduction in soil integrity. Furthermore, during the thawing phase, the entry of water into the porous soil system, together with a relative decrease in dry density and weakening of interparticle

* Corresponding author. Tel.: +980000000000; e-mail: Ata.jafary@iau.ac.ir.

bonds, reduces the shear and compressive strengths of the soil [1-4]. Experimental evidence from cyclic tests under controlled conditions has shown that after only a few freeze-thaw cycles, shear strength parameters such as the angle of internal friction and cohesion decrease significantly, and the potential for sudden settlements or inelastic deformations in the soil increases.

From a geotechnical engineering perspective, the consequences of this process on the performance of structures built on such soils are significant. For example, in infrastructure such as pavements, railways, surface foundations, and buried piping systems, volume changes due to freezing can lead to local swelling (heave) and then thaw settlement, which over time can cause cracking, misalignment, or costly failures. These effects are more severe in expansive soils because water absorption before freezing is greater, and a higher volume change capacity is created in the cycles. Also, structural erosion caused by the aforementioned cycles reduces the initial impermeability, increases the effective porosity, and ultimately facilitates the movement of water and chemically aggressive substances within the soil. Considering the different dimensions of the impact of these cycles, improvement and modification of the behavior of expansive soils exposed to freezing is an undeniable necessity in civil and infrastructure projects [5-9]. One common method is to use chemical additives such as lime, cement, fly ash, or nanomaterials that, by creating pozzolanic or cementation reactions, strengthen the bonds between soil particles and reduce their sensitivity to temperature and humidity changes [10-12]. Fly ash is a by-product of coal combustion in thermal power plants and has pozzolanic behavior due to its high content of silica (SiO_2), alumina (Al_2O_3), and calcium oxide (CaO). Pozzolanic reactions between fly ash and soil compounds, especially in the presence of water, lead to the formation of cementitious compounds such as hydrated calcium silicate (C–S–H) and hydrated calcium aluminate (C–A–H), which increase the adhesion of soil particles, reduce permeability, and improve the compressive and shear strength of the soil. In addition to mechanical properties, fly ash changes the soil structure from a dispersed state to a compact and cementitious structure by reducing the cation exchange potential and surface water absorption by clay particles. Additionally, due to the alkaline nature of fly ash, the soil pH increases, providing a suitable environment for accelerating pozzolanic chemical reactions. From an environmental and economic perspective, the use of fly ash as a substitute for expensive chemicals such as lime or cement has significant advantages. As an industrial waste, this material causes environmental pollution if not used properly. However, if scientifically exploited in soil improvement projects, not only are geotechnical problems solved, but also a sustainable use cycle of waste materials is established [13-17].

In recent decades, the emergence of nanotechnology, and especially the application of carbon nanomaterials such as carbon nanotubes (CNTs), graphene and its derivatives, and carbon black nanoparticles, has opened new horizons in advanced soil improvement. Due to their unique physical and chemical properties, including very high specific surface area, high Young's modulus, significant thermal and electrical conductivity, and remarkable chemical stability, carbon nanomaterials have the ability to interact effectively with soil particles. When these nanomaterials are added to soil, based on microscopic and spectroscopic studies, it has been observed that they increase structural cohesion, reduce permeability, and improve soil shear strength by creating physical and chemical bonds with clay particles. One of the most important mechanisms of action of carbon nanomaterials is to fill the empty space between soil particles and strengthen interparticle bonds [18-22]. Carbon nanotubes penetrate the space between fine soil particles and act like reinforcing strips, reducing deformability and increasing soil hardness. On the other hand, the presence of carbon nanomaterials can accelerate the hydration process of cement or other additives, and when combined with pozzolanic materials, improve the chemical reactions of geopolymers [23-25]. Graphene Oxide (GO) is one of the newest carbon nanomaterials that has been considered as an innovative additive in engineering soil improvement in recent years. This material, which is an oxidized derivative of graphene and has a two-dimensional structure with active functional groups such as hydroxyl, epoxy, and carboxyl, has the ability to interact effectively with soil particles due to its high specific surface area, suitable polarity, and stability in aqueous environments, and can cause significant changes in their physical and mechanical properties [26-29].

Numerous studies have shown that adding very small amounts of graphene oxide leads to a significant improvement in compressive and shear strength, reduced permeability, improved compressibility, and increased volumetric stability in expansive clay soils. The mechanism of action of graphene oxide is based on increasing interparticle bonds and creating reinforcing microscopic networks between soil particles. This nanomaterial, by being placed in the space between fine-grained particles, increases adhesion and cohesion between them and transforms the dispersed structure of clay soils into a flocculated and dense structure. The presence of active functional groups on the surface of graphene oxide provides suitable reactivity conditions for the formation of hydrogen and ionic bonds with the surface of soil particles, which results in increased hardness, elastic modulus, and chemical stability of the soil. In addition, due to the polar

Table 1.
Summary of research on the role of fly ash and graphene oxide in soil improvement

R	Year	Type of additive	Percent of additive (%)	Results	References
1	2004	Fly ash	0 – 46	Fly ash addition lowers soil dry density, increases void ratios and porosity, and enhances shear strength nonlinearly	[35]
2	2005	Fly ash	0 – 20	High calcium fly ash forms tobermorite, enhancing the density and stability of the soil	[36]
3	2006	Fly ash	0 – 20	Due to the lower specific gravity of the fly ash than that of the soil, the maximum dry density decreased, and the optimum moisture content increased with increasing fly-ash content	[37]
4	2007	Fly ash	0 – 16	The compressive strength of sludge ash/soil was less than fly ash/soil. The bearing capacities for both fly ash/soil and sludge ash/soil were five to six times and four times, respectively, higher than the original capacity	[38]
5	2012	Fly ash	0 – 25	The UCS and CBR values increased by adding optimum fly ash content and lime	[39]
6	2015	Graphene oxide (GO)	0 – 0.5	GO altered the morphology of geopolymers from a porous nature to a substantially pore-filled morphology with increased mechanical properties	[40]
7	2016	Fly ash	0 – 10	Bearing capacity of soft soil can be improved substantially, and swell can be reduced significantly by using Class C fly ash	[41]
8	2016	Graphene oxide (GO)	0 – 0.1	GO reduced soil plasticity and compressibility while increasing tensile and shear strength of the treated soil	[42]
9	2017	Graphene oxide (GO)	0 – 0.1	The addition of GO into the soil generally decreased the soil's void ratio under a given hydrostatic consolidation pressure, while increasing its undrained shear strength	[43]
10	2018	Fly ash	0 – 50	Incorporation of biocement in fly ash It is an effective means of increasing the strength of expansive soils	[44]
11	2020	Fly ash	0 – 9	When Microbially induced carbonate precipitation (MICP)-treated sand mixed with Fly ash, the deviator stress increased, caused by the bonding of precipitated $CaCO_3$ in MICP	[45]
12	2021	Graphene oxide (GO)	0 – 0.12	The SEM results showed that due to the synergistic filling effect and hydration effect of cement/GO, the microstructure was denser, and the characteristics of cracks were refined	[46]
13	2021	Graphene oxide (GO)	0 – 0.1	As the curing time of graphene oxide increases, the soil compressibility (Cc and Cs) decreases. The coefficient of consolidation (Cv) decreases as the curing time of graphene oxide increases	[47]
14	2023	Graphene oxide (GO)	0 – 0.1	The addition of graphene oxide significantly improved the UCS with a substantial reduction in failure strains, showing relatively brittle behavior	[48]
15	2023	Fly ash	0 – 30	Increasing the sawdust ash/high calcium fly ash (HCFA/SDA) mixture and cement content enhanced expansive soil properties while lowering the liquid limit (LL) and plasticity index (PI)	[49]
16	2024	Graphene oxide (GO)	0 – 0.1	SEM test results reveal that due to nucleation effects, GO promotes the generation of hydration product C-S-H, enhancing the resistance of cement soil samples to external salt erosion	[50]
17	2024	Graphene oxide (GO)	0 – 0.05	GO improves stiffness and reduces energy consumption and damping ratio in modified coastal cement soil	[51]
18	2024	Graphene oxide (GO)	0 – 0.06	The effect of GO and its strong bonding with the cement matrix significantly improved the microstructure of the specimens by reducing pores and defects	[52]
19	2024	Graphene oxide (GO)	0 – 0.1	The GO-incorporated hydrophobic geopolymer exhibits a compressive strength comparable to the unmodified geopolymer	[53]
20	2025	Graphene oxide (GO)	0 – 0.02	GO improved the compressive strength of alkali-activated fly ash-based geopolymer and reduced the decrease in compressive strength over freeze-thaw cycles	[54]

and highly hydrophilic properties of graphene oxide, this material absorbs and stabilizes water in the micropores of the soil and significantly prevents the swelling and shrinkage of soils sensitive to moisture changes [30-34].

Given the positive properties of fly ash and graphene oxide in soil improvement, researchers have drawn attention to studying and evaluating their role in improving the geotechnical properties of problematic soils, especially fine-grained soils. Table 1 summarizes the most important

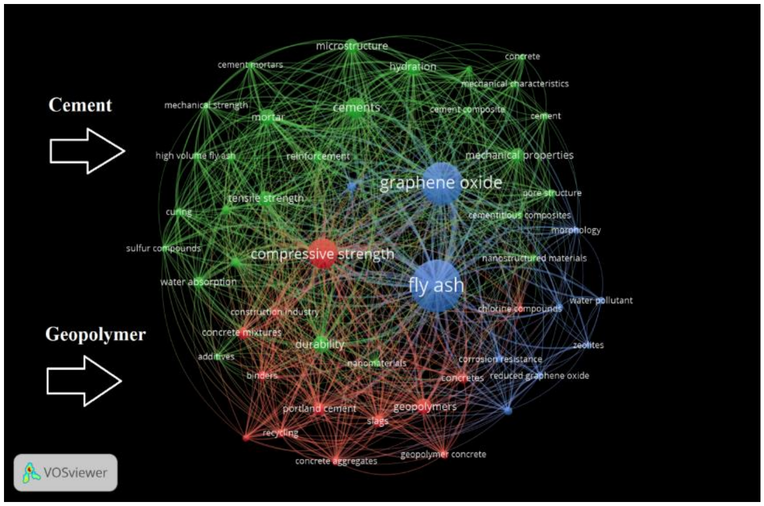

Fig. 1. Co-occurrence analysis of scientific terms in studies of GO and fly ash related to the construction field

research conducted on the effect of fly ash and graphene oxide on the geotechnical properties of soils. This table includes information on the type of additive and the optimal percentage of the material used, and the key results of each study.

In recent years, with the exponential growth of scientific production in various fields, the need for analytical tools to better understand the structure, process, and impact of scientific studies has increased. Bibliometric analysis, as one of the most important quantitative methods in the evaluation of scientific and research information, allows for the systematic examination of scientific publications, collaboration patterns, citation networks, and conceptual evolution in a specific field. This type of analysis, using bibliographic data extracted from reliable databases such as Web of Science, Scopus, or Dimensions, allows researchers to identify and analyze the dynamics of knowledge production, key researchers, leading institutions, and emerging topics. One of the prominent and widely used tools in the field of bibliometric data analysis and visualization is the VOSviewer software, developed by the Center for Science and Technology Studies at Leiden University in the Netherlands. This free software, using clustering and network drawing algorithms, has a high ability to graphically display relationships between data. VOSviewer's main capabilities include drawing co-authorship maps, co-occurrence maps, co-citation maps, and bibliographic coupling maps, each of which displays some type of relationship between bibliographic elements such as authors, institutions, countries, keywords, and articles.

Fig. 1 is the output of bibliometric analysis using VOSviewer software, which displays a network of synonyms in the field of research related to fly ash and graphene oxide, based on data extracted from scientific databases. In this map, each node represents a frequently occurring keyword in scientific texts, and the size of the nodes is determined in proportion to the frequency of use of that word in different articles. The links between nodes represent the intensity of their co-occurrence in a document, and the color clustering is the result of the VOSviewer clustering algorithm, which places related topics together based on conceptual relationships. In this network structure, three main color clusters can be seen: the blue cluster, which is centered around keywords such as fly ash, graphene oxide, cementitious composites, nanostructured materials, and reduced graphene oxide, and represents the field of research related to nanomaterials and new cementitious compounds; The green cluster, which includes concepts such as microstructure, hydration, cements, mechanical strength, tensile strength, and cement mortars, indicates the focus of research on microscopic behavior, hydration processes, and mechanical properties of mortars and cement; and the red cluster, which includes concepts such as compressive strength, durability, geopolymers, concrete aggregates, slags, and recycling, focuses on the field of durability, the use of alternative materials, recycled concrete, and geopolymer systems. A careful examination of the position of graphene oxide and fly ash in this map shows that these two terms not only have the highest frequency and the highest connection with other concepts, but also play a role as the central core of many researches in the field of modern building materials. The strong connection of these two terms with terms such as compressive strength, cementitious composites, durability, nanomaterials, and mechanical properties indicates the extensive focus of scientific studies on their application in improving the physical and mechanical properties of building materials. However, it is very striking in this analysis that throughout this conceptual network, no terms related to soil, geotechnical engineering, soil stabilization, clay soils, or concepts related to soil improvement are seen.

This apparent absence in the map vocabulary indicates that despite the widespread use of these two materials in the field of concrete, cement mortars, and even geopolymer compounds, their application in the field of soil improvement has not been seriously and organizedly reflected in the scientific literature. On the other hand, concepts such as geopolymer and geopolymer concrete, which are in the red cluster, although they are present in the map, the relatively small size of the nodes and their peripheral position in the network structure indicate that this field is still in the early stages of growth and development and has not yet reached the stage of study saturation. This indicates that research on geopolymers, despite their high potential, is still in a secondary position compared to studies on traditional cementitious systems. Overall, the presented analysis of this bibliometric picture reveals that although the application of fly ash and graphene oxide in the cement and concrete industry has reached relative maturity and has occupied a large part of the scientific literature, areas such as geopolymers and especially geotechnical engineering are still not saturated in terms of research, and this issue can be considered as a serious scientific gap and at the same time a valuable research opportunity to expand the frontiers of knowledge in the future.

2. Significance and Novelty of the Study

Expansive soils pose one of the most persistent challenges in geotechnical engineering due to their severe shrink–swell behavior under seasonal moisture fluctuations. This behavior often results in structural instability, foundation damage, and costly maintenance in infrastructure projects, particularly in cold regions where freeze–thaw cycles exacerbate the problem. While various chemical stabilizers have been used to improve the strength and deformation characteristics of expansive clays, their long-term performance under harsh environmental conditions remains a critical concern. Therefore, exploring durable, cost-effective, and environmentally responsible additives has become a key research priority in sustainable ground improvement.

This study introduces a dual-stabilization approach using graphene oxide and fly ash, aiming not only to improve the mechanical behavior of expansive clay but also to enhance its freeze–thaw durability, an aspect that has received limited attention in the literature. The novelty of this work lies in the systematic evaluation of UCS, elastic modulus (E50), and stress–strain responses under successive F–T cycles, which provides a comprehensive understanding of both strength enhancement and long-term degradation behavior. Furthermore, the use of nano-scale GO in combination with industrial by-product FA offers a promising synergy between high-performance nanomaterials and sustainable geotechnical practices.

3. Materials used

3.1. Soil

In this research, a type of expansive clay soil was selected, which is widely recognized for presenting critical challenges in geotechnical applications. Its tendency to undergo considerable volumetric changes upon moisture variation makes it highly susceptible to shrinkage and swelling, potentially compromising the stability of overlying structures. The particle size distribution of the selected clay was analyzed based on ASTM D422 standards [55], and its key physical properties are summarized in Table 2.

Table 2.
Physical characteristics of the expansive clay studied

Property	Value	Unit	Standard
Gs	2.65	Dimensionless	ASTM D854 [56]
LL	146.2	%	ASTM D4318 [57]
PL	43.9	%	ASTM D4318 [57]
PI	102.3	%	ASTM D4318 [57]
MDUW	14.7	KN/m³	ASTM D698 [58]
OMC	24.6	%	ASTM D698 [58]

3.2. Graphene oxide powder

Graphene oxide has been utilized as a nanomaterial to enhance the engineering properties of expansive soil in the present research. Due to its unique two-dimensional structure, high specific surface area, and the presence of active functional groups, graphene oxide has the potential to improve the soil's mechanical properties and reduce its swellability. This material interacts with soil particles and modifies the soil structure through physical and chemical bonding. The specifications of the graphene oxide used in this study are presented in Table 3.

Table 3.
Characteristics of graphene oxide used

Specification	Unit	Value
Appearance	-	Powder
Color	-	Grey - Black
Density	(g/cm3)	1.9-2.2
Specific Surface Area	(m^2/gr)	1000-15000
Abbreviation	-	GO

3.3. Fly Ash powder

In this study, a processed fly ash known commercially as Pozzocrete 63, manufactured by Dirk India Pvt. Ltd., was used. This artificial pozzolanic material is derived from coal-fired power plants and undergoes industrial treatment to produce a finely divided, uniform powder. Its chemical composition is rich in silica and alumina, contributing to its favorable pozzolanic reactivity. These properties enhance the bonding within the cementitious matrix, reduce permeability, and improve the mechanical performance of the final product. Due to its consistent physical characteristics and controlled quality, Pozzocrete 63 is considered a suitable additive in various civil engineering applications, including soil stabilization, special concretes, and engineered mortars.

3.4. Sample Preparation and Experimental Program Design

The primary objective of this study is to evaluate the strength improvement of expansive clay through stabilization using fly ash (FA) and graphene oxide (GO). For specimen preparation, the soil was first oven-dried and sieved through a No. 40 mesh. Then, fly ash was blended with the dry soil at predetermined weight percentages. Based on the results of the Standard Proctor compaction test, the optimum moisture content was gradually added to the mixture in stages, followed by mechanical mixing for 10 minutes. This process was repeated for samples containing varying percentages of graphene oxide as well as for combined mixtures of FA and GO. The blended materials were then used to fabricate cylindrical specimens with a diameter of 38 mm and a height of 76 mm. Each specimen was compacted in four layers inside lubricated steel molds, with each layer receiving four uniform blows. After compaction, the specimens were carefully demolded and immediately sealed in plastic bags to preserve moisture and allow for 28 days of curing under controlled conditions. Unconfined compressive strength (UCS) tests were performed in accordance with ASTM D2166 [59]. To evaluate the influence of freeze–thaw cycling, the cured samples were subjected to 3, 6, and 9 cycles using a specialized freezer.

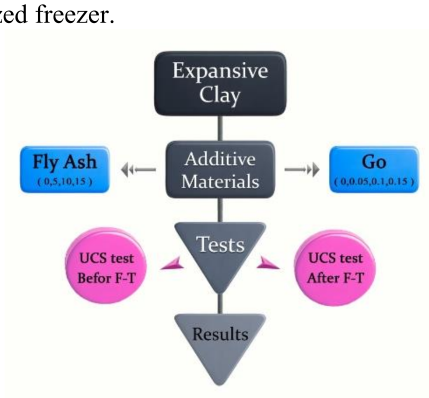

Fig. 2. Schematic representation of the experimental procedure followed in this study

For the freezing stage, the specimens were placed at temperatures ranging from −15°C to −20°C, while thawing was conducted at 20°C or ambient temperature [60,61]. The mix designs and experimental variables are summarized in the following tables. The tested FA contents were 5%, 10%, and 15% by weight, and GO contents were 0.05%, 0.10%, and 0.15% by weight. These percentages were selected based on typical ranges reported in the literature. The overall experimental procedure is illustrated in Fig. 2.

4. Results and Discussion

4.1. Improvement of UCS Using GO and FA under F–T Cycles

The variations in unconfined compressive strength (UCS) of the samples containing graphene oxide (GO) and fly ash (FA) under different freeze–thaw cycles are presented in Fig.3. According to the results, at each fixed percentage of fly ash, increasing the amount of graphene oxide leads to a noticeable improvement in compressive strength. This trend suggests that GO effectively contributes to the mechanical reinforcement of the soil by enhancing interparticle bonding and improving structural cohesion. Among all the tested combinations, the sample with 10% fly ash and 0.1% graphene oxide exhibited the highest strength, showing an increase of approximately 76% compared to the untreated expansive clay. This superior performance can be attributed to the synergistic effect of the pozzolanic activity of fly ash and the stabilizing action of graphene oxide, which together enhance interparticle adhesion and reduce detrimental porosity. As the number of freeze–thaw cycles increases, a gradual reduction in strength is observed across all specimens, which is a typical behavior in soils subjected to thermal cycling. Repeated freezing and thawing induce volumetric stresses within the soil mass, leading to the degradation of mechanical bonds and partial disintegration of the compacted structure. However, the inclusion of GO and FA mitigates the severity of this decline. The slower rate of strength loss in treated samples suggests that the additives play an important role in limiting the damage induced by freeze–thaw actions [53,62].

4.2. Stress–Strain Behavior of Optimized Soil Under Freeze–Thaw Cycles

Fig. 4 shows the stress–strain curves of the optimized soil samples subjected to different freeze-thaw cycles (0, 3, 6, and 9 cycles). These curves are used to examine the failure mode and ductility of the samples. At cycle zero, the curves exhibit more brittle behavior characterized by high peak strength and low failure strain. With an increasing number of cycles, the curve characteristics gradually change, and the material behavior tends to

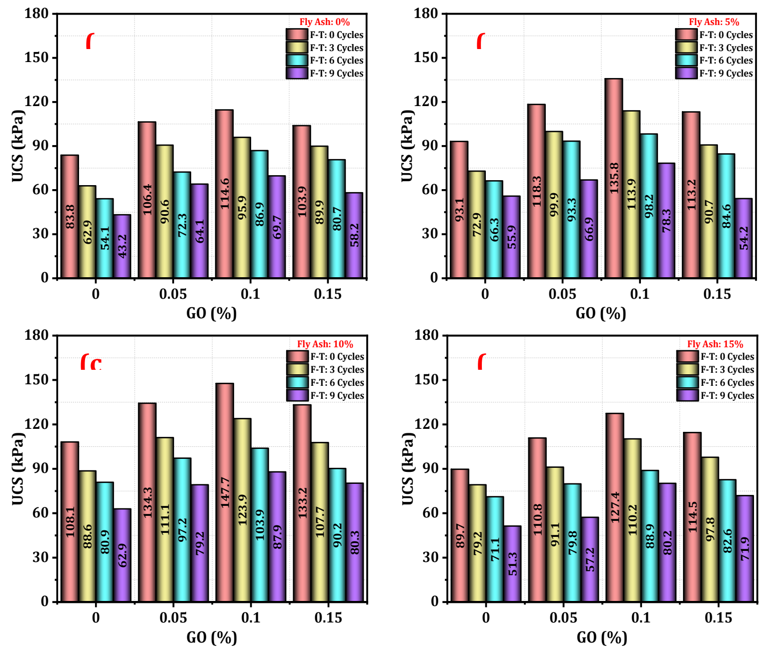

Fig. 3. Variations in UCS of expansive clay containing different percentages of GO under various F-T cycles, for: (a) 0% fly ash, (b) 5% fly ash, (c) 10% fly ash, and (d) 15% fly ash

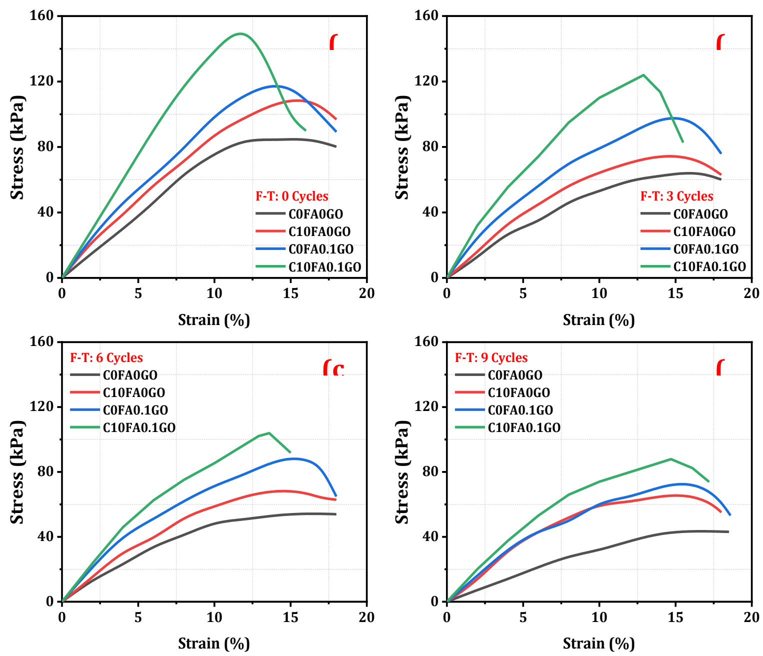

Fig. 4. Effect of the number of freeze–thaw cycles on the stress–strain behavior of the optimized samples: (a) 0 cycles, (b) 3 cycles, (c) 6 cycles, (d) 9 cycles

become softer. The reduction in peak stress and the relative increase in failure strain in subsequent cycles indicate that the soil has shifted from a quasi-brittle state toward a more ductile behavior. This behavioral change can be directly attributed to the destructive effects of the freeze-thaw cycles. With each freezing event, the water in the pores expands and exerts pressure on the soil's internal walls. These repeated pressures eventually cause microcracks, deterioration of inter-particle bonds, and a reduction in microstructure cohesion. However, samples modified with graphene oxide (GO) and fly ash (FA), compared to those without additives, experience a more controlled reduction in strength while maintaining adequate ductility. These features are highly important from a geotechnical design perspective, as materials that maintain strength while allowing greater deformation exhibit more stable performance under various loadings. In summary, the addition of GO and FA not only helps increase material strength but also improves post-peak behavior by reducing the soil structure's sensitivity to freeze-thaw induced damage, an issue of great significance in construction projects in cold regions [48,51].

4.3. Effect of GO and Fly Ash on the E50 of Expansive Clay During Freeze–Thaw Cycling

Fig. 5 illustrates the variations in the initial elastic modulus (E50) of expansive clay treated with different percentages of graphene oxide (GO) and fly ash (FA) under successive freeze–thaw cycles. The E50 parameter represents the soil's initial stiffness within small strain ranges and plays a critical role in the performance assessment of geotechnical structures under service conditions, such as embankments, retaining walls, and subgrade layers. According to the results, in the absence of freeze–thaw exposure (cycle 0), the inclusion of GO significantly increases the E50 values across all levels of fly ash. This improvement can be attributed to enhanced soil compressibility, improved interparticle contact, and a reduction in effective porosity, all resulting from the structural modification induced by GO. As freeze–thaw cycles progress, a gradual reduction in E50 is observed, primarily due to the deterioration of internal bonding, the formation of microcracks, and the increased heterogeneity within the soil matrix caused by thermal stresses. Nonetheless, samples incorporating higher FA contents demonstrate better retention of stiffness. This behavior is closely linked to the formation of secondary cementitious compounds through pozzolanic reactions between fly ash and soil constituents, which contribute to structural stability and mitigate the propagation of freeze-induced cracking. Notably, in specimens with 10% and 15% FA, the E50 values remain within an acceptable range even after extended cycling, indicating a favorable structural response under repeated thermal loading. These findings highlight the significance of selecting optimal GO and FA contents in designing geotechnical materials resilient to freeze–thaw conditions. It is also worth noting that the loss in stiffness caused by cyclic freezing and thawing may, in some cases, exceed the reduction in peak strength. This underscores the greater sensitivity of elastic response characteristics to environmental degradation, especially under early-stage loading conditions [63-65].

4.4. Durability of Expansive Clay Treated with GO and FA Under Freeze–Thaw Cycles

Fig. 6 illustrates the reduction ratio of unconfined compressive strength (UCS) in various samples containing graphene oxide (GO) and fly ash (FA) subjected to successive freeze–thaw cycles. This parameter serves as a direct indicator of the mechanical durability of soils under harsh environmental conditions, particularly in cold regions. The results indicate that incorporating GO at all FA levels effectively reduces the rate of strength loss. In other words, GO contributes to stabilizing the soil structure against degradation induced by freeze–thaw actions. Its role can be attributed to enhancing interparticle bonding, reducing permeability, and limiting the propagation of

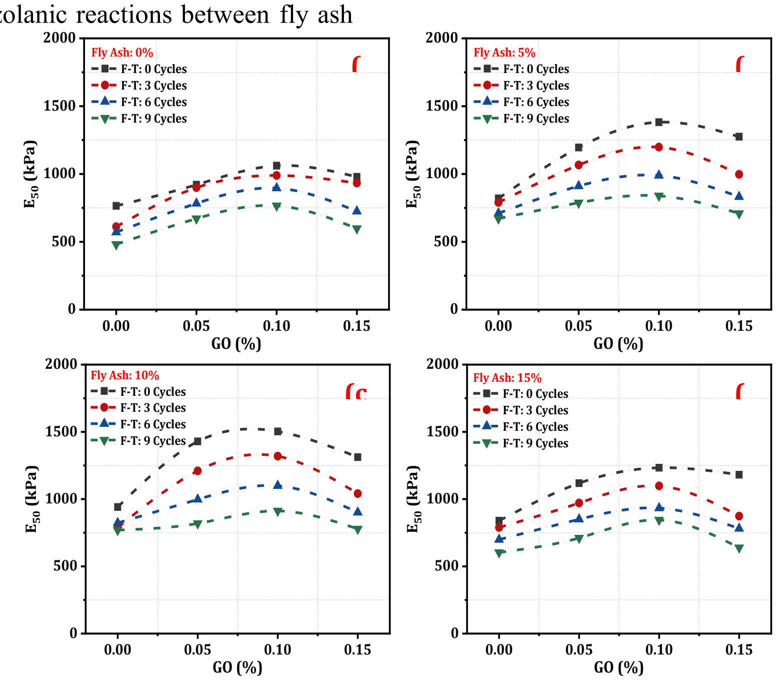

Fig. 5. Variations in E50 of expansive clay containing different percentages of GO under various F-T cycles, for: (a) 0% fly ash, (b) 5% fly ash, (c) 10% fly ash, and (d) 15% fly ash

microcracks, all of which collectively delay the onset and progression of structural deterioration. Nevertheless, the most significant impact on mitigating strength loss is associated with the presence of fly ash. Increasing the FA content, especially to 10% and 15%, leads to a considerable reduction in the UCS loss ratio. This improvement is primarily due to the pozzolanic nature of FA, which reacts with active soil components to form secondary cementitious phases. These reaction products fill pore spaces, reduce effective porosity, and ultimately enhance the structural integrity of the treated soil. Notably, in specimens with higher FA content, the rate of strength reduction becomes more gradual and stable beyond the sixth freeze–thaw cycle, suggesting a progressive structural development and stabilization of pozzolanic reactions within the soil matrix. From an engineering perspective, materials that exhibit lower strength loss under freeze–thaw cycling are more suitable for use in pavement subgrades, embankments, earth dams, and other geotechnical structures exposed to temperature fluctuations. Accordingly, a blend of GO with 10% to 15% fly ash is recommended as an effective strategy for enhancing the cyclic durability of soils in cold and frost-prone environments [66-68].

5. Conclusion

This study evaluated the mechanical performance and freeze–thaw durability of expansive clay stabilized with varying contents of graphene oxide (GO) and fly ash (FA). A series of laboratory tests, including unconfined compressive strength (UCS), stress–strain behavior, and elastic modulus (E50), were conducted on samples subjected to 0, 3, 6, and 9 freeze–thaw cycles. The analysis aimed to understand how these additives influence strength development, stiffness retention, and long-term degradation under cyclic thermal loading. Based on the experimental findings, the following conclusions can be drawn:

- The combined use of graphene oxide and fly ash significantly enhanced the unconfined compressive strength of expansive clay. The most effective performance was observed in the sample containing 10% FA and 0.1% GO, which showed approximately 76% higher UCS compared to untreated soil.
- GO contributed to improved interparticle bonding and microstructural stability, while FA provided long-term benefits through pozzolanic reactions and secondary cementation.
- As the number of freeze–thaw cycles increased, all samples exhibited reduced peak strength and increased failure strain, indicating a transition from brittle to more ductile behavior. However, treated samples showed more stable post-peak performance and better deformation capacity.
- The E50 values showed initial improvement due to GO and FA addition, with better stiffness retention in samples containing 10% and 15% FA even after repeated cycles. This highlights the role of FA in enhancing the soil's resistance to structural degradation.

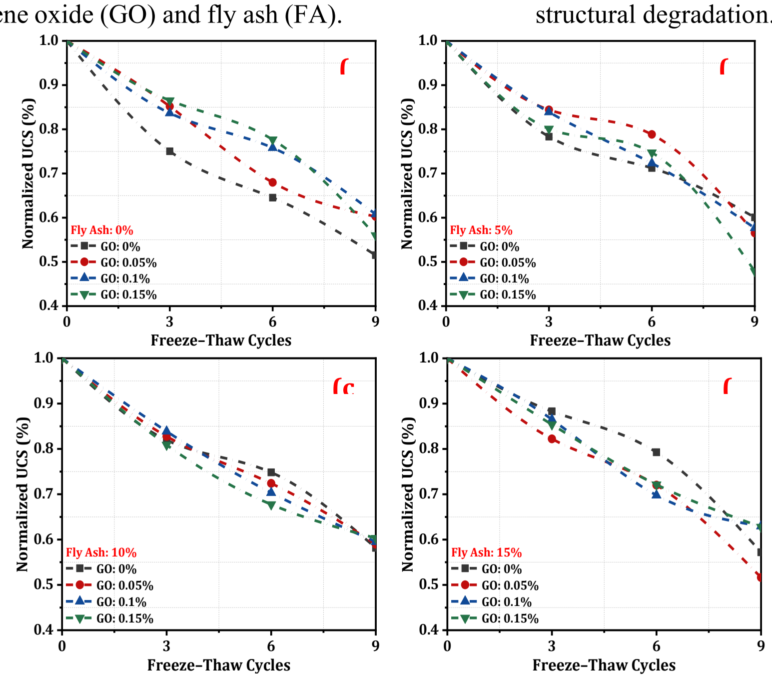

Fig. 6. Reduction ratio of unconfined compressive strength in samples containing various percentages of graphene oxide under different freeze–thaw cycles for: (a) 0% fly ash, (b) 5% fly ash, (c) 10% fly ash, and (d) 15% fly ash

- The reduction in elastic stiffness under freeze–thaw conditions was in some cases more pronounced than the loss in strength, underscoring the importance of evaluating both parameters in durability assessments.
- Durability, as measured by the UCS loss ratio, was significantly improved in samples with higher FA content. Beyond six freeze–thaw cycles, the rate of strength loss became more gradual in these mixtures, indicating stabilization of the internal soil structure.
- Overall, the use of GO in combination with 10–15% FA is recommended as a practical and effective solution for enhancing both the mechanical performance and long-term freeze–thaw durability of expansive soils in geotechnical applications, particularly in cold regions.

References

[1] Chen, L., F. Ming, X. Zhang, X. Wei, and Y. Liu. "Comparison of the hydraulic conductivity between saturated frozen and unsaturated unfrozen soils." International Journal of Heat and Mass Transfer 165 (2021): 120718. https://doi.org/10.1016/j.ijheatmasstransfer.2020.120718

[2] Sun, L., X. Chang, X. Yu, G. Jia, L. Chen, Y. Wang, and Z. Liu. "Effect of freeze-thaw processes on soil water transport of farmland in a semi-arid area." Agricultural Water Management 252 (2021): 106876. https://doi.org/10.1016/j.agwat.2021.106876

[3] Wang, H. X., Z. Z. Wu, Y. Z. Tan, X. Z. Cui, Q. J. Zuo, L. H. Wang, and L. Q. Lu. "Characteristics of pore structure of stabilized/solidified sediments during freeze–thaw cycles." Construction and Building Materials 259 (2020): 119804. https://doi.org/10.1016/j.conbuildmat.2020.119804

[4] Shastri, A., M. Sánchez, X. Gai, M. Y. Lee, and T. Dewers. "Mechanical behavior of frozen soils: Experimental investigation and numerical modeling." Computers and Geotechnics 138 (2021): 104361. https://doi.org/10.1016/j.compgeo.2021.104361

[5] Lin, J., W. Zou, Z. Han, Z. Zhang, and X. Wang. "Structural, volumetric and water retention behaviors of a compacted clay upon saline intrusion and freeze-thaw cycles." Journal of Rock Mechanics and Geotechnical Engineering 14.3 (2022): 953-966. https://doi.org/10.1016/j.jrmge.2021.12.012

[6] Qi, J., P. A. Vermeer, and G. Cheng. "A review of the influence of freeze-thaw cycles on soil geotechnical properties." Permafrost and Periglacial Processes 17.3 (2006): 245-252. https://doi.org/10.1002/ppp.559

[7] Wu, G., Y. Xie, J. Wei, and X. Yue. "Freeze-thaw erosion mechanism and preventive actions of highway subgrade soil in an alpine meadow on the Qinghai-Tibet Plateau." Engineering Failure Analysis 143 (2023): 106933. https://doi.org/10.1016/j.engfailanal.2022.106933

[8] Ng, C. W. W., Z. Li, Q. Zhang, S. Zhang, and Y. Wang. "Effects of soil structure on cyclic freeze-thaw induced volumetric behavior using a modified double-cell triaxial system." Cold Regions Science and Technology 203 (2022): 103648. https://doi.org/10.1016/j.coldregions.2022.103648

[9] Leuther, F. and S. Schlüter. "Impact of freeze–thaw cycles on soil structure and soil hydraulic properties." Soil 7.1 (2021): 179-191. https://doi.org/10.5194/soil-7-179-2021

[10] Barman, D. and S. K. Dash. "Stabilization of expansive soils using chemical additives: A review." Journal of Rock Mechanics and Geotechnical Engineering 14.4 (2022): 1319-1342. https://doi.org/10.1016/j.jrmge.2022.02.011

[11] Ikeagwuani, C. C. and D. C. Nwonu. "Emerging trends in expansive soil stabilisation: A review." Journal of Rock Mechanics and Geotechnical Engineering 11.2 (2019): 423-440. https://doi.org/10.1016/j.jrmge.2018.08.013

[12] Zada, U., A. Jamal, M. Iqbal, S. M. Eldin, M. Almoshaogeh, S. R. Bekkouche, and S. Almuaythir. "Recent advances in expansive soil stabilization using admixtures: current challenges and opportunities." Case Studies in Construction Materials 18 (2023): e01985. https://doi.org/10.1016/j.cscm.2023.e01985

[13] Shaheen, S. M., P. S. Hooda, and C. D. Tsadilas. "Opportunities and challenges in the use of coal fly ash for soil improvements–a review." Journal of Environmental Management 145 (2014): 249-267. https://doi.org/10.1016/j.jenvman.2014.07.005

[14] Noaman, M. F., M. A. Khan, K. Ali, and A. Hassan. "A review on the effect of fly ash on the geotechnical properties and stability of soil." Cleaner Materials 6 (2022): 100151. https://doi.org/10.1016/j.clema.2022.100151

[15] Ahmad, S., M. S. A. Ghazi, M. Syed, and M. A. Al-Osta. "Utilization of fly ash with and without secondary additives for stabilizing expansive soils: A review." Results in Engineering (2024): 102079. https://doi.org/10.1016/j.rineng.2024.102079

[16] Alterary, S. S. and N. H. Marei. "Fly ash properties, characterization, and applications: A review." Journal of King Saud University-Science 33.6 (2021): 101536. https://doi.org/10.1016/j.jksus.2021.101536

[17] Zimar, Z., D. Robert, A. Zhou, F. Giustozzi, S. Setunge, and J. Kodikara. "Application of coal fly ash in pavement subgrade stabilisation: A review." Journal of Environmental Management 312 (2022): 114926. https://doi.org/10.1016/j.jenvman.2022.114926

[18] Khodabandeh, M. A., G. Nagy, and Á. Török. "Stabilization of collapsible soils with nanomaterials, fibers, polymers, industrial waste, and microbes: Current trends." Construction and Building Materials 368 (2023): 130463. https://doi.org/10.1016/j.conbuildmat.2023.130463

[19] Ghasabkolaei, N., A. J. Choobbasti, N. Roshan, and S. E. Ghasemi. "Geotechnical properties of the soils modified with nanomaterials: A comprehensive review." Archives of Civil and Mechanical Engineering 17.3 (2017): 639-650. https://doi.org/10.1016/j.acme.2017.01.010

[20] Chaudhary, V., J. S. Yadav, and R. K. Dutta. "Durability performance of soil stabilized with nano additive's: a review." Indian Geotechnical Journal (2024): 1-13. https://doi.org/10.1007/s40098-024-00906-9

[21] Mathur, R. B., B. P. Singh, and S. Pande. "Carbon nanomaterials: synthesis, structure, properties and applications." Taylor & Francis (2016). https://doi.org/10.1201/9781315371849

[22] Taha, M. R., J. M. Alsharef, T. A. Khan, M. Aziz, and M. Gaber. "Compressive and tensile strength enhancement of soft soils using nanocarbons." Geomechanics and Engineering 16.5 (2018): 559-567. https://doi.org/10.12989/gae.2018.16.5.559

[23] Al-Mansob, R. A., L. Y. Jia, J. Alsharef, T. M. Jassam, J. L. Ng, S. I. A. Ali, and S. B. Surol. "Effects of carbon-nanotube and lime on the weak soil stability." In AIP Conference Proceedings 2401.1 (2021). AIP Publishing. https://doi.org/10.1063/5.0073028

[24] Kumar, A. and S. Sinha. "Support vector machine-based prediction of unconfined compressive strength of Multi-Walled Carbon nanotube doped soil-fly ash mixes." Multiscale and

Multidisciplinary Modeling, Experiments and Design 7.6 (2024): 5365-5386. https://doi.org/10.1007/s41939-024-00524-1

[25] Kishore, K., M. N. Sheikh, and M. N. Hadi. "Doped multi-walled carbon nanotubes and nanoclay based-geopolymer concrete: An overview of current knowledge and future research challenges." Cement and Concrete Composites (2024): 105774. https://doi.org/10.1016/j.cemconcomp.2024.105774

[26] Hansora, D. P., N. G. Shimpi, and S. Mishra. "Graphite to graphene via graphene oxide: an overview on synthesis, properties, and applications." Jom 67.12 (2015): 2855-2868. https://doi.org/10.1007/s11837-015-1522-5

[27] Sun, L. "Structure and synthesis of graphene oxide." Chinese Journal of Chemical Engineering 27.10 (2019): 2251-2260. https://doi.org/10.1016/j.cjche.2019.05.003

[28] Akarsh, P. K., D. Shrinidhi, S. Marathe, and A. K. Bhat. "Graphene oxide as nano-material in developing sustainable concrete–A brief review." Materials Today: Proceedings 60 (2022): 234-246. https://doi.org/10.1016/j.matpr.2021.12.510

[29] Hu, Z. Y., Y. Wan, Y. J. Duan, Y. H. Shi, C. P. Gu, R. Ma, and D. Cui. "A Review of the Impact of Graphene Oxide on Cement Composites." Nanomaterials 15.3 (2025): 216. https://doi.org/10.3390/nano15030216

[30] Huang, C. Y., Y. C. Lin, J. H. Chung, H. Y. Chiu, N. L. Yeh, S. J. Chang, and G. Y. Chen. "Enhancing cementitious composites with functionalized graphene oxide-based materials: surface chemistry and mechanisms." International Journal of Molecular Sciences 24.13 (2023): 10461. https://doi.org/10.3390/ijms241310461

[31] Alex, A. G., A. Kedir, and T. G. Tewele. "Review on effects of graphene oxide on mechanical and microstructure of cement-based materials." Construction and Building Materials 360 (2022): 129609. https://doi.org/10.1016/j.conbuildmat.2022.129609

[32] Liu, C., X. Huang, Y. Y. Wu, X. Deng, J. Liu, Z. Zheng, and D. Hui. "Review on the research progress of cement-based and geopolymer materials modified by graphene and graphene oxide." Nanotechnology Reviews 9.1 (2020): 155-169. https://doi.org/10.1515/ntrev-2020-0014

[33] Zhang, C., W. Wang, Z. Zhu, L. Shao, Y. Wan, and Y. Zhang. "Mechanical and microscopic properties of cement composite expansive soil with graphene oxide: ecofriendly modification material." International Journal of Geomechanics 23.6 (2023): 04023071. https://doi.org/10.1061/IJGNAI.GMENG-8574

[34] Sedaghat, A., M. K. Ram, A. Zayed, R. Kamal, and N. Shanahan. "Investigation of physical properties of graphene-cement composite for structural applications." Open Journal of Composite Materials 4.1 (2014): 12-21. https://doi.org/10.4236/ojcm.2014.41002

[35] Prabakar, J., N. Dendorkar, and R. K. Morchhale. "Influence of fly ash on strength behavior of typical soils." Construction and Building Materials 18.4 (2004): 263-267. https://doi.org/10.1016/j.conbuildmat.2003.11.003

[36] Kolias, S., V. Kasselouri-Rigopoulou, and A. Karahalios. "Stabilisation of clayey soils with high calcium fly ash and cement." Cement and Concrete Composites 27.2 (2005): 301-313. https://doi.org/10.1016/j.cemconcomp.2004.02.019

[37] Sezer, A., G. İnan, H. R. Yılmaz, and K. Ramyar. "Utilization of a very high lime fly ash for improvement of Izmir clay." Building and Environment 41.2 (2006): 150-155. https://doi.org/10.1016/j.buildenv.2004.12.009

[38] Lin, D. F., K. L. Lin, and H. L. Luo. "A comparison between sludge ash and fly ash on the improvement in soft soil." Journal of the Air & Waste Management Association 57.1 (2007): 59-64. https://doi.org/10.1080/10473289.2007.10465294

[39] Sharma, N. K., S. K. Swain, and U. C. Sahoo. "Stabilization of a clayey soil with fly ash and lime: a micro level investigation." Geotechnical and Geological Engineering 30.5 (2012): 1197-1205. https://doi.org/10.1007/s10706-012-9532-3

[40] Saafi, M., L. Tang, J. Fung, M. Rahman, and J. Liggat. "Enhanced properties of graphene/fly ash geopolymeric composite cement." Cement and Concrete Research 67 (2015): 292-299. https://doi.org/10.1016/j.cemconres.2014.08.011

[41] Ozdemir, M. A. "Improvement in bearing capacity of a soft soil by addition of fly ash." Procedia Engineering 143 (2016): 498-505. https://doi.org/10.1016/j.proeng.2016.06.063

[42] Naseri, F., M. Irani, and M. Dehkhodarajabi. "Effect of graphene oxide nanosheets on the geotechnical properties of cemented silty soil." Archives of Civil and Mechanical Engineering 16.4 (2016): 695-701. https://doi.org/10.1016/j.acme.2016.04.008

[43] Zhou, G. X., J. Zhong, H. Zhang, X. Hu, J. Wu, N. Koratkar, and X. Shi. "Influence of releasing graphene oxide into a clayey sand: physical and mechanical properties." RSC Advances 7.29 (2017): 18060-18067. https://doi.org/10.1039/C7RA01539A

[44] Li, M., C. Fang, S. Kawasaki, and V. Achal. "Fly ash incorporated with biocement to improve strength of expansive soil." Scientific Reports 8.1 (2018): 2565. https://doi.org/10.1038/s41598-018-20921-0

[45] Zhang, J., P. Su, K. Wen, Y. Li, and L. Li. "Mechanical performance and environmental effect of coal fly ash on MICP-induced soil improvement." KSCE Journal of Civil Engineering 24.10 (2020): 3189-3201. https://doi.org/10.1007/s12205-020-1931-z

[46] Li, D., P. Lei, H. Zhang, J. Liu, and W. Lu. "Co-Effects of Graphene Oxide and Cement on Geotechnical Properties of Loess." Advances in Materials Science and Engineering 2021 (2021): 7429310. https://doi.org/10.1155/2021/7429310

[47] Fattah, M. Y., S. A. Al-Haddad, A. A. Shahoobe, and K. R. Al-Khafaji. "Characteristics of soft clays enhanced by graphene oxide." In IOP Conference Series: Earth and Environmental Science 856.1 (2021): 012018. IOP Publishing. https://doi.org/10.1088/1755-1315/856/1/012018

[48] Aziz, M., M. Hamza, A. M. Rasool, U. Ali, T. Ahmed, Z. N. Kharal, and Z. U. Rehman. "Use of graphene oxide nanomaterial to improve mechanical properties of cement-treated silty soil." Arabian Journal for Science and Engineering 48.4 (2023): 5603-5618. https://doi.org/10.1007/s13369-022-07530-w

[49] Mohamed, A. A. M. S., J. Yuan, M. Al-Ajamee, Y. Dong, Y. Ren, and T. Hakuzweyezu. "Improvement of expansive soil characteristics stabilized with sawdust ash, high calcium fly ash and cement." Case Studies in Construction Materials 18 (2023): e01894. https://doi.org/10.1016/j.cscm.2023.e01894

[50] Zhang, J., J. Zhang, P. Miao, and Y. Shu. "Experimental investigation and analysis of the impact of salinity erosion on the strength of graphene oxide cement soil." Case Studies in Construction Materials 21 (2024): e03413. https://doi.org/10.1016/j.cscm.2024.e03413

[51] Jiajia, F., W. Wei, F. Tianhong, W. Xudong, W. Hongxiang, and X. Mengqi. "Dynamic characteristics and microscopic mechanism of graphene oxide modified coastal soft soil under small strain." Construction and Building Materials 448 (2024): 138257. https://doi.org/10.1016/j.conbuildmat.2024.138257

[52] Zhang, J. and J. Zhang. "Experimental study and analysis of the static and dynamic mechanical properties of graphene oxide cement soil under composite salinity erosion." Construction and Building Materials 451 (2024): 138848. https://doi.org/10.1016/j.conbuildmat.2024.138848

[53] Li, Y., Z. Zhong, X. Ma, Y. Gan, and X. Kang. "High-performance superhydrophobic fly ash based geopolymers with graphene oxide reinforcement for enhanced durability and repellency." Construction and Building Materials 452 (2024): 138944. https://doi.org/10.1016/j.conbuildmat.2024.138944

[54] Li, Z. and X. Shi. "Influence of Graphene Oxide on Resistance of A Fly Ash-Based Geopolymer Paste to Cyclic Freeze-Thaw Damage and Post-Damage Carbonation." Cement and Concrete Composites (2025): 106023. https://doi.org/10.1016/j.cemconcomp.2025.106023
[55] ASTM D422-63. "Standard Test Method for Particle-Size Analysis of Soils." ASTM International, Pennsylvania, United States (2007). https://doi.org/10.1520/D0422-63R07
[56] ASTM D854-14. "Standard Test Methods for Specific Gravity of Soil Solids by Water Pycnometer." ASTM International, Pennsylvania, United States (2014). https://doi.org/10.1520/D0854-14
[57] ASTM D4318-17e1. "Standard Test Methods for Liquid Limit, Plastic Limit, and Plasticity Index of Soils." ASTM International, Pennsylvania, United States (2017). https://doi.org/10.1520/D4318-17E01
[58] ASTM D698-12e2. "Standard Test Methods for Laboratory Compaction Characteristics of Soil Using Standard Effort." ASTM International, Pennsylvania, United States (2012). https://doi.org/10.1520/D0698-12E02
[59] ASTM D2166/D2166M-13. "Standard Test Method for Unconfined Compressive Strength of Cohesive Soil." ASTM International, Pennsylvania, United States (2013).
[60] Wang, E., T. Zhou, H. Jiang, X. Liu, and C. Wu. "Effects of carbon nanotubes treatment on engineering properties of sandy fine-grained soils subject to freeze-thaw cycles." Research in Cold and Arid Regions (2025). https://doi.org/10.1016/j.rcar.2025.03.003
[61] Cwirzen, A. and K. Habermehl-Cwirzen. "The effect of carbon nano- and microfibers on strength and residual cumulative strain of mortars subjected to freeze-thaw cycles." Journal of Advanced Concrete Technology 11.3 (2013): 80-88. https://doi.org/10.3151/jact.11.80
[62] Yuan, X., M. Dai, Y. Gao, F. Liu, and M. Zhang. "Pore morphology based on graphene oxide modified steel fibre concrete for freeze–thaw resistance." Construction and Building Materials 409 (2023): 133877. https://doi.org/10.1016/j.conbuildmat.2023.133877
[63] Saride, S. and T. T. Dutta. "Effect of fly-ash stabilization on stiffness modulus degradation of expansive clays." Journal of Materials in Civil Engineering 28.12 (2016): 4016166. https://doi.org/10.1061/(ASCE)MT.1943-5533.000167
[64] James, J., S. Vijayasimhan, and E. Eyo. "Stress-strain characteristics and mineralogy of an expansive soil stabilized using lime and phosphogypsum." Applied Sciences 13.1 (2022): 123. https://doi.org/10.3390/app13010123
[65] Ranjbar, N., M. Mehrali, M. Mehrali, U. J. Alengaram, and M. Z. Jumaat. "Graphene nanoplatelet-fly ash based geopolymer composites." Cement and Concrete Research 76 (2015): 222-231. https://doi.org/10.1016/j.cemconres.2015.06.003
[66] Hotineanu, A., M. Bouasker, A. Aldaood, and M. Al-Mukhtar. "Effect of freeze–thaw cycling on the mechanical properties of lime-stabilized expansive clays." Cold Regions Science and Technology 119 (2015): 151-157. https://doi.org/10.1016/j.coldregions.2015.08.008
[67] Fakhrabadi, A., A. J. Choobbasti, and S. S. Kutanaei. "Durability evaluation of clayey sandy soil stabilized with copper-slag-based geopolymer under freezing–thawing cycles." International Journal of Pavement Research and Technology 18.1 (2025): 256-273. https://doi.org/10.1007/s42947-023-00341-8
[68] Tiwari, N., N. Satyam, and A. J. Puppala. "Strength and durability assessment of expansive soil stabilized with recycled ash and natural fibers." Transportation Geotechnics 29 (2021): 100556. https://doi.org/10.1016/j.trgeo.2021.100556

Author Guidelines EditEdit Author Guidelines

GENERAL GUIDELINES FOR AUTHORS

Journal of civil engineering researches invites unsolicited contributions of several forms: articles, reviews and discussion articles, translations, and fora. Contributions should fall within the broad scope of the journal, as outlined in the statement of scope and focus. Contributors should present their material in a form that is accessible to a general anthropological readership. We especially invite contributions that engage with debates from previously published articles in the journal.

Submissions are double-blind peer-reviewed in accordance with our policy. Submissions will be immediately acknowledged but due to the review process, acceptance may take up to three months. Submissions should be submitted via our website submission form (see links above for registration and login). Once you login, make sure your user profile has "author" selected, then click "new submission" and follow the instructions carefully to submit your article. If problems arise, first check the FAQ and Troubleshooting guide posted below. If you are still experiencing difficulty, articles can be submitted to the editors as email attachments.

Each article should be accompanied by a title page that includes: all authors' names, institutional affiliations, address, telephone numbers and e-mail address. Papers should be no longer than 10,000 words (inclusive of abstract 100-150 words, footnotes, bibliography and notes on contributors), unless permission for a longer submission has been granted in advance by the Editors. Each article must include a 100 words "note on contributor(s)" together will full institutional address details, including email address. We request that you submit this material (title page and notes on the contributors) as "supplementary files" rather than in the article itself, which will need to be blinded for peer-review.

We are unable to pay for permissions to publish pieces whose copyright is not held by the author. Authors should secure rights before submitting translations, illustrations or long quotes. The views expressed in all articles are those of the authors and not necessarily those of the journal or its editors. After acceptance, authors and Special Issue guest editors whose institutions have an Open Access library fund must commit to apply to assist in article production costs. Proof of application will be requested. Though publication is not usually contingent on the availability of funding, the Journal is generally under no obligation to publish a work if funding which can be destined to support open access is not made available.

Word template and guidelines

Our tailored Word template and guidelines will help you format and structure your article, with useful general advice and Word tips.

(La)TeX template and guidelines

We welcome submissions of (La)TeX files. If you have used any .bib files when creating your article, please include these with your submission so that we can generate the reference list and citations in the journal-specific style

Artwork guidelines

Illustrations, pictures and graphs, should be supplied with the highest quality and in an electronic format that helps us to publish your article in the best way possible. Please follow the guidelines below to enable us to prepare your artwork for the printed issue as well as the online version.

Format: TIFF, JPEG: Common format for pictures (containing no text or graphs).

EPS: Preferred format for graphs and line art (retains quality when enlarging/zooming in).

Placement: Figures/charts and tables created in MS Word should be included in the main text rather than at the end of the document.

Figures and other files created outside Word (i.e. Excel, PowerPoint, JPG, TIFF, EPS, and PDF) should be submitted separately. Please add a placeholder note in the running text (i.e. "[insert Figure 1.]")

Resolution: Rasterized based files (i.e. with .tiff or .jpeg extension) require a resolution of at least 300 dpi (dots per inch). Line art should be supplied with a minimum resolution of 800 dpi.

Colour: Please note that images supplied in colour will be published in colour online and black and white in print (unless otherwise arranged). Therefore, it is important that you supply images that are comprehensible in black and white as well (i.e. by using colour with a distinctive pattern or dotted lines). The captions should reflect this by not using words indicating colour.

Dimension: Check that the artworks supplied match or exceed the dimensions of the journal. Images cannot be scaled up after origination

Fonts: The lettering used in the artwork should not vary too much in size and type (usually sans serif font as a default).

Authors services:

For reformatting your manuscript to fit the requirement of the Journal of Civil Engineering Researchers and/or English language editing please send an email to the following address:

researchers.services@gmail.com

Noted: There is a fixed charge for these mentioned services that is a function of the manuscript length. The amount of this charge will be notified through a reply email.

FAQ AND TROUBLESHOOTING FOR AUTHORS

I cannot log in to the system. How do I acquire a new user name and password?

If you cannot remember your username, please write an email to (journals.researchers@gmail.com), who will locate your username and notify you. If you know your username, but cannot remember your password, please click the "Login" link on the left-hand menu at homepage. Below the fields for entering your username and password, you will notice a link that asks "Forgot your password?"; click that link and then enter your email adddress to reset your password. You will be sent an automated message with a temporary password and instructions for how to create a new password. TIP: If you do not receive the automated email in your inbox, please check your SPAM or Junk Mail folder. For any other issues, please contact our Managing Editor,Kamyar Bagherinejad (admin@journals-researchers.com).

How do I locate the online submission form and fill it out?

First you need to register or login (see above). Once you are logged in, make sure the "roles" section of your profile has "Author" selected. Once you assign yourself the role of "Author," save your profile and then click the "New Submission" link on your user home page.

Once you arrive at the submission form page, please read the instructions carefully filling out all necessary information. Unless specified otherwise by the editors, the journal section to be selected for your submission should be "Artlcles." Proceed to the remaining sections, checking all boxes of the submission preparation checklist, and checking the box in the copyright notice section (thus agreeing to journals-researchers's copyright terms). Once the first page is completed, click "Save and Continue." The next page allows you to upload your submission. Use the form to choose your file from your computer. Make sure you click "Upload." The page will refresh and you may then click "Save and Continue." You will then proceed to a page for entering the metadata for your article. Please fill out all required fields and any further information you can provide. Click "Save and Continue." The next page allows you to upload supplementary files (images, audiovisual materials, etc.). These are not required, but if you wish to provide supplementary materials, please upload them here (do no forget to click "Upload." Then click "Save and Continue." This brings you to the final page of the submission form. Please click "Finish Submission" in order to close the submission process. You wil then be notified by email that your article has been successfully submitted. TIP: If you do not receive the automated email in your inbox, please check your SPAM or Junk Mail folder. For any other issues, please contact our Managing Editor, Kamyar Bagherinejad (admin@journals-researchers.com).

Why am I not receiving any email notifications from HAU?

Unfortunately, some automated messages from Open Journal Systems arrive in users' Spam (or Junk Mail) folders. First, check those folders to see if the message was filtered into there. You may also change the settings of your email by editing your preferences to accept all mail from [jcer] and related journals-researchers.com email accounts.

I am trying to upload a revised article following an initial round of peer-review, but I cannot locate where to upload the article. Where do I submit a revised article?

Follow the login process outlined above and when you successfully login you will see on your user home page a link next to "Author" for "active" articles in our system (usually it is only one article, but if you have mulitple submissions currently in our system, the number could be higher. Click the "Active" link and you will be led to a page that lists your authored articles currently in our system. Click the link under the column labeled "Status" and this will take you to a page showing the current review status of your article. At the very bottom of the screen, you will see an upload form under the heading "Editor decision." Here you may upload your revised article. An automated email will be sent to the editors and you may also notify them directly via email. You may then logout.

I successfully submitted an article; how long will it take for the editors to respond to me with a decision.

For all articles that are recommended for peer-review, the editors of JCER strive to notify authors of a decision within 4-6 weeks. You may contact JCER's Managing Editor, Kamyar Bagherinejad (admin@journals-researchers.com). if you have any questions relating to the review process and its duration.

For all other inquiries, please contact: Kamyar Bagherinejad (Managing Editor)

Privacy Statement

The names and email addresses entered in this journal site will be used exclusively for the stated purposes of this journal and will not be made available for any other purpose or to any other party.

Articles

Section default policy

Make a new submission to the Articles section.

Copyright Notice EditEdit Copyright Notice

Journal of Civil Engineering Researchers follows the regulations of the International Committee on Publication Ethics (COPE) and the ethical principles of publishing articles in this journal are set based on the rules of this committee, and in case of problems, it will be treated according to these rules.

Privacy Statement EditEdit Privacy Statement

The names and email addresses entered in this journal site will be used exclusively for the stated purposes of this journal and will not be made available for any other purpose or to any other party.

Scholars Pavilion

Scholars Pavilion or **Scholars Chartagi** is a monument donated by the Islamic Republic of Iran to the United Nations Office at Vienna. The monument architecture is claimed by the Islamic Republic News Agency of Iran to be a combination of Islamic and Achaemenid architecture, although the latter clearly predominates in the decorative features, with Persian columns and other features from Persepolis and other remains from the Achaemenid dynasty. The Chahartaq pavilion form runs through the architecture of Persia from pre-Islamic times to the present.

Statues of four famous Persian medieval scholars, Omar Khayyam, Al-Biruni, Muhammad ibn Zakariya al-Razi and Ibn-Sina are inside the pavilion. This monument donated in June 2009 in occasion of Iran's peaceful developments in science.

J-Researchers